Crystalline Silver Plasmonic Nanocircuitry for Efficient Coupling with Single Organic Molecules

Von der Universität Bayreuth
zur Erlangung des Grades eines
Doktors der Naturwissenschaften (Dr. rer. nat.)
genehmigte Abhandlung

von
CHRISTIAN ANDREAS SCHÖRNER
geboren in Naila

Angefertigt am
Lehrstuhl für Experimentalphysik III
der Universität Bayreuth

1. Gutachter:	Prof. Dr. Markus Lippitz
2. Gutachter:	Prof. Dr. Richard Hildner
3. Gutachter:	Prof. Dr. Bert Hecht

TAG DER EINREICHUNG:	18.03.2021
TAG DES KOLLOQUIUMS:	12.11.2021

Dedicated to plasmonics

— may the field live up to its visions and enter the everyday world.

ABSTRACT

Quantum emitters such as atoms, quantum dots or single organic molecules, with a size of a few *Å*ngström to a few nanometer, are among the tiniest light sources imaginable. The coupling of a single quantum emitter to an optical waveguide is particularly interesting, as the quantum mechanical state of the emitter can be accessed and modified via optical signals propagating along the waveguide. At room temperature, the interaction of a quantum emitter embedded in a solid with light is typically a weak effect, as the cross-section for absorption and scattering is by many orders of magnitude smaller than a diffraction-limited spot of light. Future applications of the waveguide-emitter system in nanophotonic circuitry, however, require an efficient coupling of the emitter and the waveguide circuit in order to achieve a successful implementation of functionalities, such as the realization of a single-photon transistor. Plasmonic nanostructures from noble metals break the diffraction limit by mixing optical fields with electronic excitations and thus promise to open up regimes of much more efficient light-matter interaction by confining the light to the position of the quantum emitter. In this regard, this thesis considers complex-shaped plasmonic nanocircuits fabricated from crystalline silver in order to realize an efficient emitter-waveguide junction in the visible spectral range. To address this issue, high-quality materials and nanofabrication protocols are required, sensitive experimental setups are designed and operated, and comprehensive numerical modeling is performed to compare theoretical expectations with experimental results.

At first, different numerical models are presented, which allow to calculate fundamental properties of plasmonic nanostructures. These include absorption and scattering calculations, eigenmodes of waveguides, propagation parameters, incoupling and collection efficiencies, and the full three-dimensional simulation of dipole-emission near a plasmonic waveguide. Furthermore, the theoretical framework for far-field imaging is briefly reviewed and implemented numerically.

The following part is dedicated to high aspect ratio single-crystalline silver flakes, which form the general basis of all plasmonic nano-constructs throughout this thesis. Chemical synthesis protocols are presented that allow to fabricate laterally large (several 10 µm) but thin (< 100 nm) flakes of extraordinarily high quality. This quality is characterized by an elemental composition of pure silver, single-crystallinity across the whole structure and a truly atomically-smooth surface. Therefore, the flakes are ideal platforms for the top-down fabrication of plasmonic nanostructures of nearly arbitrary shape by focused ion beam milling. Furthermore, atomic layer deposition of few-nanometer cover layers is applied to protect the flakes and nanostructures from degradation.

Based on these new opportunities of nanofabrication with single-crystalline silver, in the next part, the first successful fabrication and application of a complex-shaped silver plasmonic circuit is presented. Its central waveguide part is given by two silver nanowires separated by only 60 nm. By using silver instead of the conventionally used gold, the circuit can operate in the visible spectral range where a variety of dye molecules with high fluorescence quantum yield exists. A tiny (~20 nm) polystyrene bead doped with a few tens of fluorophores is attached to the circuit and its excitation is found to depend sensitively on the excited near-field close to the structure. Further, a controlled remote excitation of the bead via different coherent superpositions of waveguide modes, as well as the subsequent efficient funneling of the majority of the fluorescence (~63 %) back into the waveguide, is demonstrated.

In the following chapter, single organic dye molecules located inside the 60 nm gap between two silver nanowires are investigated. A newly constructed optical setup allows to detect for the first time a single-molecule nonlinearity in a plasmonic waveguide. This effect is demonstrated fully remotely, i.e., by applying the necessary optical pulse-sequence via propagating plasmonic modes traveling along the waveguide gap toward the molecule. A strong drop in the single-molecule fluorescence emission by stimulated emission is detected, signaling a nonlinear plasmon-plasmon interaction in the waveguide at the single molecule. Particularly, due to the plasmonic field confinement, the efficiency of triggering the stimulated emission transition is found to be about 30 times higher in the waveguide compared to a diffraction-limited Gaussian focus.

Finally, isolated crystalline silver nanowires in a few nanometer distance to an underlying silver flake surface are investigated with regard to the extreme light-confinement in the gap. In particular, along the short nanowire axis, the structure represents a nanoscale metal-insulator-metal Fabry-Pérot cavity for gap-plasmons with a length of 20-30 nm and a height of about 2 nm only. The resonances of several silver cavities are investigated experimentally, finding a good agreement with numerical scattering simulations. Furthermore, an optical setup is presented that probes the reflected light from the sample with an auto-balanced photodetector, reaching a sensitivity of about 10^{-6} at 1 Hz bandwidth. First steps and measurements toward such an ultra-sensitive probing of plasmonic nano-cavities are performed, with the future goal of enhancing the coherent light-matter interaction of single quantum emitters placed in the hot-spot region.

ZUSAMMENFASSUNG

Quantenemitter wie Atome, Quantenpunkte oder einzelne organische Moleküle, mit Größen von einigen *Å*ngström bis Nanometern, zählen zu den kleinsten denkbaren Lichtquellen. Die Kopplung eines solchen Quantenemitters an einen optischen Wellenleiter ist besonders interessant, da der quantenmechanische Zustand des Emitters über optische Signale im Wellenleiter zugänglich und modifizierbar ist. Bei Raumtemperatur ist die Wechselwirkung eines Quantenemitters mit Licht meist schwach, da der Wechselwirkungs-Querschnitt für die Absorption bzw. Streuung um viele Größenordnungen kleiner als ein beugungslimitierter Lichtfleck ist. Zukünftige Anwendungen des Wellenleiter-Emitter Systems in nanophotonischen Schaltkreisen benötigen jedoch eine effiziente Kopplung des Emitters mit dem Wellenleiter, um letztendlich eine Funktionalität zu erreichen, z.B. die eines Einzelphotonen-Transistors. Plasmonische Nanostrukturen aus Edelmetallen erlauben es das Beugungslimit durch das Mischen von optischen Feldern mit elektronischen Anregungen zu umgehen. Sie versprechen es, eine effizientere Licht-Materie Wechselwirkung zu ermöglichen, indem das Licht auf die Position des Quentenemitters konzentriert wird. In diesem Hinblick befasst sich die vorliegende Arbeit mit komplex geformten plasmonischen Schaltkreisen aus kristallinem Silber, um eine effiziente Emitter-Wellenleiter Wechselwirkung im sichtbaren Spektralbereich zu ermöglichen. Um diesem Ziel näher zu kommen, werden einerseits hoch-qualitative Materialien und Fertigungsprozesse auf der Nanoskala benötigt sowie empfindliche experimentelle Aufbauten entworfen und betrieben. Andererseits werden umfangreiche numerische Simulationen durchgeführt, die es erlauben theoretische Erwartungen mit den experimentellen Ergebnissen zu vergleichen.

Zunächst werden verschiedende numerische Modelle präsentiert, die es ermöglichen die grundlegenden Eigenschaften plasmonischer Nanostrukturen zu berechnen. Diese beinhalten die Berechnung von Absorption und Streuung, Eigenmoden von Wellenleitern, Propagations-Parametern, Einkoppel- und Aufsammel-Effizienzen sowie Simulationen eines abstrahlenden elektrischen Dipols nahe des Wellenleiters. Weiterhin wird der theoretische Rahmen von Fernfeld-Abbildungen erläutert und numerisch implementiert.

Der folgende Teil widmet sich einkristallinen Silber-Flocken, die die grundlegende Basis aller plasmonischen Konstrukte dieser Arbeit darstellen. Mittels einer chemischen Synthese werden lateral große (einige 10 µm) aber dünne (< 100 nm) Kristalle von außerordentlich hoher Qualität hergestellt. Bezeichnend für diese Qualität sind die elementare Zusammensetzung aus purem Silber, die Kristallinität über die vollständige Größe sowie atomar glatte Oberflächen. Daher stellen diese Kristalle eine ideale Ausgangsbasis für die Herstellung von fast beliebig beformten plasmonischen Nanostrukturen mittels eines fokussierten Ionenstrahls dar. Weiterhin wird die Atom-

lagenabscheidung von Schutzschichten weniger Nanometer Dicke angewendet, um die Degradation der Kristalle und Nanostrukturen zu verhindern.

Auf Grundlage dieser neuen Möglichkeiten der Nanofabrikation mit Silber-Kristallen, wird im nächsten Teil die erste erfolgreiche Herstellung und Anwendung eines komplex geformten plasmonischen Schaltkreises aus Silber vorgestellt. Der zentrale Wellenleiter-Teil besteht dabei aus zwei parallelen Silber-Nanodrähten in 60 nm Abstand. Durch den Einsatz von Silber anstelle des konventionell eingesetzen Goldes, kann der Schaltkreis im sichtbaren Spekralbereich eingesetzt werden, wo eine Vielzahl von Farbstoffmolekülen mit hoher Quantenausbeute verfügbar ist. Eine winzige (~20 nm) Polystyrol Kugel mit wenigen zehn Fluorophoren darin wird an den Wellenleiter gebracht. Es wird beobachtet, dass die Anregung der Fluorophore empfindlich vom herrschenden Nahfeld an der Struktur abhängt. Weiterhin wird eine kontrollierte Anregung der Fluorophore mittels einer kohärenten Überlagerung von verschiedenen Wellenleiter-Moden sowie die anschließende effizente Bündelung des Großteils der Fluoreszenz (~63 %) zurück in den Wellenleiter nachgewiesen.

Im folgenden Kapitel werden einzelne organische Moleküle im 60 nm Spalt zwischen zwei Silber-Nanodrähten untersucht. Ein neu konstruierter optischer Aufbau ermöglicht es zum ersten Mal eine Einzelmolekül-Nichtlinearität in einem plasmonischen Wellenleiter zu detektieren. Dieser Effekt wird nachgewiesen, indem die nötige optische Puls-Sequenz vollständig mittels propagierender plasmonischer Moden im Spalt zum Molekül geleitet wird. Ein starker Einbruch der Fluoreszenz des Moleküls durch stimulierte Emission wird detektiert, was eine nichtlineare Plasmon-Plasmon Wechselwirkung im Wellenleiter durch das Molekül darstellt. Durch die starke Konzentration des Licht-Feldes im plasmonischen Wellenleiter steigt die Effizient der stimulierten Emission um einen Faktor von etwa 30 gegenüber Referenzexperimenten mit einem beugungslimitieren Laser-Fokus.

Zum Abschluss werden einzelne kristalline Silber-Nanodrähte in einen Abstand von wenigen Nanometern zur Oberfläche eines Silber-Kristalls gebracht, was eine extreme Licht-Konzentration im Spalt zur Folge hat. Besonders in Richtung der kurzen Nanodraht Achse stellt das Konstrukt einen nano-skaligen Fabry-Pérot Resonator für propagierende Plasmonen im Spalt dar, mit einer Länge von nur 20-30 nm und einer Höhe von etwa 2 nm. Die Streuung der Silber-Resonatoren wird in guter Übereinstimmung zwischen Experiment und numerischen Simulationen charakterisiert. Zudem wird ein optischer Aufbau vorgestellt, der das reflektierte Licht einer Probe mit einem empfindlichen Photodetektor aufzeichnet und dabei eine Sensitivität von circa 10^{-6} bei 1 Hz Bandbreite erreicht. Erste Schritte und Messungen in Richtung von derartig empfindlichen Untersuchungen von plasmonischen Resonatoren werden unternommen, mit dem zukünftigen Ziel die kohärente Wechselwirkung eines Quantenemitters mit Licht zu erhöhen.

PUBLICATIONS

Articles in scientific journals, part of this thesis

1. C. Schörner, and M. Lippitz, *High-Q plasmonic nanowire-on-mirror resonators by atomically smooth single-crystalline silver flakes*, **Journal of Chemical Physics 155(23), 234202 (2021)**.

2. C. Schörner, and M. Lippitz, *Single Molecule Nonlinearity in a Plasmonic Waveguide*, **Nano Letters 20(3), 2152-2156 (2020)**.

3. C. Schörner, S. Adhikari, and M. Lippitz, *A Single-Crystalline Silver Plasmonic Circuit for Visible Quantum Emitters*, **Nano Letters 19(5), 3238-3243 (2019)**.

Articles in scientific journals, not part of this thesis

4. C. Schörner, C. Neuber, and R. Hildner, *Two-path self-interference in PTCDA active waveguides maps the dispersion and refraction of a single waveguide mode*, **APL Photonics 4(1), 016104 (2019)**.

5. C. Schörner, S. Motamen, L. Simon, G. Reiter, and R. Hildner, *Self-Interference of Exciton Emission in Organic Single Crystals Visualized by Energy-Momentum Spectroscopy*, **ACS Omega 3(6), 6728-6736 (2018)**.

6. C. Schörner, D. Wolf, T. Schumacher, P. Bauer, M. Thelakkat, and M. Lippitz, *Nondestructive Probing of a Photoswitchable Dithienylethene Coupled to Plasmonic Nanostructures*, **The Journal of Physical Chemistry C 121(30), 16528-16532 (2017)**.

7. S. Motamen, C. Schörner, D. Raithel, J.-P. Malval, T. Jarrosson, F. Serein-Spirau, L. Simon, R. Hildner, and G. Reiter, *Low loss optical waveguiding in large single crystals of a thiophene-based oligomer*, **Physical Chemistry Chemical Physics 19(24), 15980-15987 (2017)**.

Contributions on international conferences

Talks

1. C. Schörner, S. Adhikari, and M. Lippitz, *Visible light operation of a single-crystalline silver plasmonic nanocircuit*, DPG spring meeting 2019 - Regensburg/Germany

2. C. Schörner, S. Adhikari, and M. Lippitz, *Coupling of IR140 dye molecules to a plasmonic two-wire waveguide*, DPG spring meeting 2018 - Berlin/Germany

Posters

1. C. Schörner, S. Adhikari, and M. Lippitz, *Visible light operation of a plasmonic nanocircuit fabricated from single-crystalline silver*, Nanometa 2019 - Seefeld (Tirol)/Austria

2. C. Schörner, S. Motamen, L. Simon, G. Reiter, and R. Hildner, *Self-interference of exciton emission in organic single crystals visualized by energy-momentum spectroscopy*, Gordon Research Conference 2018 - Lucca/Italy

3. C. Schörner, C. Neuber, J. Köhler, H.-W. Schmidt, and R. Hildner, *Single mode active waveguiding in ultrathin layers of PTCDA*, Light harvesting processes 2017 - Banz/Germany

Further talks on workshops, seminars and symposiums

1. C. Schörner, *Stimulated emission of gap-plasmons by a single terrylene molecule*, seminar, october 2019 - Hirschegg, Kleinwalsertal/Austria

2. C. Schörner, *Stimulated emission of plasmons by single organic molecules*, workshop, september 2019 - Dresden/Germany

3. C. Schörner, S. Adhikari, and M. Lippitz, *Visible light operation of a single-crystalline silver plasmonic nanocircuit*, GRK1640 symposium, july 2019 - Bad Honnef/Germany

4. C. Schörner, S. Adhikari, and M. Lippitz, *Visible light operation of a single-crystalline silver plasmonic circuit*, workshop, march 2019 - Bayreuth/Germany

5. C. Schörner, *Propagating surface plasmon polaritons for probing molecular systems*, GRK1640 workshop, october 2017 - Silberbach/Germany

6. C. Schörner, *Propagating surface plasmon polaritons for probing molecular systems*, seminar, september 2017 - Hirschegg, Kleinwalsertal/Austria

CONTENTS

1 PREFACE AND OUTLINE

Nanooptics is an evolving field of research dealing with the various optical phenomena near or even beyond the diffraction limit of light. Originally driven by the miniaturization and integration of electronic computer circuits, the increasing interest for the nano-world is based on the hope that new physical effects at the nanoscale and beyond might find their way into future technological applications such as functional nano-optical circuitry and sensors. Current technologies for the fabrication, manipulation and characterization of materials range from chemical synthesis via electron beam lithography, focused ion beam milling and atomic force microscopy to high-resolution electron microscopy and electron diffraction, among others. Due to their increasing precision, research in nanooptics is able to explore the fundamental light-matter interaction in continuously shrinking volumes. Traditionally, the optical resolution, theoretically described by Ernst Abbe in 1873 [1] and Lord Rayleigh in 1879 [2], cannot be improved arbitrarily. The diffraction of light imposes a limit, which states that light cannot be focused to scales smaller than about half of its wavelength with far-field optics. However, several nanooptical methods have been developed during the last years, opening up investigations beyond the diffraction limit.

Electronic and vibrational transitions of matter are situated in the energetic range of visible to near-infrared light. Optical spectroscopy opens up a great capability to study the fascinating dynamics within the electronic structure of matter. The invention of confocal microscopy [3], where a small pinhole is put in the detection path in front of the detector, has enabled high axial resolution combined with a lateral resolution even slightly beyond the Abbe limit. Nonlinear optical processes, such as multiphoton excitation [4], second-harmonic and third-harmonic generation, and coherent anti-Stokes Raman scattering [5], can be used for high-resolution microscopy as well. Moreover, besides localization-based super-resolution techniques, such as stochastic optical reconstruction microscopy (STORM) [6] and photoactivated localization microscopy (PALM) [7], stimulated emission depletion (STED) microscopy has become very popular for imaging beyond the diffraction limit [8]. In STED microscopy, the excited state of molecules is selectively depopulated in certain volumes close to the focal area of the excitation by stimulated emission. In particular, the highly nonlinear saturation of the stimulated emission as a function of the depletion pulse energy allows for theoretically unlimited lateral resolution, which has been demonstrated experimentally down to about ten nanometers [9, 10].

In contrast to such far-field optical methods, light-matter interaction can also be studied in the near-field. Edward Hutchinson Synge proposed in 1928 to construct a subwavelength aperture in an opaque plate [11]. When placed in close proximity to the sample surface of interest, an illumination spot size not limited by diffraction

is achieved that can be used for optical imaging. This idea can be considered as the basis of the various near-field microscopy methods developed later [12]. A different approach to define subwavelength "hot-spots" of enhanced electromagnetic fields are properly shaped metal nanoparticles. Driven by the quest to understand the effect of surface-enhanced Raman scattering close to rough metal surfaces, the field of *plasmonics* emerged. Depending on the dielectric function of the metal and surrounding, as well as shape and size of the metal particle, certain resonances in the oscillation of the metal's free electrons can appear that are coupled to enhanced subwavelength electromagnetic near-fields. Today, metal nanoparticles find wide applications, e.g., as metamaterials [13], sensors [14], optical antennas [15], as part of plasmonic circuits [16] and also as part in biomedical applications [17]. The electromagnetic near-fields can be shaped by the geometry of the metal, enabling the confinement on a few-nanometer scale down to extreme light-localization at single adatoms at surfaces, called pico-cavities [18–20].

In the last years, the field of plasmonics merged with quantum optics, forming the innovative field of *quantum plasmonics* [21]. Here, the light-matter interaction is engineered to unprecedented strength within nanoscale volumes. The quantumness has its origin either in nonclassical states of the electromagnetic field or in a coupled quantum emitter, or in both of them. Quantum effects in the interaction between localized or propagating plasmons and quantum systems like molecules or quantum dots promise a rich fundamental physics which has yet to be explored. The high interaction between confined plasmonic modes and matter can eventually drive the coupled system into the strong-coupling regime where hybrid light-matter ("polariton") states are formed [22], which, e.g., can lead to a control of photochemical reactions by modifying the excited state manifold [23]. Current plasmonic nanopatch antennas also generate very fast (~10 ps) and bright spontaneous emission from single coupled quantum emitters [24], while approaching the regime of (sub-)nanometer gaps, where further quantum effects such as electron tunneling and nonlocal effects need to be considered [25].

Furthermore, distant quantum emitters can be coupled via the exchange of propagating plasmons along a waveguide structure and form entangled states [26, 27]. For a disordered ensemble of emitters, when being strongly coupled with surface plasmons, a coherent emission can be observed [28]. A lot of fascinating research is performed in this direction, e.g., also at low temperature in photonic crystal waveguides, realizing super-radiance of two separated quantum dots [29] or a single-photon nonlinearity at a single quantum emitter [30]. Such a quantum single-photon nonlinearity at an emitter-waveguide junction is particularly interesting, as it enables the operation of a single-photon transistor. Here, a single incident ("gate") photon could completely control the transmission of (multiple) subsequent ("signal") photons by its influence on the coupled emitter's state. The realization of such a device is long-envisioned on a plasmonic platform [31] and could lead to low-power optical switches and deterministic quantum-information processing with photons [32].

In this regard, the efficient coupling between a quantum emitter and multiple optical fields in a waveguide circuit is an important goal and subject to intense current research. This thesis aims for developing a high-quality plasmonic platform capable

of studying the interaction between strongly confined near-fields in plasmonic nanowaveguides and fluorescent dye molecules at room temperature down to the limit of single molecules as quantum emitters. Two aspects clearly separate this thesis from recent work of the community. First, in contrast to the broad application of gold for plasmonic nanostructures, crystalline silver is applied throughout this thesis as the currently most preferred low-loss plasmonic material, realizing the first complex-shaped silver plasmonic waveguide circuit operating in the visible spectral range. Second, the interaction of quantum emitters with multiple plasmonic fields is studied both by applying a coherent superposition of modes to the waveguide and by applying for the first time optical pulse sequences to a quantum emitter via a plasmonic waveguide. This content of the thesis is embedded in a comprehensive framework, which can be briefly outlined as follows:

Chapter 2 reviews the variety of phenomena taking place in typical organic dye molecules and discusses important aspects of the quantum nature of electronic excitations, including the interaction of single molecules with light. In chapter 3, the basic electromagnetic theory for propagating surface plasmon polaritons is presented. Particularly, the case of a single metal nanowire is discussed, which serves as a building block of the waveguide geometries investigated in this thesis. Furthermore, the theory of emitter-waveguide coupling is reviewed, which can predict the yields of different decay channels of quantum emitters near a plasmonic nanostructure. Complex plasmonic nanostructures embedded in an inhomogeneous environment demand for the numerical simulation of optical near-fields and related properties. Chapter 4 presents different numerical models for predicting the optical properties of plasmonic nanostructures, including their waveguiding characteristics and the emission of dipolar emitters close to the waveguide. High aspect ratio single-crystalline silver flakes as an ideal platform for plasmonic applications are introduced in chapter 5, including a comprehensive characterization of their properties. In chapter 6, the optical properties of a plasmonic nanocircuit fabricated from single-crystalline silver are investigated. In particular, the multi-mode visible wavelength operation and an efficient coupling with organic dye molecules are demonstrated. Further advanced measurements of single organic dye molecules located in a 60 nm gap between two silver nanowires and the interaction of the molecule with an optical two-pulse sequence traveling along the waveguide are subject to chapter 7. Finally, in chapter 8, isolated silver nanowires in a few-nanometer distance to a silver flake surface are investigated, realizing a strong confinement to the nanogap via resonant cavity modes. A general conclusion and an outlook are given in chapter 9.

2 PHOTOPHYSICS OF ORGANIC MOLECULES

During the last decades, the optical spectroscopy of single molecules in solids generated a huge interest in diverse research fields, ranging from physics and chemistry to biology [33]. In contrast to the large ensemble averaging effects that dictate the outcome of experiments with a large number of molecules, single-molecule experiments give access to subtle processes taking place within the molecule's nanoenvironment [34]. Thus, single molecules are nanoscopic point-like probes, e.g., of their local interaction with phonons and of several other quantities such as electric [35], magnetic and optical fields, and strain [36].

The first absorption spectra of single molecules were observed in the pioneering experiment by Moerner and Kador in 1989 [37]. They investigated pentacence molecules in a p-terphenyl crystal at low temperatures using a double modulation method, i.e., frequency modulation and Stark-shift modulation, and thereby achieved a signal-to-noise ratio in the order of just 5. Only one year later, Orrit and Bernard detected not the absorption of a single pentacene molecule but its fluorescence [38]. Since then, fluorescence detection became the method of choice in single-molecule experiments. The easy separation of the red-shifted fluorescence from the laser background with optical filters together with high quantum-yield detectors has enabled much higher signal-to-noise ratios. Single-molecule experiments have soon been pushed to room temperature, where absorption cross-sections are strongly reduced [33].

About two decades after the pioneering experiments, in 2010 and 2011, very sensitive techniques involving ground-state depletion modulation (Xie group) [39], photothermal contrast (Orrit group) [40] and modulation-free auto-balanced detection (Sandoghdar group) [41, 42] demonstrated single-molecule sensitivity in absorption or extinction even at room temperature. These methods try to push single-molecule experiments from the limited range of fluorescent probes to the much larger group of nonfluorescent molecular systems.

In this thesis, single organic dye molecules are applied as single-photon sources and as tiny nonlinear elements in plasmonic waveguide circuits. Thus, the basic photophysics of organic molecules is briefly reviewed here, including their electronic structure, radiative and nonradiative transitions between different energy levels, and broadening mechanisms that dictate the spectral lineshapes at room temperature. Finally, the achievable extinction cross-section of a single molecule at room temperature is discussed.

2.1 BORN OPPENHEIMER APPROXIMATION

A molecule consisting of K nuclei and N electrons can, according to quantum theory, be described by a total wavefunction Ψ with corresponding energy E that is a solution of the Schrödinger-equation

$$\hat{H}_0\Psi = E\Psi \quad . \tag{2.1}$$

The Hamiltonian operator $\hat{H}_0$ can be written as a sum of the kinetic energy of all electrons, the kinetic energy of the nuclei, the Coulomb repulsion between the nuclei, the attraction between electrons and nuclei, and the repulsion between the electrons [43]. Further interactions associated with the electron or nuclear spins are neglected here.

Even for the most simple molecule, the H_2^+-ion, the Schrödinger equation 2.1 is not exactly solvable. Besides numerical techniques, the fundamental approximation of molecular physics is the adiabatic approximation [44]. It is based on the fact that the electron's mass is negligible compared to the nucleus's mass. As a result, the nuclei move much slower than the electrons, which can adapt adiabatically to the (vibrating) configuration of the nuclei. Within a perturbative approach, a set of coupled equations for the electronic wavefunctions and the nuclear wavefunctions can be derived.

A further simplification is achieved if all coupling terms between the movement of the nuclei and the electrons are neglected, which is called *Born-Oppenheimer approximation* [43, 44]. Then, the Schrödinger equation 2.1 can be converted into two separate, decoupled equations for the electronic wavefunctions $\phi_n^{el}(\mathbf{r})$ at the nuclear configuration $\mathbf{R}$ and the nuclear wavefunctions $\chi_{n,\nu}(\mathbf{R})$. Here, $\mathbf{r}$ denotes the electronic coordinates and $\mathbf{R}$ the nuclei coordinates. The electronic wavefunction depends parametrically on the nuclei coordinates $\mathbf{R}$. Within the Born-Oppenheimer approximation, the total wavefunction of a molecular eigenstate in the n-th electronic state and corresponding ν-th nuclear state is reduced to a simple product of the respective wavefunctions given by

$$\Psi_{n,\nu}(\mathbf{r},\mathbf{R}) = \phi_n^{el}(\mathbf{r}) \cdot \chi_{n,\nu}(\mathbf{R}) \quad . \tag{2.2}$$

As a result, the total energy is just the sum of the energy of the nuclei and the electrons' energy. The pure electronic energy of the molecule in the n-th electronic state is considered as a potential energy that forms a higher-dimensional hypersurface $E_n^{el}(\mathbf{R})$ in the space of the nuclei coordinates $\mathbf{R}$ determined by the electronic part of the Schrödinger equation. It should be noted that at configurations where two potential hypersurfaces of different electronic states cross, the adiabatic approximation breaks down [44]. At the minima $\mathbf{R}_{0,n}$ of a potential surface $E_n^{el}(\mathbf{R}_{0,n})$, the nuclei can perform quantized oscillations (c.f. figure 2.1). In the general case of a polyatomic molecule, several normal modes i of frequency ω_i are available. However, it is most instructive

to discuss a single normal mode of frequency ω_0 in harmonic approximation. In this case, the total energy is given by [45]

$$E_{n,\nu} = E_n(\mathbf{R}_{0,n}) + \hbar\omega_0(\nu + \frac{1}{2}) \quad , \tag{2.3}$$

with $\hbar$ being the reduced Planck constant. In conclusion, quantized energy levels of the molecule result. The total energy is composed of a pure electronic energy and an energy of the quantized oscillations of the nuclei relative to each other. While the energy of nuclei normal modes are typically in the infrared spectral region, the electronic states have energy-differences ranging from the vacuum-ultraviolet and visible to the near-infrared spectral range. A contribution of molecular rotations [44] has been neglected here, since the molecules in this thesis are fixed in a surrounding solid, which inhibits the free rotation.

2.2 LIGHT–MATTER INTERACTION

The wavefunctions $\Psi_{n,\nu}(\mathbf{r}, \mathbf{R})$ describe stationary states of the molecule, in which it would reside in case of no external perturbation. In spectroscopy, the perturbation relevant to most transitions is given by a radiation field acting on the molecule. Three main optical processes can occur: absorption, stimulated emission and spontaneous emission. Absorption refers to the process of capturing a quantum of the radiation field, i.e., a photon of energy $\hbar\omega$, leading to a transition of the molecule to a state of higher energy. Stimulated emission can be regarded as the reverse process of emitting a photon accompanied by a transition to a state of lower energy. For both absorption and stimulated emission, the transition rate in a weak field regime is proportional to the intensity of the incident radiation field. Spontaneous emission refers to the emission of a photon into an unoccupied radiation mode [46] and is thus rather triggered by the zero-point radiation field [47]. Hence, a complete description of light-matter interaction demands for a full quantum mechanical treatment of radiation and matter [46]. Particularly in the strong coupling regime, sophisticated quantum-optical models are necessary, as demonstrated by Groß *et al.* [48]. However, in the weak coupling regime, the semi-classical model of light-matter interaction leads to identical results for the absorption and stimulated emission rate compared to an interaction with the quantized radiation field [46]. Furthermore, the rate of spontaneous emission and stimulated emission just differ by the number of photons in the radiation mode considered for stimulated emission [49]. Due to these reasons, in the following, the radiation field is treated classical, while the matter is described by quantum mechanics. This approach is referred to as *semi-classical light-matter interaction*.

Light-matter interaction with a one-electron atom can be approximated by considering a single electron of negative elementary charge $-e$ and mass m in a fixed Coulomb potential $V(\mathbf{r})$, and an electromagnetic field described by its vector potential $\mathbf{A}(\mathbf{r}, t)$. Here, in the following, Coulomb gauge $\nabla \cdot \mathbf{A} = 0$ is used and the scalar potential

is set to zero. Neglecting the electron's spin, the Hamiltonian of the electron in the electromagnetic field is given by [49, 50]

$$\hat{H} = \frac{1}{2m}(\hat{\mathbf{p}} + e\mathbf{A})^2 + V(\mathbf{r}) \quad , \tag{2.4}$$

with the momentum operator $\hat{\mathbf{p}} = -i\hbar\nabla$. Equation 2.4 can be rewritten using the fact that $\hat{\mathbf{p}}$ and $\mathbf{A}$ commute in Coulomb gauge, yielding [49]

$$\hat{H} = \underbrace{\frac{1}{2m}\hat{\mathbf{p}}^2 + V(\mathbf{r})}_{\hat{H}_0} + \underbrace{\frac{e}{m}\mathbf{A}\cdot\hat{\mathbf{p}}}_{\hat{H}'(t)} + \underbrace{\frac{e^2}{2m}\mathbf{A}^2}_{\substack{\approx 0 \\ (weak\ field)}} \quad , \tag{2.5}$$

where the term proportional to $\mathbf{A}^2$ is neglected relative to the linear term (weak field approximation), considering only the absorption and emission of one photon at a time [49]. Thus, the total Hamiltonian is composed of the time-invariant original Hamiltonian $\hat{H}_0$ of the electron (or molecule) and a time-dependent perturbative Hamiltonian $\hat{H}'(t)$ describing the electromagnetic interaction that causes transitions between eigenstates of $\hat{H}_0$ [45, 46]:

$$\hat{H} = \hat{H}_0 + \hat{H}'(t) \quad . \tag{2.6}$$

A monochromatic electromagnetic plane wave is described by a vector potential given by [46, 50]

$$\mathbf{A}(\mathbf{r}, t) = \frac{\mathbf{A}_0}{2}\left[\mathrm{e}^{i(\mathbf{k}\cdot\mathbf{r}-\omega t)} - \mathrm{e}^{-i(\mathbf{k}\cdot\mathbf{r}-\omega t)}\right] \quad , \tag{2.7}$$

with amplitude vector $\mathbf{A}_0$, wavevector $\mathbf{k}$ and angular frequency ω. The real amplitude of the electric field E_0 is obtained from the amplitude of the vector potential via $E_0 = -\omega A_0$ [50]. In order to further simplify the interaction, the exponential $\exp(i\,\mathbf{k}\cdot\mathbf{r})$ is expanded in a Taylor series according to

$$\mathrm{e}^{\pm i\,\mathbf{k}\cdot\mathbf{r}} = 1 \pm i\,\mathbf{k}\cdot\mathbf{r}\ldots \tag{2.8}$$

Following McHale [50], the matrix elements of $\hat{H}'(t)$ between two eigenstates of $\hat{H}_0$, i.e., an initial state $|i\rangle$ and a final state $|f\rangle$, are considered. Taking the expansion in equation 2.8 up to the second term into account, the matrix elements $\langle f|\hat{H}'(t)|i\rangle$ can be decomposed into the sum of an electric dipole $V_{fi}^{ED}(t)$, magnetic dipole $V_{fi}^{MD}(t)$ and electric quadrupole term $V_{fi}^{EQ}(t)$ given by [46, 49, 50]

$$V_{fi}^{ED}(t) = \frac{-i\omega_{fi}}{2\omega}\,\langle f|\hat{\boldsymbol{\mu}}\cdot\mathbf{E}_0|i\rangle\,\left(\mathrm{e}^{i\omega t} + \mathrm{e}^{-i\omega t}\right) \quad , \tag{2.9}$$

$$V_{fi}^{MD}(t) = \frac{-ieE_0}{2mc}\,\langle f|\hat{L}_x|i\rangle\,\left(\mathrm{e}^{i\omega t} - \mathrm{e}^{-i\omega t}\right) \quad , \tag{2.10}$$

$$V_{fi}^{EQ}(t) = \frac{-eE_0\omega_{fi}}{2c}\,\langle f|\hat{y}\,\hat{z}|i\rangle\,\left(\mathrm{e}^{i\omega t} - \mathrm{e}^{-i\omega t}\right) \quad . \tag{2.11}$$

Here, c is the speed of light in vacuum and $\omega_{fi} = (E_f - E_i)/\hbar$ represents the energy difference between the final state $|f\rangle$ and initial state $|i\rangle$. The electric dipole term in equation 2.9, with the electric transition dipole operator $\hat{\boldsymbol{\mu}} = -e\mathbf{r}$ and electric field amplitude vector $\mathbf{E}_0$, is typically the most important term in optical spectroscopy. This is based on the fact that for far-field optical modes (i.e., plane waves), the field strength of the electric field hardly varies over the spatial dimension l of a molecule [46]. In the visible spectrum $kl \ll 1$ is well fulfilled and the electric dipole term dominates. Taking only this term into account refers to as the *electric dipole approximation* of light-matter interaction. The second term of the expansion in equation 2.8 leads to the typically much smaller magnetic dipole and electric quadrupole terms in equation 2.10 and 2.11, which here assume a plane wave specifically polarized along $\hat{z}$ and propagating along $\hat{y}$. $\hat{L}_x$ represents the x-component of the angular momentum operator, which is responsible for magnetic dipole transitions, as the magnetic dipole moment is proportional to the orbital angular momentum. The electric quadrupole term is characterized by two different cartesian coordinates, in contrast to the single position operator in the electric dipole operator $\hat{\boldsymbol{\mu}}$.

From the above consideration, it becomes clear that in case of non-uniform electromagnetic fields, as encountered in nanooptics, light-matter interactions might go beyond the electric dipole approximation. A modification of the electric dipole contribution with a term of higher order can be observed, e.g., when wavefunctions get mesoscopic in size and field gradients become sufficiently strong close to plasmonic structures, as demonstrated by the Lodahl group [51, 52]. In this thesis, the discussion will be restricted to the electric dipole approximation, as the results presented in chapters 6 and 7 are in agreement with this approximation within experimental uncertainties. In chapter 8, plasmonic constructs featuring sub-2 nm gaps are demonstrated. Future experiments with molecules placed inside such plasmonic cavities should reconsider the assumption of the electric dipole approximation.

Following the dipole approximation, the consideration of a single electron is generalized to a collection of charged particles, i.e., a molecule, by an electronic and nuclear dipole moment operator $\hat{\boldsymbol{\mu}}_{el}$ and $\hat{\boldsymbol{\mu}}_{nuc}$ [46, 47, 50]:

$$\hat{\boldsymbol{\mu}} = \hat{\boldsymbol{\mu}}_{el} + \hat{\boldsymbol{\mu}}_{nuc} = -\sum_i e\mathbf{r}_i + \sum_j Z_j e\mathbf{R}_j \quad , \tag{2.12}$$

summing over all electrons of charge $-e$ at positions $\mathbf{r}_i$ and nuclei of charge $+Z_j\, e$ at positions $\mathbf{R}_j$. Furthermore, again the wavefunctions Ψ of a molecule are considered (c.f. equation 2.2).

The forces induced by the electromagnetic interaction are typically rather small compared with those being present without the external electric field, justifying a perturbative treatment of the interaction [46]. The wavefunction of the system is then described to a good approximation by a superposition of the unperturbed eigenstates of $\hat{H}_0$ with time-dependent coefficients. Within the framework of time-dependent perturbation

theory, a rate k_{fi} for transitions between an initial molecular state Ψ_i and a final state Ψ_f can be obtained to first order in the perturbation given by [46, 50]

$$k_{fi}^{ED} = \frac{2\pi}{\hbar^2}\left(\frac{E_0}{2}\right)^2 |\langle\Psi_f|\hat{\boldsymbol{\mu}}\cdot\hat{\mathbf{e}}|\Psi_i\rangle|^2\delta(\omega-\omega_{fi}) \quad , \tag{2.13}$$

with the delta distribution $\delta(\omega)$ and the unit vector $\hat{\mathbf{e}}$ of the electric field. Thus, a transition from the initial state of energy E_i to the final state of energy E_f is only possible if the frequency ω of the perturbation matches $\omega_{fi} = (E_f - E_i)/\hbar$. Here, the case $E_f > E_i$ is considered, i.e., absorption of a photon of energy $\hbar\omega_{fi}$. Stimulated emission, i.e., emission of light via a downward electronic transition ($E_f < E_i$), can be regarded as the reverse of absorption and can be considered analogously by changing the argument of the delta distribution in equation 2.13 to $(\omega + \omega_{fi})$ [47, 49, 50]. Note that, when the dipole operator $\hat{\boldsymbol{\mu}}$ is sandwiched between $|\Psi_f\rangle$ and $|\Psi_i\rangle$, the contribution of the nuclear dipole moment operator $\hat{\boldsymbol{\mu}}_{nuc}$ cancels out due to orthogonality of the different electronic states and only the contribution of $\hat{\boldsymbol{\mu}}_{el}$ remains [50].

In realistic conditions, transitions from one initial state are performed to a continuum of final states characterized by their density of states $\rho(\omega)$, which is the number of states per unit frequency. Thus, the transition rate in equation 2.13 is modified to [46]

$$k_{fi}^{ED} = \frac{2\pi}{\hbar^2}\left(\frac{E_0}{2}\right)^2 |\langle\Psi_f|\hat{\boldsymbol{\mu}}\cdot\hat{\mathbf{e}}|\Psi_i\rangle|^2\rho(\omega_{fi}) \quad , \tag{2.14}$$

known as Fermi's golden rule, in particular, applied here to electric dipole transitions [45–47, 50, 53, 54]. Thus, the relevant quantity is the component of the electric transition dipole matrix element $\boldsymbol{\mu}_{fi} = \langle\Psi_f|\hat{\boldsymbol{\mu}}|\Psi_i\rangle$ in the direction of the electric field [49].

In addition to the semi-classical treatment of absorption and stimulated emission discussed above, a full quantum treatment gives the following transition rate of spontaneous emission [46, 55]

$$k_{fi}^{ED} = \frac{n\,\omega_{fi}^3}{3\pi\hbar c^3\epsilon_0}|\boldsymbol{\mu}_{fi}|^2 \quad , \tag{2.15}$$

considering here the free space photon density of states in a homogeneous medium of refractive index n. Note that in a nanophotonic environment rather the projected local density of optical states needs to be considered (see chapter 3). ϵ_0 represents the vacuum permittivity.

2.3 RADIATIVE AND NONRADIATIVE TRANSITIONS

The square magnitude of the transition dipole matrix element $\boldsymbol{\mu}_{fi}$ is called dipole strength D_{fi} and determines the intensity of an optical transition, e.g., the absorption strength. Within the Condon approximation, the overall transition dipole can be

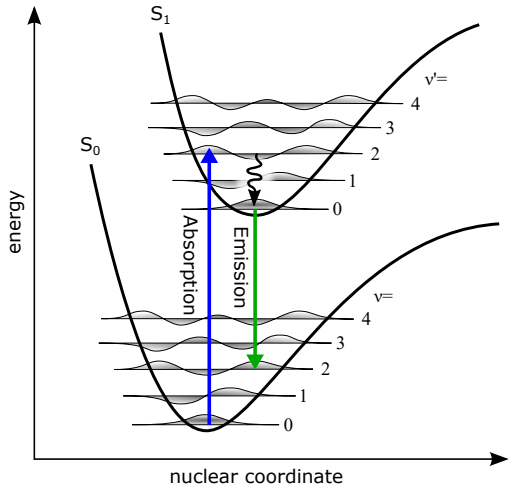

Figure 2.1: Illustration of the potential surfaces of the electronic ground singlet state S_0 and first excited singlet state S_1, together with the vibrational wavefunctions of a normal mode of the nuclei with quantum numbers v and v', respectively. Absorption (blue arrow) and emission (green arrow) appear vertical in the diagram (Frack-Condon principle).

factorized into a nuclear overlap integral $\langle \chi_{v_f} | \chi_{v_i} \rangle$ and an electronic transition dipole $\langle \phi_f^{el} | \hat{\mu}_{el} | \phi_i^{el} \rangle$ averaged over nuclear coordinates [47]. Taking further into account an overlap between spin wavefunctions of the initial and final state $\langle \Phi_f^{spin} | \Phi_i^{spin} \rangle$, the dipole strength can be approximately separated into three factors given by [45]

$$D_{fi} = |\boldsymbol{\mu}_{fi}|^2 \approx \underbrace{|\langle \phi_f^{el} | \hat{\boldsymbol{\mu}}_{el} | \phi_i^{el} \rangle|^2}_{electronic\ factor} \cdot \underbrace{|\langle \chi_{v_f} | \chi_{v_i} \rangle|^2}_{vibrational\ factor} \cdot \underbrace{|\langle \Phi_f^{spin} | \Phi_i^{spin} \rangle|^2}_{spin\ factor} \quad . \tag{2.16}$$

If any of the three factors in equation 2.16 is zero, the transition is called "forbidden". Particularly, the electronic dipole operator flips its sign under spatial inversion. Thus, the electronic factor $|\langle \phi_f^{el}(\mathbf{r}) | \hat{\boldsymbol{\mu}}_{el} | \phi_i^{el}(\mathbf{r}) \rangle|^2$ can be zero if the parity of the initial and final electronic wavefunction are the same. In this case, the transition is called dipole-forbidden, otherwise dipole-allowed. The vibrational factor contains the overlap integral between the involved vibrational wavefunctions (Franck-Condon integral), whose squared magnitude $|\langle \chi_{v_f} | \chi_{v_i} \rangle|^2$ is called Franck-Condon factor. The introduced spin factor can ideally be either 0 or 1, which corresponds to a different or equal total spin of initial and final state, respectively. Therefore, transitions between two singlet states are spin-allowed, while the transition from a triplet to a singlet state is spin-forbidden. However, the latter can be weakly allowed due to a certain singlet admixture to the excited state triplet wavefunction, e.g., mediated by spin-orbit coupling [45].

Optical transitions between two eigenstates of the molecule occur on a femtosecond timescale, which is so short that the nuclear configuration is hardly changed during the transition [56]. As a result, optical transitions appear vertical in the potential

diagram 2.1, which is called Franck-Condon principle [44]. At room temperature, the thermal energy is small compared to the vibrational energy and thus absorption typically occurs from the lowest vibrational level in the electronic ground state to some vibrational level in an excited electronic state. Upon excitation, the changed electron density in the electronic excited state relative to the ground state leads to a shifted potential energy surface (figure 2.1). As a result of relaxation processes, emission occurs at a different nuclear configuration than absorption. The relative probability of the vibronic transitions is determined by the squared overlap between the involved vibrational wavefunctions, i.e., the Franck-Condon factor $f^2_{\nu',\nu}$ and is thus sensitive to the shift of the potential surfaces. Considering shifted harmonic potential surfaces of equal shape, the Franck-Condon factor from the o-th vibrational level in the electronic ground state to the ν'-th vibrational level in the electronic excited state can be described analytically by [45, 50]

$$f^2_{\nu',\nu=0} = |\langle \chi_{\nu'} | \chi_0 \rangle|^2 = \frac{S^{\nu'}}{\nu'!} \mathrm{e}^{-S} \quad , \tag{2.17}$$

with the Huang-Rhys parameter S describing the relaxation energy in units of the vibrational energy $\hbar\omega_0$. It quantifies the coupling of the vibrational mode to the electronic excitation and the relative shift of the potential surfaces, respectively [45, 47].

In addition to the radiative transitions driven by an oscillatory perturbation of frequency ω in equation 2.13, a constant perturbation can cause radiationless transitions between an initial state and isoenergetic final states [46]. Prominent examples of such processes are internal conversion and intersystem crossing (see below).

The different radiative and nonradiative processes in an organic molecule are illustrated by a Jablonski diagram (figure 2.2). For most organic molecules, the electron spins are paired in the ground state, i.e., the ground state is a singlet state S_0 with total spin quantum number $S = 0$. The first and second excited electronic singlet states are depicted by S_1 and S_2, while the triplet states with $S = 1$ are given by T_1 and T_2, respectively. In each electronic state, a series of vibrational energy levels separated by the vibrational energy $\hbar\omega_0$ exist. Light-absorption from S_0 typically takes place to a higher vibrational level of S_1 (blue arrows, timescale 10^{-15} s). Subsequently, the molecule usually relaxes to the lowest vibrational level in S_1, a process called vibrational relaxation taking place within about $10^{-13} - 10^{-11}$ s (wavy downward arrow) [45, 57]. Subsequently, a radiative transition from S_1 to a vibrational level of the electronic ground state S_0 can take place. Such spin-allowed optical transitions are called *fluorescence* (green arrows), with typical fluorescence lifetimes in the nanosecond range. Notably, the fluorescence emission is red-shifted compared to the absorption. Important reasons for this Stokes-shift, among others, are the vibrational relaxation in S_1 and S_0 to the respective lowest vibrational level [56] and also electron-phonon coupling involving the surrounding host system [58].

Further, less probable processes in S_1 are, first, the isoenergetic nonradiative internal conversion (IC) to S_0, followed by vibrational relaxation in S_0. Second, also a

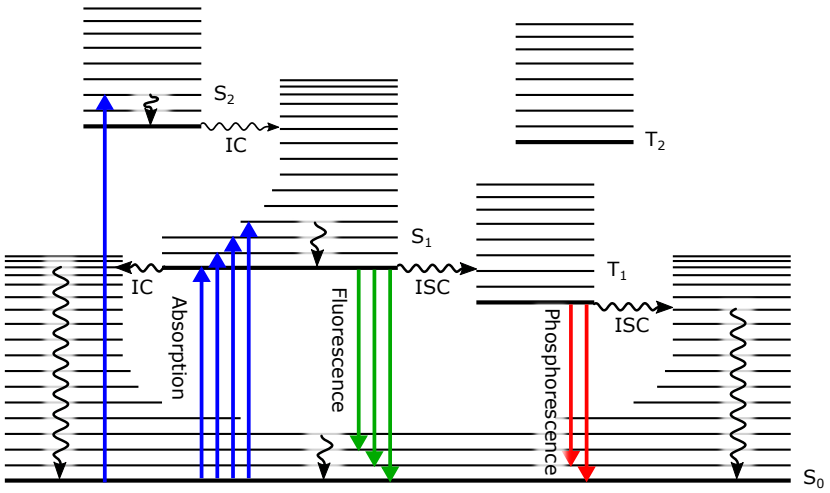

Figure 2.2: Jablonski diagram of a typical organic dye molecule with singlet states $S_0, S_1, \ldots$ and triplet states $T_1, T_2, \ldots$ vertically arranged according to their energy. Radiative processes are sketched as solid vertical lines and nonradiative processes are represented by wavy arrows. While vibrational relaxation is illustrated as vertical curved arrow, intersystem crossing (ISC) and internal conversion (IC) are depicted by horizontal arrows. Inspired from ref. [57].

nonradiative transition from S_1 to T_1, involving a spin conversion, can take place (intersystem crossing, ISC). From T_1, the spin forbidden optical transition to S_0 is called *phosphorescence* (red arrows). In organic molecules such processes involving a "spin-flip" are only weakly allowed due to spin-orbit coupling, with correspondingly low transition probabilities. The phosphorescence lifetime is thus much longer than the fluorescence lifetime and ranges from the microsecond range to minutes. If the optical absorption occurs to a higher excited state, e.g., S_2, the subsequent nonradiative internal conversion (IC) to S_1 is much faster (picosecond timescale) compared to a radiative decay from S_2 (nanosecond timescale). Thus, emission typically occurs from the lowest excited state within a spin manifold, which is called Kasha's rule [45, 56].

To define the fluorescence quantum yield QY and lifetime τ_{fl}, different rates are assigned to the available processes starting from the S_1 state. Radiative processes by spontaneous emission and nonradiative processes are described with the rate k_r and k_{nr}, respectively. The fluorophores considered in this thesis offer a high fluorescence quantum yield, defined as the radiative rate of fluorescence k_r normalized to radiative and nonradiative rate $k_r + k_{nr}$:

$$QY = \frac{k_r}{k_r + k_{nr}} \quad . \tag{2.18}$$

In addition to conventional fluorescence emission, the excited state of a molecule can also be depopulated by stimulated emission, which is triggered by an incident beam of light matching the molecule's emission spectrum. As a result of the stimulated

emission, the remaining fluorescence emission is depleted. This photophysical process, called *stimulated emission depletion* (STED), is discussed in detail in section 7.4.

In the following, a molecule initially in its (vibrationally relaxed) excited state S_1 is assumed, i.e., the probability P_1 of finding the excited molecule in S_1 is initially $P_1(t=0)=1$. The excitation process has already taken place and is not considered, as it is mostly irrelevant for the discussion of fluorescence and stimulated emission. The stimulated emission with rate $k_{STED}(t)$, triggered by an incident depletion beam, typically ends in a transient vibrational level of the electronic ground state S_0^*. From there, in principle, the re-excitation to S_1 by the depletion beam and the vibrational decay in S_0 (rate $k_{vib} \approx 10^{12}\,\mathrm{s}^{-1}$) are competing processes. When the depletion beam is an optical pulse with a duration long compared to k_{vib}^{-1}, the re-excitation is negligible. Within these approximations, the excited state S_1 is only depopulated and the probability P_1 of finding the excited molecule in S_1 decays with time according to

$$\frac{dP_1(t)}{dt} = -\Big[k_r + k_{nr} + k_{STED}(t)\Big]\, P_1(t) \quad . \tag{2.19}$$

In the absence of stimulated emission ($k_{STED}=0$), the excited state S_1 is depopulated by k_r and k_{nr}, resulting in an exponential decay of $P_1(t)$ in time with an average excited state lifetime (*fluorescence lifetime*) given by

$$\tau_{fl} = \frac{1}{k_r + k_{nr}} \quad . \tag{2.20}$$

In the opposite case, if stimulated emission dominates ($k_{STED} \gg k_r + k_{nr}$), i.e., it is triggered by a laser pulse of a short time duration τ_{STED}, P_1 is efficiently depleted by stimulated emission. Then, within the time τ_{STED}, the remaining fluorescence probability drops by the *suppression factor*

$$\eta = \exp(-k_{STED}\,\tau_{STED}) = \exp(-\sigma_{STED}\,h_{STED}\,\tau_{STED}) \quad . \tag{2.21}$$

Here, σ_{STED} is the cross-section for stimulated emission (see section 2.5 for cross-sections) and h_{STED} is the photon flux in the triggering laser pulse measured in photons / ($\mathrm{s\,m^2}$). Note that Kastrup and Hell [59] obtained the exponential dependency in equation 2.21 also for a three-level photokinetic model taking the transient vibrational state S_0^* explicitly into account when the regime $k_r + k_{nr} \ll k_{STED} \ll k_{vib}$ is considered. This condition is generally well fulfilled for picosecond depletion pulses and typical fluorescent molecules.

2.4 LINE BROADENING MECHANISMS

The spectral lines belonging to both absorption and emission are not strictly monochromatic. In all cases, a distribution $I(f)$ of the absorbed or emitted intensity as a

function of the frequency f occurs, with the full width at half maximum (FWHM) quantifying the width of the distribution.

The lower bound of the linewidth is given by the natural linewidth, which is determined by the energy-time uncertainty principle. Given a (radiative) lifetime τ_n of the excited state, its energy E_n can only be determined up to an uncertainty $\Delta E_n = \hbar/\tau_n$. The spectral line corresponding to the transition from this excited state to the ground state of infinite lifetime has therefore the *natural linewidth* [60]

$$\delta f_{nat} = \frac{\Delta E_n}{h} = \frac{1}{2\pi\tau_n} \quad . \tag{2.22}$$

A spectral line is called homogeneously broadened if all molecules in the same energy state E_n experience the same probability for absorption or emission of light with frequency f causing the transition $E_n \rightarrow E_m$ [61]. An example is the natural line broadening.

In case of a molecule embedded in a solid, the transition energies fluctuate with time by a stochastic variable as a result of interactions with the local environment. The correlation of these fluctuations decays within a characteristic time, the pure dephasing time T_2^* [50]. For short correlation times, a homogeneously broadened line profile of Lorentzian shape results, with the width given by

$$\delta f_{hom} = \frac{1}{2\pi\tau_n} + \frac{1}{\pi T_2^*} \quad . \tag{2.23}$$

The optical dephasing of single organic molecules is typically induced by scattering with phonons in the surrounding solid. While at room temperature a strong line broadening results, at cryogenic temperatures ($T < 2\,\mathrm{K}$), the phonons in the local environment are frozen out, T_2^* gets very large and the spectral lines can approach the natural linewidth [37, 38, 58].

An inhomogeneous broadening mechanism is characterized by the fact that the probability for absorption or emission of light with frequency f is not the same for all molecules within an ensemble [61]. In case of molecules in a solid, the transition energy of each molecule sensitively depends on the interaction with its environment. Thus, irregularities of the surrounding material lead to a statistical distribution of the mean transition energies. In total, the ensemble features an inhomogeneously broadened spectral line, which is built up from many slightly spectrally shifted homogeneous lineshape profiles [62]. In the general case, the spectral lineshape of absorption is given as the Fourier-transformation of a relaxation function that describes the dephasing of the ensemble. The relaxation function can vary between an exponential function and a Gaussian and thus the resulting lineshapes range from Lorentzian to Gaussian [47].

2.5 EXTINCTION CROSS-SECTION OF SINGLE MOLECULES

The absorbance A of a medium, e.g., a thin film or a solution in a cuvette, is defined as the negative decadic logarithm of the transitted intensity I normalized to the incident intensity I_0. The Beer–Lambert–Bouguer law states that this absorbance A is proportional to the concentration c_a of absorbers, the molar decadic extinction/absorption coefficient ϵ and the path length d of the sample [47]:

$$A(\lambda) = -\log(\frac{I}{I_0}) = c_a\,\epsilon(\lambda)\,d \quad . \tag{2.24}$$

For a single absorber, i.e., a single molecule, an absorption cross-section σ_{abs} can be defined, quantifying the area of photon-capture by the molecule. The relationship between the absorption cross-section and the molar decadic absorption coefficient ϵ is given by [57]

$$\sigma_{abs}(\lambda) = \frac{\epsilon(\lambda)\,\ln(10)}{N_A} \quad , \tag{2.25}$$

with the Avogadro constant N_A.

A resonantly driven ideal two-level system features a peak extinction respectively scattering cross-section under plane wave excitation as large as [63]

$$\sigma_{ext} = 3\cos^2(\theta)\frac{\lambda^2}{2\pi} \quad , \tag{2.26}$$

depending only on the resonance wavelength λ and a proper angle θ between the vector of the driving electric field and the transition dipole moment. It turns out that ideal two-level systems feature no absorption in the sense that light is converted to other forms of energy, e.g., heat. Excited by a weak continuous laser field at its resonance, the two level system would cycle between ground and excited state by absorption and stimulated emission. The extinction, i.e., the reduction of the transmitted power in forward direction, is then caused by the interference of the forward scattered field with the excitation field (c.f. optical theorem) [55]. In case of a real molecule, the emission can be red-shifted compared to the excitation, acting as a loss-channel. Extinction is then, in general, the sum of absorption and scattering [64]. The presence of an emitter in the laser beam can thus reduce the transmitted laser signal. The magnitude of the extinction effect depends on the ratio between the extinction cross-section and the area of the excitation beam focus where the emitter is placed in [65].

Several aspects lead to the fact that the experimentally achievable extinction cross-section of a single molecule is strongly reduced compared to equation 2.26. First, the dephasing processes described in section 2.4 increase with temperature and lead to homogeneously broadened spectral lines. Second, the dipole strength between ground and excited state is distributed across several vibronic transitions according to the Franck-Condon factors $f^2_{\nu',\nu}$. Third, low energy phonons of the surrounding matrix material couple to electronic transitions and lead to a phonon wing next to the zero

phonon line. The fraction of the integrated intensity of the zero phonon line compared to the sum of zero phonon line and phonon wing is called Debye-Waller factor α_{DW}. Thus, according to Wrigge *et al.* [65], the obtainable extinction cross-section is given by

$$\sigma_{ext} = 3\cos^2(\theta)\frac{\lambda^2}{2\pi}\frac{\delta f_{nat}}{\delta f_{hom}} f_{\nu',\nu}^2\, \alpha_{DW} \quad . \tag{2.27}$$

For temperatures larger than about 20-50 K, the Debye-Waller factor decreases to very small values [66], such that it cannot be quantified. In such cases, e.g., at room temperature, Moerner and Orrit [33] suggest using a simplified formula for the diminished cross-section which is given by

$$\sigma_{ext} = 3\cos^2(\theta)\frac{\lambda^2}{2\pi}\frac{k_r}{\delta f_{tot}} \quad , \tag{2.28}$$

with k_r being the radiative rate and δf_{tot} the total width of the absorption.

In chapter 7, the terrylene derivative terrylene diimide is investigated as single molecule quantum emitter. Polycyclic aromatic hydrocarbons such as perylene, terrylene, dibenzanthanthrene and dibenzoterrylene, as well studied examples of flat and rigid single impurity molecules in a solid-state system, could play a key role in future photonic quantum technologies. These molecules display a near-unity fluorescence quantum yield and a negligible intersystem crossing probability. For certain guest-host systems at cryogenic temperatures ($T < 2$ K), Toninelli *et al.* [67] demonstrated Fourier-limited linewidths of a few 10 MHz and, according to Wrigge *et al.* [65], the product of $f_{\nu',\nu}^2 \cdot \alpha_{DW}$ can reach values of about 0.2. Thus, at cryogenic temperatures, peak absorption cross-sections can reach huge levels of about $10^{-11} - 10^{-10}\,\mathrm{cm}^2 = 10^5 - 10^6\,\text{Å}^2$ [33, 34]. The Sandoghdar group [65] demonstrated, by using far-field optics close to the diffraction limit, that a single molecule can induce above 10 % extinction of a laser beam. By using optical microcavities, even 99 % extinction was reported recently [68].

At room temperature, however, molecular absorption cross-sections are typically about $6\,\text{Å}^2$, being approximately 5 orders of magnitude smaller than at low temperatures [33]. Even with a diffraction-limited laser focus, pioneering experiments of the Sandoghdar group [41, 42] have shown that the extinction of laser light caused by a single molecule is in the order of a few 10^{-6} only. Importantly, the extinction signal is determined by the ratio of the extinction cross-section and the mode area of the Gaussian laser focus [65]. As the extinction cross-section is given by the molecules in the sample under investigation, their interaction with far-field optical modes is essentially limited by the diffraction of light. In this regard, the deep subwavelength field confinement achieved with plasmonic nanostructures and waveguides presented in this thesis promises to boost the interaction of single molecules with light to a regime being inaccessible with conventional optics.

3 THEORY OF EMITTER-WAVEGUIDE COUPLING

During the last decades, the field of *plasmonics* has been established to explore the electromagnetic phenomena of metals at the nanoscale. Surface plasmon polaritons are collective oscillations of the free electrons at a metal-dielectric interface which are coupled to electromagnetic near-fields [69]. These surface modes exist at flat surfaces, but also at various other configurations of metallic nanostructures and thereby offer a wide tunability of their outstanding properties. The most unique feature of plasmonics is that the mixing of optical fields with electronic excitations offers the possibility of electromagnetic field confinement far beyond the diffraction limit. Therefore, plasmon-based operation has gained a huge interest for applications in miniaturized nanophotonic components and circuits. With the latest fabrication techniques, nanostructures can be fabricated with a complex shape (see chapter 5), which gives prospects to engineer the desired functionality. The geometry of the nanostructure is one important factor that determines the available plasmonic modes, ranging from localized surface plasmon polaritons of individual nanoparticles via propagating modes traveling along the surface of a waveguide structure up to plasmonic circuits consisting of two parallel nanowires with an attached antenna and mode detector (see chapters 6 and 7).

Particularly, while in dielectric waveguide structures the confinement of light is ultimately limited by diffraction, plasmonic waveguides offer the opportunity of deep subwavelength confinement to the position of a quantum emitter. Due to this strong confinement, a quantum emitter coupled to a plasmonic waveguide features an enhanced decay rate, with the emission being channeled efficiently into the available waveguide modes.

In this chapter, basic electromagnetic properties of noble metals are discussed that allow for the formation of surface plasmon polariton modes at the metal-dielectric interface. In particular, the propagating modes of single metal nanowires are presented, which serve as building block for the more advanced waveguide geometries investigated in this thesis. Finally, the emitter-waveguide system is investigated. The various decay channels of a dipolar emitter close to a plasmonic waveguide, including the decay rate into the waveguide and the total decay rate, are discussed. The ratio of both decay rates serves as an important measure of the waveguide-emitter coupling efficiency, called β-factor.

3.1 ELECTROMAGNETICS OF METALS

3.1.1 Maxwell's equations

As outlined above, metallic structures of nanoscale size show a variety of optical phenomena deviating strongly from the atomic and the bulk limit. As long as their size is above a few nanometers, the optical properties of metal nanostructures can be described by classical electromagnetic theory without the need of quantum mechanical descriptions. Following Maier [70], the basic equations are thus the well known *Maxwell's equations* in their macroscopic form given by

$$\nabla \cdot \mathbf{D} = \rho_{ext} \quad , \tag{3.1}$$

$$\nabla \cdot \mathbf{B} = 0 \quad , \tag{3.2}$$

$$\nabla \times \mathbf{E} = -\frac{\partial \mathbf{B}}{\partial t} \quad , \tag{3.3}$$

$$\nabla \times \mathbf{H} = \mathbf{j}_{ext} + \frac{\partial \mathbf{D}}{\partial t} \quad , \tag{3.4}$$

with the electric field $\mathbf{E}$, the dielectric displacement field $\mathbf{D}$, the magnetic field $\mathbf{H}$, the magnetic flux density $\mathbf{B}$ and the external charge and current density, ρ_{ext} and $\mathbf{j}_{ext}$, which drive the system. The electric polarization $\mathbf{P}$ and the magnetization density $\mathbf{M}$ express the respective induced (and permanent) dipole moment density in the medium caused by an alignment of microscopic dipoles with the electric and magnetic field, respectively. They represent the link between the complex macroscopic vector fields:

$$\mathbf{D} = \epsilon_0 \mathbf{E} + \mathbf{P} = \epsilon_0 \epsilon_r \mathbf{E} \quad , \tag{3.5}$$

$$\mathbf{B} = \mu_0 \mathbf{H} + \mathbf{M} = \mu_0 \mu_r \mathbf{H} \quad . \tag{3.6}$$

Here, in the last step, a linear relationship between $\mathbf{D}$ and $\mathbf{E}$, as well as $\mathbf{B}$ and $\mathbf{H}$, has been introduced. ϵ_0 and μ_0 are the electric permittivity and magnetic permeability, respectively. The relative permittivity ϵ_r and permeability μ_r are in general tensors and describe the linear response of the medium. For isotropic media, they become scalars. In the following, the magnetic response is neglected for the nonmagnetic media under investigation ($\mu_r = 1$).

Besides the external current and charge densities, $\mathbf{j}_{ext}$ and ρ_{ext}, an additional internal set, ρ and $\mathbf{j}$, exists in the medium and responds to the external stimuli. The polarization $\mathbf{P}$ is linked to the internal charge density via $\nabla \cdot \mathbf{P} = -\rho$. In order to fulfill charge conservation according to the continuity equation $\nabla \cdot \mathbf{j} = -\partial\rho/\partial t$, it follows

$$\mathbf{j} = \frac{\partial \mathbf{P}}{\partial t} \quad , \tag{3.7}$$

linking the internal current and charge densities.

In general, the relationship between **D** and **E** (**H** and **B**) is nonlocal in time and space [70, 71]. Considering a nonlocality in time means that, in the time domain, a real medium does not react instantaneously on a driving electric field. Then, $\epsilon_0\epsilon_r(t)$ represents an impulse response function of the dielectric displacement field **D** on the electric field **E**. As a consequence, in the frequency domain, a real medium can be described by a frequency-dependent relative permittivity $\epsilon_r(\omega) = \epsilon_1(\omega) + i\epsilon_2(\omega)$. This complex function of the frequency ω is called *dielectric function*. In optical experiments, the media are often described by a frequency-dependent, complex-valued refractive index $\tilde{n}(\omega) = n(\omega) + i\kappa(\omega)$. Using the relation $\tilde{n} = \sqrt{\epsilon_r}$, it follows

$$\epsilon_1 = n^2 - \kappa^2 \quad , \tag{3.8}$$

$$\epsilon_2 = 2n\kappa \quad . \tag{3.9}$$

While the real part of the refractive index n describes the evolution of the phase of a plane wave in space, the imaginary part κ quantifies the attenuation of the wave in the medium.

To describe a spatially nonlocal optical response, the linear relationship between the displacement field **D** and the electric field **E** is generalized to [72]

$$\mathbf{D}(\mathbf{r},\omega) = \epsilon_0 \int d\mathbf{r}'\, \epsilon_r(\mathbf{r},\mathbf{r}',\omega)\, \mathbf{E}(\mathbf{r}',\omega) \quad , \tag{3.10}$$

where $\epsilon_r(\mathbf{r},\mathbf{r}',\omega)$ represents the (scalar) nonlocal permittivity of the metal. As estimated by Hohenester [73] for gold and silver, nonlocal effects in plasmonics become important when the particle's geometry or the field confinement vary significantly on a length scale of about 1 nm. In the nonlocal regime, e.g., when the gap between a plasmonic dimer enters the (sub-)nanometric range, the induced surface charges of the metal are shifted with respect to the geometrical boundary. Further details of the nonlocal optical response in plasmonics are discussed in exhaustive reviews on the topic given by Raza *et al.* [72] or Zhu *et al.* [25]. Neglecting effects with a spatially nonlocal nature is referred to as *local-response approximation* of light-matter interaction, where the relative permittivity is local in space:

$$\epsilon_r(\mathbf{r},\mathbf{r}',\omega) = \epsilon_r(\mathbf{r},\omega)\delta(\mathbf{r}-\mathbf{r}') \quad . \tag{3.11}$$

According to Maier [70], this approximation is valid as long as the wavelength λ in the medium is significantly larger than characteristic dimensions such as the electrons' mean free path.

3.1.2 Drude–Lorentz theory of the dielectric function

The electromagnetic response of a metallic particle can be described by a simple but utile microscopic model proposed by Paul Drude in the year 1900 and extended five years later by Hendrik Lorentz, yielding a frequency-dependent complex dielectric

function [74]. While the Drude model treats the classical free electron dynamics in a metal, the Lorentz oscillator model considers the response of bound electrons.

Within the Lorentz model, an electron bound to a fixed atomic core at the position $\mathbf{r}_0 = 0$ via a harmonic potential is considered. The classical equation of motion for such an electron driven by a monochromatic electric field $\mathbf{E}_0\,\mathrm{e}^{-i\omega t}$ reads as [55, 70, 74]

$$m\frac{\partial^2\mathbf{r}}{\partial t^2} + m\gamma\frac{\partial\mathbf{r}}{\partial t} + m\,\omega_0^2\,\mathbf{r} = -e\,\mathbf{E}_0\,\mathrm{e}^{-i\omega t} \quad , \tag{3.12}$$

with the displacement vector $\mathbf{r}$, the effective mass of the electron m, the damping constant γ, the eigenfrequency of the bound oscillation ω_0 and the elementary charge e. The solution of the differential equation 3.12 gives the time-harmonic displacement of the electron from the core position $\mathbf{r}$ that results in a dipole moment $\mathbf{p} = -e\mathbf{r}$. For an ensemble of oscillating electrons, a multiplication with the electron density n_e results in the macroscopic polarization $\mathbf{P}$. Together with equation 3.5, the dielectric function of the system of bound electrons is found to be [55]

$$\epsilon_{r,DL} = 1 + \frac{n_e e^2}{m\epsilon_0}\frac{1}{(\omega_0^2 - \omega^2) - i\gamma\omega} \quad . \tag{3.13}$$

This complex-valued dielectric function can be decomposed into real and imaginary part according to

$$\epsilon_{r,DL} = 1 + \frac{n_e e^2}{m\epsilon_0}\frac{\omega_0^2 - \omega^2}{(\omega_0^2 - \omega^2)^2 + \gamma^2\omega^2} + i\frac{n_e e^2}{m\epsilon_0}\frac{\gamma\omega}{(\omega_0^2 - \omega^2)^2 + \gamma^2\omega^2} \quad . \tag{3.14}$$

In particular, the consideration of bound electrons oscillating at their resonance frequency ω_0 gives a classical picture of electron interband transitions, e.g., from lower lying d-bands to the sp conduction band in noble metals. However, in contrast to isolators and semiconductors, the conduction band of a metal is partially filled. The conduction electrons, and thus the optical properties of metals, can be described over a wide frequency range by a free electron gas that responds to electromagnetic fields. The lack of the restoring force of conduction electrons in the metal, i.e., $\omega_0 = 0$, simplifies the dielectric function to the Drude theory of a free electron gas given by [55]

$$\epsilon_{r,D} = 1 - \frac{\omega_p^2}{\omega^2 + \gamma_D^2} + i\frac{\gamma_D\omega_p^2}{\omega(\omega^2 + \gamma_D^2)} \quad . \tag{3.15}$$

Here, $\omega_p = \sqrt{n_e e^2/(m\epsilon_0)}$ is the plasma frequency of the free electron gas and γ_D represents a phenomenological Drude damping term due to scattering events of the electrons. For most metals, ω_p is in the ultraviolet region. Light waves with $\omega < \omega_p$ get reflected, leading to the shiny appearance of metals in the visible spectrum. For $\omega > \omega_p$ the electrons cannot respond fast enough to screen the field and the metal becomes transparent.

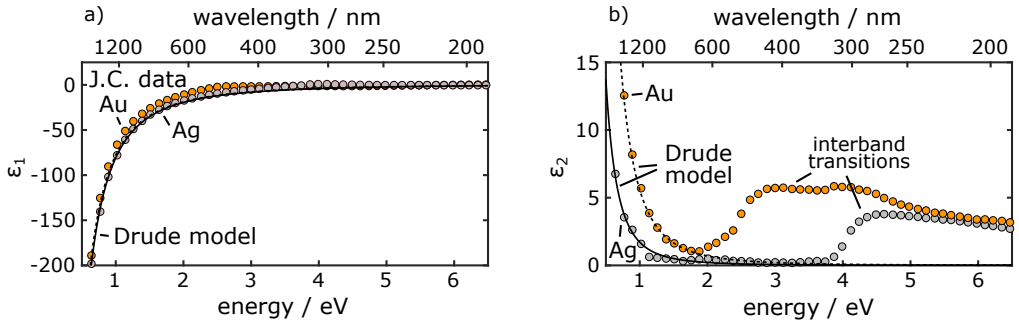

Figure 3.1: (a) Real part and (b) imaginary part of the dielectric function of gold (orange) and silver (grey) taken from Johnson and Christy [75]. A fit of the Drude theory is shown as black line (Ag: bold, Au: dashed). In (a), both fits nearly overlap. For parameters see text.

Despite its simplicity, the Drude model can reasonably well describe the experimental data for the dielectric function of gold and silver from Johnson and Christy [75], especially toward the near-infrared region. The full trend of the real part of the dielectric function is well captured by the model (figure 3.1a) using the parameters $\omega_p = 8.89\,\text{eV}$, $\gamma_D \approx 71\,\text{meV}$ for gold and $\omega_p = 9.04\,\text{eV}$, $\gamma_D \approx 21\,\text{meV}$ for silver [76]. However, strong deviations are found for the imaginary parts at higher energies (figure 3.1b). These deviations are due to interband transitions of gold and silver, which are not captured by the free electron gas model. One interband transition can be taken into account by adding a contribution according to equation 3.14, which improves the fit, but still fails to reproduce the experimental data, e.g., below ~500 nm in case of gold [55]. Furthermore, it is important to note that the interband transitions in silver appear at much higher energies compared to gold. This fact turns silver into the most preferred low-loss plasmonic material in the visible to near-infrared region and opens up new nanophotonic applications in the visible spectral range that are not possible with gold (see chapters 6, 7 and 8).

In the literature, different experimental data for the dielectric function of silver is reported and, in particular, the imaginary part is varying slightly between different reports. A 60-year span of well-known research articles investigating the dielectric function of silver is summarized in the review by Baburin *et al.* [77]. In the considered articles, silver samples fabricated by different methods have been investigated with various methods at different conditions. Important factors for the determined dielectric function are grain boundaries, defect scattering and silver sulfide formation at the Ag/air surface. Therefore, care has to be taken by adopting values from the literature. For convenience, in the following, the dielectric data of Johnson and Christy [75] is used for all simulations throughout the thesis.

3.2 PROPAGATING SURFACE PLASMON POLARITONS

A surface plasmon polariton refers to the excitation of the charge oscillation at the metal surface (*surface plasmon*) which is coupled to an electromagnetic near-field at the surface (*polariton*). These surface modes appear at the interface between a dielectric medium and a conductor if certain conditions of the dielectric functions are fulfilled. An important aspect of noble metals for supporting such modes is their large negative real part of the dielectric function in the visible to near-infrared region (c.f. figure 3.1a). Many different configurations to guide propagating surface plasmon polaritons exist, each offering specific advantages and disadvantages [78]. In this section, the two fundamental cases of a plane metal-dielectric interface and a cylindrical metal nanowire are considered. In the absence of external charge and current densities, Maxwell's equations 3.3 and 3.4 can be combined to the wave equation in frequency domain, which reads as [55]

$$\nabla \times \Big[\nabla \times \mathbf{E}(\mathbf{r},\omega)\Big] - \frac{\omega^2}{c^2}\epsilon_r(\mathbf{r},\omega)\mathbf{E}(\mathbf{r},\omega) = 0 \quad , \tag{3.16}$$

with the speed of light $c = 1/\sqrt{\epsilon_0\mu_0}$. In order to determine the surface mode's electric field $\mathbf{E}$ for a specific geometry, equation 3.16 needs to be solved either analytically or numerically (see chapter 4).

3.2.1 Surface plasmon polaritons at plane interfaces

The most simple geometry supporting propagating surface plasmon polaritons is given by a plane interface between two media (figure 3.2). To determine the desired surface modes, the wave equation has to be solved in the two media 1 and 2, with $\epsilon_r^{(1)}(\omega)$ for $z < 0$ and $\epsilon_r^{(2)}(\omega)$ for $z > 0$. In both directions perpendicular to the interface, i.e., in positive and negative z-direction, surface modes decay exponentially, while a homogeneous field in y-direction and a one-dimensional propagation along the interface in x-direction is assumed. It can be shown that transverse-electric (TE) surface plasmon polariton modes do not exist, since purely transverse electric fields cannot be coupled to the longitudinal electron oscillation along the metal surface. Therefore, surface plasmon polaritons at a plane interface only exist with transverse-magnetic (TM) polarization [70]. In this latter case, the electric field vector is fully restricted to the x-z plane, i.e., the propagation plane. Following Novotny and Hecht [55], the solutions of TM-polarized surfaces waves in both media $j = 1, 2$ are of the form

$$\mathbf{E}^{(j)} = E_x^{(j)} \begin{pmatrix} 1 \\ 0 \\ -k_x/k_z^{(j)} \end{pmatrix} \cdot \mathrm{e}^{ik_x x - i\omega t}\mathrm{e}^{ik_z^{(j)} z} \quad , \quad j = 1, 2. \tag{3.17}$$

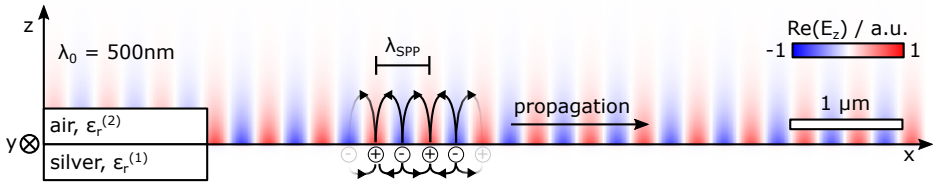

Figure 3.2: Out-of-plane electric field component E_z of a propagating surface plasmon polariton with wavelength λ_{SPP} at an Ag-air interface at a vacuum wavelength $\lambda_0 = 500\,\text{nm}$. A clear decrease of the field strength in the direction normal to the surface z can be observed. The oscillating surface charges and field directions are sketched for clarity. For $\epsilon_r^{(1)}$ the dielectric data of silver from Johnson and Christy is used [75], $\epsilon_r^{(2)} = 1$ represents air. The tiny field penetration into the silver is not visible for the shown scale.

Here, k_x and k_z are the components of the surface mode wavevector in x- and z-direction, respectively. The complex in-plane wavevector component k_x describes the evolution of the phase of the electric field and possible attenuation along the propagation direction x. This in-plane wavevector component k_x is called propagation constant $\tilde{\beta}$ and is given at a single plane interface by [55, 79]

$$\tilde{\beta}(\omega) = k_0 \sqrt{\frac{\epsilon_r^{(1)} \epsilon_r^{(2)}}{\epsilon_r^{(1)} + \epsilon_r^{(2)}}} \quad , \tag{3.18}$$

with $k_0 = \frac{2\pi}{\lambda_0}$ being the wavevector in vacuum corresponding to a wavelength λ_0. Furthermore, the out-of-plane wavevector component describing the exponential decay perpendicular to the surface in both media reads as [55]

$$(k_z^{(j)})^2 = \frac{(\epsilon_r^{(j)})^2}{\epsilon_r^{(1)} + \epsilon_r^{(2)}} k_0^2 \quad , \quad j = 1, 2. \tag{3.19}$$

Propagating surface modes require that the out-of-plane wavevector component $k_z^{(j)}$ in equation 3.19 is purely imaginary, leading to exponentially decaying solutions in both media j, and that a real part of $\tilde{\beta}$ in equation 3.18 exists. As a result, two necessary conditions for the existence of surface modes concerning the dielectric functions of both media can be derived [78]:

$$\text{Re}\left(\epsilon_r^{(1)} + \epsilon_r^{(2)}\right) < 0 \quad , \tag{3.20}$$

$$\text{Re}\left(\epsilon_r^{(1)} \cdot \epsilon_r^{(2)}\right) < 0 \quad . \tag{3.21}$$

In other words, one of the two media, e.g., medium 1, must have a negative real part of the dielectric function with the absolute value exceeding the value of the dielectric medium: $\text{Re}\left[\epsilon_r^{(1)}(\omega)\right] < -\epsilon_r^{(2)}$, with $\epsilon_r^{(2)} > 0$. Silver and gold, together with other

metals, have a large negative real part and a small imaginary part of the dielectric function (c.f. figure 3.1). Thus, for a typical metal-dielectric interface, these conditions are fulfilled and surface modes do exist.

In the general case of a complex dielectric function of the metal, the propagation constant $\tilde{\beta}$ of the surface mode is complex. The real part of $\tilde{\beta}$ describes the evolution of the phase of the electric field in the direction of propagation at a fixed time. A visualization of the electric field component in z-direction for a propagating surface plasmon polariton at a silver-air interface at $\lambda_0 = 500\,\mathrm{nm}$ is shown in figure 3.2. A clear periodicity in propagation direction can be observed that defines the surface plasmon polariton wavelength $\lambda_{SPP} < \lambda_0$. In analogy to plane waves in dielectric media, a complex effective refractive index $\tilde{n}_{eff}$ of the mode (*effective mode index*) is introduced, whose real part n_{eff} relates the plasmon wavelength with the vacuum wavelength via

$$\lambda_{SPP} = \frac{\lambda_0}{\mathrm{Re}(\tilde{n}_{neff})} = \frac{\lambda_0}{n_{eff}} \quad . \tag{3.22}$$

While the normal component of the electric field (z-component) is dominant in the dielectric, the tangential component is dominant in the metal. The bound character of surface plasmon polaritons can be easily seen in the dispersion relation (figure 3.3a). For an Ag-air interface, two branches can be observed, one high energy and one low energy branch. The high-energy branch describes radiation into the metal medium, while the low energy branch corresponds to the true surface plasmon polaritons. In the loss-less limit, the propagation constant can be infinite at the surface plasmon frequency $\omega_{SP} = \frac{\omega_p}{\sqrt{1+\epsilon_r^{(2)}}}$ defined via the condition $\epsilon_r^{(1)}(\omega) + \epsilon_r^{(2)} = 0$. In real metals like silver, the propagation constant remains finite and a back-bending of the dispersion relation between the two branches is observed. In the following, the low energy branch is considered, where the real part of the propagation constant is located right of the light line in air given by the energy of photons $E_{ph} = \hbar c k_0$. This implies that surface plasmon polaritons are bound to the surface because they cannot decay into a photon. Thus, the momentum-mismatch requires further wavevector matching techniques for both excitation as well as detection of surface plasmon polaritons via far-field optics, e.g., offered by prisms, gratings or different surface discontinuities [78, 79]. The imaginary part of $\tilde{\beta}$ describes the attenuation of the traveling wave due to electron scattering and interband damping. The distance after which the intensity of the surface wave decreases by $1/e$ in the direction of propagation is called propagation length, which is given by

$$l_p = \frac{1}{2\,\mathrm{Im}(\tilde{\beta})} = \frac{\lambda_0}{4\pi\,\mathrm{Im}(\tilde{n}_{eff})} \quad . \tag{3.23}$$

This propagation length strongly increases for higher wavelengths. In particular, the different dielectric function of silver compared to gold leads to a strongly increased propagation length for the whole range from the visible to near-infrared spectral range (figure 3.3b, solid lines). A further important quantity is the confinement of

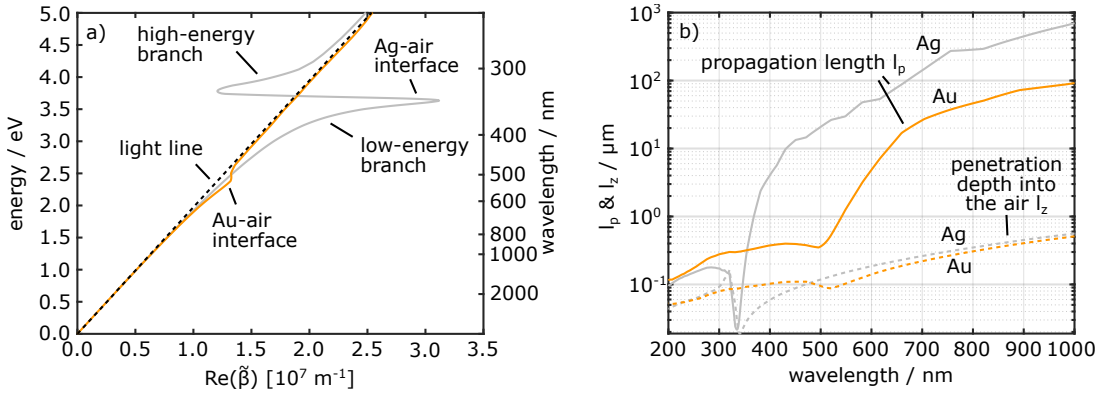

Figure 3.3: (a) Dispersion relation of propagating surface plasmon polaritons at a silver-air interface (grey) and at a gold-air interface (orange). The light line in air is shown as black dashed line. (b) Propagation lengths for the Ag (grey) and Au (orange) surface in air. The corresponding penetration depth into the air medium is shown as dashed lines. For all plots, the dielectric data from Johnson and Christy is used [75].

the surface mode, quantified here by the intensity decay length into the dielectric l_z (figure 3.3b, dashed lines). In a wide wavelength range above 600 nm, the intensity of surface plasmon polaritons at a plane interface decays within a few 100 nm into the dielectric and within about 10-15 nm into the metal. As the wavelength decreases, both the confinement and losses are increasing nonlinearly. As can be observed in figure 3.3b, a better confinement (dashed lines) is tightly linked to a decreasing propagation length (solid lines). This trade-off between confinement of the electric fields and losses is omnipresent in plasmonics. The squeezing of electromagnetic fields into small areas is accompanied by an increasing fraction of electromagnetic energy being located inside the metal, where it gets absorbed due to the ohmic loss present. However, the link between confinement and losses turns out to be different for different waveguide geometries, as demonstrated by Bozhevolnyi and coworkers [78, 80]. Therefore, different waveguide configurations can be designed and optimized for a specific application.

3.2.2 Surface plasmon polaritons at metal nanowires

Besides plane metal-dielectric interfaces, also different geometries like metal nanowires [81], grooves in a metal layer [82], dielectric ridges on a metal interface [80], among others, support propagating surface plasmon polaritons. In this thesis, particularly metal nanowires are considered and are arranged into the more complex geometry of a two-wire transmission line (c.f. chapters 6 and 7) and the related nanowire-on-mirror construct (c.f. chapter 8). All these geometries have in common that the field is now confined in the plane perpendicular to the one-dimensional propagation direction. For metal nanowires, the propagation is directed along the nanowire's long axis, while

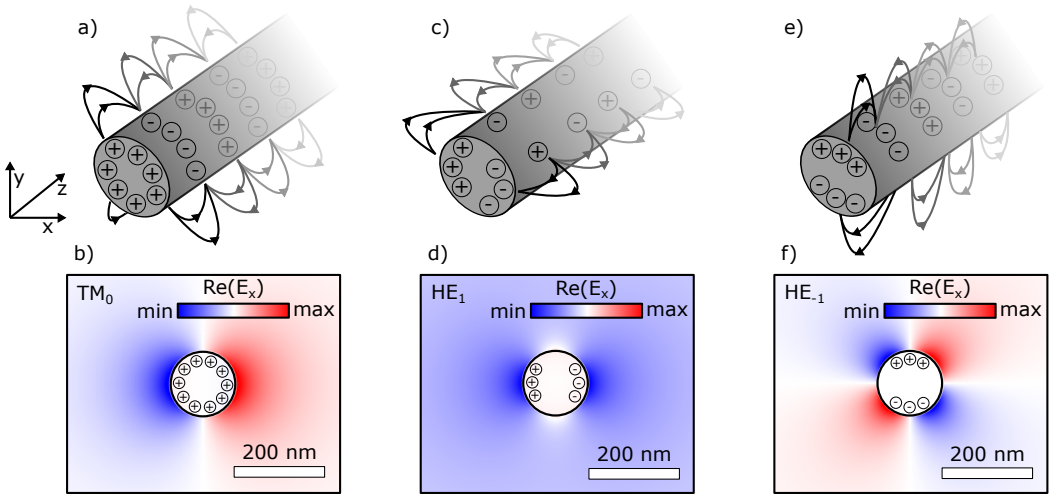

Figure 3.4: Sketch of the charge distribution and electric-fields for the (a) fundamental TM_0 mode and (c,e) higher-order HE_1 and HE_{-1} modes with a transverse charge oscillation. (b,d,f) Corresponding electric near-field x-component for a silver wire of diameter 150 nm in air at $\lambda_0 = 600$ nm vacuum wavelength. The dielectric data of silver from Johnson and Christy [75] is used.

the field in the transverse plane is tightly confined to the nanowire surface. According to Novotny [83, 84], the propagating modes of a cylindrical wire in a homogeneous dielectric environment can be calculated analytically by solving the wave equation. In regard of the more complex geometries in this thesis, here, the propagating modes are obtained from a numerical mode analysis calculation described in more detail in chapter 4. The output of such a mode analysis is the complex field $\mathbf{E}(x, y, \omega)$ in a transverse (x,y)-plane of the wire together with the propagation constant $\tilde{\beta}$ of the considered mode. The time-dependency and the evolution of the electric field along the wire (assumed to be infinitely long) in propagation direction z can be obtained by multiplication with the term $e^{i\tilde{\beta}z - i\omega t}$ (see section 4.1.2).

The *fundamental propagating mode* of a round metal-nanowire in a homogeneous environment is the TM_0-mode, which features a homogeneous charge distribution in a transverse plane along the circumference of the wire together with an associated radial polarization of the electric near-field (c.f. the sketch in figure 3.4a). As a result, the x-component of the electric field points in opposite direction at the different sides of the wire along the x-direction (figure 3.4b). In addition to the radial field component, in a plane shifted by $\lambda_{SPP}/4$ along the waveguide direction (phase-shift of $\pi/2$), the fields are rotated into the propagation direction as sketched by the black arrows in figure 3.4a. For certain conditions which are further discussed below, two *higher-order modes* called HE_1 and HE_{-1} appear that are degenerate in a homogeneous medium [85]. In these modes, the charge distribution oscillates not only along the wire but also horizontally or vertically in the transverse plane, respectively (c.f. the sketch in figures 3.4c, e). As a result, the x-component of the HE_1 modal field does not feature a change of sign across the wire in x-direction (figure 3.4d). The HE_{-1} mode in a homogeneous

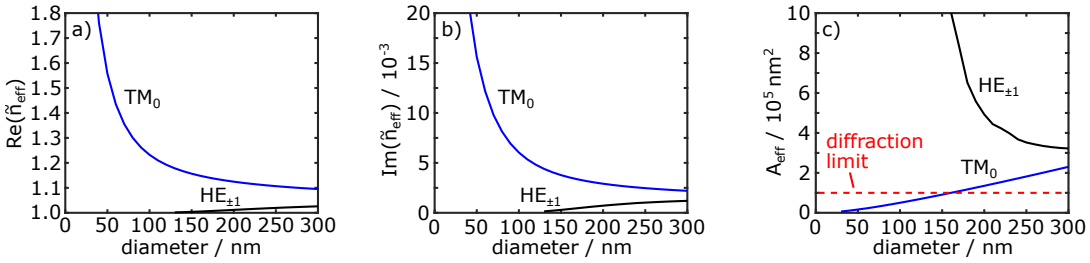

Figure 3.5: (a) Real part of the effective mode index n_{eff} of the fundamental TM_0 and higher-order HE_1 & HE_{-1} propagating modes on a silver nanowire wire of varying diameter in air. (b) Corresponding imaginary part of the mode index. (c) Effective mode area A_{eff} as a function of the diameter. The dielectric data of silver from Johnson and Christy [75] at $\lambda_0 = 600\,\text{nm}$ has been used for the simulations.

environment is just the rotation of the HE_1-mode by 90° around the z-axis. The resulting x-component of the electric field can be understood by recognizing the dipolar character of the transverse field-components (figure 3.4f).

These higher-order HE_1 and HE_{-1} modes feature effective mode indices with a real part only differing significantly from the environmental refractive index above a certain wire-diameter (figure 3.5a). As the diameter decreases, the losses associated with $\text{Im}(\tilde{n}_{eff})$ decrease (figure 3.5b) and the mode-area increases strongly (figure 3.5c). The effective mode-area, accounting for the lateral field confinement, is defined here as [86, 87]

$$A_{eff} = \frac{\left(\int |E|^2\, dA\right)^2}{\int |E|^4\, dA} \quad , \tag{3.24}$$

with the integrations performed over the entire transverse plane. The fundamental TM_0 mode, compared to the higher-order modes, shows a completely different behavior as the diameter of the wire tends to zero. In this limit, the real part of the effective mode index $\text{Re}(\tilde{n}_{eff})$ strongly increases (figure 3.5a), however, also losses get more and more dominant (figure 3.5b). Furthermore, the effective mode-area A_{eff} for the TM_0 mode decreases to values well below the diffraction limit ($\sim(\frac{\lambda}{2})^2 \sim 10^5\,\text{nm}^2$), which is referred to as *sub-diffraction plasmonic confinement* (figure 3.5c).

The real part of the effective mode index n_{eff} presented in figure 3.5a is not only dependent on the diameter of the wire but also on the operation wavelength and refractive index of the surrounding medium. Briefly, n_{eff} increases for increasing energy of the plasmonic mode, similar to the dispersion relation of surface plasmon polaritons at plane interfaces (c.f. figure 3.3a). An increasing refractive index of the surrounding medium leads to a corresponding increase of n_{eff} of the plasmonic mode. Furthermore, higher environmental refractive indices result in larger propagation loss, as the field penetration in the dielectric gets smaller and an increasing fraction of the modal power is shifted into the lossy metal.

The cross-section of real wires is not round but rather pentagonal for most chemically grown metal nanowires or features a certain edge rounding when milled in a metal flake. Despite these deviations of real wires from the ideal round cross-section, all the plasmonic waveguide modes are recovered qualitatively [88, 89]. In case of a substrate medium below the metal wire, the surrounding medium is not homogeneous anymore, as the refractive index of the substrate, e.g., $n = 1.5$, is larger than the top dielectric, e.g., air. As a result, the degeneracy of the higher-order $HE_{\pm 1}$ modes is lifted. Furthermore, depending on geometry, materials and operation wavelength, the plasmonic modes can be cut-off and a single-mode operation can be achieved, as observed by Zia *et al.* [90]. For a nanowire, there is no cutoff of the fundamental propagating plasmonic mode, but higher-order modes can be cut-off when the real part of their effective mode index gets below the refractive index of an adjacent dielectric medium. In this *leaky mode* regime, the modes experience an additional radiation loss into the medium with highest refractive index, e.g., the substrate. While the radiation loss allows to image leaky modes during propagation via leakage radiation microscopy [89], additional loss channels are in general unfavorable for long-range circuit applications.

This thesis aims at achieving high field confinement for an enhanced light-matter interaction with quantum emitters. The fundamental mode of a metal nanowire best matches these requirements in the diameter range of about 40-100 nm. Here, a good trade-off between loss and confinement is achieved (c.f. figures 3.5b,c). Higher-order modes of such thin nanowires feature a much larger mode area and are nearly not excited by a laser focus at the wire end, as quantified by Li *et al.* [88]. Thus, higher-order modes and leaky mode waveguiding can be mostly avoided by choosing a thin nanowire diameter. In some cases, a superposition of a confined fundamental and a long-range higher-order mode can be desired because, as observed by Castro-Lopez *et al.* [91], the overall propagation length can be increased while maintaining a high confinement at local hot-spots. A further concept to modify the confinement and propagation properties of a waveguide is to design more complex structures. In chapters 6 and 7, the fundamental waveguide modes of two parallel silver nanowires hybridize into a symmetric and antisymmetric hybrid mode. Moreover, in chapter 8, a silver nanowire interacts with its mirror image in an underlying silver surface across a few-nanometer gap.

3.3 DECAY RATES OF AN EMITTER CLOSE TO A PLASMONIC STRUCTURE

Placing a quantum emitter in the proximity of a plasmonic waveguide typically leads to an enhanced decay rate due to additional decay channels opening up. In the ideal case of emitter-waveguide coupling, mainly the radiative rate of the quantum emitter is enhanced, with the emission being efficiently channeled into propagating plasmonic modes of the waveguide overwhelming all other decay channels. For this effect, the theoretical treatment by Chen *et al.* [92] shows that the dipole moment, position and

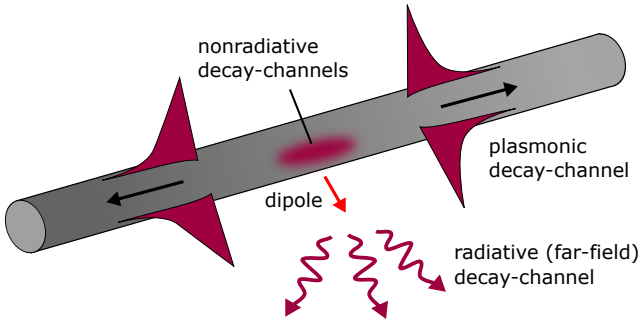

Figure 3.6: Available decay-channels for a quantum emitter represented by a dipole (red arrow) close to a plasmonic waveguide: A far-field radiation channel, a channel into plasmonic modes propagating along the waveguide and a nonradiative channel exist. Inspired from ref. [92].

orientation of the quantum emitter within the near-field, as well as the properties of the waveguide mode, i.e., its group velocity and mode confinement, are important aspects.

Close to a plasmonic nanostructure, a quantum emitter's excited state can decay via three decay channels (figure 3.6). First, it can decay via far-field radiation, i.e., emission that is not guided along the waveguide. Here, it is important to note that the point-spread function of this far-field radiation can be strongly modified due to the presence of a metal nanostructure [93–96]. Second, the emitter can decay via emission into the available waveguide mode(s). This emission channel can be detected at waveguide ends, e.g., by an interconversion to far-field photons. Third, nonradiative decay channels exist close to the surface of the metal that lead to ohmic loss in the metal. Note that the nonradiative decay channel inherent to the emitter is not captured in the modeling by an electric dipole. Good fluorophores such as polycyclic aromatic hydrocarbons feature a near-unity fluorescence quantum yield (c.f. section 2.5) and thus their inherent nonradiative decay is neglected here.

The desired channel for applications of the nanostructure as plasmonic circuit is the decay into waveguide mode(s). Therefore, an important parameter to quantify the emitter-waveguide coupling is the ratio of the decay rate into a waveguide mode normalized to the total decay rate, called β-factor.

3.3.1 Decay rate into propagating plasmons

The spontaneous emission decay rate of a quantum emitter with transition dipole moment $\boldsymbol{\mu}$ in an arbitrary optical environment can be calculated according to

$$\gamma = \frac{\pi\omega}{3\hbar\epsilon_0}|\boldsymbol{\mu}|^2\rho_p(\mathbf{r_0},\omega) \quad . \tag{3.25}$$

Here, $\rho_p(\mathbf{r_0}, \omega)$ is called *partial* (or *projected*) *local density of optical states* (LDOS) [55, 97]. It represents the number of modes per unit volume and frequency into which a point-like quantum system at position $\mathbf{r_0}$ with defined dipole axis $\hat{e}_D$ can spontaneously emit a photon of energy $\hbar\omega$. In vacuum, the density of electromagnetic modes is given by $\rho_0 = \frac{\omega^2}{\pi^2 c^3}$, which results in the radiative decay rate of the quantum emitter in vacuum given by

$$\gamma_0 = \frac{\omega^3 |\boldsymbol{\mu}|^2}{3\pi\epsilon_0 \hbar c^3} \quad . \tag{3.26}$$

For a nanophotonic environment, the projected LDOS can be obtained from the electric dyadic Green's function $\bar{\bar{\mathbf{G}}}(\mathbf{r}, \mathbf{r}', \omega)$, which is defined by [55]

$$\nabla \times \nabla \times \bar{\bar{\mathbf{G}}}(\mathbf{r}, \mathbf{r}', \omega) - k_0^2 \epsilon_r(\mathbf{r}, \omega) \bar{\bar{\mathbf{G}}}(\mathbf{r}, \mathbf{r}', \omega) = \bar{\bar{\mathbf{I}}} \delta(\mathbf{r} - \mathbf{r}') \quad , \tag{3.27}$$

with the unit dyad (tensor) $\bar{\bar{\mathbf{I}}}$. The three different columns of the Green's tensor correspond to the electric field due to a point source at position $\mathbf{r}'$ with x-, y- and z-orientation of the dipole axis, respectively. According to Novotny and Hecht [55], the LDOS projected on an arbitrary dipole orientation $\hat{e}_D$ is accessible from the electric dyadic Green's function evaluated at the dipole origin $\mathbf{r_0}$ by the universal relation

$$\rho_p(\mathbf{r_0}, \omega) = \frac{6\omega}{\pi c^2} \left[\hat{e}_D \cdot \mathrm{Im}\left\{ \bar{\bar{\mathbf{G}}}(\mathbf{r_0}, \mathbf{r_0}, \omega) \right\} \cdot \hat{e}_D \right] \quad . \tag{3.28}$$

Following the in-depth theoretical treatment of Chen *et al.* [92] based on the electric dyadic Green's function, the local density of optical states for one specific plasmonic mode projected on the dipole orientation $\hat{e}_D$ can be expressed in terms of the eigenmode's complex electric field $\mathbf{E}$ and magnetic field $\mathbf{H}$ in a transverse x-y plane by

$$\rho_{pl}(\mathbf{r_0}, \omega) = \frac{6\epsilon_0 |\hat{e}_D \cdot \mathbf{E}(x,y)|^2}{2\pi \int_{A_\infty} (\mathbf{E} \times \mathbf{H}^*) \cdot \hat{e}_z \, dA} = \frac{6 |\hat{e}_D \cdot \mathbf{E}(x,y)|^2}{N v_g} \quad , \tag{3.29}$$

with the group velocity of the propagating mode

$$v_g = \frac{\int_{A_\infty} (\mathbf{E} \times \mathbf{H}^*) \cdot \hat{e}_z \, dA}{\int_{A_\infty} \epsilon_0 \epsilon_r(x,y) |\mathbf{E}(x,y)|^2 \, dA} \quad , \tag{3.30}$$

and the normalization factor

$$N = 2\pi \int_{A_\infty} \epsilon_r(x,y) |\mathbf{E}(x,y)|^2 \, dA \quad . \tag{3.31}$$

Here, $\hat{e}_z$ represents the unit vector along the propagation direction. The integrations are performed over the entire transverse plane A_∞. As evident from equation 3.29, a maximum projected LDOS requires a dipole moment parallel to the electric field ($\hat{e}_D \parallel \mathbf{E}$), a small group velocity v_g of the mode and a tight mode confinement (for high values of $\mathbf{E}$).

Equation 3.29 can be plugged into equation 3.25 to yield the spontaneous emission rate into the plasmonic mode. Normalized to the decay rate in vacuum γ_0 and expressed in terms of the numerically accessible modal fields, it follows [92]

$$\frac{\gamma_{pl}}{\gamma_0} = \frac{3\pi c\epsilon_0 |\hat{e}_D \cdot \mathbf{E}(x,y)|^2}{k_0^2 \int_{A_\infty} (\mathbf{E} \times \mathbf{H}^*) \cdot \hat{e}_z \, dA} \quad . \tag{3.32}$$

Here, the integrand in the denominator equals twice the time-averaged pointing vector in propagation direction. It should be noted that the validity of equations 3.29 - 3.32 is limited to cases where the imaginary part of the propagation constant of the considered waveguide mode is negligible compared to the real part. This situation is often met also for lossy plasmonic modes, e.g., those supported by a plasmonic nanowire (c.f. figure 3.5). The general full theoretical treatment is given by Chen *et al.* [92].

3.3.2 Total decay rate

To calculate the β-factor, also the total decay rate needs to be calculated. It includes the radiative channels in far-field modes, the decay into the plasmonic waveguide mode and the nonradiative decay channels. This information is most conveniently retrieved from a 3-dimensional numerical model, which naturally includes all decay channels. A source term needs to be included in the wave equation that describes an oscillating electric point dipole (see chapter 4).

After numerically solving the wave equation with source term, the total emitted power P_{tot} of the dipole is calculated by integrating the time-averaged power outflow density over the surface of a small sphere enclosing the dipole emitter. P_0 can be obtained analogously by a reference calculation with removed environment, i.e., the simulation is performed in vacuum. The latter numerical value has to match the average radiated power from an oscillating dipole with a classical dipole moment $\boldsymbol{\mu}$ given by [55]

$$P = \frac{|\boldsymbol{\mu}|^2}{4\pi\epsilon_0\epsilon_r} \frac{n^3\omega^4}{3c^3} \quad , \tag{3.33}$$

which yields P_0 for the case of a vacuum environment ($n = \sqrt{\epsilon_r} = 1$). In contrast to this classical treatment of the radiated power P, in quantum mechanics, photons with energy $\hbar\omega$ are emitted with a certain probability per unit time, i.e., with the decay rate γ. Taking the proportionality of P and γ into account[1], the link between classical powers and quantum decay rates is given by [55, 73]

$$\frac{\gamma_{tot}}{\gamma_0} = \frac{P_{tot}}{P_0} \quad . \tag{3.34}$$

1 Note that $\boldsymbol{\mu}$ in equation 3.25 refers to a quantum mechanical matrix element, while it refers to a classical dipole moment in equation 3.33, where the former differs by a subtle factor of 1/2 from the latter, as pointed out e.g. by Hohenester [73].

Thus, the total decay rate γ_{tot} normalized to the free-space value γ_0 can be easily obtained from the normalized total emitted power P_{tot}/P_0 of a classical oscillating point dipole.

3.3.3 β-factor

Having determined both the decay rate into the plasmonic mode and the total decay rate, their ratio yields the β-factor

$$\beta = \frac{\gamma_{pl}}{\gamma_{tot}} \quad . \tag{3.35}$$

It is important to note that the β-factor does not need to be maximum at the position where γ_{pl} is maximum. Nonradiative contributions captured by γ_{tot} also increase close to the metal surface and non-trivial optimum positions for an emitter result.

In case of a silver nanowire of diameter 100 nm in a homogeneous environment of refractive index 1.414 at $\lambda_0 = 1\,\mu$m considered by Chen *et al.* [92], the ratio γ_{pl}/γ_0 reaches a maximum value of about 8-9 directly at the surface, while the β-factor reaches a maximum of about 0.5 in a distance of about 20 nm to the surface. Furthermore, Li *et al.* [98] considered experimentally the coupling of quantum dots to 80 nm diameter silver nanowires on glass. In their work, the highest surface plasmon quantum yield is found for an emitter-nanowire distance of about 10 nm. Emitter-waveguide coupling efficiencies exceeding those of single silver nanowires can be obtained in more complex-shaped waveguide geometries, e.g., in nanoscale gaps between two metal nanowires (c.f. chapters 6 and 7) or between a nanowire and a metal surface (c.f. chapter 8).

4 NUMERICAL SIMULATIONS

The field of plasmonics has meanwhile become one of the most important cornerstones of nanophotonics, enabling localization of electromagnetic near-fields on deep sub-wavelength scales. Plasmonic nanostructures and their interaction with light have been explored, modeled and engineered for decades by classical electromagnetic theory using a local dielectric function of the materials [70]. Besides this classical regime, Zhu *et al.* [25] discuss that a quantum regime opens up when the gap between two plasmonic nanostructures enters the few-nanometer to sub-nanometer scale. In this regime, the classical description fails to describe the correct localization of the induced surface charges. In particular, the surface charges can be effectively shifted with respect to the geometrical boundary of the metal (nonlocal regime) and electrons can even tunnel quantum mechanically across a sub-nanometric gap (tunneling regime), which was investigated theoretically by Teperik *et al.* [99]. The plasmonic nanostructures investigated in this thesis are separated by 60 nm in chapters 6 and 7. In chapter 8, few-nanometer gaps are realized, without entering the sub-nanometric regime. Thus, rather small deviations from the classical description are expected and the following simulations are performed by solving Maxwell's equations together with the local-response approximation of light-matter interaction. Nevertheless, surface plasmons have a true quantum nature and preserve many quantum mechanical properties such as entanglement [100] and antibunching [101] when interconverted with photons.

This chapter first discusses several numerical models that allow to calculate electromagnetic near-fields and related properties of plasmonic nanostructures in inhomogeneous environments, with special emphasis on scattering and waveguiding simulations. Subsequently, the general framework for the imaging of arbitrary electromagnetic near-fields with far-field calculations is provided. Finally, this framework is applied and demonstrated for the case of dipole emission, yielding the point-spread functions of an optical imaging system. The validity of the numerical implementation is demonstrated by comparing the results to data in the literature.

4.1 ELECTROMAGNETIC NEAR-FIELD CALCULATIONS

The electromagnetic near-field simulations in this thesis are performed with Comsol Multiphysics (version 5.3a and 5.4, RF module), a commercial software package based on the *finite-element method* (FEM). The FEM is a numerical method for obtaining an approximate solution to a boundary value problem defined by a differential equation in a domain Ω and certain boundary conditions on the boundary enclosing Ω [102]. For

the electromagnetic modeling of plasmonic nanostructures, the underlying differential equations are the Maxwell's equations. The computational domain can consist of an arbitrary inhomogeneous dielectric environment with sources placed inside. This domain Ω, which is typically two- or three-dimensional, is discretized into the *finite elements* Ω^e:

$$\Omega = \bigcup_e \Omega^e \quad . \tag{4.1}$$

In a three-dimensional domain, these elements are typically of tetrahedral shape but also different shapes like hexahedrons or triangular prisms can be applied. The size and orientation of these elements is flexible and thus interfaces between media of complex shape and different optical properties can be approximated very accurately. The collection of elements with their nodal points, called mesh, is generated automatically by the pre-processor of Comsol Multiphysics in consideration of the user's specified parameters, such as the maximum mesh element size. A finer mesh can be used in areas that are critical to the analysis in order to get more accurate results.

Noteworthy, the solution of the differential equation will not only be available at the given discrete mesh nodal points, but also continuously inside each element. The key to this continuous solution is a set a of N_e finite element basis functions (or interpolation functions) ϕ_k that are linearly independent on the element. Usually, polynomials of first, second or higher order are used. These polynomial basis functions are zero outside the considered finite element, while inside the element e they constitute the continuous unknown solution u^e according to an interpolation given by

$$u^e = \sum_{k=1}^{N_e} u_k^e \, \phi_k^e \quad . \tag{4.2}$$

Briefly, by applying certain procedures such as the Galerkin's method to the boundary value problem, a set of algebraic equations results for each element. Taking all elements and the boundary conditions into account, finally a system of equations is obtained [102, 103]. Typically, a sparse (banded) matrix results that allows for efficient numerical calculation of the unknown coefficients u_k^e. Once the system of equations is solved, the results can be post-processed in Comsol Multiphysics and desired parameters can be calculated. Besides simple data export options, a Matlab-Comsol livelink allows for more complex data processing.

Comsol Multiphysics and thus this section uses the positive sign-convention in the time-dependent factor for the complex representation of the time-harmonic electric field:

$$\mathbf{E}(\mathbf{r}, t) = \mathrm{Re}\left[\mathbf{E}(\mathbf{r}, \omega) \cdot \mathrm{e}^{i\omega t}\right] \quad . \tag{4.3}$$

When the field calculated with Comsol Multiphysics is post-processed with the standard $\mathrm{e}^{-i\omega t}$ convention, its complex conjugate has to be taken. In the frequency domain,

the complex electric field is calculated for each frequency ω of interest as a solution of the vector wave equation of the electric field $\mathbf{E}$ given by [55, 102]

$$\nabla \times \Big[\nabla \times \mathbf{E}(\mathbf{r},\omega)\Big] - k_0^2 \epsilon_r(\mathbf{r},\omega)\mathbf{E}(\mathbf{r},\omega) = -i\mu_0\omega\, \mathbf{j}_{ext}(\mathbf{r},\omega) \quad . \tag{4.4}$$

with the complex dielectric function $\epsilon_r(\mathbf{r},\omega)$, the magnitude of the wavevector $k_0 = \omega/c$ and the current density $\mathbf{j}_{ext}(\mathbf{r},\omega)$ imposed by an external source, e.g., a dipole emitter. The magnetic permeability is again set to the vacuum value μ_0 here.

In order to quantitatively evaluate the interaction of electromagnetic fields with a plasmonic nanostructure, e.g., the scattering by a resonant particle or the in-/outcoupling of a waveguide, the energy flux density has to be considered, which is given by the Poynting vector

$$\begin{aligned}\mathbf{S}(\mathbf{r},t) &= \mathbf{E}(\mathbf{r},t) \times \mathbf{H}(\mathbf{r},t) \\ &= \frac{1}{2}\mathrm{Re}\Big[\mathbf{E}(\mathbf{r},\omega) \times \mathbf{H}^*(\mathbf{r},\omega)\Big] + \frac{1}{2}\mathrm{Re}\Big[\mathbf{E}(\mathbf{r},\omega) \times \mathbf{H}(\mathbf{r},\omega) \cdot \mathrm{e}^{2i\omega t}\Big] \quad .\end{aligned} \tag{4.5}$$

Regarding the time-averaged energy flux density, the second time-dependent term in equation 4.5 vanishes and only the time-independent term remains [104]:

$$\big\langle \mathbf{S}(\mathbf{r},\omega) \big\rangle = \frac{1}{2}\mathrm{Re}\Big[\mathbf{E}(\mathbf{r},\omega) \times \mathbf{H}^*(\mathbf{r},\omega)\Big] \quad . \tag{4.6}$$

The time-averaged Poynting vector is used in several Comsol Multiphysics models described in the following subsections, investigating the scattering of resonant plasmonic nanostructures and the properties of waveguide nanostructures. All models have in common that different parts of the domain, e.g., substrate, superstrate, metal nanostructures and dielectric cover layers, can be modeled by different refractive indices. For silver, the dielectric data of Johnson and Christy is used [75]. Glass, poly(methyl methacrylate) (PMMA) and poly-(vinylpyrrolidinone) (PVP) are modeled by $n = 1.5$ and air by $n = 1$. For Al_2O_3 the dielectric data of Malitson from Comsol's database is used [105].

4.1.1 Absorption and scattering by a plasmonic structure

Scattering spectra of plasmonic nanostructures monitor the resonances at specific wavelengths that are strongly determined by the shape, size and material of the scattering structure, and by its environment [106]. Therefore, scattering spectra give important insights into these parameters on the nanoscale. In particular, in chapter 8, the size of a few-nanometer gap formed between a silver nanowire and a silver surface is determined by the scattering spectrum of the structure, an information that is very hard to access otherwise.

In order to calculate the scattering of a plasmonic nanowire arising from plasmon oscillations in a transverse direction, it is a reasonable approximation to treat the

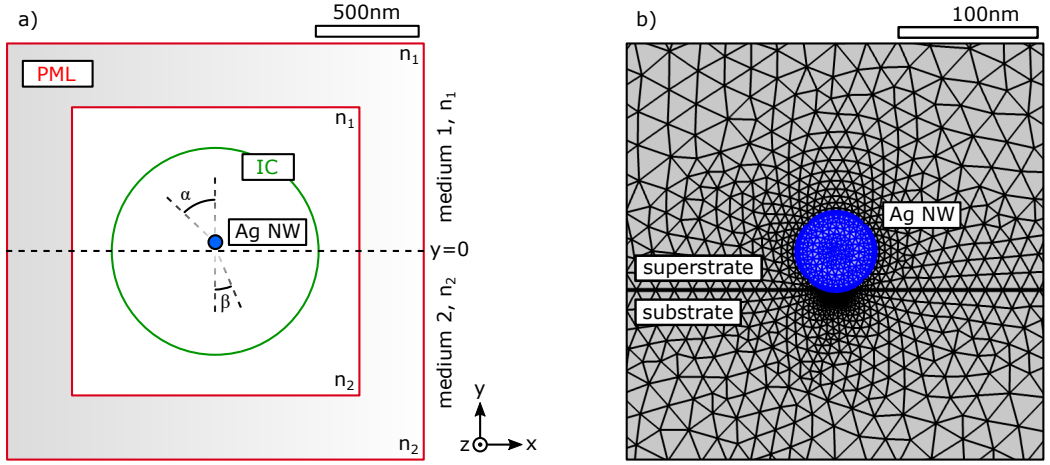

Figure 4.1: (a) Sketch of the two-dimensional Comsol Multiphysics model to simulate the scattered field of an infinitely extended plasmonic structure in the transverse plane, e.g., by a single silver nanowire. A perfectly matched layer (PML, marked red), an integration circle (IC, marked green) and the interface between substrate and superstrate are taken into account. (b) Exemplary mesh generated by Comsol Multiphysics around the nanowire (Ag NW, marked blue).

nanowire as infinitely extended along the z-direction. Then, the electric field only needs to be calculated in the transverse x-y-plane, while it is assumed to be homogeneous in the z-direction. This way, transverse plasmon oscillations are considered, while longitudinal Fabry-Pérot resonances, as observed by Dorfmüller *et al.* [107] in shorter, finite-length wires, are not taken into account. The two-dimensional simulation domain used here is sketched in figure 4.1a with a part of the mesh shown in figure 4.1b. The boundary $y = 0$ separates the model into a substrate ($y < 0$) and superstrate ($y > 0$) part that may have different refractive indices n_1 and n_2, respectively. The plasmonic structure, e.g., a round nanowire of diameter 60 nm, is located on top of this boundary. The model is truncated by a perfectly matched layer (PML) with a swept mesh that absorbs the outgoing scattered fields. Furthermore, a transparent integration circle (IC) is included that offers a closed boundary around the isolated scattering nanostructure for analysis purposes (see below). The total size of the simulation domain is chosen such that the integration circle is outside the near-field of the structure, e.g., with a diameter of the integration circle of 1 µm (c.f. figure 4.1a).

To calculate the scattering spectrum of a plasmonic structure, it is convenient to split the total electric field into a background field $\mathbf{E}_b(\mathbf{r}, \omega)$ and a scattered field $\mathbf{E}_s(\mathbf{r}, \omega)$ according to [108]

$$\mathbf{E}(\mathbf{r}, \omega) = \mathbf{E}_b(\mathbf{r}, \omega) + \mathbf{E}_s(\mathbf{r}, \omega) \quad . \tag{4.7}$$

The background field exciting the structure of interest is analytically defined as a p-polarized plane wave of amplitude E_0 that is incident from the superstrate with

an angle of incidence α measured against the substrate normal. In the superstrate medium 1 (e.g., air), the background field is given by

$$E_{b,x}^{(1)} = E_0 \left(\mathrm{e}^{-ik_0 n_1 x \cdot \sin(\alpha) + ik_0 n_1 y \cdot \cos(\alpha)} - r_p \mathrm{e}^{-ik_0 n_1 x \cdot \sin(\alpha) - ik_0 n_1 y \cdot \cos(\alpha)} \right) \cdot \cos(\alpha) \quad , \tag{4.8}$$

$$E_{b,y}^{(1)} = E_0 \left(\mathrm{e}^{-ik_0 n_1 x \cdot \sin(\alpha) + ik_0 n_1 y \cdot \cos(\alpha)} + r_p \mathrm{e}^{-ik_0 n_1 x \cdot \sin(\alpha) - ik_0 n_1 y \cdot \cos(\alpha)} \right) \cdot \sin(\alpha) \quad . \tag{4.9}$$

It is composed of an incident plane wave and its superposition with the reflected wave from the interface. Accordingly, in the substrate medium 2 (e.g., glass or silver), the background field is given by

$$E_{b,x}^{(2)} = E_0 t_p \mathrm{e}^{-ik_0 n_2 x \cdot \sin(\beta) + ik_0 n_2 y \cdot \cos(\beta)} \cdot \cos(\beta) \quad , \tag{4.10}$$

$$E_{b,y}^{(2)} = E_0 t_p \mathrm{e}^{-ik_0 n_2 x \cdot \sin(\beta) + ik_0 n_2 y \cdot \cos(\beta)} \cdot \sin(\beta) \quad . \tag{4.11}$$

The reflection and transmission at the interface involves Fresnel coefficients for p-polarization defined as

$$r_p = \frac{n_2 \cos(\alpha) - n_1 \cos(\beta)}{n_2 \cos(\alpha) + n_1 \cos(\beta)} \quad , \tag{4.12}$$

$$t_p = \frac{2 n_1 \cos(\alpha)}{n_1 \cos(\beta) + n_2 \cos(\beta)} \quad . \tag{4.13}$$

The angle of incidence α of the plane wave is mapped on a propagation angle β in the substrate via Snell's law $n_1 \sin(\alpha) = n_2 \sin(\beta)$, which can yield a complex-valued β.

Having calculated the scattered electric and magnetic fields $\mathbf{E}_s(\mathbf{r}, \omega)$ and $\mathbf{H_s}(\mathbf{r}, \omega)$ via Comsol Multiphysics, the time-averaged energy flux density of the scattered field is given by

$$\left\langle \mathbf{S}_s(\mathbf{r}, \omega) \right\rangle = \frac{1}{2} \mathrm{Re} \left[\mathbf{E}_s(\mathbf{r}, \omega) \times \mathbf{H}_\mathbf{s}^*(\mathbf{r}, \omega) \right] \quad . \tag{4.14}$$

In three dimensions, where the scatterer is embedded in a non-absorbing medium enclosed by an arbitrary surface ∂V, the absorption and scattering cross-sections of the scatterer can be calculated according to [109]

$$C_{abs}(\omega) = \frac{W_{abs}}{I_i} = -\frac{1}{I_i} \int_{\partial V} \left\langle \mathbf{S}(\mathbf{r}, \omega) \right\rangle \cdot \hat{n}(\mathbf{r}) \, dA \quad , \tag{4.15}$$

$$C_{scat}(\omega) = \frac{W_{scat}}{I_i} = +\frac{1}{I_i} \int_{\partial V} \left\langle \mathbf{S}_s(\mathbf{r}, \omega) \right\rangle \cdot \hat{n}(\mathbf{r}) \, dA \quad , \tag{4.16}$$

with W_{abs} and W_{scat} being the rates at which energy is absorbed and scattered by the scatterer, respectively. $I_i = \frac{1}{2} c \epsilon_0 n_1 E_0^2$ is the spatially constant average intensity of the incident plane wave, which is independent of frequency ω. $\hat{n}(\mathbf{r})$ represents the surface normal unit vector pointing in outward direction. The extinction cross-section

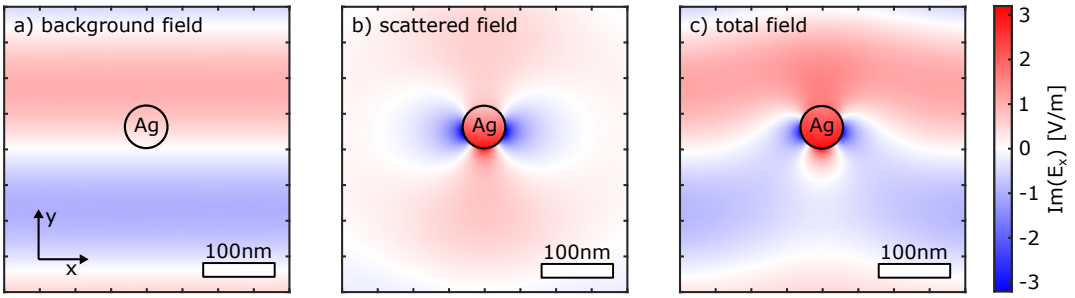

Figure 4.2: Two-dimensional simulation in the transverse plane of an Ag nanowire of 60 nm diameter embedded in a homogeneous medium ($n_1 = n_2 = 1$) at a wavelength $\lambda = 340$ nm. (a) Background plane wave with p-polarization incident from the top ($\alpha = 0°$). (b) Corresponding scattered field of the nanowire. (c) Total field as superposition of (a) and (b). In each panel the x-component of the electric field (imaginary part) is plotted.

is the sum of both the absorption and scattering cross-section $C_{ext} = C_{abs} + C_{scat}$. To determine scattering and absorption in the two-dimensional case, analogously a line-integration over the integration circle is performed (c.f. figure 4.1a). This yields a quantity with dimensions of length instead of area that can be interpreted as cross-section per length of the structure in z-direction.

As an instructive example, a silver nanowire with 60 nm diameter in a homogeneous medium ($n = 1$) is investigated. The driving background field is incident with $\alpha = 0°$ from the top (figure 4.2a). The scattered field at 340 nm displays a dipolar pattern around the silver nanowire corresponding to a transverse plasmon oscillation of the wire that is excited by the p-polarized background wave (figure 4.2b). The total field is a superposition of both background and scattered field (figure 4.2c). The calculated cross-sections per length show a resonance at 340 nm (figure 4.3), in good agreement with analytical results of Scaffardi *et al.* [110]. For thin silver wires the quasi-static limit is reached, where an analytical condition for the plasmon resonance is available: $\mathrm{Re}\left[\epsilon_r^{(Ag)}(\lambda)\right] = -\epsilon_r^{(env)}$ [55]. In air, i.e., $\epsilon_r^{(env)} = 1$, this condition yields a resonance wavelength of about 340 nm for the dielectric function of silver $\epsilon_r^{(Ag)}(\lambda)$ (c.f. figure 3.1a), in agreement with the resonance wavelength calculated here (figure 4.3). The

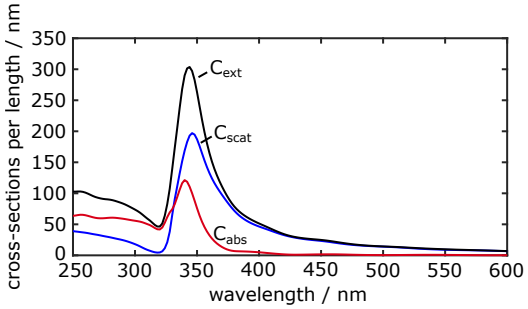

Figure 4.3: Calculated absorption (red), scattering (blue) and extinction cross-section (black) per length of a 60 nm diameter Ag nanowire in air.

resonance wavelength can be shifted, e.g., by changing the dielectric environment $\epsilon_r^{(env)}$, which is the basic concept behind plasmonic sensing via resonance shifts [111]. As the wire diameter increases further, the quasi-static approximation becomes more and more inappropriate, the resonance further broadens and shifts to longer wavelengths.

The model presented in this section is used in chapter 6 to determine the near-field around a plasmonic two-wire waveguide on a glass-air interface upon plane wave illumination. Furthermore, in chapter 8, the plasmonic resonances of a silver nanowire in a few-nanometer separation to a silver surface are investigated. In order to account for the experimental condition during darkfield spectroscopy, the background plane wave in the simulation can be incident under a non-zero angle α and the finite collection angle of the objective can be taken into account by integrating the time-averaged energy flux density of the scattered field only over a corresponding segment of the integration circle (c.f. figure 4.1a).

4.1.2 Waveguide mode analysis

In contrast to the purely transverse plasmon oscillation in an Ag nanowire considered in subsection 4.1.1, propagating eigenmodes of an infinitely extended waveguide feature a non-homogeneous and oscillating field-distribution along the propagation direction (c.f. section 3.2). In order to compute such propagating eigenmodes, again a transverse x-y-plane is considered. Comsol Multiphysics provides the boundary mode analysis [108], which solves for the complex propagation constant $\tilde{\beta}(\omega)$ and the complex modal field in the transverse plane $\mathbf{E}(x, y, \omega)$. The real part of $\tilde{\beta}(\omega)$ determines the evolution of the phase along the waveguide, while the imaginary part determines the damping according to the propagation length l_p. Given these results, the evolution of the eigenmode in the direction of propagation z is determined by

$$\mathbf{E}(x, y, z, \omega) = \mathbf{E}(x, y, \omega) \cdot \mathrm{e}^{-i\tilde{\beta}(\omega)z} = \mathbf{E}(x, y, \omega) \cdot \mathrm{e}^{-ik_0 n_{eff}(\omega)z} \cdot \mathrm{e}^{-\frac{z}{2l_p}} \quad . \tag{4.17}$$

The full spatio-temporal evolution of the (complex) modal field at the waveguide includes a time-dependent term $\mathrm{e}^{i\omega t}$, yielding

$$\mathbf{E}(x, y, z, t) = \mathbf{E}(x, y, \omega) \cdot \mathrm{e}^{i\omega t - i\tilde{\beta}(\omega)z} \quad , \tag{4.18}$$

with the sign-convention used by Comsol Multiphysics. In comparison to the scattering model presented in the last subsection, several changes to the two-dimensional domain and boundary conditions need to be applied (c.f. figure 4.1a). First, the integration circle (IC), as well as the perfectly matched layer (PML), is removed. Instead, the waveguide boundary mode analysis model is truncated by a perfect electric conductor boundary condition. It imposes the condition $\hat{n} \times \mathbf{E} = 0$ on the electric field at the outer boundary of the computational domain with normal vector $\hat{n}$, i.e., the tangential component of the electric field vanishes at the boundary. As the desired waveguide modes are bound to the waveguide placed in the center of the domain, their near-field

is decaying rapidly toward the outer domain boundaries. The size of the simulation domain has to be sufficiently large so that the calculated modal field is negligible at the perfect electric conductor boundary.

In total, the boundary mode analysis allows to calculate the eigenmode(s), the effective mode index, as well as related properties such as the propagation length and mode area, for a waveguide structure of arbitrary cross-section. The results for a single silver nanowire in air are presented in section 3.2. The model is further applied to the geometry of two parallel silver nanowires separated by a nanoscale gap (see chapters 6 and 7) and to a pentagonal silver nanowire in a few-nanometer distance to a silver surface (see chapter 8).

Note for leaky modes: Special care has to be taken for the simulation of leaky modes. These modes are characterized by a real part of the effective mode index n_{eff} being smaller than the refractive index of the adjacent medium of highest refractive index, e.g., the substrate medium. As a consequence, during propagation, radiation losses into the substrate appear, which can be experimentally observed by leakage radiation microscopy [89]. However, for simulation purposes, the applied perfect electric conductor boundary condition becomes inappropriate, as the leakage radiation propagates toward this boundary. Instead, a perfectly matched layer can be applied, which absorbs these outgoing waves. The position and thickness of this layer is crucial in the case of leaky modes. Song *et al.* [89] observed that a 50-100 nm thick PML at about $\lambda/4$ away from a specific waveguide gives results in agreement with the analytical solution. Another approach applied by the Linden group [112] is to determine the effective mode index and propagation loss of a leaky mode by using a full three-dimensional model and fitting a one-dimensional damped harmonic wave to the calculated field along the waveguide. The operation of plasmonic circuits in this thesis is dominated not by leaky modes but by bound modes, which are considered mostly in the following.

4.1.3 Waveguide incoupling efficiency

As discussed in section 3.2, true waveguide modes are bound to the supporting waveguide structure and do not radiate into the far-field. This property manifests itself in a real part of the effective mode index n_{eff} that is larger than the refractive index of the adjacent media (substrate and superstrate), i.e., the dispersion relation of the waveguide mode does not cross the light line (c.f. figure 3.3a). As a result of this momentum mismatch, waveguide modes of an infinitely long structure also cannot be excited by a far-field optical mode. However, the additional momentum can be provided for example by a grating coupler where the reciprocal lattice vector matches the momentum mismatch between the incident light and the waveguide mode [81]. Moreover, for plane metal surfaces, Bozhevolnyi [113] mentioned that the diffractive scattering at even a single subwavelength groove can be an efficient source of propagating plasmons. Analogously, for nanowire waveguides, the bare

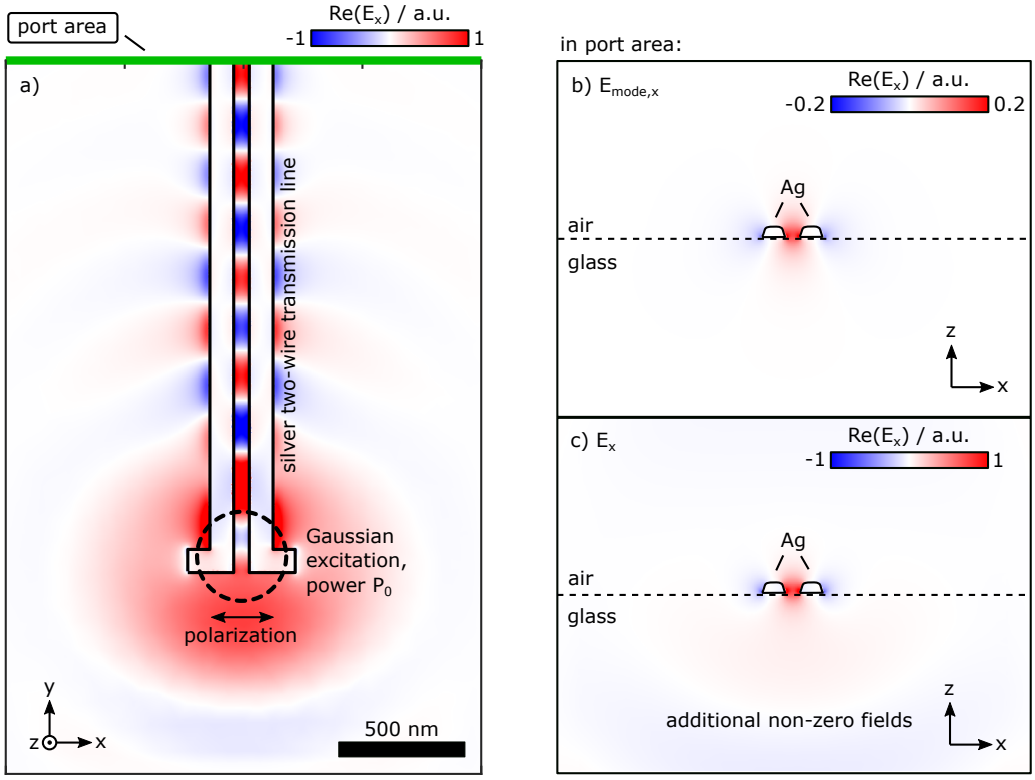

Figure 4.4: Three-dimensional Comsol model for the numerical calculation of waveguide incoupling efficiencies (c.f. text). A linearly polarized Gaussian focus is centered on the incoupling element of a waveguide (black dashed circle). Here, the Gaussian ($\lambda_0 = 750\,\text{nm}$) polarized in x-direction and incident from the glass-substrate is centered on an antenna attached to a silver two-wire waveguide. (a) Resulting electric field in a plane 20 nm above the glass-air interface. (b) In the port area (marked green in (a)), a boundary mode analysis yields the eigenmode field $\mathbf{E}_{mode}$. (c) Simulated total electric field in the port area. All panels show the real part of the electric field's x-component. More details about this waveguide geometry are given in chapters 6 and 7.

wire termination can be used to launch propagating plasmonic modes by a far-field laser focus [85, 88]. For more complex waveguide geometries, such as two parallel nanowires with a nanoscale gap in between, the Hecht group [16, 114] has put forward certain antenna geometries that allow for efficient conversion of incident photons to propagating plasmons.

The incoupling efficiency η_{in} of the incoupling element is defined as the launched modal power of the considered waveguide mode P_{wg} normalized to the power P_0 of the incident far-field mode:

$$\eta_{in} = \frac{P_{wg}(\omega)}{P_0(\omega)} \quad . \tag{4.19}$$

This efficiency is of central importance, since it determines the amount of power that is launched in the desired plasmonic mode. In a three-dimensional Comsol model (figure 4.4), an incident Gaussian beam with a defined linear polarization is focused to the center of the incoupling element of the plasmonic waveguide. The Gaussian is chosen to be incident from the substrate. Furthermore, the Gaussian focus is taken to be diffraction-limited in size with a lateral full width at half maximum of the intensity FWHM $= \lambda_0/2$ (λ_0: free-space wavelength). The electric field amplitude of the Gaussian in the desired direction of polarization is set to $E_{0,x/y} = 1\,\frac{V}{m}$ in the center of the focus at the interface between glass and air. The total power of the Gaussian is given by [104]

$$P_0 = \frac{c\epsilon_0 \pi\, w_0^2}{4} |E_{0,x} + E_{0,y}|^2 \quad , \tag{4.20}$$

with the Gaussian waist radius

$$w_0 = \frac{\text{FWHM}}{\sqrt{2\ln(2)}} \quad . \tag{4.21}$$

The simulation domain includes the incoupling element and a part of the waveguide structure. After a length l, e.g., $l = 2\,\mu\text{m}$, the waveguide crosses through a port in the Comsol model (figure 4.4a). This port is well separated from the excitation position and serves as a monitor to quantitatively evaluate the propagating fields along the waveguide. At this port, in a first step, the eigenmode $\mathbf{E}_{mode}$ of the waveguide is calculated by a boundary mode analysis according to subsection 4.1.2 (figure 4.4b). In the subsequent three-dimensional simulation, the Gaussian excites the waveguide mode, which is then absorbed at the port. Hence, the propagating eigenmode is not reflected back to the incoupling element by the port. Additionally, all boundaries of the model are terminated by a perfectly matched layer (including one behind the port) to absorb further outgoing radiation.

The launched modal power P_{wg} by the incoupling element is calculated from the total field $\mathbf{E}$ calculated in the three-dimensional simulation at the port area A (figure 4.4c) by

$$P_{wg} = \underbrace{\int_A \langle S_\perp \rangle dA}_{factor\,1} \cdot \underbrace{\frac{|\int_A \mathbf{E} \cdot \mathbf{E}^*_{mode} dA|^2}{\int_A |\mathbf{E}_{mode}|^2 dA \cdot \int_A |\mathbf{E}|^2 dA}}_{factor\,2} \cdot \underbrace{e^{(4\pi l \cdot |\mathrm{Im}(\tilde{n}_{eff})|/\lambda_0)}}_{factor\,3} \quad . \tag{4.22}$$

Factor 1 describes the total power outflow through the port by integrating the time-averaged Poynting vector in propagation direction over the port area A. It is important to note that Geisler *et al.* [115] have shown that the incoupling element not only launches the bound waveguide mode but also a reasonable amount of energy is scattered into spherical waves in the substrate and superstrate. Thus, the calculated total field at the mode port $\mathbf{E}$ (figure 4.4c) consists of the eigenmode (figure 4.4b) and additional fields. In order to quantify how much of the power transmitted through the port is carried by the considered plasmonic waveguide mode, a normalized squared

mode overlap integral between the eigenmode field $\mathbf{E}_{mode}$ and the calculated total field at the port $\mathbf{E}$ is performed at the port (factor 2). Finally, propagation losses over the distance l between incoupling element and the mode port are corrected by the exponential term (factor 3) using the imaginary part of the mode index $\mathrm{Im}(\tilde{n}_{eff})$ known from the boundary mode analysis.

4.1.4 Waveguide collection efficiency

In addition to the incoupling and propagation efficiency, the collection efficiency η_{col} at the end of the waveguide determines the detected signal in a transmission experiment through the whole waveguide. The collection efficiency is defined as the collected radiated power at the considered waveguide termination normalized to the modal power in the considered waveguide mode. In a three-dimensional Comsol Multiphysics model, an eigenmode of the waveguide is first calculated in a two-dimensional port area. Subsequently, the mode is launched in the three-dimensional model by the port and propagates toward a termination where it is outcoupled into super- and substrate. In order to quantitatively evaluate the radiated power, a transparent sphere of 300 nm radius is placed around the center of the waveguide termination of interest. The normal component of the time-averaged pointing vector is integrated on the sphere surface corresponding to the collection solid angle of the objective, e.g., with $NA = 1.35$ on the substrate side. This power is corrected by the propagation loss of the waveguide between port and termination and is normalized to the applied power at the mode port, yielding the collection efficiency η_{col}.

The product of incoupling, propagation and collection efficiency is investigated in chapter 6 to model the full transmission through a plasmonic two-wire transmission line waveguide.

4.1.5 Dipole radiation

In contrast to far-field optical modes, radiating electric dipoles are a local source of radiation and, once they are placed into the near-field region of a plasmonic structure, they can radiate into the available plasmonic modes. As discussed in section 3.3, the full quantification of dipole emission close to a plasmonic nanostructure, including the nonradiative decay channels, demands for a three-dimensional numerical simulation. In Comsol Multiphysics, a radiating electric dipole can be easily modeled by a point-dipole with a specific orientation of the dipole axis. The total power radiated by the dipole is evaluated by a surface integration of the normal component of the time-averaged Poynting vector over a transparent integration sphere surrounding the dipole (radius 20 nm, figure 4.5a). When the dipole is located in the near-field region of a plasmonic waveguide, e.g., in the gap between two silver nanowires, waveguide eigenmode(s) will be launched by the dipole (figure 4.5b). The eigenmode

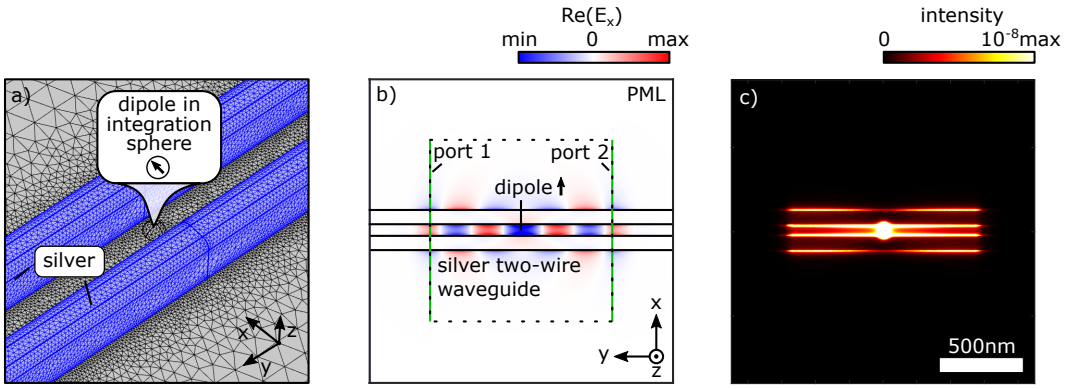

Figure 4.5: Three-dimensional Comsol model for the numerical calculation of electric dipole radiation within an (infinitely long) waveguide. (a) Exemplary mesh of parts of the model. The dipole (black arrow) is placed in the center of an integration sphere close to a waveguide. Here, an x-oriented electric dipole at a glass-air interface in the gap of a silver two-wire waveguide (marked blue) is displayed. (b,c) Resulting electric near-field (real part of x-component) and intensity at the glass-air interface, respectively. Details see text. More information about this waveguide geometry is given in chapters 6 and 7.

is absorbed at the two ports on either side of the guide, analogously to the model described in subsection 4.1.3. Furthermore, the whole model is surrounded by a perfectly matched layer (PML) to absorb all other free-space radiation. As a result, no back-reflections from the ports appear, as visible by a smooth intensity profile in direction of propagation without a standing-wave pattern (figure 4.5c). This way, the dipole emission near an infinitely long waveguide can be modeled.

In particular, this model allows to calculate the total emitted power P_{tot} of the dipole, which, according to the framework of section 3.3, is one of the important parameters to determine the waveguide-emitter coupling efficiency, i.e., the β-factor. In case the dipole radiation in a waveguide of finite length needs to be considered, the two ports are removed and the whole waveguide is included in the domain inside the PML.

In total, these simulations give access to the near-field excited by the dipole, which is strongly dependent on the geometry of the waveguide, the used materials, as well as position, orientation and frequency of the dipole. In this way, the system consisting of electric dipole and plasmonic nanostructure can be studied numerically in detail and can be compared to experimental results. In chapters 6 and 7, this model is used to simulate the fluorescence emission of organic dye molecules close to a plasmonic waveguide.

4.2 ELECTROMAGNETIC FAR-FIELD CALCULATIONS

In this thesis, the detectors of all experimental setups are placed outside the near-field of the nanostructure of interest. Before being detected, the near-fields are propagating in the far-field zone and pass an imaging system (objective and a tube lens) where they are focused onto the detector plane. In particular, the transition from near- to far-fields inevitably removes the contribution of evanescent waves. This has profound consequences, e.g., the emission of a point-like dipole emitter does not appear as a point-like intensity feature on the detector but rather appears as an extended optical intensity pattern, called *point-spread function*. As a consequence, the optical resolution of a far-field imaging system is limited. While the imaging of a radiating point-like dipole can be treated analytically in a homogeneous environment, an extended plasmonic nanostructure imposes a reasonable inhomogeneity and near-fields need to be calculated numerically (c.f. section 4.1). Thus, a general framework needs to be considered that allows for numerical imaging of arbitrary near-fields onto a detector plane. This framework is provided by the angular spectrum representation of optical fields together with simple rules for the refraction of optical fields at a lens, which are briefly reviewed here. A comprehensive discussion can be found in textbooks of nanooptics, e.g., of Novotny and Hecht [55].

4.2.1 Angular spectrum representation of optical fields

The *angular spectrum representation* of optical fields is a very powerful method to describe light propagation and focusing in homogeneous media by decomposing optical fields into evanescent and plane waves of different amplitude and propagation direction. In particular, it can be used for the far-field imaging of radiated electromagnetic fields, a process commonly encountered in optical microscopes. In the following, a time-harmonic electric field with convention $\mathbf{E}(x,y,z,t) = \mathrm{Re}[\mathbf{E}(x,y,z)\mathrm{e}^{-i\omega t}]$ is considered in a cartesian coordinate system x,y, z. Given the field $\mathbf{E}(x,y,z)$ is known at a specific time t in a plane with $z =$ constant, the two-dimensional Fourier transform relations between the fields in real and reciprocal space read as

$$\hat{\mathbf{E}}(k_x,k_y,z) = \frac{1}{4\pi^2}\iint_{-\infty}^{+\infty} \mathbf{E}(x,y,z)\,\mathrm{e}^{-i[k_x x+k_y y]}\,dx\,dy \quad , \tag{4.23}$$

$$\mathbf{E}(x,y,z) = \iint_{-\infty}^{+\infty} \hat{\mathbf{E}}(k_x,k_y,z)\,\mathrm{e}^{i[k_x x+k_y y]}\,dk_x\,dk_y \quad . \tag{4.24}$$

Here, k_x, k_y and k_z represent the corresponding coordinates in Fourier space, called spatial frequencies. For homogeneous, isotropic, linear and source-free media, the evolution of the Fourier spectrum $\hat{\mathbf{E}}$ in space can be described by a propagator. Starting

from the plane $z =$ constant, e.g., $z = 0$, the evolution of $\hat{\mathbf{E}}$ along the z-axis is given by $e^{\pm ik_z z}$, which is called the propagator in reciprocal space:

$$\hat{\mathbf{E}}(k_x, k_y, z) = \hat{\mathbf{E}}(k_x, k_y, 0)\, e^{\pm i[k_z z]} \quad . \tag{4.25}$$

The plus (minus) sign corresponds to propagation in positive (negative) z-direction. In terms of linear response theory, the propagator represents the optical transfer function between input $\hat{\mathbf{E}}(k_x, k_y, 0)$ and output $\hat{\mathbf{E}}(k_x, k_y, z)$. Plugging in the propagator expression in equation 4.24, it follows for arbitrary z

$$\mathbf{E}(x, y, z) = \iint_{-\infty}^{+\infty} \hat{\mathbf{E}}(k_x, k_y, 0)\, e^{i[k_x x + k_y y \pm k_z z]}\, dk_x\, dk_y \quad , \tag{4.26}$$

which is called the *angular spectrum representation*. For divergence-free fields and lossless materials, the k-vectors can be subdivided into two regimes, which describe plane waves and evanescent waves [55]:

$$\text{plane wave}: \quad e^{i[k_x x + k_y y]} \cdot e^{\pm i|k_z| z}, \quad k_x^2 + k_y^2 \leq k^2 \tag{4.27}$$

$$\text{evanescent wave}: \quad e^{i[k_x x + k_y y]} \cdot e^{-|k_z||z|}, \quad k_x^2 + k_y^2 > k^2 \tag{4.28}$$

Here, k represents the magnitude of the wavevector. For plane waves, the propagator $e^{\pm ik_z z}$ has an oscillatory behavior, whereas for evanescent waves an exponential decay results. Plane waves are represented by points in the transverse k_x-k_y plane within a circle of radius k. The center of this circle (spatial frequency 0) is given by a plane wave propagating in z-direction. The evanescent waves are lying outside this circle. Besides the evolution of the Fourier spectrum $\hat{\mathbf{E}}$, also the evolution of the real space field $\mathbf{E}$ from an object plane at $z = 0$ to an arbitrary image plane at $z =$ constant can be calculated according to

$$\mathbf{E}(x, y, z) = \frac{1}{4\pi^2} \iint_{-\infty}^{+\infty} \mathbf{E}(x', y', 0) \iint_{-\infty}^{+\infty} e^{i[k_x(x-x') + k_y(y-y') \pm k_z z]}\, dx'\, dy'\, dk_x\, dk_y \quad , \tag{4.29}$$

which can be seen as a convolution of the input $\mathbf{E}(x', y', 0)$ with an impulse response (or propagator) in direct space.

4.2.2 Far-fields

In a distance r far away of the origin of the coordinate system, the far-field zone opens up, defined by the limit $kr \to \infty$. Evanescent waves in the object plane cannot reach this far-field zone as they decay exponentially with distance. However, importantly,

the (real space) far-fields $\mathbf{E}_\infty$ are entirely defined by the Fourier spectrum of the object plane fields $\hat{\mathbf{E}}(k_x, k_y, 0)$ [55, 73]:

$$\mathbf{E}_\infty\left(\frac{k_x}{k}, \frac{k_y}{k}\right) = -2\pi i\, k_z \frac{\mathrm{e}^{ikr}}{r}\, \hat{\mathbf{E}}(k_x, k_y, 0) \quad . \tag{4.30}$$

The importance of this relation is that each plane wave of the object plane Fourier spectrum entirely defines the far-field in the direction of that plane wave. The contribution of all other plane waves propagating in other directions destructively interfere in the far-field zone and cancel out. Thus, in the far-field, the simplified laws of geometrical optics hold and the fields can be traced through the optical system along rays. The relation between the real space field in the object plane $\mathbf{E}(x, y, z = 0)$ and its far-field $\mathbf{E}_\infty(\frac{k_x}{k}, \frac{k_y}{k})$ is essentially a Fourier transform, up to a prefactor and the k_z-term.

Practical calculations of far-fields from near-fields in the object plane are hindered by the fact that the field has to be known in the entire plane $z = 0$ for the calculation. The numerical calculation of near-fields in this thesis is done by Comsol Multiphysics within a limited volume truncated by appropriate boundary conditions (c.f. section 4.1). However, the knowledge of electric and magnetic near-fields on a closed surface is also sufficient to calculate the far-field. This surface can even span different layers of a stratified structure with local inhomogeneities enclosed inside. In order to calculate the far-field from the near-field, the Lorentz reciprocity theorem is used. Briefly, plane waves incident from the far-field are impinging onto the stratified medium (without inhomogeneities), resulting in vectorial fields that can be calculated analytically. An overlap integral of these fields with the numerically simulated near-field is performed on the surface enclosing the inhomogeneities. This issue is addressed by a freely available software package called RETOP, which is developed by the group of Prof. Philippe Lalanne. RETOP is used for the near-to-far-field transformation using the near-fields calculated by Comsol Multiphysics via a Matlab-COMSOL livelink. Further details about RETOP can be found in the corresponding publication of Yang *et al.* [116] and the comprehensive user guide.

4.2.3 Imaging the far-field

Having calculated the far-fields, they need to be traced properly through the imaging system and focused to the image plane. In the year 1959, Richards and Wolf [117, 118] developed the theory of electromagnetic diffraction in optical systems to describe the imaging and focusing of fields to an image plane. The fields near optical lenses are described by geometrical optics. The aplanatic lenses, which are free of spherical and coma aberration, are described by the following two rules:

$$\text{sine condition:} \quad h = f \sin(\theta) \quad , \tag{4.31}$$

$$\text{intensity law:} \quad |\mathbf{E_2}| = |\mathbf{E_1}| \sqrt{\frac{n_1}{n_2}} \left[\cos(\theta)\right]^{-1/2} \quad . \tag{4.32}$$

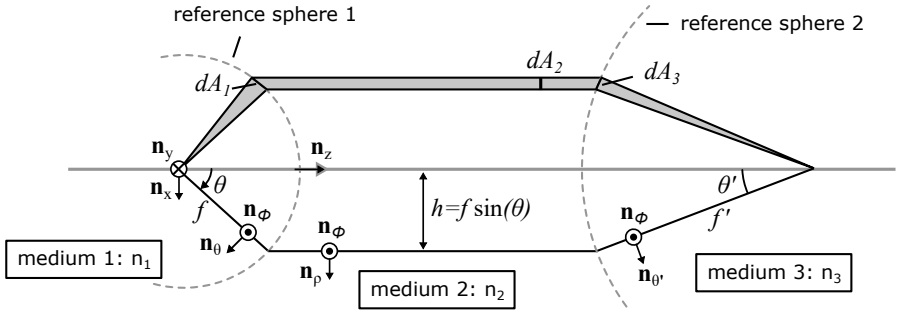

Figure 4.6: Imaging in an optical system consisting of two aplanatic lenses described by a Gaussian reference sphere of radius f and f', respectively. The object is located in the focus of sphere 1 (object plane). Emerging rays from the focus are refracted to a parallel ray at the reference sphere (and vice versa). The sine condition and intensity law need to be considered. After being refracted by reference sphere 2, the rays are directed to the focus in medium 3 (image plane).

The sine condition describes the refraction of an optical ray at the aplanatic lens. h denotes the distance of the parallel optical ray from the optical axis, f is the focal length of the lens and θ is the angle of the refracted ray to the optical axis (figure 4.6, left part). The intensity law (here for nonmagnetic media) is a consequence of energy conservation along each ray of infinitesimal cross-section dA. It relates the field amplitudes before ($\mathbf{E_1}$, medium refractive index n_1) and after refraction ($\mathbf{E_2}$, n_2) at a reference sphere (e.g., sphere 1, figure 4.6). The aplanatic lens can be considered as a reference sphere of radius f (Gaussian reference sphere). The refraction at this sphere transforms between a spherical coordinate system (focused beam) and a cylindrical coordinate system (parallel beam). The unit vectors $\mathbf{n}_\phi$, $\mathbf{n}_\rho$ and $\mathbf{n}_\theta$ are linked to the cartesian unit vectors $\mathbf{n}_x$, $\mathbf{n}_y$, $\mathbf{n}_z$ (c.f. figure 4.6) via

$$\begin{pmatrix} \mathbf{n}_\phi \\ \mathbf{n}_\rho \\ \mathbf{n}_\theta \end{pmatrix} = \begin{pmatrix} -\sin(\phi) & \cos(\phi) & 0 \\ \cos(\phi) & \sin(\phi) & 0 \\ \cos(\theta)\cos(\phi) & \cos(\theta)\sin(\phi) & -\sin(\theta) \end{pmatrix} \cdot \begin{pmatrix} \mathbf{n}_x \\ \mathbf{n}_y \\ \mathbf{n}_z \end{pmatrix} \quad . \tag{4.33}$$

Here, the imaging process is considered, where the light is emitted from the sample plane in the focus f of the first lens. The far-field components of this light field are then refracted at the reference sphere 1 (objective) that is described by an ideal aplanatic lens. The field components along $\mathbf{n}_\phi$ (s-polarized) and along $\mathbf{n}_\theta$ (p-polarized) refract differently at the aplanatic lens. Thus, the field is split into both components according to

$$\mathbf{E}_\infty = (\mathbf{E}_\infty \cdot \mathbf{n}_\phi)\mathbf{n}_\phi + (\mathbf{E}_\infty \cdot \mathbf{n}_\theta)\mathbf{n}_\theta \quad . \tag{4.34}$$

While the component along $\mathbf{n}_\phi$ remains unaffected by refraction at a reference sphere, the spherical unit vector $\mathbf{n}_\theta$ is mapped on a cylindrical unit vector $\mathbf{n}_\rho$ (c.f. figure 4.6, left part). Furthermore, the intensity law requires a multiplication with the factor

$\sqrt{\frac{n_1}{n_2}}[\cos(\theta)]^{-1/2}$ due to energy conservation. Possible Fresnel transmission coefficients are neglected here for simplicity assuming antireflection coatings of the involved lenses.

In the case of an objective followed by a tube lens considered here, the light now propagates from reference sphere 1 (objective) to reference sphere 2 (tube lens) as collimated beam parallel to the optical axis. At the reference sphere 2, the refraction is again described by mapping the cylindrical unit vector $\mathbf{n}_\rho$ on the spherical vector $\mathbf{n}_{\theta'}$ (c.f. figure 4.6, right part). Moreover, the intensity law again requires a multiplication with the factor $\sqrt{\frac{n_2}{n_3}}[\cos(\theta')]^{1/2}$. The angle θ' of the ray after being refracted by reference sphere 2 can be calculated from the angle θ before reference sphere 1 (c.f. figure 4.6) according to

$$\frac{\sin(\theta)}{\sin(\theta')} = \frac{f'}{f} \quad . \tag{4.35}$$

In total, the far-field directly after reference sphere 2 in medium 3, i.e., $\mathbf{E}_{\infty,3}$, can be calculated from the far-fields before reference sphere 1 in medium 1, i.e., $\mathbf{E}_\infty$, by the relation

$$\mathbf{E}_{\infty,3}(\theta',\phi) = \left[(\mathbf{E}_\infty \cdot \mathbf{n}_\phi)\mathbf{n}_\phi + (\mathbf{E}_\infty \cdot \mathbf{n}_\theta)\mathbf{n}_{\theta'}\right]\sqrt{\frac{n_1\cos(\theta')}{n_3\cos(\theta)}} \quad . \tag{4.36}$$

$\mathbf{E}_{\infty,3}$ can be expressed in terms of the spatial frequencies k_x, k_y, k_z using the relations

$$k_x = k\,\sin(\theta')\cos(\phi), \quad k_y = k\,\sin(\theta')\sin(\phi), \quad k_z = k\,\cos(\theta') \quad . \tag{4.37}$$

The prime of the cartesian coordinates x,y and z, as well as of the spatial frequencies k_x, k_y and k_z, in medium 3 is dropped here for simplicity of the notation. Combining equation 4.30 and the angular spectrum representation in equation 4.24, the real space fields in the image plane of medium 3 (detector plane, in focus) are calculated from the far-fields $\mathbf{E}_{\infty,3}$ by

$$\mathbf{E}_3(x,y,0) = -\frac{if'\,\mathrm{e}^{-ikf'}}{2\pi}\iint \mathbf{E}_{\infty,3}\left(\frac{k_x}{k},\frac{k_y}{k}\right)\mathrm{e}^{i[k_x x + k_y y]}\,\frac{1}{k_z}\,dk_x\,dk_y \quad . \tag{4.38}$$

Here, the distance between the reference sphere 2 and the focal point in medium 3 is given by the focal length f' and the minus sign originates from taking the far-field at $z \to -\infty$ [55]. In order to account for a finite numerical aperture $NA = n_1\sin(\theta_{max})$ of the reference sphere 1 (objective), only the field components with $\theta < \theta_{max}$ are considered. Thus, the integration in equation 4.38 is limited to a corresponding finite range of k_x and k_y in medium 3. Summing up, by the procedure described in this section, an imaging of the near-fields from the object plane to the image plane is achieved with a total magnification M given by

$$M = \frac{n_1}{n_3}\frac{f'}{f} \quad . \tag{4.39}$$

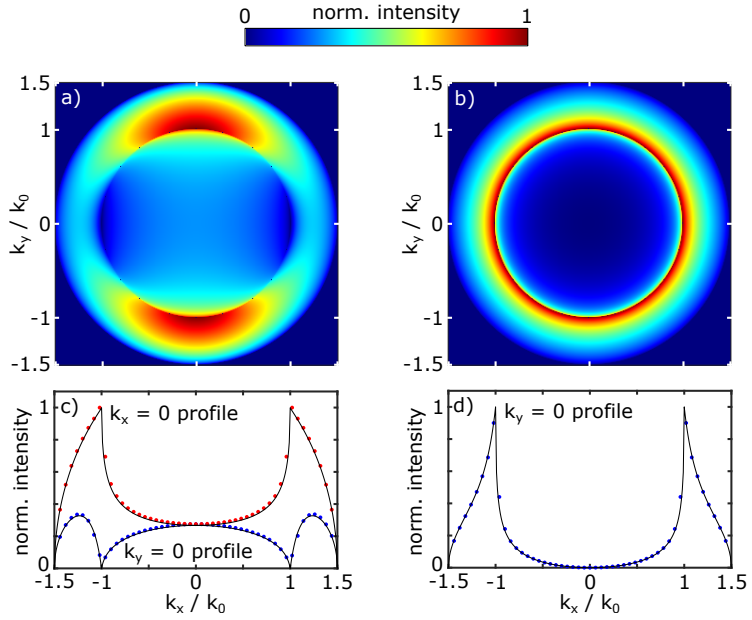

Figure 4.7: (a,b) Back-focal-plane image of an x- and z-oriented dipole 1 nm above an air-glass interface (x-y plane) emitting into the glass substrate. (c,d) Cross-sections through the center of calculated back-focal-plane images for $k_x = 0$ (red dotted) and $k_y = 0$ (blue dotted). The solid black line represents the simulation result with analytical formulas [119], while the colored dots are profiles simulated according to section 4.2 from a Comsol dipole radiation model, subsequent far-field transformation via the RETOP software package and projection into the back-focal-plane.

4.3 POINT-SPREAD FUNCTION AND LATERAL RESOLUTION LIMIT

The concepts presented in section 4.1 and 4.2 allow to study the whole imaging process of arbitrary near-fields in the object plane through a system of objective and tube lens to an image plane. In the following, simple dipole fields are considered and examples of their radiation pattern and their point-spread function after passing an imaging system are presented. A comparison of the simulations with analytical calculations and results in the literature confirms the numerical implementation.

In contrast to the doughnut-like emission pattern of dipoles in a homogeneous environment, the dipole emission at an air-glass interface into the glass substrate is already strongly modified. Experimentally, the radiation pattern is observed in the back-focal-plane of the objective, which is the k_x-k_y space. The back-focal-plane emission pattern of an in-plane and out-of-plane dipole 1 nm above an air-glass interface is shown in figure 4.7a,b, which is calculated via analytical formulas [119]. The strong angular dependence of the Fresnel-factors at the interface leads to fairly complex radiation patterns, as evident also in intensity profiles along $k_x = 0$ and $k_y = 0$ through the back-focal-plane images (figure 4.7c,d). For all profiles, the simulation result of a Comsol Multiphysics dipole radiation model, subsequent far-field transformation via

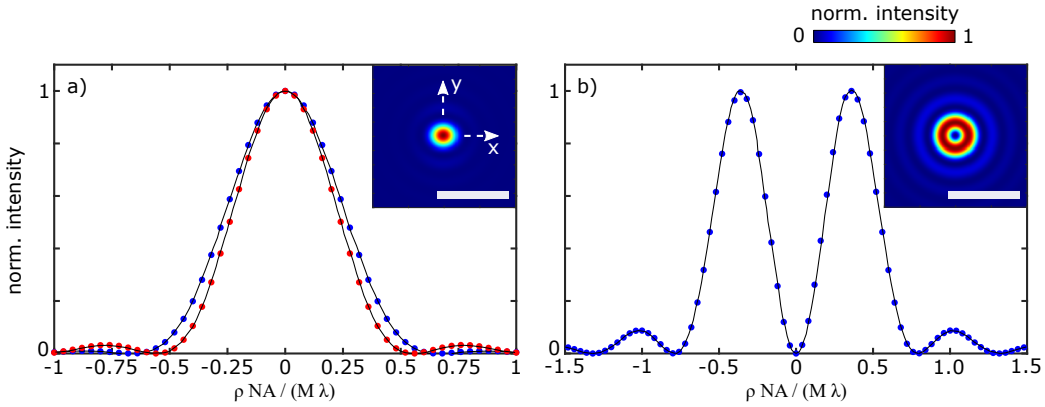

Figure 4.8: (a,b) Intensity-profiles of the point-spread function of an in-plane (x-oriented) and out-of-plane (z-oriented) electric dipole calculated from a Comsol dipole radiation model according to section 4.2. The calculations are performed for a dipole embedded in a refractive index $n = 1.518$ and an objective of $NA = 1.4$. The simulated profiles along the x-direction ($y = 0$, blue dotted) and y-direction ($x = 0$, red dotted) are compared to profiles taken from Novotny and Hecht (black solid) [55]. ρ represents the radial coordinate. The inset shows the full point-spread function for each case. The scale bars correspond to 1 µm in the object plane.

the RETOP software package and projection into the back-focal-plane (blue and red dots) matches the result using analytical formulas very well (black lines).

A further step is the imaging of the far-field via the objective and tube-lens into the image plane of a detector. In the following, dipole near-fields are calculated with Comsol Multiphysics in a homogeneous medium, transformed into the far-field via the RETOP software package and then imaged onto a detector. Evanescent wave components and all plane-wave components beyond the numerical aperture of the objective are lost, leading to a broadening of the point-spread function of the imaging system. Figure 4.8 displays the simulated point-spread functions for an in-plane and an out-of-plane dipole source embedded in a refractive index of 1.518 which is imaged with an objective of $NA = 1.4$. The in-plane dipole features an Airy-like intensity pattern. As a result of the, in general, non-isotropic radiation characteristics of the dipole (c.f. figure 4.7a, at a glass-air interface), also slightly different profiles along the x- and y-direction result in the image plane, even when considering a homogeneous medium (figure 4.8a). This asymmetry gets less pronounced in the paraxial limit, i.e., for a low numerical aperture NA, and the point-spread function gets rotationally symmetric along the optical axis. By contrast, the out-of-plane dipole features, in all cases, a symmetric doughnut-like point-spread function (figure 4.8b). Notably, all simulated intensity profiles along the x- and y-direction (blue and red dots) agree very well with profiles taken from Novotny and Hecht (black lines) [55].

In total, the accurate simulation of dipole fields in the back-focal-plane and their point-spread functions in an image plane demonstrates the correct implementation of the whole numerical imaging technique, involving the near-field calculation with Comsol Multiphysics, the far-field transformation via the RETOP software package

and subsequent imaging into the image plane. If needed, this numerical procedure gives access to all three spatial components of the electric field in the image plane. Importantly, the technique can further be applied to the more complex situation of imaging the radiation of an electric dipole close to a waveguide nanostructure (c.f. chapters 6 and 7) that cannot be treated in an analytical fashion.

As a result of the finite size of the point-spread function (PSF), the resolution of an optical system is limited. In the paraxial limit, the radial distance of the point-spread function (of an in-plane dipole) to the first minimum is given by the Airy-disk radius

$$r_{Airy} = 0.61 \frac{M\lambda}{NA} \quad , \tag{4.40}$$

with the magnification M of the imaging system. In the object plane, this radius defines a minimal resolvable distance between two point sources. Note that this definition is strictly valid only for incoherent, in-plane dipole emitters. The Airy-disk radius is similar to the well-known *Abbe diffraction-limit* [1], which defines the minimal resolvable distance d in the object plane with a slightly different prefactor

$$d = \frac{\lambda}{2\,NA} \quad \text{Diffraction-limit of Abbe.} \tag{4.41}$$

Besides conventional microscopy where the whole sample is illuminated and imaged, a further very popular imaging technique is *confocal microscopy*. Here, only a specific spot on the sample is illuminated that is typically defined by a laser focus (selective excitation). The image forms by raster-scanning the sample with respect to the laser focus while detecting the signal of interest, e.g., the fluorescence of the sample, with a photodiode detector. Besides the detection PSF discussed above, an excitation PSF can be introduced which is determined by the field distribution of the exciting laser focus. This field distribution is mainly determined by the wavelength, the numerical aperture of the objective and the filling factor of the laser beam on the back aperture of it [55]. In confocal microscopy, the detected light is imaged onto a pinhole that only transmits the intensity at the optical axis to the detector (spatial filtering). The total PSF is then approximately given by the product of excitation and detection PSF. As a result, the width of the total PSF gets slightly smaller than the individual ones, i.e., the resolution can get beyond the Abbe diffraction-limit. In addition, the resolution in the z-direction perpendicular to the optical axis (axial resolution) is significantly enhanced in confocal microscopy compared to conventional widefield microscopy. Thus, the pinhole in confocal microscopy enhances the resolution in both transverse and axial direction. This is a clear advantage for microscopy of three-dimensional objects. In the limiting case of a very large pinhole, the lateral resolution is determined by the laser focal fields only. The general case of arbitrary pinhole size is discussed in specialized literature, e.g., of Qian and Elson [120]. Widefield imaging of molecular fluorescence with a CMOS camera, darkfield imaging and confocal-like microscopy with an avalanche photodiode are applied in chapters 6, 7 and 8.

5 NANOFABRICATION OF SINGLE-CRYSTALLINE SILVER STRUCTURES

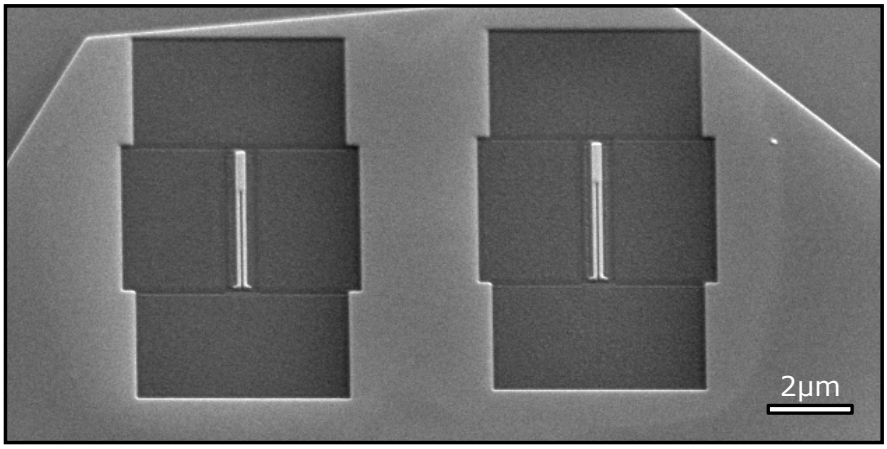

Parts of this chapter are published in *A single-crystalline silver plasmonic circuit for visible quantum emitters* by C. Schörner, S. Adhikari, and M. Lippitz, Nano Letters **19**, 5, 3238-3243 (2019).

Metal nanostructures gain a huge interest for applications in plasmonics [79], sensing [121], surface-enhanced raman scattering [122], catalysis [123] and solar energy conversion [124]. In plasmonics, gold is one of the most used materials due to pronounced plasmonic properties combined with convenient chemical stability at ambient conditions. Silver is superior in terms of optical properties and represents the currently most preferred low-loss material for plasmonic applications in the visible to near-infrared spectral range [125]. For example, propagating surface plasmon polaritons at a plane silver-air interface feature a propagation length at 600 nm vacuum wavelength that is one order of magnitude larger compared to the case of a gold-air interface (c.f. figure 3.3b). This trend is also true for different geometries, such as nanowire waveguides, where silver offers drastically reduced propagation loss compared to gold [126]. Furthermore, the crystallinity of the material plays a great role in terms of propagation, since propagating surface plasmon polaritons scatter at domain boundaries present in poly-crystalline nanostructures [127, 128]. Thus, single-crystalline silver with large-scale internal atomic order is highly desirable for applications in plasmonic nanocircuitry. Single-crystalline silver can be produced based on thermal evaporation [129], sputtering or vapor transport methods [130], but the crystallinity critically de-

pends on process parameters [128]. In the past few years also a chemical synthesis of single-crystalline silver flakes was reported [131–136]. Furthermore, geometrical properties of the single-crystalline silver have to be controlled very precisely. For example, the loss and confinement of propagating surface plasmon polaritons at single metal nanowires are well known to be sensitive to the wire's shape and size (c.f. section 3.2). In case of two parallel silver nanowires (see chapters 6 and 7), the propagating modes of the two wires hybridize into a symmetric and antisymmetric mode, depending sensitively on the specific separation between the wires. This example illustrates the need of sophisticated concepts for the fabrication of metal nanostructures in order to achieve the desired functionality. Huang *et al.* [127] introduced a promising concept for the large-scale fabrication of high-definition, ultra-smooth plasmonic nanostructures, which is based on chemically grown single-crystalline gold flakes and subsequent top-down nanofabrication with focused ion beam milling. To apply this combined methodology to silver flakes, they should be laterally large ($\gg 10\,\mu m$), cover the usual thickness-range of 30-100 nm of plasmonic nanostructures and feature clean and ultra-smooth surfaces. However, the simultaneous fulfillment of these requirements is demanding, as the precise control of size and shape of metal crystals remains a challenging task for chemical synthesis [137–140]. The synthesized silver flakes can be either too thick (above ~ 100 nm in ref. [134], tens of microns in ref. [135]), too thin (10-20 nm in ref. [131]), too small in lateral direction (~ 1 μm in ref. [132]) or feature defects [136] and small particles attached to the surface [133].

In this chapter, high aspect ratio single-crystalline silver flakes featuring a width of several 10 μm, a thickness well below 100 nm, as well as clean and atomically-smooth surfaces, are presented. After discussing fundamentals and protocols of the synthesis, the silver flakes are characterized in terms of their geometrical properties, elemental composition, internal crystal orientation and their surface roughness. Finally, the fabrication of specifically designed two-dimensional nanostructures by focused ion beam milling from the silver flakes, as well as their protection via atomic layer deposition, is discussed. Thus, the presented single-crystalline silver flakes serve as an ideal platform for the plasmonic waveguides and constructs investigated in the following chapters 6, 7 and 8.

5.1 CRYSTAL GROWTH OF COLLOIDAL METAL STRUCTURES

Anisotropic metal nanocrystals, such as nanorods, nanowires and platelets, are a fascinating class of nanostructures and their controlled growth is subject to current research [137–140]. The nanofabrication process of complex-shaped structures described in this chapter is based on highly anisotropic crystalline silver flakes (platelets), which are synthesized in a wet-chemical way. In order to understand the evolution of metal nanocrystals into an anisotropic shape during the synthesis, the phenomenon *twinning* is briefly discussed in the following.

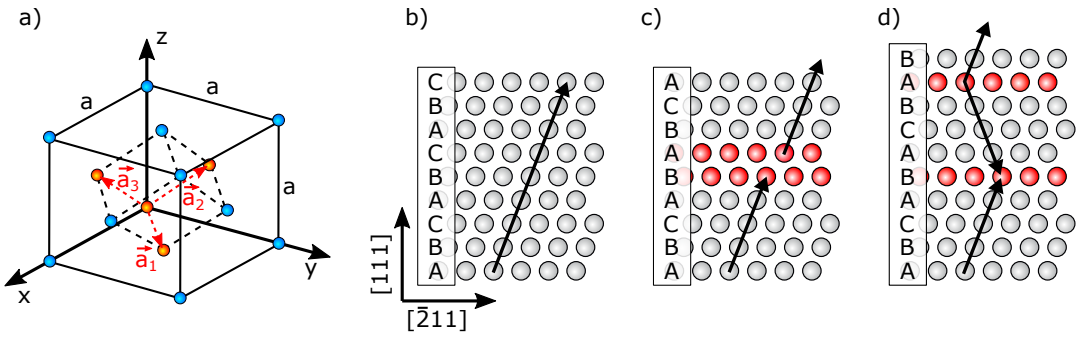

Figure 5.1: (a) Visualization of the face centered cubic (fcc) lattice and its trigonal primitive cell with lattice vectors $\vec{a}_1$, $\vec{a}_2$ and $\vec{a}_3$ shown as red dashed arrows. (b) Stacking order (ABCABC...) of the {111} layers of a defect-free crystal along the [111] direction. (c) A stacking fault results in two locally hcp coordinated layers (marked red). (d) Two twin planes (marked red).

Noble metals, like gold and silver, have a face centered cubic (fcc) crystal lattice with a single atom basis [141]. The unit cell of an fcc lattice is sketched in figure 5.1a with the lattice constant a and the lattice vectors of the primitive cell given by $\vec{a}_1 = \frac{a}{2}(\hat{e}_x + \hat{e}_y)$, $\vec{a}_2 = \frac{a}{2}(\hat{e}_y + \hat{e}_z)$ and $\vec{a}_3 = \frac{a}{2}(\hat{e}_x + \hat{e}_z)$. The defect-free crystal in an fcc material features the following stacking order of the {111} planes: ABCABCABC (figure 5.1b). In real crystals, however, *stacking faults* can occur, i.e., one layer is skipped: ABCABABCA. Then, locally two hexagonal closed packed (hcp) coordinated layers result, with a stacking order ABAB (figure 5.1c, red layers). The stacking order can also reverse, e.g., ABCABACBA (figure 5.1d). Such a (111) mirror plane in an fcc lattice where the stacking order reverses is called a *twin plane* or *twin boundary* [142]. In such a case, locally one hcp coordinated layer is formed (figure 5.1d, red layer). Gold and silver, in particular, have the lowest stacking fault energies among fcc metals [137], which means that the energy difference between the defect-free crystal and the case of a stacking-fault is small, favoring their occurrence. Thus planar defects, i.e., stacking faults and twin planes, are present in gold and silver crystals for most reaction conditions [137, 138, 143]. These planar defects direct the growth during synthesis into a particular final geometrical shape of the nanocrystal [137, 140, 144]. A great variety of final shapes exists, ranging from spheres via cubes and thin plates (triangular, hexagonal or circular profile) to rods (circular, square, rectangular, pentagonal or octagonal cross-section), among others [137–139].

Following Xia *et al.* [138], a typical solution-phase synthesis of metal nanoparticles is divided essentially into three stages: 1) nucleation, 2) formation of seeds and 3) growth of the seeds into nanocrystals. Briefly, in stage 1 of the synthesis, the concentration of metal atoms in the solution increases and eventually reaches the point of supersaturation. At this point, an aggregation of the atoms into small clusters, the nuclei, occurs and the concentration of remaining free atoms in the solution drops. The clusters continue to grow and get locked into a well-defined structure once a certain size is achieved. Structural fluctuations of the cluster after reaching this point

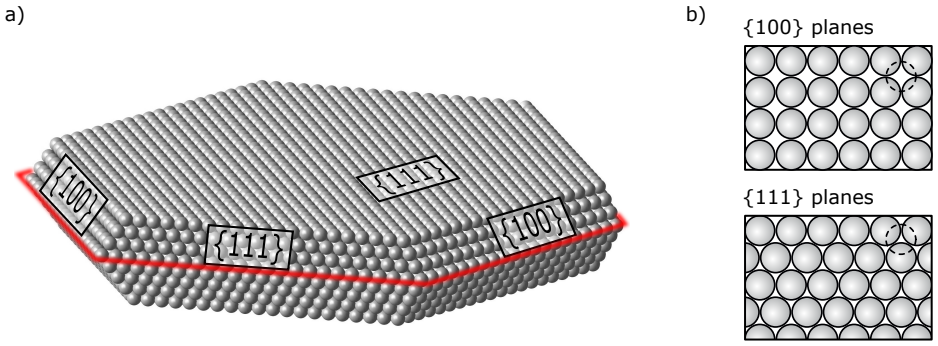

Figure 5.2: (a) Simplified sketch of a hexagonal metal flake (platelet) with a single twin plane (marked red), a top {111} layer and alternating {111} and {100} side facets. In a more realistic configuration, multiple twin planes are present and the side facets can also alternate between {111} and {100} in the vertical direction [140, 145]. In another report, lateral surfaces of hexagonal flakes are {110} planes [146]. (b) Adatoms (sketched as dashed circle) at {100} planes have four neighbors, while at {111} planes only 3 neighbors are available.

are energetically unfavorable. At this stage, the cluster is called *seed* (stage 2). The seed can grow further in size by adding metal atoms to its surface. Importantly, the final shape of the nanocrystal is determined primarily by the internal structure of the corresponding seed, including possible stacking faults and twin planes (stage 3). A further important issue for the final shape is the preferential capping of certain crystal facets by capping agents, which are either a byproduct of the synthesis or added on purpose to the synthesis in order to hinder the growth of specific crystal facets effectively. The details of the generally rather complex nucleation and growth mechanism are subject to specialized review articles, e.g., given by Xia *et al.* [138] and Rycenga *et al.* [139].

Stacking faults and twin planes within the {111} layers break the symmetry of the cubic crystal structure and enforce the two-dimensional growth into highly anisotropic hexagonal platelets with the bottom and top layer being a {111} facet (figure 5.2a) [138, 140]. In the usual case of the growth of thin hexagonal flakes, the side surfaces are composed of alternating {100} and {111} facets [138, 140, 147, 148]. An atom that adsorbs to these side facets (adatom) will get 4 neighboring atoms on the {100} planes, while it gets only 3 neighbors on the {111} planes (figure 5.2b). Thus, the {100} side facets are energetically preferred and grow faster, which results, particularly in the presence of two or more twin planes, in a large and high aspect ratio platelet [140]. In other cases, also platelets with {111} top surface and {110} side surfaces were reported [146]. Importantly, despite the inevitable presence of a few well-defined stacking faults / twin planes, the final plate-like structure (flake) is commonly referred to as *single-crystalline* in the literature [127, 134, 140, 149].

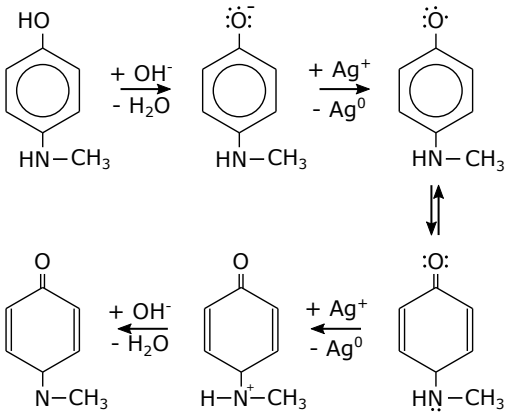

Figure 5.3: Mechanism for the reduction of silver nitrate with metol in aqueous solution according to Lyutov *et al.* [133].

5.2 SYNTHESIS PROTOCOLS OF SILVER FLAKES

As mentioned, for the fabrication of plasmonic nanostructures via focused ion beam milling, large area silver flakes with a high aspect ratio are desirable. To address this issue, a reduction of silver nitrate with metol in water is chosen based on the report of Lyutov *et al.* [133]. Silver nitrate is a salt composed of the cation Ag^+ and the anion NO_3^-. Metol, more precisely 4-(methylamino)phenol hemisulfate salt, is the composition of two 4-(methylamino)phenol molecules (c.f. figure 5.3, top left) and one sulfur acid molecule. In the salt, the two former molecules are protonated by the latter, which is neglected here for simplicity.

Reaction-mechanism According to the report of Lyutov *et al.* [133], the reduction of silver nitrate with metol is governed by the mechanism sketched in figure 5.3: First an OH^- ion in the water solution reacts with the metol, yielding an anion. This anion reduces a silver cation in the solution and forms a radical that is in equilibrium with a quinone-like structure. The latter is able to reduce another silver cation and forms an unstable organic cation. After reacting with an OH^- group, it forms the end product 4-(methyl-amino)cyclohexa-2,5-dienone.

This mechanism leads to an initially increasing concentration of silver atoms in the solution. Above the point of supersaturation, small silver clusters are formed (nucleation), evolve into seeds and grow further into high aspect ratio silver flakes (c.f. section 5.1). According to Lyutov *et al.* [133], the supersaturation and therefore the crystal growth also depends strongly on the pH value in the solution.

During the time period of this thesis, two optimized protocols for the synthesis of high aspect ratio silver flakes have been established together with Dr. Subhasis Adhikari based on the reported reduction of silver nitrate with metol. The necessary chemicals, silver nitrate and metol, have been used as received from Sigma-Aldrich (product numbers 31630 and 69750, respectively). As solvent, water (ROTISOLV® Ultra LC-MS, Carl Roth) is used. The glass substrates (24×24 mm, #1.5, Menzel) have been cleaned by ultrasonication in acetone and isopropanol before usage.

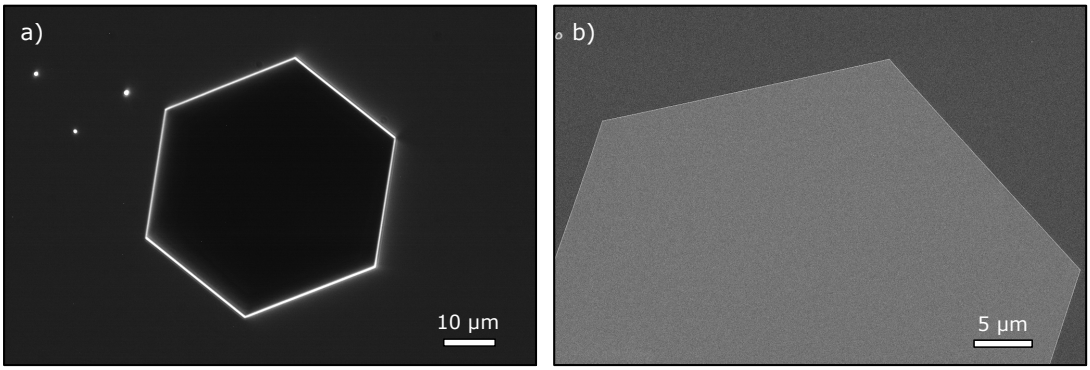

Figure 5.4: (a) Darkfield image (reflection mode) of the top area of a hexagonal silver flake fabricated via protocol 2. (b) Scanning electron micrograph of the same crystal. Adapted from J. Chem. Phys. **155**, 234202 (2021), with the permission of AIP publishing.

Synthesis protocol 1: Synthesis directly on the substrate A 34 mg/mL solution of silver nitrate in water and a 3.3 mg/mL solution of metol in water is prepared. The latter solution is ultrasonicated for about 10 minutes to dissolve the metol. Subsequently, a 50 µL drop of the silver nitrate solution is pipetted onto a cleaned substrate. Then, 50 µL metol solution is added to the drop. Within only about 30 s, the flakes grow in the droplet and stick to the coverslip. After this time, the flakes reach their final size, which can be observed via *in situ* darkfield microscopy during synthesis. The sample is gently rinsed with water, ethanol and ultrasonicated in ethanol for ~1 min with a vertical orientation of the substrate. Finally, the sample is again rinsed with ethanol and dried with nitrogen gas. In total, this method yields a high amount of single-crystalline silver flakes directly on the target substrate.

Synthesis protocol 2: Synthesis in a beaker The second protocol is based on the same chemical reaction but with a different revised procedure established based on the experience with protocol 1. A beaker with 20 mL water and a substrate in a vertical and slightly tilted orientation is prepared and cooled in the fridge for ~1 h to about 8 °C. Furthermore, two separate metol and silver nitrate solutions are prepared. First, 0.1 g metol is dissolved in 3 mL water by ultrasonication for 10 min. Second, 0.1 g $AgNO_3$ is dissolved in 3 mL water. For the synthesis, the beaker with substrate is taken out of the fridge and 200 µL silver nitrate solution is added to the water. Afterward, 100 µL metol solution is added dropwise within about 10 s. After waiting for about 1 min, the addition of silver nitrate, the addition of metol (100 µL each time) and the waiting step can be repeated about three times. During this time, the silver flakes get visible in the solution by eye and some of them stick to the coverslip. Finally, the sample is taken out of the beaker and directly dived into an ethanol bath and moved gently. The sample is further rinsed with ethanol and dried with nitrogen gas flow.

Both synthesis protocols are capable of fabricating large single-crystalline silver flakes on a substrate. Protocol 1 is used for the silver flakes characterized in the following sections 5.3, 5.4, 5.6, 5.7 and the plasmonic circuits in chapters 6 and 7. The procedure of protocol 2 represents a further optimization of protocol 1 in terms of the achievable

surface quality, as flakes attached to the backside of the substrate facing downwards during synthesis feature atomically-smooth surfaces (see section 5.5). These surfaces are applied as part of nanoscale resonators investigated in chapter 8.

In a darkfield microscope, clean silver flakes are characterized by a bright scattering from the flake edges and a dark appearance of the whole area in between (figure 5.4a). The flakes typically feature a hexagonal shape and sharp edges (figure 5.4b). Also triangles and hexagons with alternating long and short edges are observed in lower yield. This distinctive outer shape of the flakes with sharp straight edges is already an indirect evidence of their crystallinity, which is further confirmed by electron backscatter diffraction experiments (see section 5.4).

5.3 ENERGY-DISPERSIVE X-RAY SPECTROSCOPY

Energy-dispersive X-ray spectroscopy (EDX spectroscopy) is a popular non-destructive analytical method capable of determining the elemental composition of a sample. This technique is applied to demonstrate that the synthesized flakes consist of pure silver. As excitation source, typically the electron beam in a scanning electron microscope is used. Important mechanisms for electrons to lose energy when moving in a solid are the generation of Bremsstrahlung and the ionization of inner electron shells. The latter case may result in X-ray radiation with energies characteristic for the specific element. X-ray lines are named after the inner shell into which the electron returns after X-ray emission (i.e., K, L, M, ...). An additional greek letter (α, β, γ, ...) gives the difference in the main quantum number to the initial shell of the electron. A further index is needed for the case of fine structure splitting. An appropriate X-ray photodetector reports on the spectrum of the emitted X-ray fluorescence. Given a proper calibration, the relative amount of X-ray photons characteristic for different elements reports about the relative amount of the involved materials. Furthermore, in scanning electron microscopes, the location of the electron beam focus can be scanned across the sample. This allows to record images of the distribution of a specific material by monitoring the X-ray intensity at a characteristic energy as a function of the electron focus position on the sample. The X-ray generation volume extends up to several micrometers into the specimen, depending on incident electron beam energy and atomic number. For quantitative analysis, different corrections like the correction for X-ray absorption in the sample have to be considered [150].

The EDX measurements presented here were performed in collaboration with Patrick Knödler and Martina Heider using a scanning electron microscope (Leo 1530, Zeiss) equipped with an X-ray detector (EDS UltraDry SDD, Thermo Fischer Noran) using an acceleration voltage of 10 kV (KeyLab Electron and Optical Microscopy, BPI Bayreuth). The recorded spectra were analyzed with a software package (NEE 3.2, Thermo Fischer Scientific).

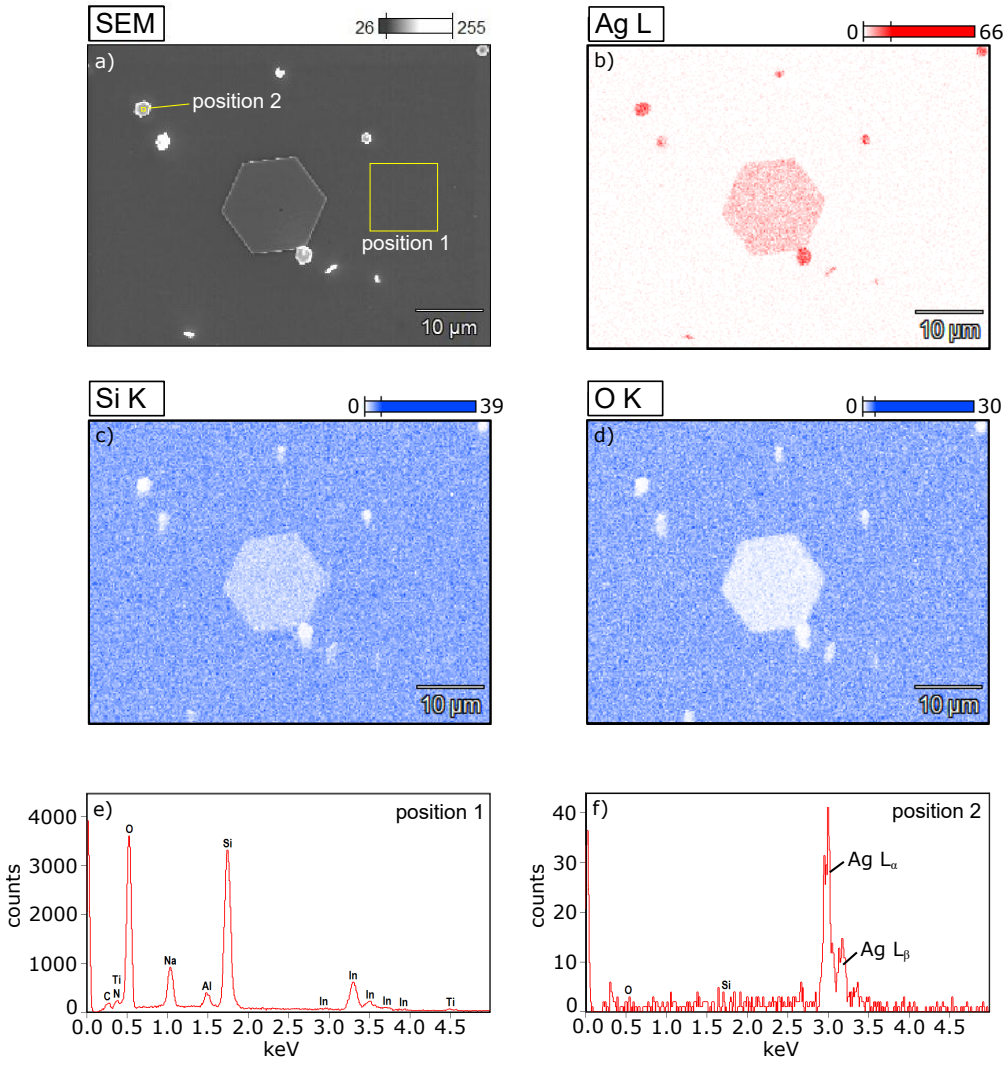

Figure 5.5: Energy-dispersive X-Ray analysis of silver flakes on a borosilicate glass substrate coated with 40 nm ITO. (a) Scanning electron micrograph of the investigated sample area. (b-d) Corresponding colormaps that display the X-ray emission net counts of the L- or K-series of Ag, Si and O, respectively. (e) EDX spectrum of an empty area on the ITO substrate (position 1 in panel (a)). (f) EDX spectrum of a small silver flake (position 2 in panel (a)) featuring the L-series of silver (L_α, L_β, ...).

EDX spectroscopy of silver flakes A silver flake sample on a borosilicate glass substrate coated with 40 nm indium tin oxide (ITO) is investigated (figure 5.5a). After spatially-resolved EDX spectroscopy, the software evaluates the net counts of the characteristic X-ray radiation, e.g., of the L-series for silver and the K-series for substrate elements such as Si and O, and calculates the relative content of the elements if needed. Silver flakes are identified by X-ray emission characteristic of silver (figure 5.5b) and a lower contribution of substrate elements (figures 5.5c,d). The EDX spectrum

of an area on the substrate free of silver flakes (position 1 in figure 5.5a) is given in figure 5.5e. Elements are assigned to their detected characteristic X-ray peaks by software, finding the expected substrate elements such as O, Si, In. At the position of a large hexagonal silver flake in the center of figure 5.5a, substrate elements are also detected (figures 5.5c,d). Laterally large flakes typically feature a height below 100 nm (see section 5.5). Thus, the electrons generate X-ray emission not only in the flake but also in the substrate below the flake, leading to the additional detection of X-ray emission characteristic of the substrate elements. By contrast, smaller flakes usually feature a thickness well above 100 nm (see section 5.5) and should therefore feature much less X-ray emission of the substrate elements. In case of the laterally small silver flake marked as position 2 in figure 5.5a, the EDX spectrum is dominated by the L-series of X-ray transitions of silver (figure 5.5f). Hence, the EDX measurements demonstrate that the synthesized flakes are composed of pure silver.

5.4 ELECTRON BACKSCATTER DIFFRACTION ANALYSIS

Besides chemical composition, the crystallinity is a further important aspect regarding the quality of the synthesized silver flakes. *Electron backscatter diffraction* (EBSD) is a well-established scanning electron microscope (SEM) based method to study crystalline and poly-crystalline material. It gives access to crystallographic information, e.g., about the crystal structure, orientation, phase and strain in the material [150]. A polished or flat sample in an SEM chamber is tilted from the horizontal toward a phosphor screen. The focused electron beam incident from the vertical direction interacts with the tilted sample by incoherent electron scattering, leading to backscattered electrons that experience Bragg diffraction by the different lattice planes in the crystalline material [151]. The diffracted electrons form flat cones with an apex semiangle of $90° - \theta_B$, where the Bragg angle θ_B is determined by Bragg's law

$$2\,d\,\sin(\theta_B) = n\,\lambda \quad n = 1, 2, 3, \ldots \tag{5.1}$$

Here, n is the order of the diffraction, d represents the distance of the considered crystal planes and λ is the electrons' de Broglie wavelength. Particularly, the electrons, after being scattered incoherently, may diffract from the front and the back of the lattice planes, leading to a pair of diffraction cones separated by $2\theta_B$ for each crystal plane [150, 151]. The Bragg angle is usually small, i.e., less than 2°, and thus each pair of cones intersects the detector plane as two closely spaced and nearly straight lines. In the diffraction pattern, the lines appear as discrete Kikuchi lines or as a band of increased intensity between the lines (Kikuchi band) [150]. The diffraction pattern is detected via the excited fluorescence of the phosphor screen by a camera detector. EBSD measurements were recorded in collaboration with Dorothea Wiesner using an EBSD detector (HKL Nordlys, Oxford Instruments) in a scanning electron microscope (Leo 1530, Zeiss) using a sample tilt of 70° from the horizontal (BGI Bayreuth). The analysis was performed with software (HKL Channel 5, Oxford Instruments), which

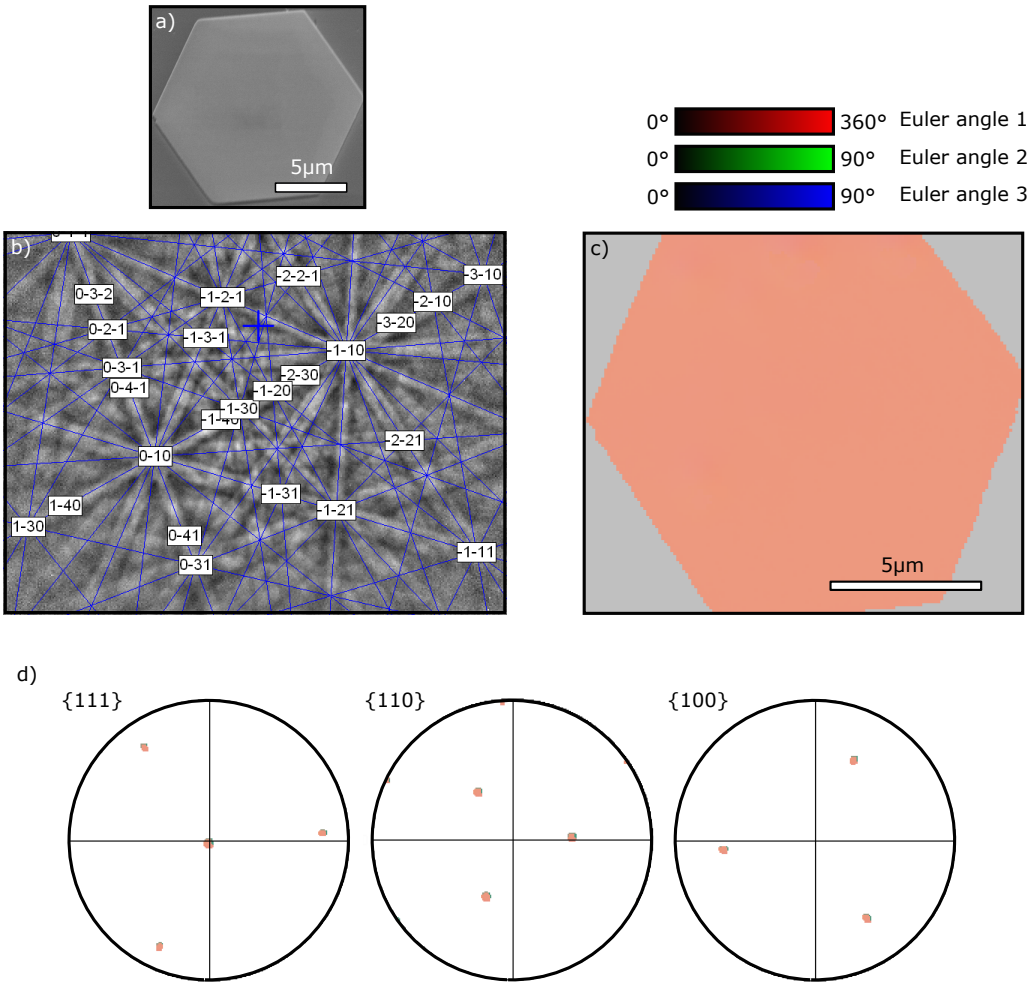

Figure 5.6: Electron backscatter diffraction (EBSD) analysis of a hexagonal silver flake. (a) Scanning electron micrograph of the investigated silver flake. (b) EBSD pattern detected at a single position on the flake. Kikuchi bands are identified by software (blue lines) and indexed with the corresponding reciprocal lattice vector indices, while their intersections are labeled with the corresponding direct lattice indices. (c) Euler map obtained from scanning across the flake and using the obtained Euler angles as color channels for the Euler map representation. (d) Pole figures (equal-area projection, upper hemisphere) for the {111}, {110} and {100} lattice planes, respectively. The center is given by the sample normal and the circle represents directions perpendicular to it.

uses the following parameters for the crystal structure of silver: space group 225 (Fm3m), Laue group 11 (m3m), unit-cell lengths 409 pm with 90° angles.

EBSD mapping of a silver flake In case of crystalline material, such as a silver flake (figure 5.6a), the diffraction pattern features multiple distinct bands (figure 5.6b). They are characteristic for the crystal structure and orientation in the investigated

sample volume. The depth of the investigated volume is quite small and on the order 10-100 nm. The software relates the detected bands in the diffraction pattern to the crystal orientation of the material. Each Kikuchi band is labeled with the corresponding reciprocal lattice vector indices (Miller indices). Their intersections are labeled with the corresponding direct lattice indices. In most commercial EBSD systems, the three-dimensional orientation of the investigated crystal volume is stored as a set of three Euler angles. These Euler angles can be recorded as a function of the position of the electron beam on the surface, a procedure called EBSD *mapping*. The three Euler angles are then displayed as color channels of an RGB image, yielding an Euler angle map of the sample. While different distinct colors represent poly-crystalline samples, a uniform color is found for the silver flake (figure 5.6c), demonstrating the fixed crystal orientation across the whole flake.

Pole figures of a silver flake A further method to bring three-dimensional orientational information into two dimensions are *pole figures* (figure 5.6d). In a pole figure, the normals (poles) of a specific set of crystallographic planes are projected into a circle by a stereographic or equal-area projection [152, 153]. The center of the projection is given by the sample normal. For silver flakes with cubic crystal lattice, the top surface is a (111) plane and the sample normal is given by the [111] direction. This fact can be seen in the pole figure of the {111} lattice planes, which displays the (111) plane in its center (figure 5.6d, left panel). The other points in this projection represent the $(\bar{1}11)$, $(1\bar{1}1)$ and $(11\bar{1})$ planes. Rotations by 120° around the [111] direction map the lattice on itself, i.e., the fcc lattice features a three-fold symmetry along the [111] direction. This means, equivalent sets of Euler angles exist for the same crystal orientation, i.e., for a visually identical diffraction pattern, due to symmetry arguments [152]. In the case of the silver flake, 120° shifts of Euler angle 1 have been corrected to yield the uniform color representation in figure 5.6c. For completeness, also the pole figures of the {110} and {100} lattice planes are given in the middle and right panel of figure 5.6d[1]. In conclusion, the EBSD measurements reveal a fixed orientation of the crystal lattice across the whole silver flake, which demonstrates its highly crystalline character.

5.5 ATOMIC FORCE MICROSCOPY

In addition to the crystallinity of the silver flakes, a low surface roughness is crucial for avoiding scattering loss in waveguide structures [127, 154]. *Atomic force microscopy* (AFM) has been developed since the pioneering work in 1986 by Binning *et al.* [155] into a powerful scanning probe microscopy technique to study samples at the nanoscale. The operational principle of an AFM relies on surface forces that act on a sharp tip in nanoscale proximity to the sample surface [156]. This tip is usually attached to the end of a microcantilever, whose deflections can be monitored very sensitively via the laser beam deflection method. Several modes of operation for an AFM exist. Besides static-

1 The pole figures indicate that the side facets of the specific flake under investigation are not alternating {111} and {100} planes as in the usual case of hexagonal platelets (c.f. section 5.1).

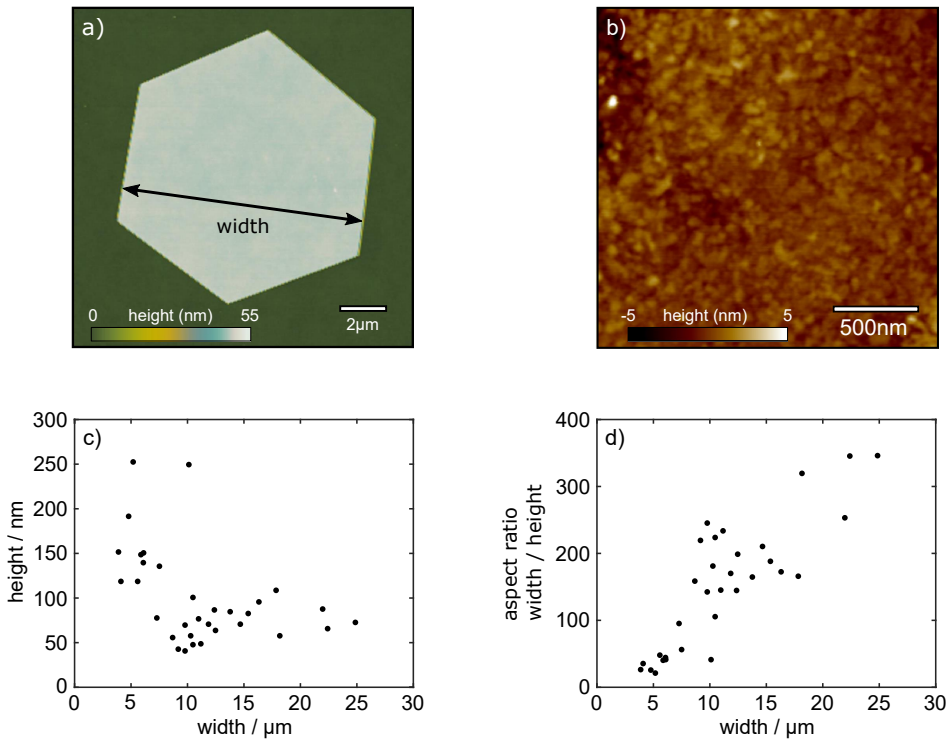

Figure 5.7: AFM characterization of silver flakes obtained with synthesis protocol 1. (a,b) AFM topography scan of a whole silver flake and a typical surface of a silver flake. (c) The height of 32 hexagonal silver flakes as a function of the width. (d) The corresponding aspect ratio (width divided by height) as a function of the flake's width.

contact mode and conventional non-contact mode, the intermittent-contact or tapping mode is most common in atomic force microscopy. Here, the cantilever is driven with fixed excitation amplitude and with fixed frequency close to its resonance frequency. An oscillation in vertical direction near the sample surface results, whose amplitude and/or phase is detected. Typically the oscillation amplitude is kept constant via a control loop that adjusts the mean tip-sample distance. During scanning, the tip periodically taps the substrate in each oscillation period. In vertical direction, an AFM usually achieves a resolution of about/below 1 Å [155]. In the lateral direction, the resolution is limited by the tip radius [156]. Under special circumstances, even atomic resolution in lateral direction is possible [157]. Hence, AFM is a well-established method to image surface topography and to determine the surface roughness at a nanoscale level. To characterize the synthesized silver flakes, a Dimension 3100 AFM from Bruker (former Veeco Instruments) equipped with a NanoScope V SPM controller and a hybrid closed-loop tip scanner was used (KeyLab Surface and Interface Characterization, University of Bayreuth). Tapping mode imaging was performed with the probes OTESPA-R3 from Bruker (7 nm nominal tip radius). Post-processing of the data was performed with software (NanoScope Analysis 1.8, Bruker).

Characterization of silver flakes synthesized via protocol 1 The synthesized silver flakes feature a uniform height across the whole top area, as demonstrated by large-area AFM measurements of their topography (figure 5.7a). The surface rms-roughness R_q, i.e., the root-mean-square of the height relative to the mean value within the sampled area, is evaluated within small areas at the top of the flake, yielding a value of about $R_q = 0.5\,\text{nm}$ rms (figure 5.7b). Besides being flat, the surface of the flake is also clean, as no larger nanoparticles stick to the surface. Furthermore, the width of the top surface, as well as the height of several flakes, have been determined. The width is measured as the perpendicular distance between opposite edges of the hexagonal shape, while the height is measured between the glass surface and the top surface of the flake. Typical heights range from a few 100 nm down to about 40 nm and the width ranges up to a few 10 µm (figure 5.7c). The correlation between these two quantities demonstrates that laterally small flakes ($< 5\,\mu\text{m}$) typically have a rather large height well above 100 nm. Flakes with lateral sizes above 10 µm typically have a thickness of 40-100 nm (average about 70 nm), offering a geometrical range well suited for large-scale focused ion beam milling of plasmonic nanostructures (see section 5.6). The aspect ratio between width and height increases for increasing width and reaches values above 300 for large flakes (figure 5.7d).

Characterization of silver flakes synthesized via protocol 2 Compared to protocol 1, the synthesis of silver flakes via protocol 2 achieved a superior surface quality of the resulting silver flakes. This important aspect is demonstrated in small-area topography scans with atomic force microscopy, finding ultra-smooth surfaces with a roughness of about 160 pm rms in a $2 \times 2\,\mu\text{m}^2$ area (figure 5.8a), which is well below typical values obtained with protocol 1 (~0.5 nm rms). More specifically, in smaller areas (e.g., figure 5.8a, green marked area), the height remains constant up to an rms-roughness below $R_q = 50\,\text{pm}$, while discrete changes of the height are visible outside these areas. In a height profile along a line in figure 5.8a (red dashed line 1), the atomic-scale steps of about 0.25 nm in height are clearly visible (figure 5.8b). On a different silver flake, terrace-like changes of the height are observed (figure 5.8c). A histogram of the measured height values in the area covering an edge (figure 5.8c, blue marked area 2) reveals a two-lobed distribution of heights (figure 5.8d). By fitting a sum of two Gaussians, a height change of about 220 pm across the investigated edge is determined.

The demonstrated height steps are consistent with the distance between the surface {111} planes of a silver flake, which is calculated for a bulk crystal according to [141]

$$d_{111} = \frac{a}{\sqrt{h^2 + k^2 + l^2}} = \frac{a}{\sqrt{3}} \approx 236\,\text{pm} \quad , \tag{5.2}$$

using $(hkl) = (111)$ and the lattice constant $a = 409\,\text{pm}$ of silver [158]. The observations are further consistent with monoatomic terraces and steps in AFM measurements of a single-crystalline silver (111) surface in UHV reported by Roobol *et al.* [159] and step sizes of about 230 pm measured via scanning tunneling microscopy by Luh *et al.* [160]. Also, for etched single-crystalline gold flakes with nearly identical lattice constant, such terrace-like AFM scans with about 200 pm step-size have been observed by Großmann *et al.* [145]. Thus, the measured atomic-scale steps seem to reflect the topography of

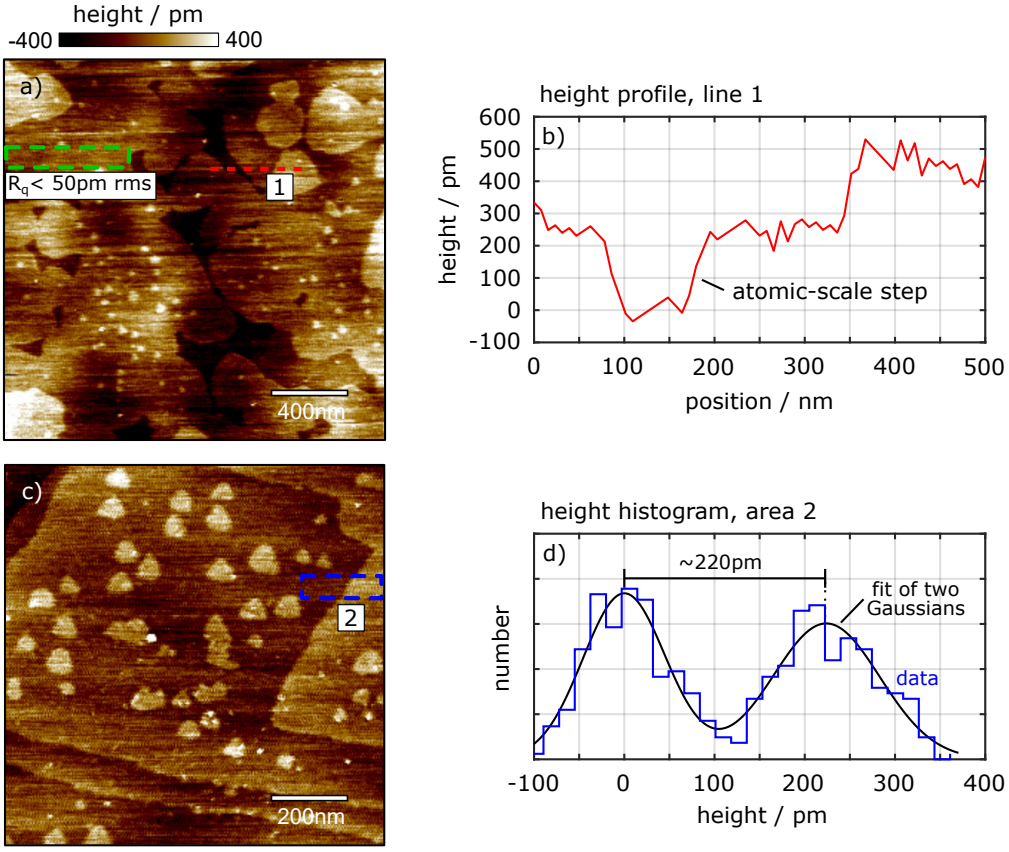

Figure 5.8: AFM characterization of silver flakes obtained with synthesis protocol 2. (a) AFM topography scan of the surface of a silver flake. The surface roughness reaches values below 50 pm rms in certain areas (marked green). (b) Height-profile along the red dashed line 1 in (a), corrected by a linear offset. Atomic-scale steps are visible in the height profile. (c) Topography scan of a different silver flake surface. (d) Height histogram of an area spanning across a step in the terrace-like surface (marked blue area 2 in (c)). Adapted from J. Chem. Phys. **155**, 234202 (2021), with the permission of AIP publishing.

the top discrete layer of silver atoms, placing the silver surfaces at the atomic limit of surface roughness. It has to be noted that at ambient conditions silver surfaces are not chemically stable and metal surfaces are typically covered with adsorbed water layers [161] and other carbon contamination like hydrocarbons [162]. Furthermore, sulfur contamination can be quite quickly detected within the first three hours after exposure to the atmosphere [163]. The AFM measurements presented here were carried out at a fresh silver flake sample that was stored in a vacuum chamber overnight and exposed to the atmosphere for only about 1 h during AFM measurements. The identification of possible elements attached to the silver flake surface remains an open question for future studies. Here, a discrete step-size in the topography of the silver surface is found that matches the expected value for a monoatomic step in single-crystalline silver. In total, the presented atomically-smooth silver surfaces belong to the highest quality reported in the literature [77].

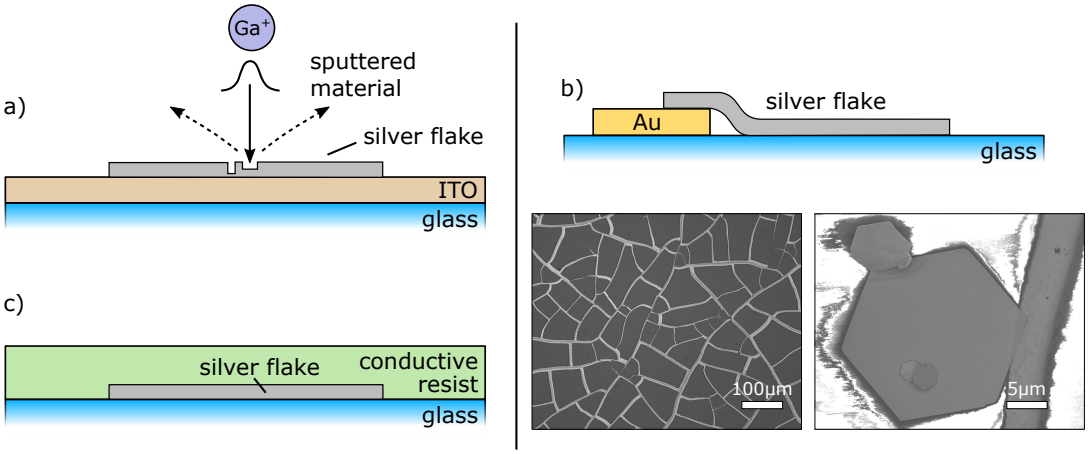

Figure 5.9: Upon focused ion beam milling with Ga^+ ions, the milled material mostly leaves the sample as sputtered material and charges accumulate in the sample. Three methods were applied to discharge the silver flakes during focused ion beam milling. (a) A conductive ITO layer between glass and silver flake. (b) A large area conductive gold network with areas of uncovered glass in between. Bottom left: Optical micrograph of a network on glass. Bottom right: SEM micrograph of a silver flake connected to the gold network. (c) A conductive polymer resist covering the whole sample including the silver flakes.

5.6 FOCUSED ION BEAM MILLING

Even more functionality and field confinement than offered by a flat silver surface can be obtained by shaping the silver into more complex nanostructures that serve as circuits for propagating plasmons. *Focused ion beam milling* (FIB milling) is one of the most popular and precise micro- and nanofabrication technique in science and industry to date. In contrast to an SEM, a FIB setup operates with a focused beam of ions, e.g., Ga^+ or He^+ [150]. Those ions are accelerated and then focused to the sample, which is oriented perpendicular to the incident beam. Within the focal area, this ion bombardment mills the sample material, which mostly leaves the sample's surface as sputtered material. The remaining material on the sample defines the resulting nanostructure. FIB milling in this thesis was performed in collaboration with Patrick Knödler on a dual-beam system (Scios, FEI company) capable of both SEM imaging and FIB milling with Ga-ions (BGI Bayreuth). For FIB milling, typically 30 kV acceleration voltage and 49 pA ion current were used. All milling procedures are performed via autoFIB scripts that mill geometrical elements such as lines and rectangles in a predefined manner into the sample.

Discharging of the sample Due to the charged nature of the Ga^+ ions incident on the sample, the accumulated charges at the sample surface have to be neutralized. To address this issue, three methods were employed to discharge the milled flake via a conductive connection to a ground contact attached to the side of the sample. First, an indium tin oxide (ITO) layer can be coated on the substrate (figure 5.9a). A

layer thickness of about 40 nm was found to offer both sufficient conductivity and high optical transmission in the visible spectral range. Second, the silver flakes can be contacted not via a planar layer but via a conductive grid consisting of gold with Cr adhesion layer (figure 5.9b). Such a large area gold network can be fabricated by a cracked polymer template[2] [164] (figure 5.9b, bottom left). The silver flakes can be directly synthesized on the substrate containing the network. In some cases, a silver flake is connected at an edge to the gold network, while most of the flake's area sticks directly to the glass substrate. This conductivity via the gold network was found to be sufficient for FIB milling and SEM imaging (figure 5.9b, bottom right). A drawback of this method is the low yield of appropriately network-contacted silver flakes on a sample, preventing the fabrication of large amounts of nanostructures on one sample. The third method to discharge the flake during FIB milling is a thin layer of a conductive polymer resist (Electra 92, Allresist) easily covering all the silver flakes on a glass substrate sample (figure 5.9c). The resist can be removed after milling via deionized water and the milled structures remain on the glass substrate.

The discharging via the ITO layer is a convenient option that was applied for SEM imaging, EDX spectroscopy and EBSD analysis of silver flakes. However, with regard to focused ion beam milling, waveguides fabricated directly on glass show a permanent superior optical transmission as compared to the ITO-coated substrate case where absorption in ITO significantly increases the damping [165]. Thus, the circuits investigated in chapters 6 and 7 were fabricated using the gold network and conductive polymer resist, respectively.

Optimization of the FIB milling To obtain highest resolution of the resulting FIB milled nanostructure, the ion beam has to be free of astigmatism and has to be focused precisely to the sample surface. The adjustment is optimized by milling a sequence of crosses into the surface with a successively changed astigmatism or focus setting, an approach first introduced by Dr. Xiaofei Wu in Bayreuth. On the one hand, the astigmatism can be corrected by the x- and y-stigmator. The x- and y-stigmator setting is changed in fixed steps within a two-dimensional array of crosses milled into the silver flake. For optimum stigmator adjustment, the milled cross in the center of the array appears as the sharpest (figure 5.10a, top). On the other hand, to check/optimize the general focus setting, a linear sequence of crosses is milled with a fixed change in the focus setting between the individual crosses. Analogously, for best focus setting, the milled cross in the center of the sequence appears as the sharpest (figure 5.10a, bottom). Furthermore, the height varies from flake to flake, which has to be considered in the milling procedure. Most importantly, an incomplete milling results in undesired metal residue that most probably changes the plasmonic properties of the nanostructure. Therefore, a slight milling into the substrate is desired. To address this issue, a sequence of rectangles is milled into the flake of interest with a stepwise increase in depth (figure 5.10b). The proper milling depth can be estimated from an SEM image of the milled flake area and is used for the subsequent milling of nanostructures into this flake. The milling depth can be further checked *in situ* during the milling process by imaging

2 The gold network was fabricated by Dr. Christian Heinrich (Macromolecular Chemistry I, University of Bayreuth).

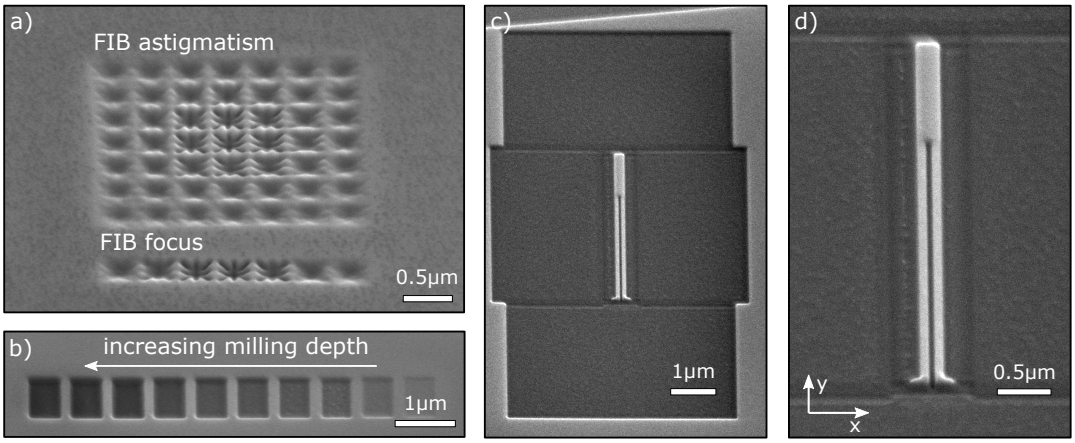

Figure 5.10: (a) FIB adjustment patterns for optimizing the astigmatism (top) and focus (bottom) of the Ga-ion beam. (b) Sequence of milled rectangles of different milling depth. (c) Example of a milled silver nanostructure. (d) Zoomed view of the structure shown in (c), demonstrating the smooth surfaces. All images were recorded by scanning electron microscopy with 52° tilt, i.e., the y-axis appears compressed by $\cos(52°)$.

the secondary electrons, where the transition from silver to glass is visible as a clear change of the image contrast.

FIB milling of a plasmonic circuit Using FIB milling, plasmonic waveguide circuits have been fabricated from the single-crystalline silver flakes (c.f. figure 5.10c). The performance of such a nanostructure as functional optical nanocircuit for the coupling with visible wavelength quantum emitters is discussed in detail in chapters 6 and 7. The following fabrication strategy for waveguide structures turned out to be most successful: A serial milling of all individual elements (rectangles, lines) is used, i.e., element after element is milled into the flake. First, micrometer-scale rectangles are milled into the flake to ensure that the final silver nanocircuit is separated by more than 2 µm in lateral direction from the silver flake for optical measurements. Afterward, smaller rectangles are milled around the center structure, defining its outer edges. A small overlap between those rectangles, leading to deeper total milling, can be observed in SEM images (figure 5.10c). After the rectangles, additional lines are milled at the outer edges of each of the two waveguide wires to define their smooth outer edges. Lastly, the small gap between the two wires is milled by two single lines at the same position. Two lines are found to be necessary for finalizing the milling of the gap. As a result of the Ga-ion distribution in the focus, a minimum gap-width of about 60 nm is achieved and a finite edge steepness of the nanostructure is unavoidable.

In contrast to the single-crystals used here, vapor-deposited metal layers consist of grains with a typical size of several tens of nanometers. As pointed out by Huang *et al.* [127], FIB milling in such poly-crystalline layers leads to unpredictable structural defects. Furthermore, Ditlbacher *et al.* [166] and Kuttge *et al.* [154] demonstrated that poly-crystalline structures, in general, lead to enhanced scattering of plasmons. In

order to obtain the desired functionality of the final nanostructure, typically very small fabrication tolerances are required. Those fabrication tolerances become more and more important as the confinement of plasmonic fields is pushed to strongly subwavelength scales. In case of a plasmonic two-wire waveguide like in figure 5.10d, it is evident that a small defect in the gap can already lead to strong undesired reflections of waveguide modes propagating in the gap. By focused ion beam milling in single-crystalline material, ultra-smooth structures with fine features like a nanogap extending over micrometer distances can be fabricated. Huang *et al.* [127] demonstrated for gold flakes that the crystallinity at milled edges is hardly affected and only a small surface contamination with particles is expected. Also, the implantation of Ga-ions into the surface was found to be very low. In total, the combined bottom-up and top-down approach of FIB milling in chemically-grown, single-crystalline silver flakes presented here opens up a fabrication route of high-quality, ultra-smooth functional silver plasmonic circuits (see chapters 6 and 7).

5.7 SURFACE PROTECTION BY ATOMIC LAYER DEPOSITION

As mentioned in section 5.5, silver surfaces suffer from poor chemical stability and certain processes have to be applied to protect the flakes and nanostructures from degradation. Wang *et al.* [161] demonstrated a dehydration process to get enhanced chemical and thermal stability of silver structures under ambient conditions. The authors point out that the degradation of silver nanostructures is closely linked to surface-adsorbed water. This adsorbed liquid water layer serves as a catalyst for the migration of ionic Ag at the surface responsible for the degradation. In their study, dehydrated structures have been demonstrated to be geometrically and optically stable for 14 weeks. Different approaches to get long-term stability of silver are the protection via graphene [129] or via a few-nanometer thick layer deposited by *atomic layer deposition* (ALD) [135, 167].

Atomic layer deposition of Al_2O_3 ALD can fabricate totally conformal thin films on any geometrical shape with sub-nanometer thickness control. Deposited films are typically pinhole-free and thus are well suited as surface passivation. In the ALD setup, the sample is placed in the reaction chamber, which is evacuated before deposition. Besides a small constant flow of an inert carrier gas (e.g., Ar) that flows through the system, precursor chemicals can be injected as short pulses into the system. Usually, two precursor chemicals react sequentially with the sample surface, leading to a conformal layer by layer film growth. In case of atomic layer deposition of Al_2O_3, the precursor chemicals are trimethylaluminum (TMA) and water. The deposition cycle is sketched in figure 5.11. The starting point is an activated surface with surface hydroxyl groups. In a first step, a TMA pulse enters the chamber, triggering a surface reaction with the hydroxyl groups. These reactions are self-terminating due to limited reaction sites at the surface. The excess precursor, as well as gaseous reaction products, are evacuated from the chamber via the vacuum pump. Second, a water vapor pulse

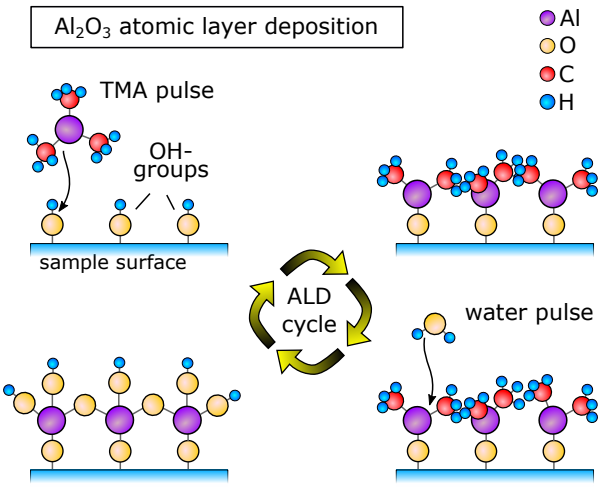

Figure 5.11: Sketch of an atomic layer deposition cycle of Al_2O_3 using TMA and H_2O precursor chemicals. The elements aluminum Al, oxygen O, carbon C and hydrogen H are represented by violet, yellow, red and blue spheres, respectively. Details see text. Inspired from ref. [168].

enters the chamber triggering a further surface reaction. Analogously, excess water and gaseous products are evacuated. These two sequential surface reactions terminate again with hydroxyl groups at the surface, enabling a further cycling of the surface reactions. The film growth is precise, repeatable and typically features a growth of about 0.1 nm per cycle depending on the material and process parameters [167]. The deposition was performed with a commercial ALD setup (Savannah, Ultratech/Cambridge NanoTech, KeyLab Device Engineering, University of Bayreuth).

Thickness control The growth of the ALD layer can be monitored during the deposition via the eigenfrequency shift of a crystal oscillator, a method that has to be properly calibrated in order to yield accurate results. Another method to determine the growth rate is a test deposition on a commercial Si waver that is already coated with about 300 nm SiO_2. The wafer has a pronounced second-order reflection minimum[3] at about 560 nm due to destructive interference between the light reflected at the air-SiO_2 and the SiO_2-Si interface (figure 5.12, violet curve). The spectral position of this minimum is very sensitive to the thickness of an additional dielectric layer deposited on top of the wafer. In the most simple case of depositing further SiO_2 on top of the existing SiO_2 layer, the total thickness d_{SiO_2} can be calculated from the reflection minima $\lambda_{min,k}$ according to

$$d_{SiO_2} = \frac{\lambda_{min,k} \cdot (2k-1)}{4\, n_{SiO_2}} \quad , \quad k \in \mathbb{N}. \tag{5.3}$$

For 200 cycles of SiO_2 ALD, a shift of the $k = 2$ minimum by about 34 nm was

3 measured with a reflection spectrometer (Semiconsoft, Inc) equipped with a bifurcated optical fiber (QR400-7-VIS-NIR, Ocean Optics) and software (TFCompanion, Semiconsoft).

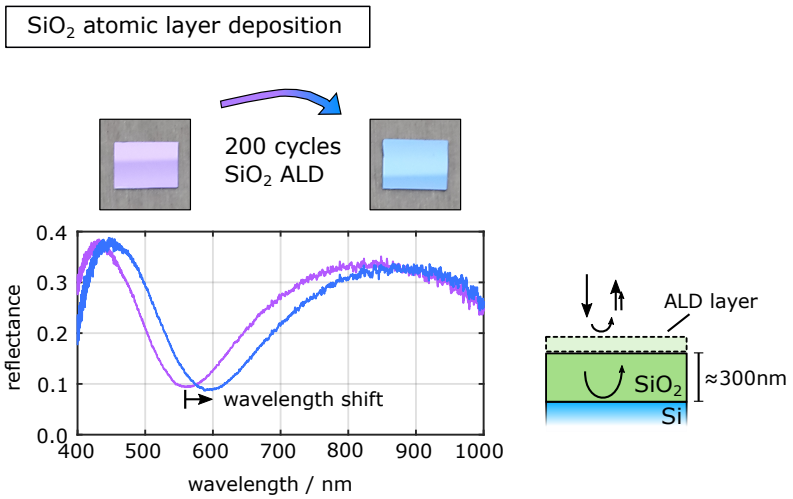

Figure 5.12: A Si wafer with 300 nm of SiO_2 appears violet (top left photograph) and features a pronounced reflectance minimum at about 560 nm (violet curve). This minimum is caused by a destructive thin-film interference (c.f. sketch at the right side). After depositing further SiO_2 by 200 cycles of atomic layer deposition, the color of the wafer changes to blue (top right photograph) and the reflectance minimum is shifted in wavelength (blue curve). From the wavelength shift and the number of applied ALD cycles (here 200), the growth rate of the deposition can be determined (see text).

detected (figure 5.12, blue curve). Assuming a refractive index of $n_{SiO_2} = 1.45$ of SiO_2, the shift of the minimum corresponds to an increase of the total SiO_2 thickness by about 18 nm, yielding a growth rate of 0.09 nm per cycle. In the general case of a different deposited material such as Al_2O_3, a theoretical reflectance spectrum can be fitted to the experimental spectrum via a software in order to determine the thickness of the deposited layer. For the deposition of Al_2O_3 at 80°C, a similar growth rate of about 0.08-0.09 nm per cycle was determined, in accordance with typical growth rates given by the manufacturer of the ALD system. After the calibration of the growth rate, the thickness of further deposited layers can be calculated based on the linear relationship between number of ALD cycles and the resulting layer thickness [169], e.g., 60 cycles are necessary for about 5 nm Al_2O_3.

Encapsulation of silver flakes and nanostructures Hiller *et al.* [170] and Broas *et al.* [167] demonstrated that layers of Al_2O_3 and SiO_2 deposited by ALD are chemically stable in the presence of different common chemicals. An encapsulation of silver flakes and nanostructures with SiO_2 instead of Al_2O_3 would offer a lower refractive index of the protection layer, which would be advantageous in terms of plasmonic propagation loss (c.f. section 3.2). However, after ALD deposition of SiO_2 using the precursors tris(dimethylamino)silane (TDMASi) and ozone (O_3), the silver flakes have been strongly degraded, rendering the SiO_2 encapsulation inappropriate. In order to test the impact of Al_2O_3 layers on the chemical stability of embedded silver flakes, two fresh flake samples were fabricated, one successfully covered by an Al_2O_3 layer and one uncovered. For the ALD encapsulation, 125 cycles at 80°C deposition temperature

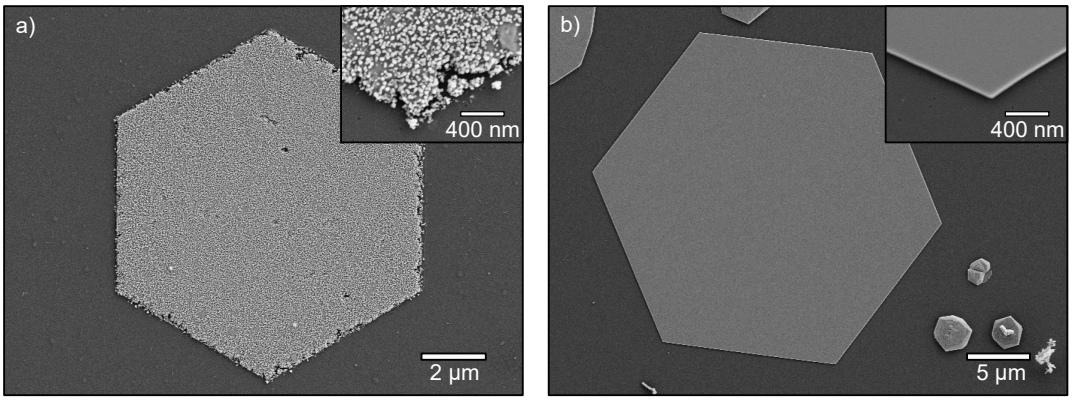

Figure 5.13: (a) Scanning electron microscope (SEM) image of a non-protected silver flake on glass. (b) SEM image of a silver flake on glass protected by a thin (~10 nm) layer of Al_2O_3 deposited by atomic layer deposition. The insets give a zoom to the edges of the respective flake. Images were recorded after 6 weeks of storage at ambient conditions and chemical treatments. Blister-formation of the Al_2O_3 layer is mostly avoided in panel (b) by a short exposure to electron-beam irradiation (see text).

were used, yielding a thickness of about 10 nm. The two samples have been stored at ambient conditions for 6 weeks and exposed several times to acetone, isopropanol and water. After that time, both samples were investigated by scanning electron microscopy (SEM). It was found that the unprotected silver sample was strongly degraded (figure 5.13a), while the Al_2O_3-protected sample remained unaffected (figure 5.13b), demonstrating its successful encapsulation. It has to be noted that for Al_2O_3 layers with a thickness larger than about 10 nm, a blistering has been observed during SEM imaging. In such a case, the Al_2O_3 layer detaches from the silver flake in a circular area, probably caused by gas accumulation at the interface between silver and Al_2O_3 upon electron-beam irradiation, as suggested by Liu *et al.* [171].

In case of silver nanostructures that are covered with only 5 nm Al_2O_3, no blistering during SEM imaging was observed, while preserving an adequate protection of the silver from air and chemical treatments. Thus, the silver nanostructures investigated in chapters 6 and 7 are encapsulated with an Al_2O_3 layer of thickness 5 nm, enabling long-term optical investigations of their plasmonic properties.

6 A SINGLE-CRYSTALLINE SILVER PLASMONIC CIRCUIT FOR VISIBLE QUANTUM EMITTERS

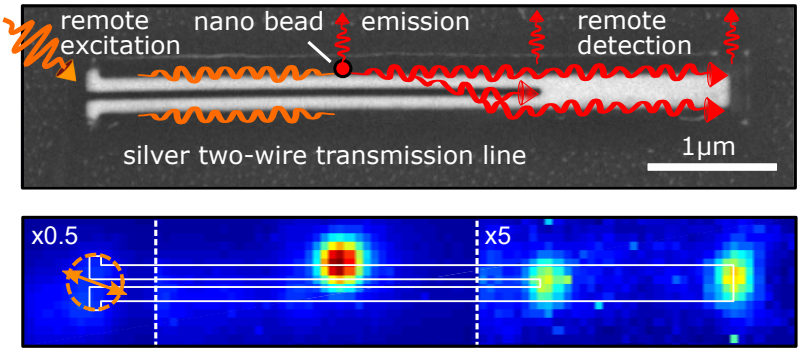

far-field fluorescence image

The above image and parts of this chapter are published in *A single-crystalline silver plasmonic circuit for visible quantum emitters* by C. Schörner, S. Adhikari, and M. Lippitz, Nano Letters **19**, 5, 3238-3243 (2019). Figure adaptations with permission. Copyright 2019 American Chemical Society.

6.1 INTRODUCTION

Plasmonic waveguides are key elements in nanophotonic circuitry, featuring a transverse mode area of the propagating modes that can be confined to deep subwavelength scales [172]. The study of coupling individual quantum emitters to confined near-fields of waveguide nanocircuits is a very promising field of research, as it might contribute to applications of emerging quantum information technologies, including optical communication, sensing and computation [14, 173, 174]. A great variety of different waveguide geometries exists, with each having distinct advantages as well as disadvantages. The overall performance of a plasmonic waveguide system to efficiently capture and transmit single photons from a quantum emitter can be quantified by a figure of merit (FOM) defined by Bozhevolnyi, Quidant and coworkers [82, 175] as the product of quantum emitter – waveguide coupling efficiency β, plasmonic propagation length l_p and total decay rate enhancement γ_{tot}/γ_0 (c.f. chapter 3) normalized to the operation vacuum wavelength λ_0: $\text{FOM} = 1/\lambda_0 \cdot \beta\, l_p \cdot \gamma_{tot}/\gamma_0$.

Chemically-grown single-crystalline silver nanowires[1] (c.f. section 3.2 and the review by Wei *et al.* [81]) are widely used by researchers for plasmonic waveguide applications due to several reasons. First of all, these nanowires are commercially available within a big range of nanowire diameters, i.e., a few tens to a few hundreds of nanometers, and a length of up to about hundred micrometers. At the same time, the surface is ultra-smooth and clearly superior to poly-crystalline nanowires [81, 166]. As a result, the propagation loss of single-crystalline wires is strongly reduced, turning them into high-quality waveguides and resonators [176]. However, also common drawbacks exist, limiting the application of chemically-grown nanowires. One drawback is certainly the lack of precise control of the geometry of the nanowires because length and diameter of the individual wires are distributed over a fairly broad range, e.g., the diameter of as-synthesized wires varies by several tens of nanometers (c.f. figure 8.3b in chapter 8). Furthermore, the modal field of the propagating plasmonic mode of a simple metal nanowire is rather distributed all around the wire than confined to a specific spot where a quantum emitter is placed (c.f. section 3.2), resulting in a low overall value of the FOM defined above [175].

Other waveguide geometries with a higher FOM include V-grooves [82], wedge waveguides [177] and dielectric-loaded surface plasmon polariton waveguides [80]. While the latter features one of the largest total figure of merits reported so far, its mode area remains rather large, limiting the achievable emitter-waveguide coupling efficiency. By contrast, Kumar *et al.* demonstrated that nanoscale gaps between two metal nanowires [178] or between a nanowire and a surface [179] offer the possibility of superior field confinement and strong light-matter interaction, at the cost of long-range propagation. Plasmonic two-wire transmission lines, in particular, offer two fundamental waveguide modes which, according to Geisler *et al.* [114], can be excited selectively by an optical antenna and detected *in situ* via a mode detector. Such waveguides find application in polarization manipulation [180], local mode-conversion [181], coherent control of plasmon propagation [182], spin-dependent flow on the nanoscale [183, 184] and modal symmetry controlled second-harmonic generation [185].

Plasmonic circuits such as the two-wire transmission line with antenna and mode detector offer a higher degree of functionality and confinement compared to waveguide geometries built up from chemically-grown silver nanowires, which are limited to rather simple geometries [178, 186, 187]. Complex-shaped plasmonic nanostructures have been fabricated by focused ion beam milling of single-crystalline gold flakes, yielding high-quality nanostructures of designed dimensions at well-defined positions [127, 149, 188, 189]. However, the coupling of dye molecules to nanostructures fabricated from gold is unfavorable for quantum plasmonic experiments. One the one hand, strong ohmic losses of gold structures in the visible range limit long-range plasmonic waveguiding to the near-infrared spectral range [190–192]. On the other hand, dye molecules feature a high quantum yield for fluorescence emission typically only in the visible spectral range [193, 194] where gold waveguides do not perform well. Silver, in contrast to gold, features strongly reduced losses in the visible to near-infrared range [125, 126]. Furthermore, single-crystalline silver [128, 195] promises to reduce

1 To be more precise, the wires typically feature a five-fold twinned crystal structure [138].

the scattering loss present in poly-crystalline nanostructures [127, 154, 166]. Hence, the fabrication of plasmonic circuits from single-crystalline silver (c.f. chapter 5) appears to be very promising for quantum plasmonic experiments with molecular systems in the visible spectral range.

This chapter demonstrates for the first time a visible light operation of a multi-mode plasmonic nanocircuit fabricated by focused ion beam milling from a single-crystalline silver flake. The circuit is fabricated by the procedure described in chapter 5 and consists of several distinct elements, i.e., an optical antenna, a two-wire transmission line and a mode detector. The overall transmission through the circuit is quantified in a broad range of wavelengths from 550 nm to 740 nm. Moreover, the emission of an individual 20 nm-sized fluorescent bead into waveguide modes is studied by directly exciting the bead with a laser focus as well as by a remote excitation via different superpositions of waveguide modes. In both cases, the excitation of the bead's fluorescence is found to depend sensitively on the subwavelength near-field distribution around the silver nanostructure. Thus, the approach presented in this chapter opens up the study of the nanoscale light-matter interaction between complex-shaped silver plasmonic waveguide circuits and a large variety of quantum emitters available in the visible spectral range.

6.2 EXPERIMENTAL SETUP

The experiments in this chapter have been performed with a home-built room temperature optical setup (figure 6.1a). The main laser source is a Ti:Sapphire laser (Mira-HP, Coherent) that pumps an optical parametric oscillator (Mira-OPO, Coherent) at 76 MHz repetition rate and about 150 fs pulse duration. The wavelength of the visible output of the latter can be tuned across a broad range from about 550 to 740 nm. To define a linear polarization that can be controlled with the computer, first, a circular polarization is generated by a quarter-wave plate. Second, a linear polarizer that can be rotated remotely is passed. As a result, a linear polarization is defined with an optical power nearly independent of the polarizer angle. Subsequently, a spatial filter (two lenses with 10 cm focal length and a 30 µm pinhole in between) is passed that cleans up the intensity profile of the laser beam to yield a Gaussian-like intensity profile. Furthermore, the pinhole in the spatial filter reduces the slight beam-pointing changes that appear during wavelength tuning of the optical parametric oscillator or during rotations of the linear polarizer. The excitation beam passes a 50:50 beamsplitter (BS016, Thorlabs) and is focused onto the sample with a high-NA oil immersion objective (UPlanSAPO, 60×, NA=1.35, Olympus). The sample can be positioned relative to the objective with three linear stages and a piezo cube (P-611.3SF with E-503.00 amplifier, Physik Instrumente), enabling a precise position control along all three spatial dimensions. Optionally, the small sample-chamber can be flushed with nitrogen or helium atmosphere to reduce the photobleaching of fluorescent emitters during the measurements.

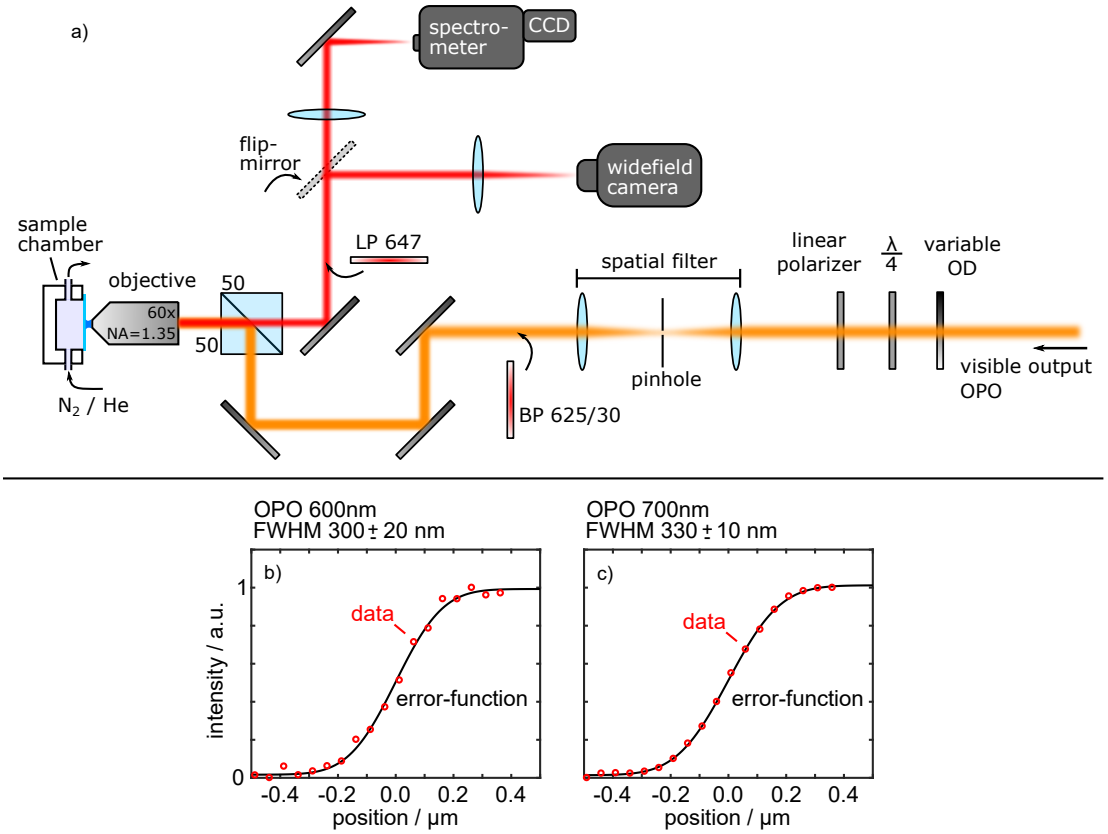

Figure 6.1: (a) Simplified sketch of the experimental setup explained in the text. The excitation path is sketched in orange, while the detection path is displayed in red. (b,c) Laser spot sizes achieved using the high-NA oil immersion objective for the visible output of the optical parametric oscillator (OPO) at 600 nm and at 700 nm. A sharp edge of a silver plate was scanned across the laser focus with the piezo actuator and the reflected intensity was recorded (colored circles). A fit of an error-function (solid black line) allows to estimate the full width at half maximum of the laser focus.

The reflected / scattered laser light is collected by the same objective, passes again the beamsplitter and can be guided to several detectors. As first option, the light can be guided to an sCMOS camera (Zyla 4.2, Andor) via a 30 cm focal length tube lens. This camera allows widefield imaging, e.g., of waveguide samples, with a magnification of 100 using the high-NA objective. To locate the tiny waveguide structures on the sample, a low-magnification air objective is used. In a second detection path, selected via a flip-mirror, a 50 cm focal length tube lens focuses the light into the entrance slit of a spectrometer (Isoplane SCT 320, Princeton Instruments, blaze wavelength 600 nm) equipped with a back-illuminated CCD camera (Pixis 400, Princeton Instruments). Spatially resolved emission spectra can be recorded along the direction defined by the entrance slit. For fluorescence experiments, the center wavelength of the optical parametric oscillator is tuned to an excitation wavelength of about 620 nm and a clean-up filter (bandpass 625/30, AHF Analysentechnik) is flipped in the excitation path. Furthermore, a dielectric filter (longpass LP647, AHF Analysentechnik) is flipped

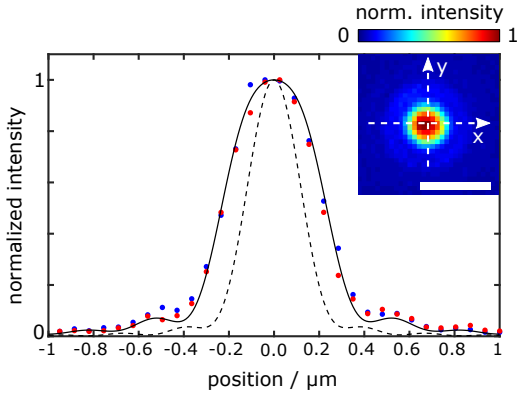

Figure 6.2: Experimental point-spread function toward the imaging camera determined by imaging the fluorescence of a 20 nm dark red bead. From the fluorescence image (inset, scale bar is 1 µm in the sample plane), the intensity profiles through the center along the x- and y-direction (blue and red dots) are extracted and compared to simulated point-spread functions taking only in-plane electric dipoles (black dashed lines) and both in-plane and out-of-plane dipoles into account (solid black line). Details of the simulation are given in the text.

into the detection path to separate the red-shifted fluorescence from the exciting laser light.

An important parameter for the waveguide experiments in this chapter is the spot-size of the laser in the sample plane. To estimate this spot-size, a sharp straight edge of a silver flake is scanned in a direction perpendicular to the edge across the laser focus with the piezo while recording the reflected intensity (red dots in figure 6.1b,c). By fitting an error-function to the data (black line in figure 6.1b,c), the full width at half maximum (FWHM) of the laser focus can be estimated. A focus size close to the diffraction-limit is determined, e.g., FWHM = 330 nm (300 nm) at 700 nm (600 nm) operation wavelength, that depends on the operation wavelength and the filling factor of the back aperture of the objective [55].

The point-spread function of the imaging system toward the widefield imaging camera is quantified by recording the fluorescence image of a 20 nm polystyrene bead that is doped with a few tens of randomly oriented dark red fluorescent molecules (Thermo Fischer Scientific) emitting around 700 nm (c.f. figure 6.13) upon linearly polarized excitation at 620 nm. The intensity profiles through the center of the fluorescence image along the x- and y-direction are calculated and compared to the profiles of simulated point-spread functions (figure 6.2, colored dots and black lines, respectively). For the simulations, an incoherent superposition of electric dipoles in 10 nm height above an air-glass interface at 700 nm is used and imaged via an optical system with an $NA = 1.35$ objective from the glass side and total magnification of $M = 100$ (c.f. section 4.3). Taking only in-plane electric dipoles into account cannot reproduce the experimental intensity profiles (figure 6.2, black dashed line). This is expected, as a fluorescent bead is an isotropic emitter with the emission being depolarized even after a linearly polarized excitation [196]. Therefore, the consideration of additional out-of-

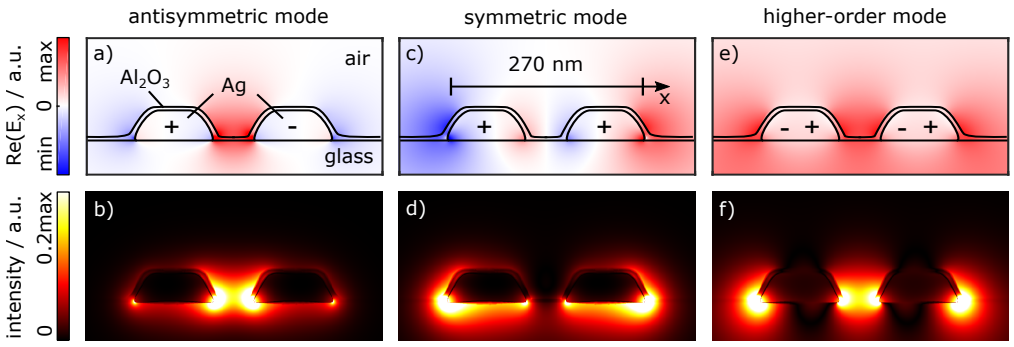

Figure 6.3: Simulated near-field distributions of the eigenmodes of a silver two-wire transmission line at a vacuum wavelength of 620 nm. The real part of the electric field pointing across the gap (x-component) and the corresponding intensities are given for the antisymmetric mode in panel (a) and (b), for the symmetric mode in (c) and (d), and for the higher-order mode in (e) and (f), respectively. The intensity is evaluated as magnitude of the time-averaged Poynting vector due to the inhomogeneous environment. The charge distribution is sketched in (a), (c) and (e) for clarity. The colorscale in (b), (d) and (f) is limited to 20 % of the maximum value of each panel for a better visibility.

plane oriented electric dipoles leads to a very good match of the calculated intensity profile with the experiment (figure 6.2, solid black line). For the best match, the out-of-plane component needed to be increased by about 40 % compared to both in-plane components, probably due to a partly bleaching of the in-plane oriented molecules in the experiment or a non-isotropic orientation of the molecules. Thus, diffraction-limited imaging is performed with the widefield camera. Typical excitation powers used in this chapter were 10 nW for laser transmission experiments of waveguide structures and 10 µW for remote excitation of fluorescent emitters via the waveguide.

6.3 PLASMONIC TWO-WIRE WAVEGUIDE MODES

In this section, the plasmonic waveguide modes of two parallel silver nanowires are considered first isolated from the final circuit which further includes an antenna and a mode detector attached to the wires. The two parallel silver nanowires, separated by a gap of a few tens of nanometers, represent the central waveguide part called plasmonic two-wire transmission line, which is simulated here by the numerical mode analysis described in subsection 4.1.2. Particularly, the silver wires are modeled with a height of 40 nm, a width of about 110 nm, a gap separation of about 60 nm and are placed on a glass-air interface (c.f. figure 6.3). Furthermore, a 5 nm cover layer of Al_2O_3 has been considered. This modeling matches the dimensions of the experimentally investigated wires (c.f. figure 6.7a). Each nanowire considered separately features a fundamental (TM_0-like) plasmonic waveguide mode with a charge distribution of fixed sign in a transverse plane (c.f. subsection 3.2.2). Bringing two nanowires in close proximity

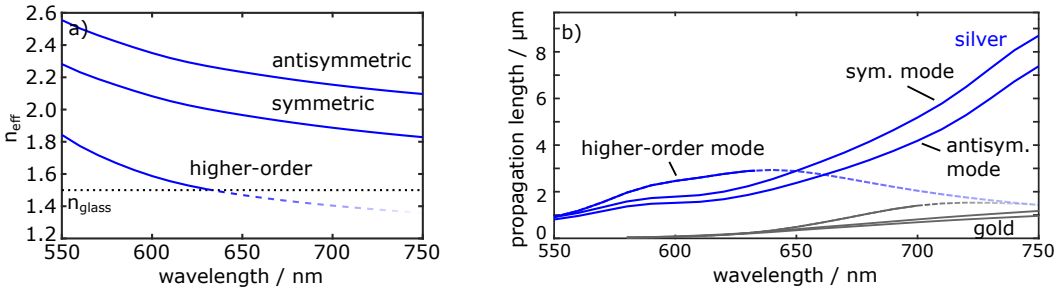

Figure 6.4: (a) Simulated real part of the effective mode index of the antisymmetric, symmetric and higher-order mode as a function of the vacuum wavelength for the two-wire waveguide geometry shown in figure 6.3. (b) Propagation lengths of the antisymmetric, symmetric and higher-order mode of a two-wire waveguide fabricated from silver (blue) compared to gold (gray). The higher-order mode gets leaky ($n_{eff} < n_{glass}$) above a certain wavelength (dashed lines in panel (a) and (b)).

leads to a hybridization effect, yielding two fundamental eigenmodes of the two-wire waveguide. The simulated eigenmodes are labeled according to the symmetry of their charge distribution in a transverse plane which can be either *symmetric* or *antisymmetric* between the two wires. An antisymmetric charge distribution between the wires leads to a strong near-field directing across the nanogap (figure 6.3a) with high intensity in the gap (figure 6.3b). In the symmetric case, by contrast, the electric near-field component across the gap features a change of sign (figure 6.3c). The near-field is pushed out of the nanogap toward the outer edges of both wires, where, as a result, the intensity is highest (figure 6.3d). For low wavelengths and certain geometries of the two wires also a *higher-order mode* appears [197]. This mode can be more precisely identified as an antisymmetric combination of the higher-order (HE_1 -like) mode described in section 3.2 (figure 6.3e) and features an intensity that is distributed across the gap as well as both outer edges (figure 6.3f). The plasmonic waveguide modes displayed in figure 6.3, i.e., the antisymmetric mode, the symmetric mode and the higher-order mode, feature effective mode areas A_{eff} (c.f. equation 3.24) at $\lambda_0 = 620\,\text{nm}$ vacuum wavelength of $1.1 \cdot 10^4\,\text{nm}^2$, $2.3 \cdot 10^4\,\text{nm}^2$ and $2.6 \cdot 10^4\,\text{nm}^2$, respectively. Compared to a Gaussian focus of FWHM $= \lambda_0/2$ with a mode area of $A_{eff} = 22 \cdot 10^4\,\text{nm}^2$, the plasmonic modes are confined strongly beyond the diffraction limit.

As a result of the hybridization effect, the antisymmetric and symmetric mode feature different real parts of the effective mode index n_{eff}, which are both located above the value of the higher-order mode (figure 6.4a). Reducing the operation wavelength leads to an increase of n_{eff} and a reduction of the bound modes' propagation lengths (figure 6.4b). Above a certain wavelength (here ~640 nm), the higher-order mode gets leaky. Due to the favorable dielectric function of silver (c.f. figure 3.1), the propagating modes of a silver two-wire waveguide structure feature much longer propagation lengths in the whole visible to near-infrared spectral range compared to a gold structure of the same geometry (figure 6.4b). Despite the decreasing propagation lengths toward lower wavelengths, the performance of the silver structure in the visible range still

surpasses the gold structure in the near-infrared. As a consequence, a silver two-wire waveguide, just as plane interfaces and single nanowires (c.f. section 3.2), offers superior performance when fabricated from silver and is best suited for quantum plasmonic experiments with fluorescent dye molecules in the visible spectral range.

6.4 NUMERICAL SIMULATIONS OF THE PLASMONIC CIRCUIT

In this section, the whole plasmonic circuit consisting of a two-wire transmission line, an optical antenna [16] and a mode detector [114] at either end is considered in simulations. In order to best match the experimentally investigated circuit (c.f. figure 6.7a), two 3.5 µm long silver wires are placed on a glass-air interface with the cross-section displayed in figure 6.3. Furthermore, a 1.5 µm long mode detector is attached at the right side and tiny cuboid optical antennas (180 nm × 90 nm) are attached at the left side with 40 nm height in each case (c.f. figure 6.5).

To demonstrate the functionality of the circuit in its entirety first, a full three-dimensional simulation of the structure is performed using the basic numerical model described in subsection 4.1.3 and including the whole circuit inside the simulation domain. An Al_2O_3 layer is neglected in this case for numerical simplicity. When exciting the optical antenna with a Gaussian focus from the substrate side (FWHM $= \lambda_0/2$), the waveguide modes can be selectively launched depending on the incident polarization direction [114]. In case of a polarization direction perpendicular to the long wire axis, the antisymmetric mode is launched by the antenna (figure 6.5a). The modal field of this mode propagates mainly within the nanogap and is thus strongly reflected and radiated at the gap termination, i.e., at the near end of the mode detector. Due to the back-reflections, standing wave intensity patterns built up along the gap (not shown). The radiation of the antisymmetric mode can be observed via far-field imaging at the gap termination performed according to section 4.2 (figure 6.5b). By contrast, a parallel polarization of the Gaussian excites the symmetric mode (figure 6.5c). This mode has a low amplitude in the gap and features a very good mode matching (~95 %[2]) with the fundamental mode of the mode detector. Thus, the symmetric mode can propagate beyond the gap termination up to the far end of the mode detector, where it is reflected and radiated into the far-field (figure 6.5d). The function of the antenna is therefore given by the efficient interconversion of far-field photons and propagating plasmonic modes along the waveguide part (c.f. Huang *et al.* [16]). In particular, the fundamental symmetric and antisymmetric waveguide mode can be selectively launched depending on the linear polarization incident on the antenna. The mode detector, by contrast, spatially separates the contributions of both waveguide modes, reaching a nearly perfect mode selectivity in far-field imaging detection, as pointed out by Geisler *et al.* [114].

2 The mode matching is evaluated here by a squared mode overlap integral as defined in equation 4.22, factor 2.

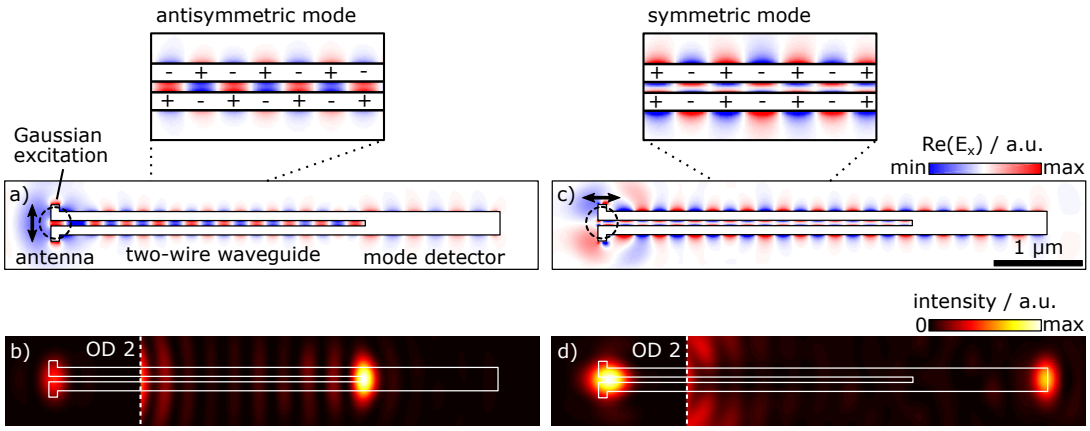

Figure 6.5: Three-dimensional simulation of the electric near-field along the full plasmonic silver circuit upon focused Gaussian beam excitation on the antenna's center (dashed circle in (a) and (c)). The polarization of the Gaussian is set (a) perpendicular and (c) parallel to the long waveguide axis (black arrows), exciting predominantly the antisymmetric and symmetric mode, respectively. A Gaussian of full width at half maximum of $\lambda_0/2$ incident from the substrate side at a vacuum wavelength $\lambda_0 = 720\,\text{nm}$ is chosen. The real part of the electric near-field component directing across the gap (x-component) is displayed at the glass-air interface. The charge distribution along the wires is sketched in the zoom-in panels above. In (b) and (d), the corresponding far-field imaging simulation toward the substrate side is shown ($\lambda_0 = 720\,\text{nm}$, $NA = 1.35$). The intensity at the excitation area is software-attenuated by 100 (OD 2). The Al_2O_3 layer is neglected for numerical simplicity.

Besides being numerically very expensive, such a three-dimensional simulation of the full plasmonic circuit does not provide a detailed understanding of the performance of the individual elements, in particular, when varying a parameter such as the operation wavelength λ_0. Therefore, in the following, the wavelength-dependent performance of the circuit for light transmission is split up into an incoupling efficiency of the antenna η_{in}, a propagation efficiency along the two-wire part η_{prop} and a collection efficiency by the objective at the mode detector η_{col}.

Incoupling efficiency The incoupling efficiency η_{in} of waveguide modes in the two-wire waveguide by the antenna is simulated using the numerical model described in subsection 4.1.3. In addition to the circuit's geometry defined above, an Al_2O_3 cover layer of thickness 5 nm is considered to best match the experimentally investigated nanostructure. It is found that the calculated incoupling efficiency for both the antisymmetric and symmetric waveguide mode upon Gaussian excitation with the corresponding polarization on the antenna is very sensitive to details such as the exact antenna geometry [114] and the covering with an Al_2O_3 layer. Using the described fixed circuit geometry, the wavelength dependency of the incoupling efficiencies η_{in} for both the antisymmetric and symmetric mode is determined (figure 6.6a). According to these simulations, the incoupling in the considered wavelength range (550-750 nm) is more efficient for the symmetric mode than for the antisymmetric mode, reaching values η_{in} above 5 % at about 700 nm for the symmetric mode.

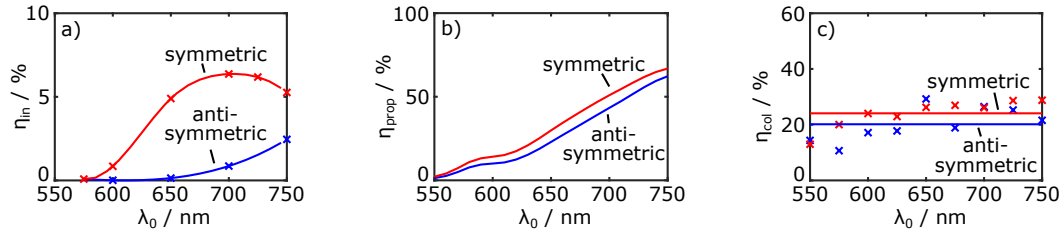

Figure 6.6: (a) Simulated incoupling efficiency η_{in} of the symmetric and antisymmetric mode into the two-wire transmission line upon a Gaussian excitation with the corresponding polarization direction incident on the antenna as a function of the vacuum wavelength λ_0. Crosses are simulated values, lines represent a spline interpolation as a guide to the eye. (b) Simulated propagation efficiency η_{prop} of the 3.5 µm long two-wire transmission line only. (c) Simulated collection efficiency of the modes via collecting the mode detector emission by the objective of $NA = 1.35$ at the substrate side. Crosses represent simulated values, while the lines display an averaged level. In all cases, the symmetric and antisymmetric mode is displayed in red and blue, respectively.

Propagation efficiency The propagation of a waveguide mode along the $l = 3.5\,\mu m$ long two-wire transmission line involves losses which lower the transmitted power by the propagation efficiency $\eta_{prop} = e^{-l/l_p(\lambda)}$. Here, $l_p(\lambda)$ is the wavelength-dependent propagation length of the corresponding waveguide mode (c.f. figure 6.4b) determined by a two-dimensional mode analysis simulation according to subsection 4.1.2. As a result of the slightly lower propagation length of the antisymmetric mode compared to the symmetric mode (c.f. figure 6.4b), also its propagation efficiency is slightly lower. Furthermore, the calculated propagation efficiency of both modes increases toward the near-infrared region, but still allows for visible light operation in case of silver (figure 6.6b).

Collection efficiency After propagation along the two-wire part, the waveguide mode reaches the mode detector. The amount of power radiated into the collection angle of the objective relative to the modal power at the junction with the mode detector is considered as collection efficiency η_{in}. The integration sphere of the numerical model described in subsection 4.1.4 is centered to the near (far) end of the mode detector in case of the antisymmetric (symmetric) mode. The collection efficiency of the symmetric mode at the far end of the mode detector includes the propagation losses along the mode detector. The thin Al_2O_3 layer is neglected in this case for numerical simplicity, as a minor influence on η_{out} was found. The simulated collection efficiencies are rather spectrally flat in the considered wavelength range (figure 6.6c, crosses). In order to average out the observed variations of the numerical values that might originate from reflections and standing waves within the model, in the following the averaged levels of the collection efficiency given by 25 % and 20 % for the symmetric and antisymmetric mode, respectively, are used (figure 6.6c, horizontal lines).

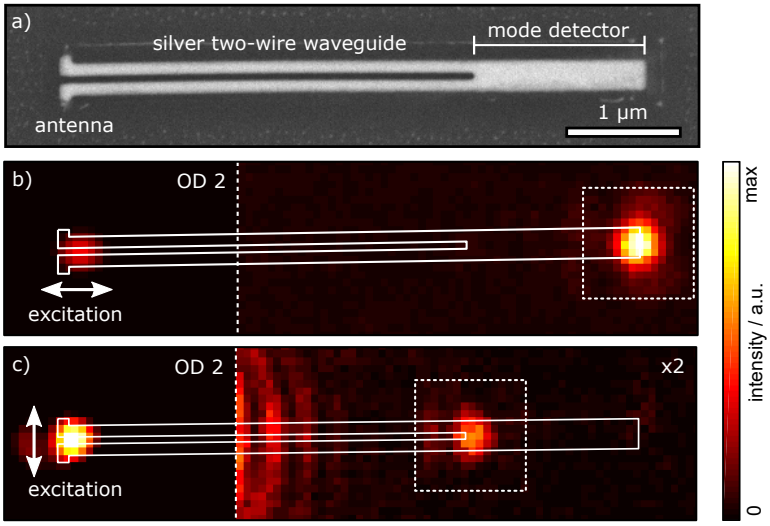

Figure 6.7: (a) Scanning electron micrograph of the silver two-wire transmission line (60 nm gap, 110 nm wire width) with an attached antenna and mode detector on either side. (b,c) Widefield images of the circuit upon focused laser excitation at $\lambda = 720$ nm on the antenna with a parallel and perpendicular polarization (white arrows), respectively. In panel (b), the symmetric mode is launched and radiated at the far end of the mode detector. In panel (c), the antisymmetric mode is launched and detected at the near end of the mode detector. The transmitted signal at the mode detector is framed by a dotted square area for clarity. The intensity in the area around the antenna is software-attenuated by a factor of 100 (OD 2) and the whole data in (c) is multiplied by a factor of two compared to panel (b) due to a lower total transmitted signal.

6.5 MULTI-MODE TRANSMISSION CHARACTERIZATION

In this section, the plasmonic circuit, consisting of the antenna, the two-wire transmission line and the mode detector, is characterized experimentally with regard to the transmission of laser light through it. The nanostructure is fabricated by focused ion beam milling from a single-crystalline silver flake of about 40 nm in height (c.f. chapter 5). Particularly, the silver flake synthesis protocol 1 (c.f. section 5.2) is used and the flake is discharged during focused ion beam milling via a large area gold network (c.f. section 5.6). The resulting nanostructure features a 3.5 µm long two-wire transmission line (gap ~60 nm, wire width ~110 nm) as well as an antenna and mode detector (length 1.5 µm) attached to either side of the wires (figure 6.7a). After milling, the silver structure is protected from air and chemical treatments by a thin (~5 nm) conformal layer of Al_2O_3 deposited by atomic layer deposition.

Selective excitation and detection of waveguide modes To demonstrate the selective excitation of the symmetric and antisymmetric waveguide mode and their *in situ* detection via the mode detector, the optical antenna is excited by a linearly polarized laser focus at 720 nm vacuum wavelength and the scattered light is detected by widefield imaging. In case of a polarization parallel to the long waveguide axis

exciting the antenna, the mode detector emits at its far end as characteristic for the symmetric mode (figure 6.7b). Remarkably, the whole waveguide part, as well as the near end of the mode detector, appears dark due to the bound nature of the symmetric waveguide mode. Rotating the exciting polarization to a perpendicular direction on the antenna, the mode detector emission switches to its inner end as characteristic of the antisymmetric mode propagating mainly in the gap (figure 6.7c).

Experimental waveguide transmission The visible light performance of the circuit is investigated by tuning the wavelength of the optical parametric oscillator over the range 550–740 nm while maintaining a close to diffraction-limited excitation spot-size (c.f. figure 6.1b,c). The overall transmission of the waveguide is defined as the ratio of the detected power at the mode detector normalized to the incident power on the antenna. The latter is determined from the reflection at a reference glass surface, corrected by the surface reflectivity of 4 %. The transmitted signal of the symmetric mode is integrated in a 1 µm square area evaluated at the far end of the mode detector (c.f. figure 6.7b), while the antisymmetric mode is evaluated at the near end (c.f. figure 6.7c). In both cases, an integrated signal of a neighboring square area of equal size is subtracted for background removal. The above definition of the overall waveguide transmission includes all the three factors simulated in figure 6.6, i.e., the incoupling efficiency η_{in}, propagation efficiency η_{prop} and collection efficiency η_{col}.

A selection of widefield images displaying the emission of the mode detector for parallel and perpendicular excitation polarization on the antenna at different excitation wavelengths is given in figure 6.8a. In case of a parallel excitation polarization launching the symmetric mode, the overall transmission is plotted as a function of wavelength in figure 6.8b (red dots). A plateau above 700 nm is observed for the symmetric mode with an experimental transmission of about $2 \cdot 10^{-3}$. As the wavelength is reduced, the transmission drops down continuously to values $< 1 \cdot 10^{-4}$ below 600 nm wavelength. In case of a perpendicular polarization on the antenna expected to launch the antisymmetric mode detected at the near end of the mode detector, a reduced transmission of the antisymmetric mode compared to the symmetric mode is found for wavelengths around 700 nm (figure 6.8b, blue dots). Surprisingly, as the wavelength is lowered, the transmission first reaches a value close to zero at 660 nm and then passes through an additional maximum centered around 590 nm.

Comparison to simulations To gain insight into these wavelength-dependent transmission features, the simulated efficiencies for incoupling, propagation and collection as a function of wavelength are considered (c.f. figure 6.6a,b,c), which use a geometry similar/best-fitting to the experiment. A multiplication of all three factors[3] yields a reasonably good match with the experimental data concerning the spectral dependency of the transmission (figure 6.8b, black dashed lines) for both the symmetric and antisymmetric mode. The experimental transmission data is, in general, a factor of about 5 lower than predicted by the simulations. One possible reason for this reduced transmission could be related to the dielectric data of silver, which slightly varies in

3 This approach neglects any interference of the transmitted signal with free-space propagating modes as well as Fabry-Pérot effects along the waveguide [115].

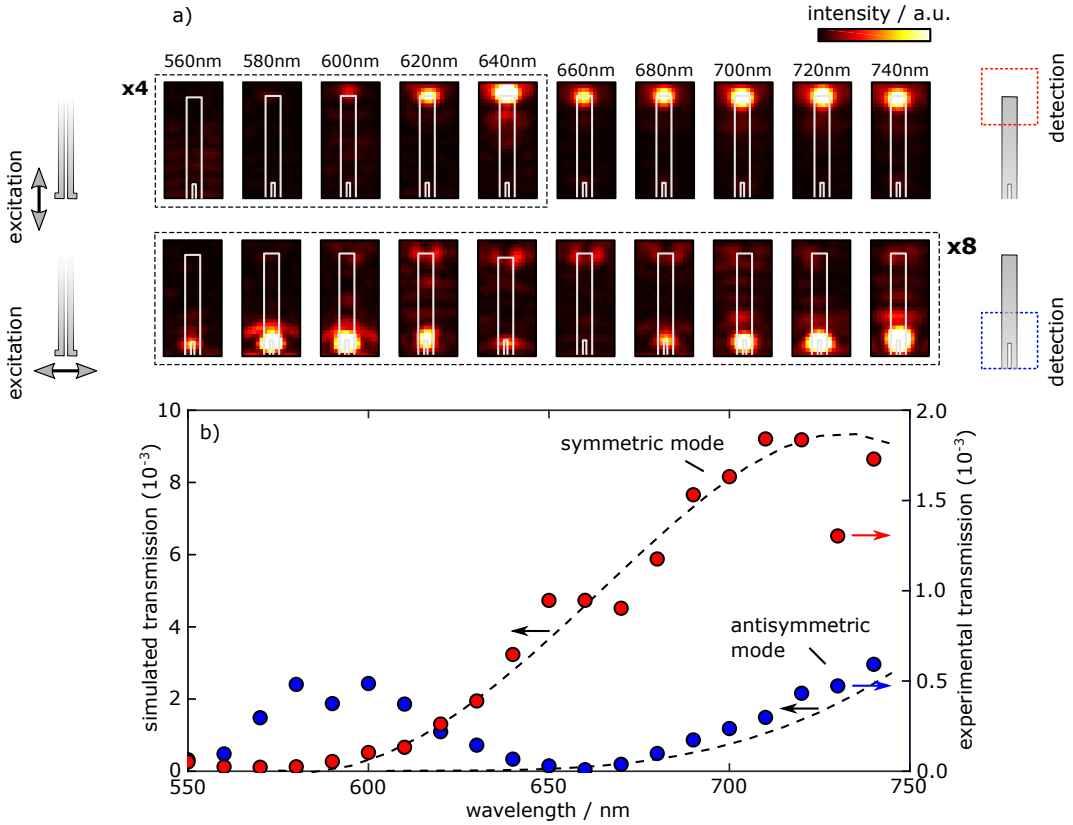

Figure 6.8: (a) Widefield images of the experimental mode detector emission for parallel (upper row) and perpendicular excitation polarization (lower row) on the antenna for different vacuum wavelengths. The intensity in specific labeled panels is multiplied by 4 or 8 to ensure a visibility of the transmitted signals. (b) Experimental full transmission of the waveguide circuit as a function of vacuum wavelength. The red (blue) dots correspond to a parallel (perpendicular) excitation polarization and integration of the transmitted signal in a square area at the far (near) end of the mode detector (c.f. sketches in (a), left and right). The black dashed lines are theoretical predictions given as the product of the incoupling, propagation and collection efficiency shown in figure 6.6 and use a differently scaled axis (left axis) compared to the experimental data (right axis).

the literature. However, compared to different reports, the data from Johnson and Christy [75] used for the simulations rather over-estimates the losses in the visible range than under-estimates them [77]. Grain boundary scattering is an important plasmonic loss mechanism in poly-crystalline films [154], which, however, should be largely avoided here due to the crystalline material. Another important point is that the simulations do not take into account the surface roughness of the nanostructure which is known to increase the scattering loss [198]. In particular, the plasmonic modes of a two-wire waveguide are tightly confined to the edges fabricated by focused ion beam milling (c.f. figure 6.3). These edges feature a certain roughness with nanoscale particles attached to them due to redeposition during focused ion beam milling [127]. In total, this fact supposably leads to additional scattering loss during propagation,

explaining the decreased experimental transmission values compared to the idealized simulation conditions.

As the mode detector collection efficiency remains spectrally flat (c.f. figure 6.6c), the spectral shape of the transmission is mainly determined by the antenna incoupling efficiency and the propagation efficiency of the two-wire transmission line (c.f. figures 6.6a,b). These two factors explain the continuous decrease of the symmetric mode transmission toward lower wavelengths (figure 6.8b, red dots). In case of the antisymmetric mode, the simulations further explain the lowered transmission compared to the symmetric mode mostly by a lowered incoupling efficiency of the antenna (c.f. figure 6.6a). For a different antenna geometry, a different ratio between the incoupling of symmetric and antisymmetric mode [114] as well as different spectral dependencies are expected. The increased transmission at the near end of the mode detector with a maximum at about 590 nm found in experiments is not captured by the simulation of the antisymmetric mode only (figure 6.8b) and needs a particular consideration in the following section 6.6.

Note that at an operation wavelength of 620 nm, where the silver nanostructure offers equally strong transmission for both incident excitation polarizations (c.f. figure 6.8b), a gold two-wire transmission line features a simulated propagation length of the symmetric mode of ~150 nm only (c.f. figure 6.4b). As a result, already the bare expected propagation efficiency over the distance 3.5 µm, i.e., $e^{-3.5\,\mu m/150\,nm} < 10^{-10}$, is more than six orders of magnitude smaller than the full transmission performance of the silver nanostructure investigated here.

6.6 WAVEGUIDE MODE INTERFERENCE

This section discusses the circuit transmission detected at the mode detector in more detail, particularly to gain more insight into the observed minimum in the transmission at 660 nm followed by the maximum centered around 590 nm for a perpendicular excitation on the antenna (c.f. figure 6.8b, blue dots). To address this issue, the mode detector emission behavior is studied at a fixed vacuum wavelength of 620 nm and, additional to the linear polarization of the excitation beam, a polarizer is inserted in the detection path. For parallel polarization at the antenna exciting the symmetric mode, an emission spot at the far end of the mode detector is observed (figure 6.9a, left panel). Full three-dimensional simulations show that the symmetric mode of the two-wire waveguide is transformed at the gap termination into a fundamental (TM_0-like) waveguide mode propagating along the mode detector and radiated at its far end (c.f. figure 6.5c,d). This emission spot has a strong single-lobed profile for a parallel orientation of the detection polarizer (figure 6.9a, middle panel), while a much weaker two-lobed emission profile is detected for perpendicular orientation of the detection polarizer (figure 6.9a, right panel). Thus, the mode detector indicates the propagation of the symmetric two-wire waveguide mode by an emission at its far end

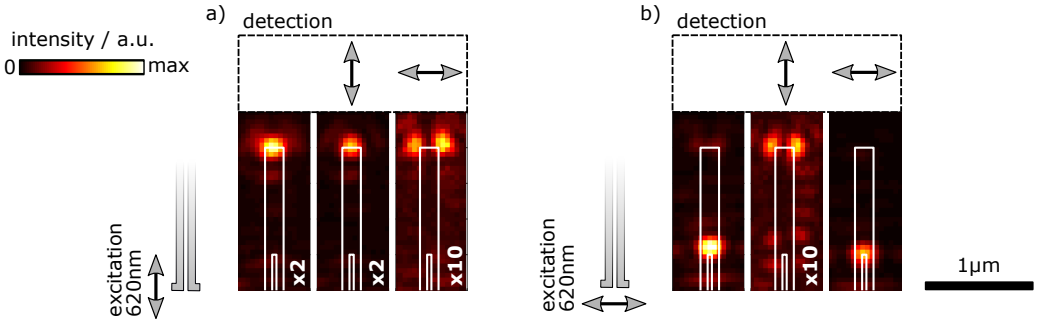

Figure 6.9: (a) Widefield images of the experimental mode detector emission upon 620 nm excitation with (a) parallel and (b) perpendicular polarization on the antenna (c.f. sketch at the left side). In each case, the mode detector is imaged unpolarized (left panel) as well as with a parallel (middle panel) and perpendicular orientation of the detection polarizer (right panel). The relative intensity between the panels is multiplied in some cases by the factor specified at the bottom right side of the respective panel to ensure a visibility of the transmitted signals.

with strong parallel polarization components in the image plane. Weak multi-lobed emission profiles, as observed in the right panel of figure 6.9a, are also familiar for simple dipole fields imaged by a high-NA objective when detected with a polarizer not being oriented parallel to the dipole axis.

A different behavior is observed for perpendicular excitation polarization on the antenna. In this case, the mode detector typically emits mostly at its near end (figure 6.9b, left panel) with a strong perpendicular polarization (figure 6.9b, right panel). In addition, a weaker two-lobed emission profile is observed at the far end of the mode detector for parallel orientation of the detection polarizer (figure 6.9b, middle panel). Full three-dimensional simulations show that this emission at the far end is caused by a finite mode overlap of the propagating two-wire waveguide mode with a higher-order mode of the mode detector (c.f. figure 6.5a). This higher-order mode detector waveguide mode has a different symmetry of charge density (c.f. figure 3.4, HE_1 mode) and electric near-fields (c.f. figure 6.5a, mode detector area) compared to the corresponding fundamental waveguide mode and thus features the different polarization dependency of the emission characteristics described here. Also a pure antisymmetric mode traveling along the two-wire waveguide has a finite mode overlap with this higher-order mode of the mode detector and will qualitatively result in the mode detector radiation characteristics observed in figure 6.9b. However, at 660 nm, only the two two-lobed emission at the far end is observed, while the near end of the mode detector is dark (figure 6.8a, lower row, panel at 660 nm). This behavior cannot be explained by the antisymmetric two-wire waveguide mode only, as a pure antisymmetric mode is radiated in any case also at the near end of the mode detector. According to the simulations in figure 6.4, the higher-order eigenmode of the two-wire transmission line becomes relevant for wavelengths below ~ 700 nm. Thus, the higher-order mode of the two-wire waveguide (c.f. figure 6.3e,f) and its superposition with

the antisymmetric mode needs to be considered in order to explain the experimental observations at lower wavelengths.

Mode interference along the two wires When two propagating modes are coherently launched in the waveguide, a mode interference will result. Both modes ($i = 1, 2$) are characterized by a complex field in a transverse plane $\mathbf{E}^{(i)}(x, y)$, a real part of the effective mode index $n_{eff}^{(i)}$ and a propagation length $l_p^{(i)}$. Their evolution in the direction of propagation z reads as

$$\mathbf{E}^{(i)}(x, y, z) = \mathbf{E}^{(i)}(x, y) \cdot \mathrm{e}^{ik_0 n_{eff}^{(i)} z} \cdot \mathrm{e}^{-z/(2\, l_p^{(i)})} \quad . \tag{6.1}$$

The superposition of both modes leads to an interference pattern along the waveguide with the squared total field magnitude given by

$$\begin{aligned} &|\mathbf{E}^{(1)}(x, y, z) + \mathrm{e}^{i\Delta\phi} \cdot \mathbf{E}^{(2)}(x, y, z)|^2 = \\ &= |\mathbf{E}^{(1)}(x, y)|^2 \cdot \mathrm{e}^{-z/l_p^{(1)}} + |\mathbf{E}^{(2)}(x, y)|^2 \cdot \mathrm{e}^{-z/l_p^{(2)}} \\ &+ 2\mathrm{Re}\left[\mathbf{E}^{(1)}(x, y)\mathbf{E}^{*(2)}(x, y)\right] \cdot \cos\left(k_0\, \Delta n_{eff}\, z - \Delta\phi\right) \cdot \mathrm{e}^{-z/l_m} \quad , \end{aligned} \tag{6.2}$$

using the abbreviation $\Delta n_{eff} = n_{eff}^{(1)} - n_{eff}^{(2)}$ and introducing a possible phase difference $\Delta\phi$ of the modes at $z = 0$. Besides the individual decay of both waveguide modes with their respective propagation length $l_p^{(i)}$, an interference term appears. Notably, the decay-length of the interference term is given by the harmonic mean value l_m of the individual propagation lengths of the two involved modes given by

$$l_m = \frac{2}{\frac{1}{l_p^{(1)}} + \frac{1}{l_p^{(2)}}} \quad . \tag{6.3}$$

As a result of the interference term in equation 6.2, a spatial mode beating pattern of periodicity $\Delta z = \lambda_0 / \Delta n_{eff}$ (λ_0: vacuum operation wavelength) along the propagation direction z results.

Spatial beating between the antisymmetric and higher-order mode The interference of the antisymmetric and higher-order two-wire waveguide mode can be observed in full three-dimensional simulations performed at wavelengths below ~700 nm. A large parameter variation and fitting of the experimental data by such full three-dimensional simulations remains, however, numerically too expensive to be performed here. In the following, a simplified model is presented that calculates the beating pattern of the antisymmetric and higher-order mode of the two-wire waveguide based on the complex modal fields calculated in a transverse plane (c.f. figure 6.3a,e). Both modes are propagated along the waveguide direction according to equation 6.2, in order to deliver the explanation for the experimentally observed transmission behavior at the gap termination (c.f. figure 6.8b, blue dots). In order to keep the model as simple as possible, the following assumptions are made. A fixed $\Delta n_{eff} = n_{eff}^{as} - n_{eff}^{ho}$ between the antisymmetric (as) and higher-order (ho) mode independent of λ_0 is assumed, which is reasonable as both modes appear nearly parallel translated in the

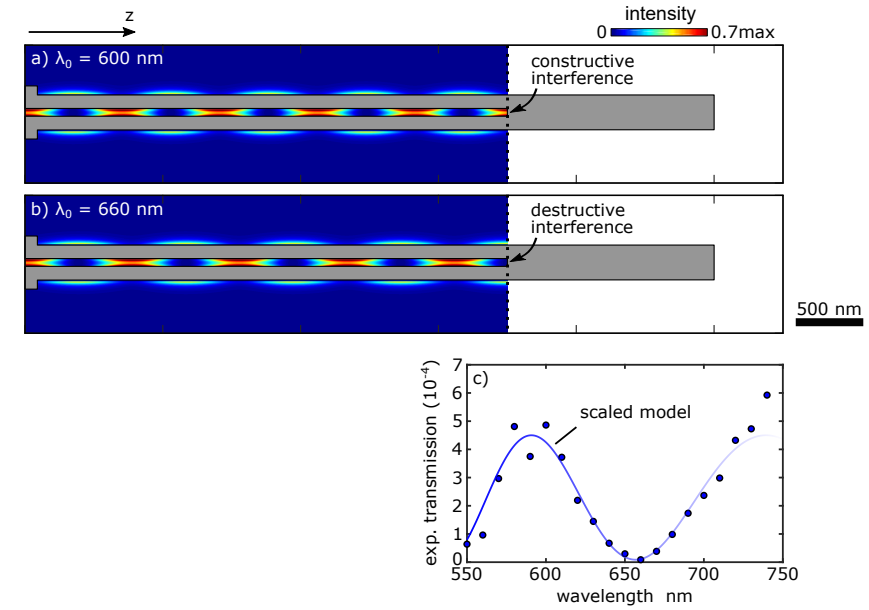

Figure 6.10: Simulated near-field intensity at (a) 600 nm and (b) 660 nm resulting from a superposition of the antisymmetric and higher-order mode along the two-wire waveguide in a plane 20 nm above the substrate. For details about the calculation and assumptions, see text. The waveguide sketch (gray) is overlaid only for the visualization of the gap termination. Back-reflections from such positions are not monitored here. (c) Simulated intensity in a plane 20 nm above the substrate integrated across the 60 nm gap termination as a function of free-space wavelength λ_0 (blue, solid). The calculated intensity is not an absolute quantity and needs to be scaled to the absolute experimental transmission data at the gap termination for perpendicular excitation polarization on the antenna (blue dots, c.f. figure 6.8b) due to the simplified model calculation (c.f. text).

dispersion relation plot (c.f. figure 6.4a). Furthermore, the two eigenmodes are taken as received from the Comsol model[4] and their propagation losses are further neglected. The transverse field profiles are taken at a fixed wavelength of 620 nm, as they hardly change with wavelength.

At $\lambda_0 = 600$ nm, the intensity simulated according to the above-described approach in a plane 20 nm above the glass-air interface displays the beating pattern with a pronounced oscillation of the near-field intensity between inside and outside the gap along the waveguide (figure 6.10a) [197]. This effect is a result of the different field directions inside and outside the gap for the antisymmetric mode compared to the higher-order mode (c.f. figure 6.3a,e), leading to an alternating constructive and destructive interference at these locations. In particular, using a value $\Delta n_{eff} = 0.85$ being close to the simulated difference of the mode indices' real part in figure 6.4a, the intensity after 3.5 µm of propagation is maximum inside the gap at the gap termination due to a constructive interference at this position (figure 6.10a). A change

4 No additional relative phase shift at $z = 0$ is introduced and, in terms of total powers carried by the modes, the higher-order mode carries ~2.9× more power than the antisymmetric mode such that their field strengths are similar within the gap.

of the vacuum operaction wavelength λ_0 leads to a change of the beating periodicity $\lambda_0/\Delta n_{eff}$ and thus the beating pattern is stretched along the two-wire waveguide. As a result, at $\lambda_0 = 660\,\text{nm}$, the beating pattern features a minimum intensity inside the gap at its termination due to a destructive interference at this position (figure 6.10b).

At 600 nm, a strong emission at the gap termination is observed experimentally (c.f. figure 6.8a, lower row). This observation is in line with a beating pattern that features a constructive interference in the gap when it terminates (figure 6.10a), leading to a strong emission at this position. In this case of a constructive interference inside the gap, the mode matching with the mode detector higher-order mode can be suppressed to values below ~1 %, such that no emission is detected at its end. At 660 nm, by contrast, no emission is detected at the gap termination in the experiment (c.f. figure 6.8a, lower row), which is in accordance with a beating pattern that features a destructive interference of the fields at the gap termination (figure 6.10b). In this case, the intensity at the gap termination is rather located at the outer edges of the two wires and the mode matching with the higher-order mode of the mode detector can reach ~94 %. Thus, the light is detected at the far end of the mode detector with the emission characteristics of the mode detector's higher-order mode (c.f. figure 6.9b, middle panel).

Besides these two extreme cases, also the wavelength-dependent evolution of the scattered signal at the gap termination can be estimated by integrating the simulated intensity at the gap termination inside the gap region as a function of λ_0. This simple consideration reproduces the spectral variation of the experimental data detected at the gap termination very well (figure 6.10c). Note that this approach is based solely on waveguide mode interference. The spectral dependency of the neglected efficiencies for the incoupling, propagation and collection of the modes as well as their amplitude-ratio might cancel each other out and contribute to the good match between the simplified calculation and the absolute experimental data in figure 6.10c. For wavelengths above ~ 700 nm deviations are visible because here the higher-order two-wire waveguide mode gets more and more leaky ($n_{eff} < n_{glass}$) and the antisymmetric mode alone dominates the transmission.

In total, the detailed evaluation of the mode detector emission in this section reveals that at wavelengths below ~700 nm, e.g., at 620 nm, a higher-order mode of the two-wire transmission line needs to be considered. In particular, while a parallel polarization at the antenna launches a symmetric mode only, a perpendicular polarization launches a superposition of the antisymmetric and higher-order mode of the two-wire waveguide. The interference of both modes leads to a spatial beating pattern that is stretched along the two-wire transmission line when the vacuum wavelength λ_0 is changed. This effect finally explains the experimental transmission data in figure 6.8b (blue dots).

6.7 NEAR-FIELD COUPLING OF FLUORESCENT NANO-BEADS

As demonstrated in section 6.5, the silver plasmonic nanocircuit allows for selective excitation of the strongly confined plasmonic waveguide modes by a focused laser excitation on the antenna. Furthermore, when bringing fluorescent molecules in the near-field region of the waveguide, a plasmonic decay channel opens up for excited molecules (c.f. section 3.3). As a result, the fluorescence of the locally positioned molecules is not only emitted directly as free-space photons but is also channeled in part into propagating plasmons traveling along the waveguide. In the remainder of this chapter, fluorescent beads (20 nm nominal size, dark red, Thermo Fischer Scientific) are used to study their nanoscale light-matter interaction with the investigated silver plasmonic two-wire transmission line. The dark red molecules inside the polystyrene bead can be excited at 620 nm and emit fluorescence with a maximum at a wavelength of 680 nm. This wavelength range becomes accessible with a waveguide structure fabricated from silver (c.f. figure 6.4b). Note that the beads, i.e., the dye molecules inside, are considered as (nearly) isotropic emitters in the following no matter how they are excited (c.f. section 6.2). The beads are spin-coated from a diluted stock solution (2 % solids stock solution, 1:20.000 dilution in water) onto the silver waveguide sample. To achieve the desired scenario of a single bead attached to the waveguide, a few spin-coating and cleaning cycles are performed. The sample is cleaned by rinsing with acetone and isopropanol, which strongly reduces the fluorescence emission of the sample. At the same time, atomic force microscopy reveals that the polystyrene beads mostly keep attaching to the sample after the cleaning procedure. Polystyrene swells in certain chemicals like acetone and isopropanol and surfaces are cracked [199]. Thus, it is assumed that the dye molecules leak out of the tiny polystyrene bead during cleaning, leaving non-fluorescent polystyrene fragments attached to the substrate.

Exciting a bead via polarization-controlled near-fields To efficiently excite fluorescent molecules in a nanoenvironment, one has to consider the exciting squared electric field at the molecules' position [200]. Exciting the two-wire waveguide with a plane wave incident from the glass side using the numerical model described in subsection 4.1.1, a strong dependency of the total near-fields on the exciting polarization direction is found, similar to the case of single wires [201]. For a polarization perpendicular to the long wire axis, a localized transverse plasmon oscillation is excited in the wires, leading to enhanced near-fields in the gap and at the edges of the two wires where a bead can be located (figure 6.11a). By contrast, a parallel polarization of the plane wave leads to much weaker near-fields in the gap and at the wire edges (figure 6.11b). This effect allows to control the excitation of a tiny 20 nm fluorescent bead that (nearly) behaves like an isotropic emitter ensemble by just changing the incident polarization direction. In the following, a bead coupled to the outer edge of one of the silver wires (called *coupled bead*) is considered together with a bead in about 150 nm distance to the wire (*uncoupled bead*, figure 6.12a). Due to the sub-diffraction-limited distance of both beads, it is not possible to excite only either one of them individually with a far-field laser focus. However, the strong polarization dependence of the excitation near-field at the position of the coupled bead (c.f. figure 6.11a,b) allows to modulate the excitation

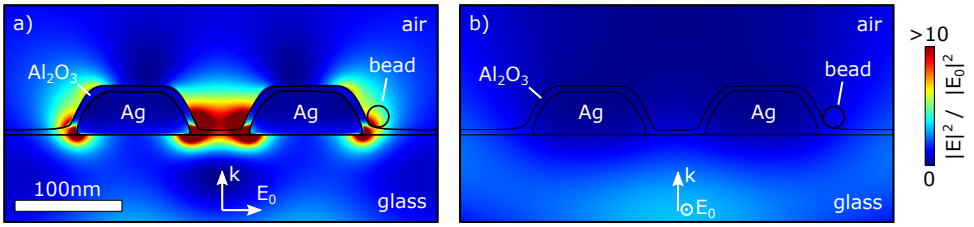

Figure 6.11: Simulated local squared total near-field magnitude $|E|^2$ at the two-wire waveguide upon plane wave excitation with amplitude E_0 incident from the glass side ($\alpha = 0°$, c.f. k-vector) with (a) perpendicular and (b) parallel polarization with respect to the waveguide axis. The simulation is performed at a vacuum wavelength of 620 nm.

of the coupled bead by rotating the incident polarization of the exciting laser focus. For a parallel polarization of the laser excitation, the coupled bead features a weaker fluorescence emission than the uncoupled bead (figure 6.12b, top). A rotation of the excitation polarization to the perpendicular direction results in a stronger emission from the coupled bead. Furthermore, a clear emission from the antenna and both mode detector positions can be observed (figure 6.12b, bottom), indicating the emission of propagating plasmons by the coupled bead that are partly converted to free-space photons at the waveguide ends.

Simulation of dipole emission To support the interpretation of the waveguide signals originating from the coupled bead's fluorescence, a three-dimensional simulation of electric dipoles (c.f. subsection 4.1.5) at the position of the coupled bead (10 nm above substrate, 10 nm next to wire) is performed. Subsequent far-field imaging simulations (c.f. section 4.2, $\lambda = 680$ nm, $NA = 1.35$) are performed for three orthogonal dipole orientations (x-,y- and z-direction) and superimposed incoherently to simulate an isotropic emitter ensemble modeling the bead (figure 6.12c). The ratio of the simulated emission spot intensities at the bead, antenna and mode detector agrees well with the experiment for the dipole emitter position chosen in figure 6.12c. Thus, the detected fluorescence intensity at the waveguide ends is consistent with local emission at the coupled bead's position. By changing the position of the emitters along the waveguide in the simulation, the detected spot intensities at the waveguide ends calculated with far-field imaging can vary. This effect is mainly caused by a position-dependent local density of optical states along the waveguide due to the presence of back-reflections within the finite-length waveguide.

Signatures of spatial mode beating The mode detector spatially separates the contributions of the fundamental symmetric and antisymmetric two-wire waveguide modes. Similar intensity levels are detected at the near and far end of the mode detector (figure 6.12b, bottom), demonstrating that both modes are excited by the bead. The higher-order mode can be neglected for the main discussion of fluorescence emission, as the wavelength range of the fluorescence emission (~650-800 nm, c.f. figure 6.13) is dominated by the two fundamental modes (c.f. figure 6.4). Furthermore, it is evident

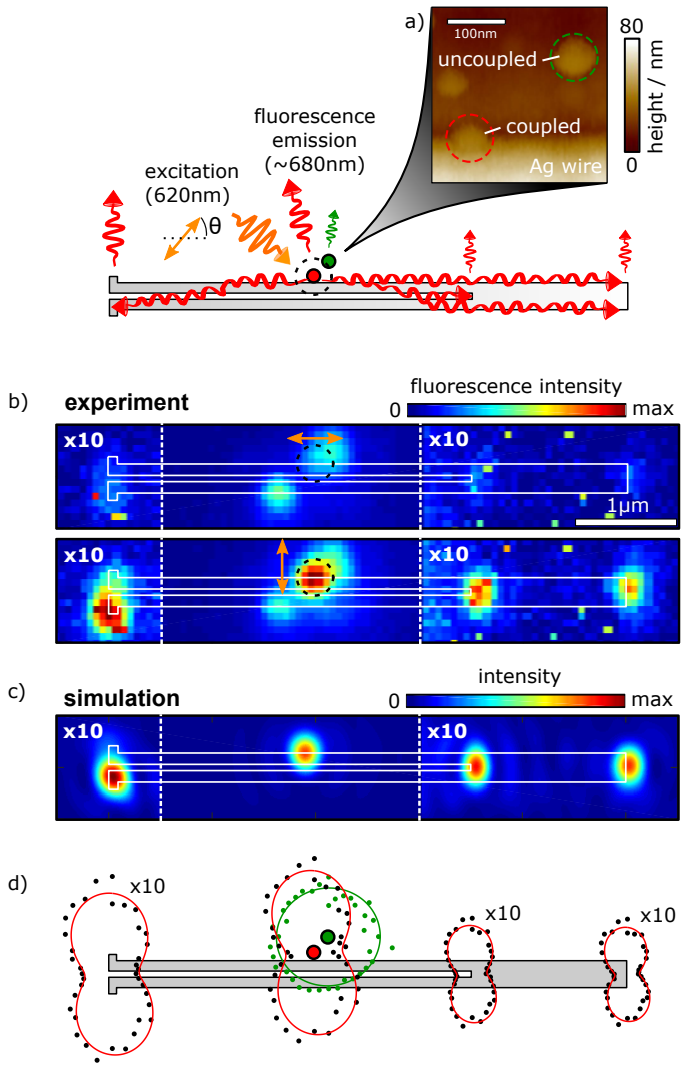

Figure 6.12: (a) Atomic force micrograph displaying the topography of one of the Ag wires, one bead directly attached to the wire (coupled bead) and another bead located about 150 nm next to the wire (uncoupled bead). The third topography feature does not show fluorescence emission and is most likely a polystyrene remainder from previous cleaning procedures. The sketch indicates the position of the beads along the waveguide. (b) Fluorescence widefield images detected upon directly exciting at the beads' position (dashed circle) with a parallel (orange arrow, top) and perpendicular polarization (bottom). The intensity in the antenna and mode detector area is enhanced by a factor of 10. (c) Far-field imaging simulation ($\lambda = 680\,\text{nm}$, $NA = 1.35$) of a radiating isotropic electric dipole ensemble at the position of the coupled bead. (d) Polar plots of the emission intensity of the coupled and uncoupled bead, as well as the antenna and mode detector positions (multiplied by a factor of 10), as a function of the exciting laser polarization angle θ defined in the sketch in panel (a). The emission of both beads is separated by fitting a sum of two Gaussian functions with fixed yet different positions. The solid lines represent a fit of a squared cosine function with a certain phase and offset (red: coupled bead, green: uncoupled bead).

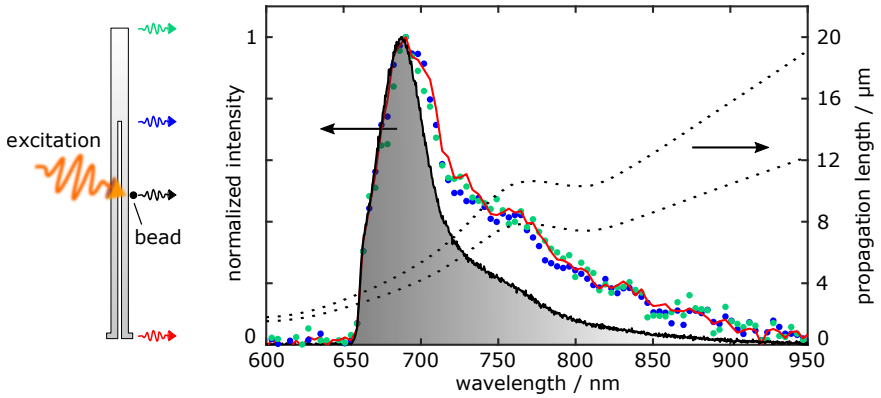

Figure 6.13: Normalized fluorescence emission spectra of a coupled bead with dark red molecules excited at 620 nm. The emission is detected at the position of the bead (solid black line), at the antenna (solid red line), as well as at the near (blue dots) and far end (green dots) of the mode detector (c.f. sketch at the left side). The spectra at the latter three positions are software-binned to reduce the relative noise. Compared to the bead's direct far field emission, the red tail of the normalized guided emission is raised due to longer propagation lengths for both the symmetric and antisymmetric modes toward the near-infrared region (dotted black line).

that the emission spot at the antenna is not centered between the two antenna arms but is shifted toward the lower antenna arm in the experiment (figure 6.12b, bottom) as well as in the simulation (figure 6.12c). This effect is caused by a coherent excitation of both fundamental waveguide modes, i.e., symmetric and antisymmetric mode, by the emitters. In analogy to section 6.6, a coherent superposition of the symmetric and antisymmetric waveguide mode will result in a spatial beating pattern along the waveguide where the intensity oscillates between both nanowires (c.f. figure A.2a,b in appendix A) with a periodicity $\Delta z = \lambda_0/\Delta n_{eff} \approx 3\,\mu$m at ~700 nm. The bead is located about half of this beating length away from the antenna along the two-wire waveguide. Thus, during propagation, the near-field intensity oscillates from the top wire where the bead is located and acts as local source toward the lower nanowire, leading to a detected emission shifted to the lower antenna arm.

Separating the impact of both beads The emission intensities of the coupled and uncoupled bead are separated by fitting a sum of two two-dimensional Gaussian functions with fixed yet different positions to the fluorescence images, which are taken in 10° steps of the exciting laser polarization angle θ. It is found that the coupled bead emission intensity, which is given by integrating the corresponding fitted Gaussian function, is strongly modulated by the excitation polarization, while the uncoupled bead shows an intensity independent of the exciting polarization (figure 6.12d). This behavior is consistent with the polarization-dependent near-field at the two-wire waveguide exciting the bead (figure 6.11a,b). The detected intensity at the antenna and both mode detector positions are evaluated by integration of a ~600 nm square area centered at the respective position corrected by a background evaluated in a neighboring area. These emission features at the waveguide ends are strongest for a

perpendicular excitation polarization and follow the polarization-dependent trend of the coupled bead. This finding justifies the assignment of one bead as coupled, while the second one is considered uncoupled to the waveguide as a result of its location outside the near-field of the waveguide [98].

Impact of propagation on the emission spectrum The emission spectrum of a dark red bead detected at the waveguide ends experiences a relative rise of the red tail of the spectrum compared to the direct far-field emission spectrum of the bead (figure 6.13). This effect is mainly caused by the increasing propagation length of the waveguide modes toward the infrared regime, i.e., the spectrum detected at waveguide ends is altered by the dispersive propagation efficiency. For increasing propagation distance, an effective overall red-shift of the spectrum would result, as demonstrated by Shegai *et al.* [202] for single nanowires.

6.8 REMOTE EXCITATION OF MOLECULAR FLUORESCENCE

In the last section, it is demonstrated that only the bead directly attached to the silver wire couples with the propagating near-fields of the two-wire waveguide. Although the excitation of the coupled bead can be modulated by the excitation polarization of a laser focus, at all time, a second bead (uncoupled bead) in a sub-diffraction-limited distance is excited too. This might be unfavorable in some cases, as the emission patterns of the two beads overlap in far-field images and fitting procedures are required to separate their direct far-field emission. An appealing solution to this issue is to excite the fluorophores not via a diffraction-limited laser spot but remotely via the sub-diffraction-limited waveguide modes. For the very same silver nanostructure and bead-configuration investigated already in figure 6.12, thus a selective excitation of the coupled bead only can be achieved, as demonstrated in this section.

First, the transmission of the excitation light (620 nm) through the silver circuit is investigated for a varying incident polarization direction. The laser focus is moved to the antenna and the transmitted signals at both mode detector positions are recorded as a function of the incident polarization angle θ on the antenna (figure 6.14). These measurements demand for a precise and stable position of the laser focus centered to the antenna during polarization rotation. The mode detector separates the contributions of the propagating modes by far-field emission at its near and far end. For a parallel polarization at the antenna, the symmetric mode is launched and the mode detector emits mostly at its far end. By contrast, for a perpendicular polarization, the antisymmetric mode beating with the higher-order mode is launched and is detected mostly at the inner end of the mode detector with an intensity similar to the case of parallel polarized excitation. Hence, both the symmetric mode and the antisymmetric mode beating with the higher-order mode are transmitted through the circuit with equal efficiency. This fact allows to launch different coherent superpositions of the waveguide modes with a varying amplitude ratio by applying different excitation

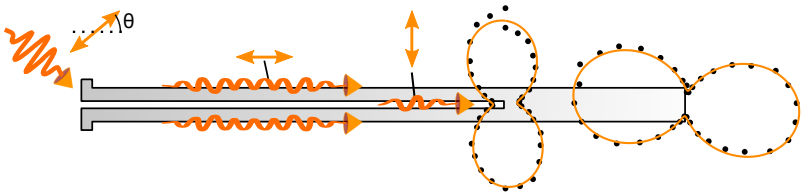

Figure 6.14: Experimental transmission of 620 nm laser light through the waveguide circuit with a focus of varying polarization angles θ centered on the antenna (c.f. sketch). The relative transmitted intensity detected at the near and far end of the mode detector is shown as dots in polar plots centered to respective position. The solid lines represent a fit of a squared cosine function with a certain phase and offset.

polarization angles θ on the antenna. For angles θ between 0° and 90°, all three modes are coherently superimposed along the waveguide.

Remote excitation of fluorescence In a second step, the scattered excitation laser light is blocked by the dielectric longpass filter (c.f. section 6.2) to record fluorescence images upon remote excitation via the antenna. For a nearly parallel excitation polarization on the antenna, launching mostly the symmetric mode traveling at the outer edges of the wires, only a single fluorescence spot appears at the position of the coupled bead (figure 6.15a, top). Additionally, at both mode detector positions nearly equally strong intensities are detected. Rotating the excitation polarization on the antenna by 90° to the nearly perpendicular direction, mostly the antisymmetric mode (beating with the higher-order mode) is launched, as demonstrated before by the mode detector signals at the laser wavelength (figure 6.14). However, in this case, nearly no fluorescence signal is detected at both the coupled bead position and the mode detector positions (figure 6.15a, bottom).

To gain a deeper understanding of this effect, the excitation polarization angle θ is rotated in 10° steps on the antenna while recording fluorescence images at each step. The intensities of the coupled bead, as well as the mode detector positions, are evaluated in a square area of about 600 nm in size centered to the respective position, subtracted by a background in a neighboring area in each case. It is found that the emission intensity of the coupled bead is modulated with high contrast, with the best excitation polarization direction tilted by about -30° with respect to the parallel direction (figure 6.15b). The detected intensities at both mode detector positions as a function of θ feature a similar trend as the intensity detected at the coupled bead position. Furthermore, the relative intensity between the different spots is similar to the case of direct excitation of the bead (c.f. figure 6.12b, bottom). This observation demonstrates that the remotely detected intensities at the mode detector originate again mainly from the emission of plasmonic modes by the coupled bead. The tilted angle θ of maximum remote excitation of the coupled bead demonstrates that a pure antisymmetric mode (beating with the higher-order mode) which is rather confined to the gap cannot efficiently excite the bead attached to the specific position at the outer edge of a wire. Even a pure symmetric mode leads not to the strongest excitation of the coupled bead, although this mode travels mostly at the outer edges of both

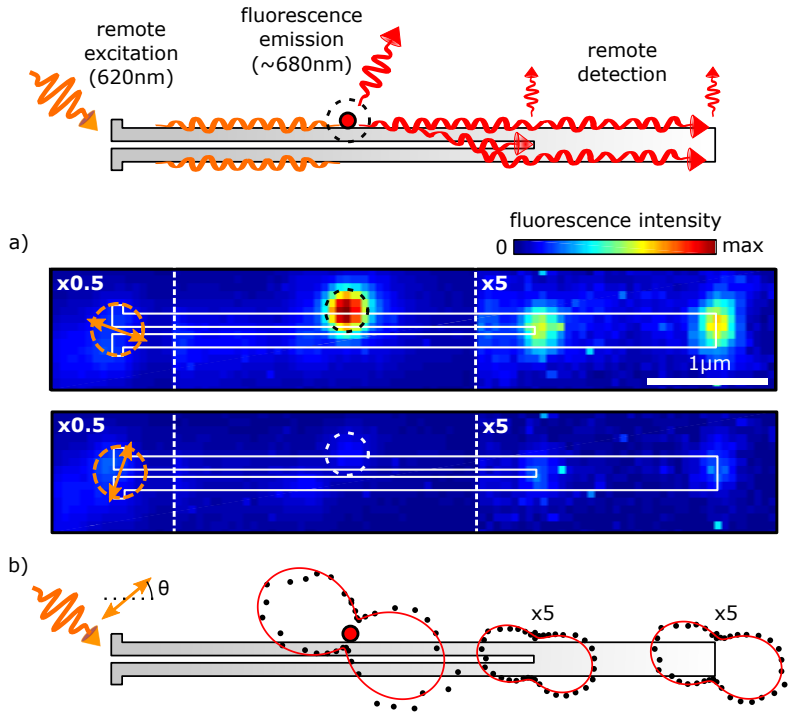

Figure 6.15: (a) Widefield fluorescence images of the coupled bead at the circuit upon 620 nm excitation at the optical antenna with nearly parallel (orange arrow, top) and nearly perpendicular polarization direction (bottom). The sketch above visualizes the experimental configuration of the plasmonic circuit and the position of the coupled bead (red dot) marked by a dashed circle (b) Relative fluorescence emission intensity (black dots) at the coupled bead's position and both mode detector positions (multiplied by a factor of 5) shown as polar plots for varying polarization angles θ. The solid lines represent a fit of a squared cosine function with a certain phase and offset.

wires. It is rather a coherent superposition of the symmetric mode with the other available waveguide modes that leads to a constructive interference of the electric near-fields at a specific side of the two wires at the position of the coupled bead. The beating patterns between all three involved waveguide modes along the two wires are rather complex (c.f. figure A.2d in appendix A). As a result, the angle θ of best remote excitation strongly depends on the position of the emitter bead along the waveguide as well as on the specific phase differences between the launched modes.

Deducing the coupling efficiency The coupling efficiency of the bead's emission into the waveguide modes can be estimated from a widefield fluorescence image. Within figure 6.15a (top panel), the relative intensities at the near and far end of the mode detector are about $I_{as} = 11\,\%$ and $I_s = 13\,\%$ compared to the direct far-field emission of the coupled bead. In case of the waveguided signal, one has to consider that only about $\eta^s_{col} = 25\,\%$ and $\eta^{as}_{col} = 20\,\%$ of the fundamental symmetric and anti-symmetric mode's power is collected by the mode detector far-field emission with the objective (c.f. figure 6.6c). Additionally, the propagation efficiency for propagating the

distance $l \approx 1.7\,\mu m$ from bead to mode detector in the symmetric and antisymmetric plasmonic modes of propagation length $l_p^s = 4.1\,\mu m$ and $l_p^{as} = 3.4\,\mu m$ (evaluated at 680 nm, c.f. figure 6.4b), respectively, need to be taken into account. Both waveguide directions are treated equally[5], leading to an additional factor of 2. The direct far-field emission channel of the bead is collected with about $\eta_{col}^{ff} = 50\,\%$ efficiency with the objective's numerical aperture, which is calculated based on a simulated dipole emission from the position 10 nm above a glass-air interface without waveguide. In total, the ratio of the emission rate into the plasmonic waveguide modes k_{wg} to the sum of k_{wg} and the direct far-field emission rate k_{ff} is calculated by

$$\eta_c = \frac{k_{wg}}{k_{ff} + k_{wg}} = \frac{2\left[I_{as}\frac{\exp(l/l_p^{as})}{\eta_{col}^{as}} + I_s\frac{\exp(l/l_p^{s})}{\eta_{col}^{s}}\right]}{\frac{1}{\eta_{col}^{ff}} + 2\left[I_{as}\frac{\exp(l/l_p^{as})}{\eta_{col}^{as}} + I_s\frac{\exp(l/l_p^{s})}{\eta_{col}^{s}}\right]} \quad . \tag{6.4}$$

This calculation leads to an estimation of about $\eta_c \approx 63\,\%$ using the numbers listed above. This means that the majority of the coupled bead's fluorescence emission is channeled into the propagating plasmonic modes of the silver two-wire waveguide. In the literature, Kumar *et al.* [203] suggest that the η_c-values determined as described above can be used as an experimental estimate of the β-factor (c.f. section 3.3), neglecting the nonradiative decay channels. The value of 63 % is larger compared to values observed by Kumar *et al.* for emitters placed in a plasmonic V-groove waveguide with typical values around 30 % [204] and is close to recent experimental values obtained for emitters placed in strongly confined plasmonic modes [179, 203]. Note that the consideration of reduced propagation lengths in the experiment instead of the simulated values used above, e.g., considering $l_p^{s/as} \approx 2\,\mu m$ estimated for the similar circuit investigated in chapter 7 (c.f. appendix C), leads to estimated values above $\eta_c = 70\,\%$.

6.9 CONCLUSION AND OUTLOOK

In conclusion, this chapter demonstrates the first visible wavelength multi-mode operation of a plasmonic nanocircuit fabricated from a single-crystalline silver flake by focused ion beam milling. The long-term chemical stability of the silver nanostructure for the optical studies is achieved by a 5 nm Al_2O_3 layer deposited by atomic layer deposition. Both the symmetric and antisymmetric waveguide mode of the two-wire transmission line can be excited selectively by a laser excitation with a linear polarization direction on the antenna and can be detected *in situ* via the mode detector. The transmission of visible light through the circuit, by focused laser excitation on the antenna and far-field detection at the mode detector, is investigated in a broad wavelength range from 550 nm to 740 nm, which now becomes accessible due to the superior optical properties of silver compared to the traditionally employed gold. For wavelengths below ~ 700 nm, it is demonstrated by a detailed evaluation of the mode

5 The antenna emission is not evaluated here because this position is directly excited with the laser focus and contains background emission of a different uncoupled close-by bead.

detector emission after perpendicular excitation on the antenna that a higher-order mode appears and interferes with the antisymmetric mode while propagating along the two-wire transmission line.

Furthermore, the coupling of tiny, ~ 20 nm -sized polystyrene beads doped with a few tens of dark red fluorophores to the silver nanocircuit is studied. It is demonstrated that a bead directly attached to the waveguide structure can couple with the waveguide modes, while a bead located in a sub-diffraction-limited distance to the waveguide does not couple. In particular, the remote excitation of the coupled bead by waveguide modes is studied. Here, a specific coherent superposition of the waveguide modes leads to a constructive interference of the modes at the specific position of the bead, resulting in a maximum excitation and fluorescence signal of the bead. Notably, using the remote excitation technique, the bead in a sub-diffraction-limited distance to the waveguide is not excited and only the bead at the waveguide surface is excited. Furthermore, the emission rate of the coupled bead into the waveguide is found to be higher than its direct far-field emission rate, demonstrating a very efficient channeling of the fluorescence emission into the waveguide. This additional strong decay channel into plasmonic modes available for the emitter molecules also leads to a strong reduction of their excited state lifetime, which is investigated in more detail in chapter 7 for the case of single molecules located within the tiny nanogap between two silver nanowires.

In total, the operation of complex-shaped, top-down fabricated plasmonic waveguides from single-crystalline silver demonstrated in this chapter is very promising for studying the nanoscale light-matter interaction with quantum emitters. In particular, the use of single-crystalline silver lowers the propagation loss compared to gold and opens up the visible spectral range for plasmonic waveguide circuitry where a large variety of high fluorescence quantum yield dye molecules are available. The fabrication by focused ion beam milling from a silver flake allows designed and engineered nanostructures to be produced, which support sophisticated sub-diffraction-limited near-fields that can be externally controlled and shaped. Especially, further quantum plasmonic experiments with single emitters are promising in terms of possible future applications in quantum information technology ranging from single-plasmon sources to single-plasmon transistors. Experiments with single molecules as quantum emitters are subject to the next chapter 7.

7 SINGLE-MOLECULE NONLINEARITY IN A PLASMONIC WAVEGUIDE

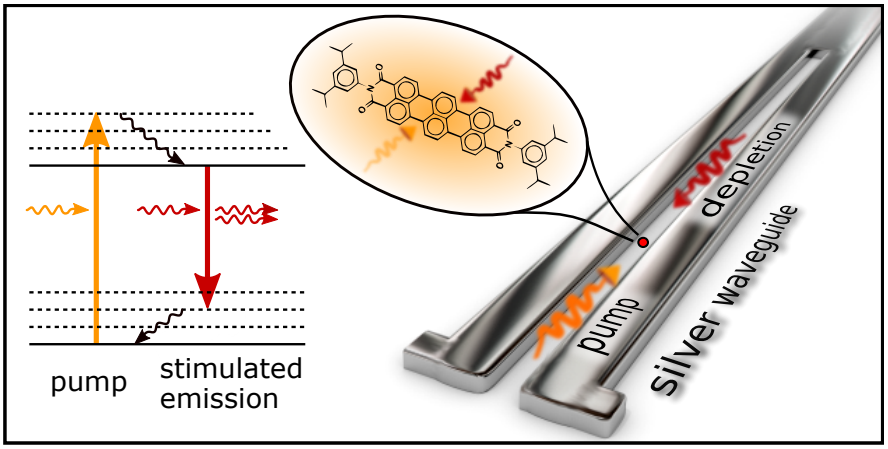

The above image and parts of this chapter are published in *Single molecule nonlinearity in a plasmonic waveguide* by C. Schörner, and M. Lippitz, Nano Letters **20**, 3, 2152–2156 (2020). Figure adaptations with permission. Copyright 2020 American Chemical Society.

7.1 INTRODUCTION

This chapter is thematically connected to chapter 6 and considers further advanced experiments with single fluorescent molecules located inside the nanogap of a silver plasmonic two-wire transmission line. In the literature, it is well established that placing single quantum emitters in the near-field of a confined plasmonic mode typically leads to a strongly increased emission rate caused by the Purcell effect [21, 205]. For certain waveguide–emitter geometries such as two parallel silver nanowires [178] or a nanowire close to a metal surface [179, 203] investigated by Kumar *et al.*, the emission into propagating modes overwhelms all other nonradiative and radiative decay channels, leading to an emitter–waveguide coupling efficiency β (c.f. section 3.3) close to unity. It is important to note that the strong dephasing processes taking place in quantum emitters at room temperature (c.f. sections 2.4 and 2.5) do not diminish this coupling efficiency of the emission, as waveguide modes are broadband in wavelength and can capture the whole homogeneously broadened linewidth of the emission. Due to the high values of β, it is straightforward to quantify the amount of the quantum emitter's spontaneous emission that is emitted into waveguide modes

at room temperature, as also performed in section 6.8. This efficient channeling of the spontaneous emission of a quantum emitter into propagating plasmonic modes is therefore subject of many previous studies [98, 101, 177–179, 186, 191, 203, 206–208].

By contrast, the linear (and nonlinear) coherent interaction of light with single quantum emitters such as single molecules is, according to the discussion in section 2.5, strongly diminished at room temperature compared to cryogenic temperatures. Thus, the coherent transmission or reflection of a waveguide mode at an embedded quantum emitter has been investigated only at low-temperatures so far, e.g., by the Sandoghdar group [209–211] with diffraction-limited waveguide modes of dielectric nanoguides. In comparison to dielectric waveguides, the deep subwavelength confinement in plasmonic waveguides offers an increased interaction with quantum emitters and opens up a perspective to push such experiments toward room temperature. In particular, the efficient, coherent interaction of a quantum emitter with multiple plasmonic fields in a waveguide circuit is an important goal of current research in order to realize devices such as the single-photon transistor on a plasmonic platform envisioned by Chang *et al.* [31].

This chapter presents an important step into this direction by demonstrating for the first time an interaction of a single quantum emitter with a sequence of two plasmonic pulses in a waveguide circuit. To address this issue, individual terrylene diimide (TDI) molecules are placed in the nanogap between two nanowires of a single-crystalline silver nanocircuit. A visible wavelength pump pulse and a red-shifted depletion pulse propagate along the waveguide-gap, leading to stimulated emission depletion (STED) in the observed fluorescence of the molecule. Stimulated emission [212], as a result of the interaction with two photons, is a nonlinear optical effect, just like two-photon absorption [213] and pump-probe spectroscopy in general. Due to the sub-diffraction-limited mode confinement of the plasmonic waveguide mode, the efficiency of triggering the stimulated emission transition raises by about 30 times in the waveguide compared to the case of a diffraction-limited far-field focus. The experiments thus demonstrate an efficient nonlinear plasmon-plasmon interaction at a single molecule and should pave a perspective for functional quantum plasmonic circuits as well as improved nonlinear single-molecule spectroscopy.

7.2 EXPERIMENTAL SETUP

To perform the experiments considered in this chapter, an optical setup was designed and built up from scratch. A simplified sketch, neglecting several elements like lens-pairs and additional mirrors, is shown in figure 7.1. The laser source is a supercontinuum white light laser (SuperK EXTREME EXR-15, NKT Photonics) equipped with a tunable single-line filter (SuperK Varia, NKT Photonics), defining the output spectrum to the range 610-770 nm. The optical pulses have a temporal length of a few ten picoseconds [214], while the repetition rate is fixed to 1.953 MHz (adjustable

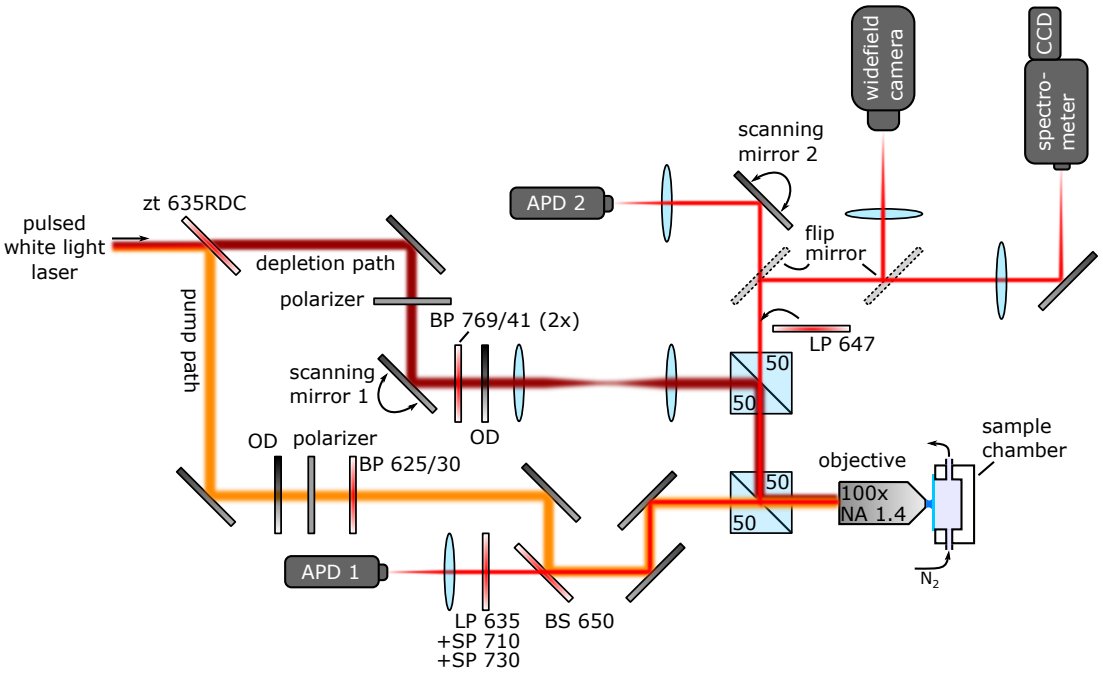

Figure 7.1: Simplified sketch of the experimental setup used in this chapter (explanation see text). The pump and depletion path are sketched in orange and dark red, respectively, while the detection paths are displayed in bright red.

up to 78 MHz). The output spectrum is split into a shorter and longer wavelength range by a dichroic beamsplitter (zt 635RDC, AHF Analysentechnik), defining two excitation paths called *pump* and *depletion path*, respectively. Bandpass filters in the pump (BP 625/30, AHF Analysentechnik) and depletion path (2× BP 769/41, AHF Analysentechnik) define the final spectral ranges of both light paths. The pulse-to-pulse intensity variation of the laser pump and depletion pulses, as well as the correlation between both of them, is determined in appendix B. Optionally, a linear polarizer (LPVIS100-MP and WP25M, Thorlabs) can be inserted in each of the two paths. The pump and depletion paths are superimposed by two 50:50 beamsplitters (BS016 and BS013, Thorlabs) in front of the oil immersion objective (UPlanSApo, 100×, $NA = 1.4$, Olympus). A sample can be positioned precisely relative to the objective by three linear stages and a 3-axes piezo positioner (TRITOR 100SG with NV40/3 CLE controller, Piezosystem Jena). A small attached sample chamber can be flushed with N_2 gas to reduce photobleaching of the used fluorescent molecules [215]. A piezo mirror platform (scanning mirror 1, S-334.2SL, Physik Instrumente) equipped with a piezo controller (E-501.00, Physik Instrumente), followed by a 4f-system consisting of two lenses (250 mm and 300 mm focal length), allows to scan the depletion pulse focus in the sample plane. The optical powers of both light paths can be adjusted by variable optical density (OD) wheels. Two mechanical shutters can block both the pump and depletion pulse pathway, respectively.

The setup offers different detection pathways and detectors. The reflected and scattered laser light, as well as possible emission of the sample, is collected by the same

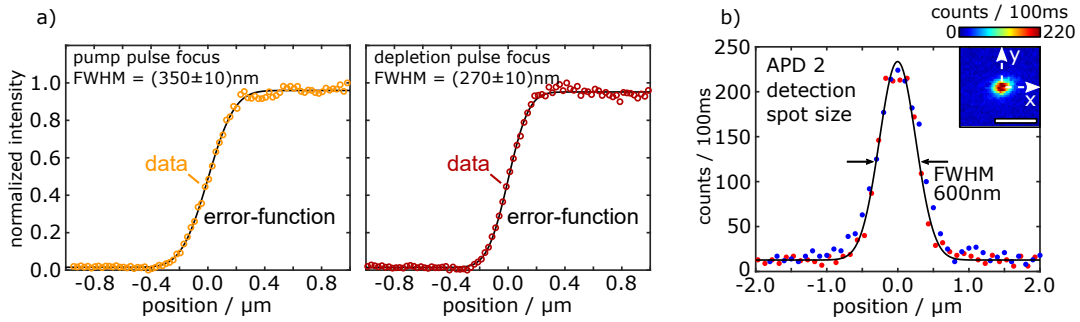

Figure 7.2: (a) Spot size of the pump (left) and depletion focus (right) in the sample plane measured by scanning a silver flake's edge in a direction perpendicular to the edge across each laser focus while recording the reflected intensity. The (normalized) experimental data is averaged over 5 consecutive scans (colored circles), while the fit of an error-function is shown as solid black line. A polarization parallel to the flake edge is used to avoid the excitation of surface plasmons. The full width at half maximum (FWHM) of the foci is calculated from the width of the error-function. (b) Detection spot size of APD 2 in the sample plane recorded by scanning the detection spot across a single fluorescent terrylene diimide molecule with scanning mirror 2 (inset, scale bar is 2 µm in the sample plane). Blue and red dots show the intensity-profile across the center maximum along the x- and y-direction, respectively. The black line is a Gaussian fit to the red dots (FWHM $\approx$ 600 nm).

objective, can pass the 50:50 beamsplitter, the dichroic beamsplitter inserted in the pump path (HC BS650, AHF Analysentechnik), a dielectric longpass (LP 635, AHF Analysentechnik), optional dielectric shortpass filters (SP710, SP730) and is finally focused to an avalanche photodiode (APD 1) via a 150 mm tube lens. As a result of the passed dielectric filters, the pump and depletion wavelengths are blocked and only the fluorescence of the sample is detected by APD 1. Furthermore, the collected light is also reflected by the first 50:50 beamsplitter behind the objective, is transmitted by the second beamsplitter, is reflected by scanning mirror 2 (PSH 25, Piezosystem Jena) equipped with a piezo controller (d-Drive, Piezosystem Jena) and is focused to APD 2 via a tube lens (150 mm focal length). Here, a longpass filter (LP647, AHF Analysentechnik) can optionally be flipped in the light path to block the pump wavelength and only detect the red-shifted emission of the sample with APD 2. The spot on the sample detected with APD 2 can be scanned via scanning mirror 2. Alternatively to APD 2, the collected light can be guided with flip mirrors toward an sCMOS camera (Zyla 4.2, Andor, tube lens 200 mm) used for widefield imaging of both scattered laser light and fluorescence emission of the sample in case the longpass LP 647 is flipped in the detection path. As a further option, the collected light can be guided to a spectrometer (Isoplane 160 with ProEM EMCCD camera, Princeton Instruments). Spatially resolved emission spectra can be recorded along the direction defined by the entrance slit. Time-correlated single photon counting (TCSPC) is performed with a multichannel picosecond event timer (Hydraharp 400, Picoquant) and the APDs. TCSPC also allows to monitor the time-delay between the pump and depletion pulses reflected from the sample. The delay is defined via the path length

difference of both light paths toward the objective, which is adjusted manually via the position of additional mirrors.

The point-spread function of the optical system toward the widefield imaging camera is very similar to the setup described in section 6.2 of chapter 6 due to both a similar numerical aperture of the objective and a similar total magnification. The spot sizes of the pump and depletion pulse foci are determined by scanning a sharp edge of a silver flake in a direction perpendicular to the edge across the laser focus while recording the reflected intensity with APD 1. For the pump pulse focus, an almost diffraction-limited full width at half maximum (FWHM) of 350 nm is determined, while the depletion pulse focus is diffraction-limited with FWHM = 270 nm (figure 7.2a). The difference in FWHM of both foci is explained by a changed wavelength and different filling factors of the back-aperture of the objective [55]. Both APDs have an active sensing area diameter of 50 µm. Together with the 83× magnification of the optical imaging system toward each APD, this yields a detection spot size of about 600 nm diameter in the sample plane, which is verified by scanning the detection spot across a single fluorescent molecule (figure 7.2b).

All pulse energies in this chapter are given in the focal plane of the objective, with typical pump pulse energies of about 0.1-1 pJ. In all camera images, a mean background is subtracted.

7.3 SINGLE MOLECULES AS SINGLE-PHOTON SOURCES

For the experiments in this chapter, the organic dye molecule terrylene diimide [216] (TDI, KU dyes ApS, Copenhagen) is used (c.f. figure 7.5b, inset). TDI is known to be extremely photostable in different polymer matrices, such as poly(methyl methacrylate) (PMMA), especially when flushing the sample with nitrogen [215]. For sample fabrication, TDI is dissolved in a PMMA resist (ARP671.015, Allresist) and diluted to the desired concentration, i.e., to about 10^{-6} to 10^{-4} M for ensemble samples and to $< 10^{-9}$ M for single-molecule samples. Subsequently, the TDI-doped resist is spin coated to a cleaned substrate, resulting in a film thickness of about 60 nm at 4000 rotations per minute spin coating speed [217]. TDI can be excited by the pump pulses and emits fluorescence in the range 650-800 nm (c.f. figure 7.5b), which is fully detected in this section (no additional dielectric shortpass filters are used). For single-molecule experiments, the sample chamber is flushed with nitrogen.

In a raster-scanned fluorescence intensity map of a TDI sample with single-molecule concentration recorded with APD 1, separated emission spots appear (figure 7.3a). The full width at half maximum of each spot FWHM $\approx$ 370 nm is determined mainly by the exciting pump pulse focal intensity distribution, as the 50µm active area diameter of the APD acts as a rather large pinhole and does not further spatially filter the point-spread function of the emission originating from the excitation focus. Thus, the

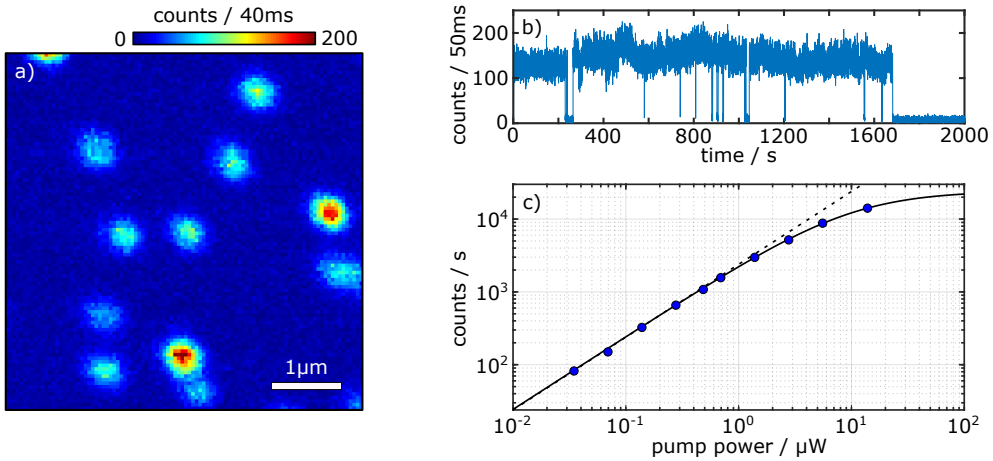

Figure 7.3: (a) Raster-scanned fluorescence intensity map of isolated terrylene diimide (TDI) molecules in a ~60 nm thick PMMA film detected with APD 1. (b) Exemplary time trace of the fluorescence of a single TDI molecule. (c) Experimental saturation curve of a single TDI molecule (blue circles). A fit of a saturation model (solid black line, c.f. text) and a linear approximation (dashed line) is superimposed.

observed FWHM agrees well with the pump focus spot size (c.f. figure 7.2a, left). In a fluorescence time trace at the position of a bright spot, a constant emission rate is detected that rarely yet abruptly falls down to the background level for a short period of time (figure 7.3b). At some specific time (at 1682 s in figure 7.3b), an irreversible drop of the detected count rate to the background level is detected. These features, called *blinking* and *single-step photobleaching* events, are characteristic of single fluorescent molecules [215]. Despite the unpolarized pump pulses used here, the detected fluorescence intensity varies from molecule to molecule. This effect is mainly related to the expected isotropic orientation of the TDI molecules in the thin PMMA film, including a possible out-of-plane orientation that lowers the excitation (and detection) probability [218].

Saturating the single-molecule optical absorption The detected emission rate γ_{fl} of a single TDI molecule as a function of the pump power P_{pump} is initially linear but saturates for higher pump powers (figure 7.3c) following a saturation function for the detected fluorescence count rate given by [208, 218]

$$\gamma_{fl} = \frac{\gamma_\infty}{1 + \frac{P_s}{P_{pump}}} \quad . \tag{7.1}$$

A fit to the experimental data yields the asymptotic detection rate at high pump power $\gamma_\infty \approx 24 \cdot 10^3 \frac{\text{counts}}{\text{s}}$ and the saturating power $P_s \approx 10\,\mu\text{W}$, with both varying from molecule to molecule due to their different orientations [218]. From such saturation curves, optical cross-sections can be determined, as mentioned by Kastrup *et al.* [59], which is demonstrated for the stimulated emission transition in section 7.4. Here, the observed saturation of the fluorescence emission results from the saturation of the single molecule's optical absorption transition.

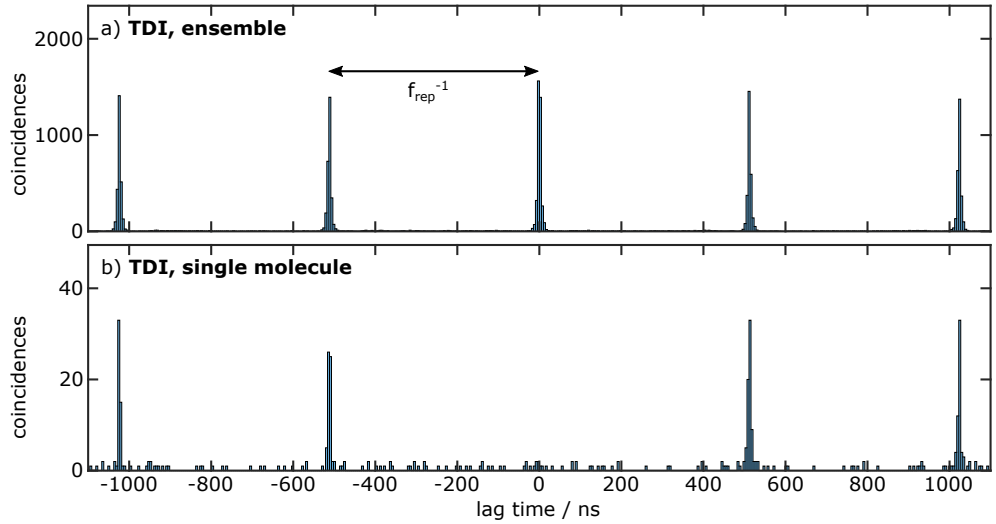

Figure 7.4: Coincidences of the counts of APD 1 and APD 2 when recording the fluorescence of (a) a TDI ensemble and (b) a single TDI molecule. The lack of coincidences at zero lag time for the single molecule, i.e., photon antibunching, demonstrates the single-photon emission character of a single TDI.

Photon antibunching The most striking feature of single molecules is their single-photon emission character, which follows from the fact that a single quantum emitter typically emits a single photon at each excitation-emission cycle. This effect can be experimentally demonstrated by detecting the sample fluorescence with two APDs (c.f. figure 7.1) and calculating the coincidences of the detected counts of both APDs as a function of a time lag τ. The detected intensities in both APD channels $I_1(t)$ and $I_2(t)$, i.e., the photon count rates, can be evaluated in the normalized correlation function of second order $g^{(2)}(\tau)$ defined as

$$g^{(2)}(\tau) = \frac{\langle I_1(t)\, I_2(t+\tau)\rangle}{\langle I_1(t)\rangle \langle I_2(t)\rangle} \quad , \tag{7.2}$$

where $\langle\cdot\rangle$ denotes the time average. This normalized correlation function is particularly connected to the (relative) probability to detect a photon in channel 2 at a time τ after a photon was detected in channel 1. For pulsed laser sources used to excite the fluorescence of the sample, the correlation function exhibits peaks separated by the inverse repetition rate $f_{rep} = 1.953\,\mathrm{MHz}$ of the laser source [219], which is here $f_{rep}^{-1} = 512\,\mathrm{ns}$. In case of an ensemble of fluorescent TDI molecules, equally strong coincidence peaks corresponding to $g^{(2)}(\tau) = 1$ result, whose width is linked to the excited state lifetime of the molecules (figure 7.4a). By contrast, for a single TDI molecule, ideally no coincidences are detected for zero lag time corresponding to $g^{(2)}(0) = 0$, which is limited here only by a few coincidences involving APD dark counts (figure 7.4b). This effect is called *photon antibunching* [219, 220]. Photon antibunching is a direct evidence of the quantization of the electromagnetic field and proves the single-photon emission character of a single fluorescent molecule.

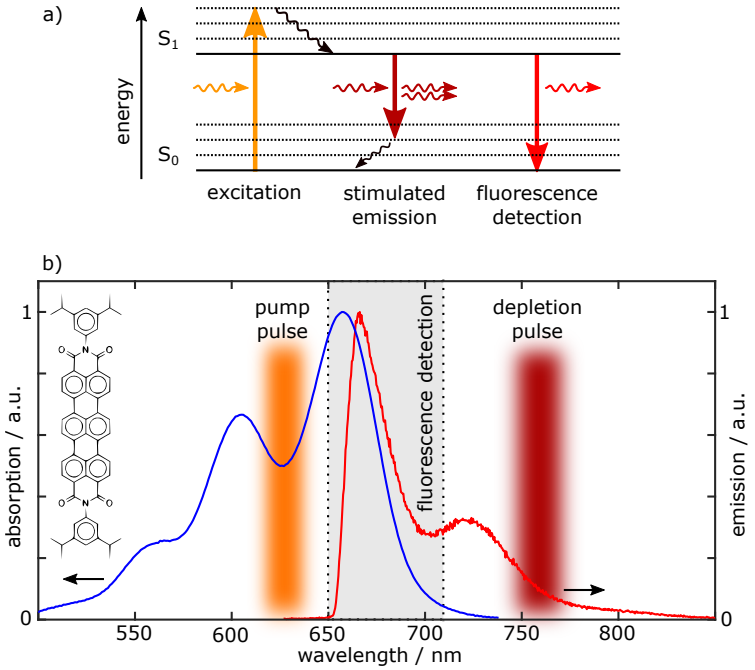

Figure 7.5: (a) Simplified sketch of the energy level scheme of a typical organic dye molecule, including its electronic ground and first excited state (S_0 and S_1, respectively) with vibrational levels (horizontal lines), visualizing the principle of stimulated emission depletion (STED). After excitation via a pump pulse (orange) and subsequent vibrational relaxation of the fluorophore (wavy black arrow), a second red-shifted laser pulse causes stimulated emission back in a vibrational level of S_0 (dark red). The depleted fluorescence is detected (red) and monitors the remaining population of the excited state S_1. (b) Normalized ensemble absorption and emission spectrum (blue and red curve, respectively) of terrylene diimide (chemical structure in inset) in a thin PMMA film. The chosen pump (orange) and depletion (dark red) wavelength ranges, as well as the range for STED fluorescence detection (gray area), are indicated.

7.4 STIMULATED EMISSION DEPLETION

After discussing important fluorescence emission characteristics of single organic dye molecules, this section demonstrates single-molecule stimulated emission depletion with diffraction-limited Gaussian laser foci. *Stimulated emission depletion* (STED) refers to the process where, after excitation of an emitter to its excited state, a transition back to the ground state is forced by stimulated emission via a second laser beam. This process is detected via the fluorescence emission, which is depleted by the stimulated emission and monitors the remaining population of the excited state (figure 7.5a). In the experiment, terrylene diimide (TDI) molecules embedded in PMMA are used, which feature the typical vibronic progression of organic dye molecules within their absorption[1] and emission spectra (figure 7.5b, blue and red curve, respectively). The

1 The absorption (c.f. equation 2.24) is recorded with an absorption spectrometer (Lambda 19,Perkin-Elmer).

TDIs are excited from the ground state S_0 by the *pump pulses* (figure 7.5b, marked orange), either directly to the lowest vibrational level in the electronic excited state S_1 or to a higher vibrational level of S_1 followed by a fast vibrational relaxation to the lowest vibrational level in S_1. The second laser pulses triggering the stimulated emission transition, called *depletion pulses*, are red-shifted with respect to the absorption spectrum of the fluorophore and are typically located in the red tail of the emission spectrum (figure 7.5b, marked dark red). This means that the stimulated emission transition ends up in an energetically high vibrational level of the ground state S_0.

Photophysical considerations for STED To determine the optimum wavelength range of the depletion pulses, the following effects should be considered. First, the depletion pulses need to be red-shifted with respect to the absorption spectrum in order to minimize the overlap and thereby avoid the excitation of the fluorophore from S_0 via the depletion pulses. Second, the red-shift should not be too large, as otherwise the cross-section of stimulated emission gets small due to a lack of overlap with the emission spectrum [221]. Third, excited state absorption of the molecule by the depletion pulses needs to be avoided both to avoid enhanced photobleaching from higher-excited states [10] and to maximize the probability for the stimulated emission transition. Rittweger *et al.* [221] demonstrated that, for a wide range of typical organic dye molecules, stimulated emission is the dominant quenching mechanism of the fluorescence by a red-shifted depletion beam. In the particular case of terrylene diimide, Bullock *et al.* [222] observed a positive band in transient absorption spectroscopy located above ~770 nm that is a result of excited state absorption, which should be avoided. Taking the above-listed effects into consideration, a depletion pulse wavelength range of about 750-770 nm is best-suited for terrylene diimide and is used in the following. As a result of the fluorophore's stimulated emission triggered by the depletion pulse, the fluorescence emission is depleted. Typically, this depleted fluorescence is detected in a wavelength range just between the pump and depletion pulses, i.e., in the range 650-710 nm for terrlene diimide (figure 7.5b, gray area). Besides the proper selection of pump and depletion wavelengths, the pulse duration and repetition rate of the laser are important setup parameters that need to be considered for maximum efficiency of the STED effect. The laser pulses should be shorter than the fluorescence lifetime, as otherwise the overall probability to induce stimulated emission via the deletion pulse is reduced. Furthermore, the depletion pulse is typically timed just after the excitation of the fluorophore by the pump pulse (and subsequent vibrational relaxation). On the one hand, if the pulses overlap temporally, the depletion efficiency decreases because the fluorophore might not yet be excited or vibrationally relaxed before triggering the stimulated emission transition via the depletion pulse. On the other hand, if the depletion pulse arrives much later, the spontaneous emission in the time span between pump and depletion pulse is not suppressed as intended. Moreover, the repetition rate of the laser pulses should be rather low. Particularly, metastable dark states such as the triplet state should have enough time to decay before the next pump pulse arrives, as otherwise photobleaching might be promoted. A more comprehensive discussion of these effects is found in specialized review articles of stimulated emission depletion and its applications in superresolution nanoscopy, such as the one given by Blom and Widengren [10]. The optical setup described in section 7.2 with ps-pulses

and 1.953 MHz repetition rate well matches the above-described considerations and also offers the required pulse energies to saturate the stimulated emission transition (c.f. figure 7.6).

STED as a nonlinear optical effect STED, as also applied in superresolution nanoscopy, involves different nonlinear optical effects. First, stimulated emission itself can be described by a nonlinear $\chi^{(3)}$-process. Second, the stimulated emission of the fluorophore can be further driven into saturation with a concomitant nonlinear dependence of the depleted fluorescence intensity on the depletion pulse energy (see below, figure 7.6b). In the description of nonlinear light-matter interaction, the susceptibilities $\chi^{(n)}$ of order n represent the expansion coefficients of the induced polarization P of the medium to higher orders in the incoming electric field E [223]:

$$P = \epsilon_0 \left(\chi^{(1)} E + \chi^{(2)} E E + \chi^{(3)} E E E + ... \right) \quad . \tag{7.3}$$

Stimulated emission in the non-saturating regime, as one particular case of pump-probe spectroscopy, is a third-order nonlinear process, where three optical fields interact to produce a third-order nonlinear polarization $P^{(3)}$ given by

$$P^{(3)} = \epsilon_0 \chi^{(3)} E_{\text{pump}} E^*_{\text{pump}} E_{\text{probe}} = \epsilon_0 \chi^{(3)} |E_{\text{pump}}|^2 E_{\text{probe}} \quad . \tag{7.4}$$

This polarization $P^{(3)}$ oscillates at the frequency of the probe beam, while the phase relation to the pump field is typically lost. The nonlinear polarization $P^{(3)}$ can be detected by interfering its radiation with the probe beam field itself. Hence, a modified transmission of the probe beam would be detected, e.g., as a result of stimulated emission [212, 224]. Alternatively, the polarization can be transferred into a population by a fourth interaction with an optical field [225] and the remaining excited state population is detected by fluorescence emission. This scheme of detecting the outcome of a nonlinear $\chi^{(3)}$-process was applied recently in ultrafast nonlinear spectroscopy of a single molecule by Liebel *et al.* [226] and in fluorescence-detected 2D-spectroscopy [227, 228] in general, and is adopted in this chapter.

Single-molecule STED in TCSPC histograms The STED effect is first visualized for a specific single molecule by time-correlated single photon counting (TCSPC), which measures the arrival time of fluorescence photons after the pump pulse. The depletion pulse of varying pulse energy (0-31 pJ) is time-delayed here to the pump pulse by about 0.6 ns and arrives at the molecule as diffraction-limited far-field focus. For 0 pJ depletion pulse energy, a single exponential decay with an excited state lifetime of about 3.6 ns is recorded (figure 7.6a, red curve). For higher depletion pulse energies, an abrupt drop in the fluorescence signal appears at the time delay of the depletion pulse (figure 7.6a, c.f. vertical arrow), which signals the depopulation of the excited state by stimulated emission [221, 222]. The steepness of the recorded drop of fluorescence in the TCPSC histogram is limited by the instrumental response function of the setup (c.f. figure 7.10a). At 31 pJ depletion pulse energy, nearly a complete suppression of the fluorescence is achieved for the single TDI under investigation (figure 7.6a, black curve). The factor by which the fluorescence is reduced by the depletion pulse is called

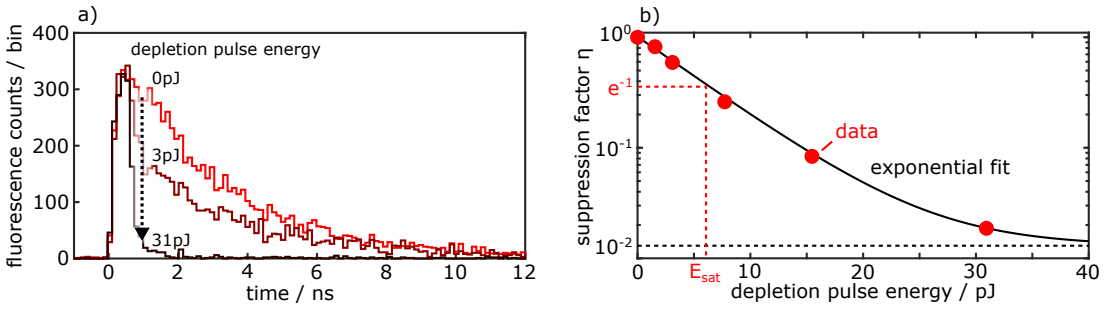

Figure 7.6: (a) Fluorescence decay curves of a single TDI molecule for three selected depletion pulse energies (0 pJ, 3 pJ, 31 pJ) recorded via APD 1 and time-correlated single photon counting (TCSPC). The time-delay of the depletion pulses to the pump pulses is about 0.6 ns. (b) Fluorescence suppression factor η (red dots) of the same molecule calculated from the TCSPC data for increasing depletion pulse energy. The black line represents an exponential fit with a background of about 1% (black dashed line). From the level $\eta = 1/e$, the saturating depletion pulse energy E_{sat} (here about 6 pJ) can be determined (c.f. dashed red line).

suppression factor η. The suppression factor η decreases continuously for increasing depletion pulse energy (figure 7.6b, red dots), closely following an exponential function (solid black curve), in agreement with equation 2.21.

Saturating depletion pulse energy for a diffraction-limited depletion focus The 1/e-level of the suppression factor η defines a saturating depletion pulse energy E_{sat} (figure 7.6b, dashed red line). After proving the validity of the exponential dependency of the suppression factor η on the depletion pulse energy E_{depl}, a single measurement at a specific value E_{depl} is essentially sufficient to determine the saturating depletion pulse energy E_{sat} for the molecule under investigation by the relation

$$E_{sat} = -\frac{E_{depl}}{\ln(\eta)} \quad . \tag{7.5}$$

In contrast to the TCSPC histograms presented in figure 7.6a, the suppression factor can also be determined from a simple fluorescence time trace measurement with APD 1. For that, a reduced optimum delay of about 50 ps [214] between pump and depletion pulses is used in order to maximize the excited state population available for stimulated emission. Both laser pulses are focused to the same position where a single TDI is located. For each individual single TDI, a time trace of the fluorescence is recorded that includes time spans where the following three levels are recorded (figure 7.7a). First, a background level I_{bg} is recorded, which is approximated by a time span where the laser pulses are switched off. Second, the unperturbed fluorescence level I_{fl} in the presence of pump pulses only is recorded. Third, the depleted fluorescence level I_{STED}, with both pump and depletion pulses focused to the molecule, is detected. From these three levels, the suppression factor η is calculated according to

$$\eta = \frac{I_{STED} - I_{bg}}{I_{fl} - I_{bg}} \quad . \tag{7.6}$$

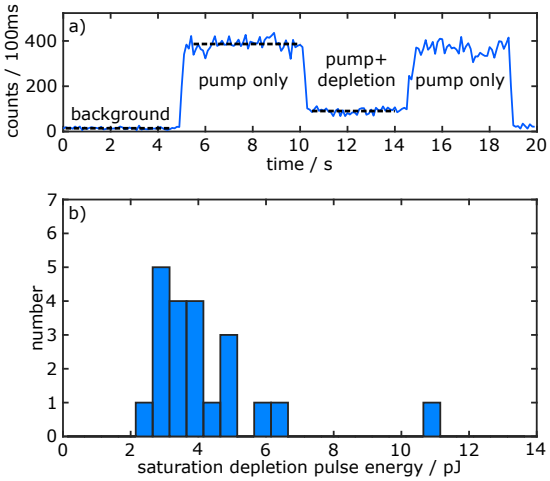

Figure 7.7: (a) Fluorescence time trace of a single TDI molecule in a thin PMMA film. The exciting pump pulses are switched on at about 5 s, while the depletion pulses of pulse energy $E_{depl} = 3.9$ pJ are added in the range of about 10-15 s. At about 19 s the pump pulses are switched off again. From the three relevant detection count levels (black, dashed), the saturating depletion pulse energy is calculated. (b) Histogram of the calculated saturation depletion pulse energies for different single TDI molecules. The measurements were performed with unpolarized depletion pulses and the single-step photobleaching was checked for each molecule.

The determined value η and the used depletion pulse energy E_{depl} yields, according to equation 7.5, the saturating depletion pulse energy for the molecule under investigation.

This procedure is performed for 21 single TDI molecules using unpolarized laser pulses and a fixed depletion pulse energy of 3.9 pJ. The determined saturating depletion pulse energies vary from molecule to molecule within the range from about 2.4 to 11 pJ (figure 7.7b). This variation is attributed mainly to the random orientation of the TDI molecules in the PMMA film. Particularly, an out-of-plane orientation of the molecules, i.e., of their transition dipole moment, leads to a reduced scalar product between transition dipole moment and the mainly in-plane depletion pulse focal field, leading to a larger value of E_{sat}. Thus, for different randomly oriented molecules, a distribution of saturating depletion pulse energies is obtained [59]. Note that an in-plane variation of the molecular orientation does not impact the measurement result due to the unpolarized depletion pulses. The lowest value of E_{sat} is found to be 2.4 pJ (figure 7.7b). According to the above consideration of the molecular orientation, this value corresponds to a molecular transition dipole moment with best in-plane alignment.

In contrast to these measurements with unpolarized depletion pulses, the waveguide modes in a plasmonic two-wire transmission line are selectively excited by a linear polarization (c.f. section 6.5). Thus, to make a fair comparison of the saturation

depletion pulse energy for a linear polarization, the value of 2.4 pJ is further divided by 2, resulting in

$$E_{sat}^{opt} = 1.2\,\mathrm{pJ} \quad . \tag{7.7}$$

This value 1.2 pJ represents the saturating depletion pulse energy for a molecule best-aligned with the focal field of a linearly polarized diffraction-limited far-field depletion pulse focus. This number is determined here as a reference that is compared in section 7.6 to the saturating depletion pulse energy estimated from single-molecule STED experiments using confined plasmonic modes instead of far-field foci.

Determination of the cross-section for stimulated emission Having determined the saturating depletion pulse energy for depleting the fluorescence by a suppression factor $\eta = 1/\mathrm{e}$, the cross-section for stimulated emission σ_{STED} can be calculated according to equation 2.21 via

$$\sigma_{STED} = \frac{1}{h_{STED,sat}\,\tau_{STED}} = \frac{A}{N_{depl,sat}} \quad . \tag{7.8}$$

Here, the product $h_{STED,sat}\,\tau_{STED}$ represents the number of photons per depletion pulse $N_{depl,sat}$ to reach $\eta = 1/\mathrm{e}$ normalized to the focal area A. The area A is calculated for a diffraction-limited Gaussian-like depletion pulse focus according to[2] [59]

$$A = \frac{\pi\, w_0^2}{2} = \frac{\pi\,\mathrm{FWHM}^2}{4\ln(2)} = 8.3 \cdot 10^4\,\mathrm{nm}^2 \quad , \tag{7.9}$$

expressing the Gaussian waist radius w_0 (e^{-2} value) by the depletion focus full width at half maximum FWHM = 270 nm (c.f. figure 7.2a). The value $N_{depl,sat}$ is calculated from the saturation depletion pulse energy of 1.2 pJ (c.f. equation 7.7) via

$$N_{depl,sat} = \frac{E_{sat}^{opt}}{E_{ph}} = 4.6 \cdot 10^6 \quad , \tag{7.10}$$

using the photon energy $E_{ph} = \frac{hc}{\lambda_{depl}}$ at the depletion wavelength of $\lambda_{depl} \approx 760\,\mathrm{nm}$. Equation 7.10 shows that at room temperature several millions of photons in a diffraction-limited laser pulse focus are necessary to trigger the stimulated emission with an adequate probability. The determined values of $N_{depl,sat}$ and A yield, according to equation 7.8, an absolute cross-section for stimulated emission of a single TDI in PMMA well aligned with respect to a linearly polarized depletion pulse (~760 nm) of

$$\sigma_{STED} = 1.8 \cdot 10^{-16}\,\mathrm{cm}^2 \quad , \tag{7.11}$$

which is in good agreement with typical values of other dyes determined by the Hell group [59, 221].

2 This definition of an area yields slightly different values than the effective mode area A_{eff} defined in equation 3.24.

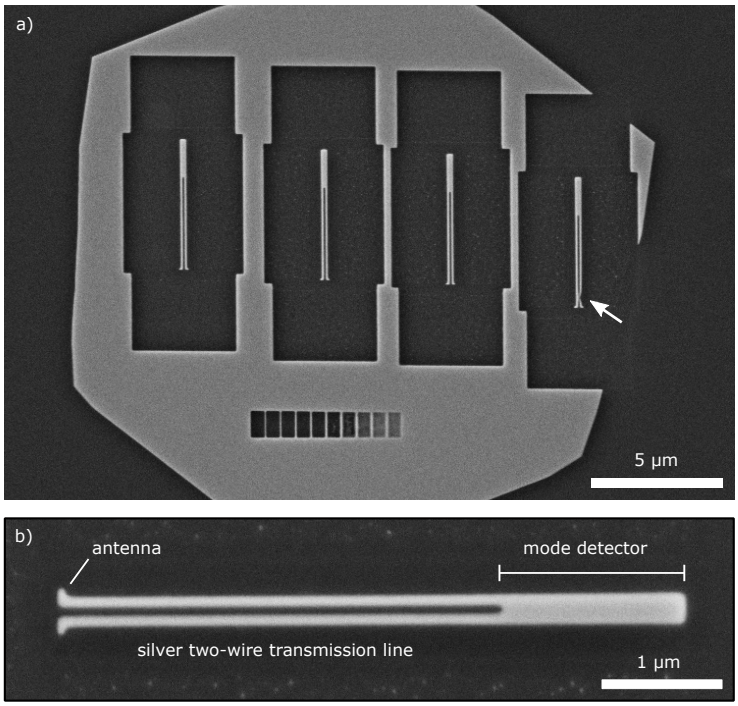

Figure 7.8: (a) Scanning electron micrograph of a single-crystalline silver flake with four waveguide circuits #1 - #4 (left to right) fabricated by the same focused ion beam milling procedure. The fourth nanostructure #4 at the right side is excluded in the experiments due to a fabrication imperfection close to the antenna where both nanowires touch each other (marked by white arrow). (b) Zoom-in to the second waveguide circuit (rotated by 90°).

7.5 COUPLING SINGLE MOLECULES TO A PLASMONIC WAVEGUIDE

In this section, the efficient coupling of single TDI molecules to a plasmonic circuit is demonstrated. Single organic dye molecules, in contrast to quantum dots, have been rarely coupled to plasmonic waveguides and have been only investigated for their spontaneous emission so far, e.g., by Su *et al.* [93] and Grandi *et al.* [208]. TDI molecules are best-suited for such investigations due to their superior photophysical properties such as an extreme photostability and a low blinking probability (c.f. section 7.3). Furthermore, TDI allows to perform nonlinear single-molecule experiments such as stimulated emission depletion (c.f. section 7.4) in a wavelength range accessible with a silver plasmonic nanocircuit. By focused ion beam milling in a single-crystalline silver flake (height 80 nm), four waveguide circuits were fabricated with the same milling procedure (figure 7.8a). Here, the flake synthesis protocol 1 (c.f. section 5.2) was used and focused ion beam milling was performed with a conductive resist (c.f. figure 5.9c, section 5.6). The silver nanostructures are encapsulated by 5 nm Al_2O_3 after milling and the resulting circuit geometry (figure 7.8b), as well as the circuit functionality, is very similar to the one discussed in detail in chapter 6. The three nanocircuits at the left side of figure 7.8a have a quasi-identical geometry, while

the fourth circuit at the right side features a clear fabrication defect. At this defect position, both nanowires touch each other, preventing the intended propagation of the plasmonic modes, particularly of the antisymmetric mode in the gap. Thus, this circuit is excluded in the following from further experiments. In case of the three properly milled circuits, both nanowires feature a width of about 90 nm and a gap-separation of about 60 nm. In this gap, the strongly confined electromagnetic near-field of the antisymmetric plasmonic waveguide mode is available (c.f. figure 6.3a,b). The gap is thus the desired position for single quantum emitters considered in the following at which a high waveguide-emitter coupling with the antisymmetric mode is expected.

Placing single TDI molecules in the gap To bring TDI molecules in the gap of the silver nanocircuits without strongly modifying the waveguides' properties, a spin coating of very thin TDI-doped PMMA films is used. The PMMA resist (ARP671.015, Allresist) is diluted from 1.5 % to 0.5 % solid content with its solvent chlorobenzene and TDI is added in a concentration $< 10^{-9}$ M that was optimized to yield a proper density of single TDI molecules in the PMMA film (~1 TDI per 1 μm^2). Spin coating with 1000-4000 rotations per second results in a film thickness in the order of 10-20 nm according to an interpolation of spin coating curves of the resist manufacturer Allresist [217]. To check for the coupling of single TDI molecules to the antisymmetric mode of the waveguide structures, the pump pulses are focused to the antenna with a perpendicular polarization launching an antisymmetric (superposition) mode (c.f. chapter 6). The propagating mode of the waveguide circuit remotely excites TDI molecules along the gap that can be identified via widefield fluorescence imaging. In case a TDI is not found in any gap of the three used waveguide circuits (c.f. figure 7.8a) or the TDI in the gap photobleaches before the experiments are performed, the PMMA film is removed by rinsing with acetone and isopropanol and a new film is spin coated. If a TDI molecule is found in the waveguide gap, typically also other TDIs at different locations of the waveguide are present and are directly or remotely excited by the pump pulses. These latter undesired TDI molecules, identified via widefield fluorescence imaging, are photobleached on purpose by focusing the pump pulses to their position. This way, within a reasonable number of attempts, the desired scenario of a single fluorescent TDI molecule located in the gap of one of the three two-wire transmission lines is achieved.

Deducing the fluorescence coupling efficiency Upon remote excitation with perpendicularly polarized pump pulses on the antenna, in the desired scenario, a single bright emission spot is observed along the gap of the waveguide in a widefield fluorescence image, signaling the position of the single TDI (figure 7.9a, top). For this specific TDI #1, a single-step photobleaching (figure 7.9a, top inset) was recorded after all experiments, justifying the single-molecule statement. Furthermore, waveguide emission is detected at the antenna and at the inner end of the mode detector, signaling the emission from the antisymmetric mode. In particular, upon photobleaching of the TDI (figure 7.9a, inset), these waveguide signals vanish (figure 7.9a, bottom), demonstrating that their dominant origin lies in a sequential plasmon emission by the TDI. A smaller emission intensity remains at the excitation position on the antenna (emission spectrum see figure 7.12d), which is attributed to the fluorescence of the

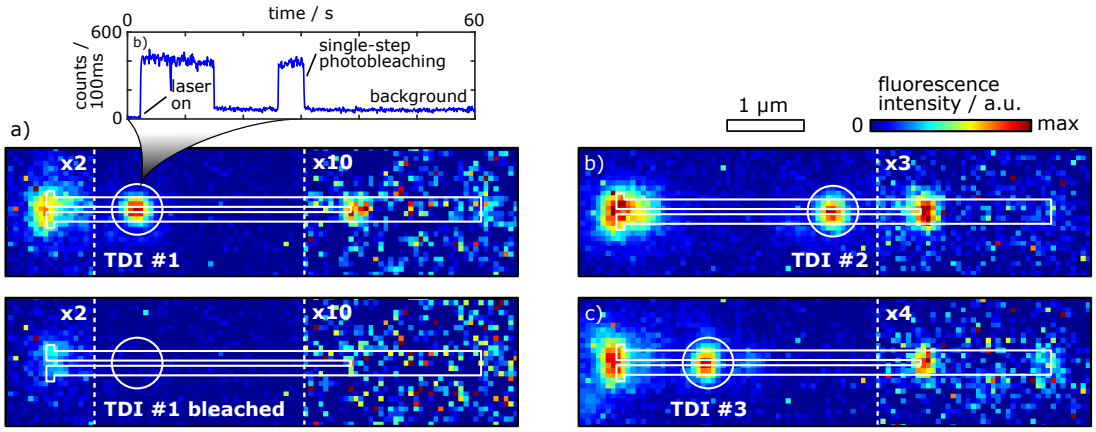

Figure 7.9: (a) Top: Widefield fluorescence image of a single TDI molecule (#1, white circle) in the gap of a silver waveguide circuit remotely excited via pump pulses focused to the antenna. Bottom: Upon photobleaching of TDI #1, most of the emission vanishes. Inset: Fluorescence time trace of TDI #1 detected with APD 1 (detection spot size 600 nm, equals white circle in (a)), demonstrating the single-step photobleaching. (b,c) Additional widefield fluorescence images of TDI molecules #2 and #3 located at a different position along the gap. The intensity at the mode detector and antenna area is enhanced by the indicated factors.

milled silver structure [195, 229]. Moreover, a reduced distance of a TDI molecule to the mode detector tends to result in an increased waveguide emission intensity at the inner end of the mode detector (c.f. TDI #1 - #3, figure 7.9a-c), which is in line with a reduced total propagation loss along the distance l between TDI and mode detector. While TDI #1 and TDI #2 are both located within the plasmonic circuit #2, TDI #3 is located within circuit #3 (c.f. figure 7.8a).

According to the above discussion, the waveguide signal at the inner end of the mode detector steams mostly from the coupled TDI molecule, while the emission at the antenna has contributions of background fluorescence. For the case of TDI #1, the waveguide emission at the mode detector vanishes completely upon photobleaching of the TDI (c.f. figure 7.9a, bottom), despite the fact that the background fluorescence at the antenna is only about 4 times weaker than the TDI's direct far-field emission. The probably weaker overall coupling of the background fluorescence into the waveguide and the obviously larger total propagation loss due to the higher distance to the mode detector, leads to the fact that TDI's emission dominates the waveguide signal at the mode detector. Thus, in the following, the waveguide signal at the mode detector for TDI #2 and #3 is considered to originate mainly from the coupled TDI, too.

Based on the widefield fluorescence images of TDI #1 - #3 (c.f. figure 7.9a-c), the coupling efficiency of the fluorescence is determined, similar to section 6.8. For quantitative analysis, the emission intensity is integrated in a ~650 nm square area centered to each emission spot, which is then subtracted by a background integrated in a neighboring square area in each case. Particularly, the ratio of the fluorescence intensity at the inner end of the mode detector and at the TDI position is considered. The deduced relative

TDI #	I_{rel}^{as}	l	η_c
1	12 %	2.5 µm	68 %
2	42 %	1.1 µm	78 %
3	32 %	2.4 µm	84 %

Table 7.1: Relative (integrated) emission intensity I_{rel}^{as} at the mode detector near end normalized to the (integrated) direct far-field intensity of the coupled TDI #1, #2 and #3 in the gap. l represents the distance measured from the TDI to the inner end of the mode detector. η_c measures the estimated fluorescence coupling efficiency according to equation 7.12.

intensity I_{rel}^{as}, as well as the distance l between TDI and the inner end of the mode detector, is listed in table 7.1. The antenna emission is not quantified, as it consists of the additional contribution of background (silver) fluorescence discussed above. Instead, only the mode detector emission intensity at the near end is evaluated and an additional factor of 2 is taken into account due to the second waveguide direction from the TDI's point of view. This approach neglects interference effects of TDI's emission within the finite-length waveguide[3]. Analogously to equation 6.4, the ratio of the TDI's emission rate into the antisymmetric plasmonic waveguide mode k_{pl}^{as} to the sum of k_{pl}^{as} and the direct far-field emission rate k_{ff} is calculated by

$$\eta_c = \frac{k_{pl}^{as}}{k_{ff} + k_{pl}^{as}} = \frac{2\left[I_{rel}^{as}\frac{\exp(l/l_p^{as})}{\eta_{col}^{as}}\right]}{\frac{1}{\eta_{col}^{ff}} + 2\left[I_{rel}^{as}\frac{\exp(l/l_p^{as})}{\eta_{col}^{as}}\right]} \quad . \tag{7.12}$$

In the calculations based on equation 7.12, the collection efficiencies $\eta_{col}^{as} = 0.2$ and $\eta_{col}^{ff} = 0.5$, as also used in section 6.8[4], are taken into account. Furthermore, for the propagation length of the antisymmetric mode l_p^{as}, an experimental estimate of 2 µm is used (c.f. appendix C). The above-described evaluation leads to estimated η_c-values ranging between 68 % and 84 % (c.f. table 7.1). This means that the majority of the coupled TDI's fluorescence emission is efficiently funneled into the antisymmetric plasmonic waveguide mode. As discussed in section 6.8, these efficiencies are among state-of-the-art experimental values obtained for emitters placed in strongly confined plasmonic waveguide modes determined by Kumar *et al.* [179, 203, 204].

Shortening of the fluorescence lifetime The coupling of single TDI molecules to the waveguide can be further quantified by the reduction of their excited state lifetime, as the additional strong radiative (and nonradiative) plasmonic decay channels (c.f. section 3.3) lead to a decreased fluorescence lifetime (c.f. equation 2.20). After identifying the coupled molecule in the gap by fluorescence widefield imaging, the

3 In general, TDI's emission in one waveguide direction may interfere constructively or destructively with back-reflected emission from the opposite waveguide end, leading to single-plasmon self-interference [186]. This effect may further change the relative intensity detected at both waveguide ends. Specially designed waveguide Bragg-reflectors, for example, allow guiding control of emitted single photons [230].

4 The subtle difference between $NA = 1.35$ considered in section 6.8 and $NA = 1.4$ used here is neglected, as the similar impact of a slightly increased NA on η_{col}^{ff} and η_{col}^{as} mostly cancels out in equation 7.12.

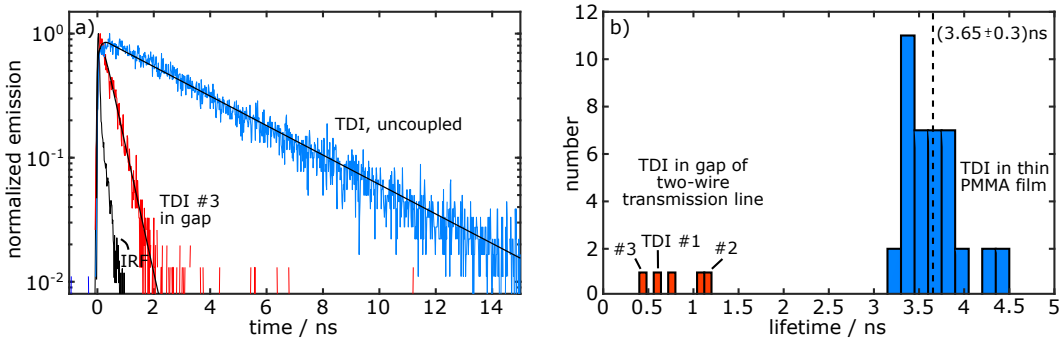

Figure 7.10: (a) Fluorescence decay curve of a typical single TDI in a thin PMMA film (blue curve, lifetime 3.65 ns) and of TDI #3 in the gap of a silver two-wire transmission line (red curve, lifetime 0.4 ns). A convolution of the instrument response function (IRF, black data) with a single exponential decay is fitted to the data (black lines). (b) Histogram of the extracted fluorescence lifetimes of single, uncoupled TDI molecules in a thin PMMA film (blue bars) and of single TDI molecules in the gap of a two-wire transmission line (red bars, detected at the TDI position). The measurements are performed by time-correlated single photon counting with a detection spot size of 600 nm in diameter (c.f. circle in figure 7.9).

detection spot of APD 2 (FWHM 600 nm) is scanned and positioned to the identified TDI. For later purposes of photon antibunching measurements, the detection of APD 1 is manually overlaid with APD 2 to the TDI position, yielding similar fluorescence decay curves in both detector channels by time-correlated single photon counting. This way, both APD detection spots are positioned on the coupled TDI, while the TDI is excited remotely via pump pulses focused to the antenna of the waveguide circuit. The resulting fluorescence decay curve (e.g., TDI #3, figure 7.10a, red curve) is fitted by a convolution of the instrument response function which is measured via detecting the pump pulses only (figure 7.10a, black data) and a single-exponential decay (figure 7.10a, black fitted lines). In the gap, the fluorescence decay is consistently faster than for uncoupled TDI molecules in a thin PMMA film (e.g., figure 7.10a, blue curve). The extracted fluorescence lifetimes for TDI #1, #2 and #3, as well as for two additional cases of a single TDI in the gap[5], are presented in figure 7.10b (red bars). Particularly, in the gap, lifetimes as short as about 0.4 ns are detected (TDI #3), which is about one order of magnitude shorter than for uncoupled TDI molecules in a thin PMMA film with a mean lifetime of (3.65 ± 0.3) ns determined from 40 TDIs (figure 7.10b, blue bars).

Numerical simulation of the β-factor The above-described experimental findings of a strongly reduced excited state lifetime of the coupled TDI molecules (c.f. figure 7.10b) together with an efficient channeling of the emission into the antisymmetric mode of the waveguide (c.f. table 7.1) suggest a high β-factor, an important figure-of-merit to quantify the coupling in waveguide-emitter systems. According to the detailed description in section 3.3, the β-factor determined by a simulation depends on several

5 These two cases are not considered before in the estimation of η_c due to a large relative background emission originating from the excitation position.

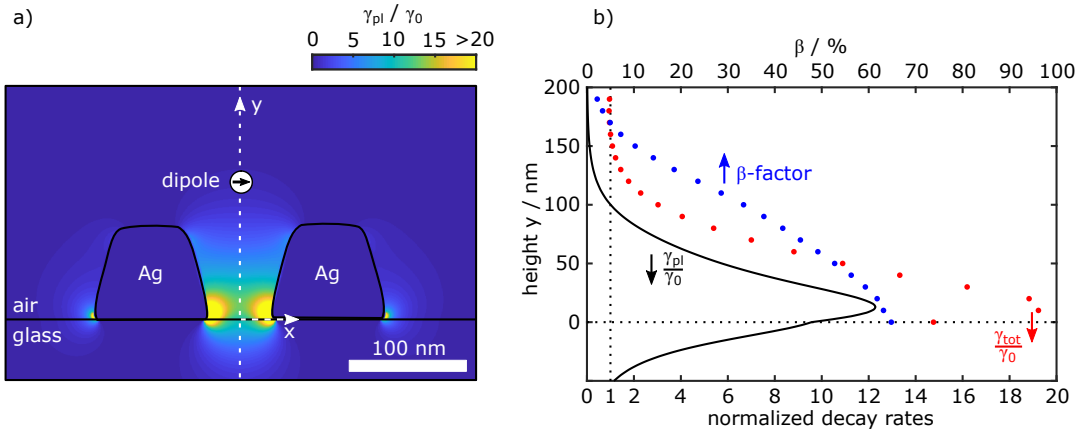

Figure 7.11: (a) Decay rate γ_{pl} of an x-oriented radiating emitter (electric dipole, black arrow, $\lambda_0 = 680\,\text{nm}$) into the antisymmetric plasmonic waveguide mode of a silver two-wire transmission line normalized to the vacuum decay rate γ_0. (b) Calculated (normalized) decay rate of the x-oriented emitter (electric dipole) positioned along the y-direction (vertical white dashed line in panel (a)) into the antisymmetric plasmonic waveguide mode (γ_{pl}, black line, lower axis) and the (normalized) total decay rate (γ_{tot}, red dots, lower axis). The ratio of both values yields the β-factor (blue dots, upper axis). The height $y = 0$ corresponds to the glass-air interface.

aspects, such as the geometry and modal field of the considered waveguide as well as the position and orientation of the radiating electric dipole. To reduce the complexity of this huge parameter space, in the following, an infinitely long silver two-wire transmission line without the Al_2O_3 and PMMA cover layers above a glass-air interface is considered (geometry c.f. figure 7.11a). Furthermore, the dipole axis of the radiating electric dipole ($\lambda_0 = 680\,\text{nm}$) is fixed to the orientation across the gap (x-direction), which is the direction of the antisymmetric mode's strongest near-field, and the dipole is placed in the center between the two nanowires with a variable height above the substrate along the vertical direction (figure 7.11a, white dashed line, called y-direction here).

From a two-dimensional mode analysis of the mentioned waveguide geometry using the numerical model described in subsection 4.1.2, the decay rate of an x-oriented emitter (electric dipole) into the antisymmetric plasmonic mode is calculated according to equation 3.32 in section 3.3. The normalized decay rate γ_{pl}/γ_0 is plotted in figure 7.11a for an arbitrary position of the emitter in the transverse x-y plane as colormap, reaching values above 20 in the gap close to the bottom corner of the nanowires. Considering the normalized decay rate γ_{pl}/γ_0 for different emitter positions along the y-direction in the center between the two nanowires (figure 7.11a, vertical white dashed line), values up to $\gamma_{pl}/\gamma_0 = 12.3$ at the position ~15 nm above the glass-air interface are found (figure 7.11b, black line).

To determine the β-factor, not only the normalized decay rate γ_{pl}/γ_0 into the antisymmetric plasmonic mode but also the total decay rate enhancement γ_{tot}/γ_0 is needed (c.f. section 3.3). The total decay rate enhancement is retrieved with the identical wave-

guide geometry incorporated in the three-dimensional numerical model described in subsection 4.1.5. Notably, this model includes all free-space and nonradiative decay channels. The three-dimensional simulation is performed for the x-oriented electric dipole at different positions in 10 nm steps above the substrate along the vertical y-direction. The determined total decay rate γ_{tot} normalized to the vacuum decay rate γ_0 reaches values close to 20 at a height of about 10 nm above the glass-air interface (figure 7.11b, red dots). As the total decay rate γ_{tot} includes the decay rate into the plasmonic waveguide mode γ_{pl} as well as all other free-space and nonradiative decay channels, its value is larger than the plasmonic decay rate only. Far above the waveguide, the total decay rate approaches γ_0. Taking the ratio of γ_{pl} and γ_{tot} finally yields the β-factor $\beta = \gamma_{pl}/\gamma_{tot}$, which reaches values of up to 65 % at the glass-air interface (figure 7.11b, blue dots).

Comparison between simulation and experiment When comparing the simulated with the experimental data, the following points need to be considered. First, the total decay rate γ_{tot} in the simulation is normalized to the vacuum decay rate γ_0. By contrast, in the experiment, the reference measurement is performed in a thin PMMA film on a glass substrate. In a homogeneous medium of refractive index $n = 1.5$ (modeling glass / PMMA), a 1.5-fold increase of the radiative decay rate would be obtained compared to vacuum (c.f. equation 2.15 or 3.33). In a thin polymer film on glass in air, the orientation of the molecule and thin-film interference effects further complicate the situation [231, 232]. Considering the rough difference of 1.5, the experimental shortening of the fluorescence lifetime in the gap of up to about 1 order of magnitude (multiplied by 1.5) is well within the range of simulated total decay rate enhancements which range up to nearly 20. The remaining deviations, also for the fluorescence lifetimes of different coupled TDIs shown in figure 7.10b, are explained with a different, non-ideal placement or orientation of the TDI within the gap, among other differences between experiment and simulation. Second, the simulated β-factor includes nonradiative decay channels that are present close to a plasmonic nanostructure and lead to ohmic loss within the metal. By contrast, the experimentally determined coupling efficiency for the fluorescence emission η_c neglects these nonradiative contributions and therefore yields an upper bound for the β-factor. Thus, the experimentally determined values $\eta_c = 68 - 84\,\%$ can be located slightly above the simulated maximum of $\beta = 65\,\%$. Also here, other unknown parameters such as the placement and orientation of the TDI / dipole within the waveguide gap easily contribute further to differences between experiment and simulations.

Despite the discussed simplifications and deviations of the idealized numerical modeling from the actual experimental situation, a good match of the experimental observations with theoretical expectations is achieved. Thus, the intended efficient coupling of single organic molecules to the antisymmetric mode of a silver plasmonic two-wire transmission line is clearly realized.

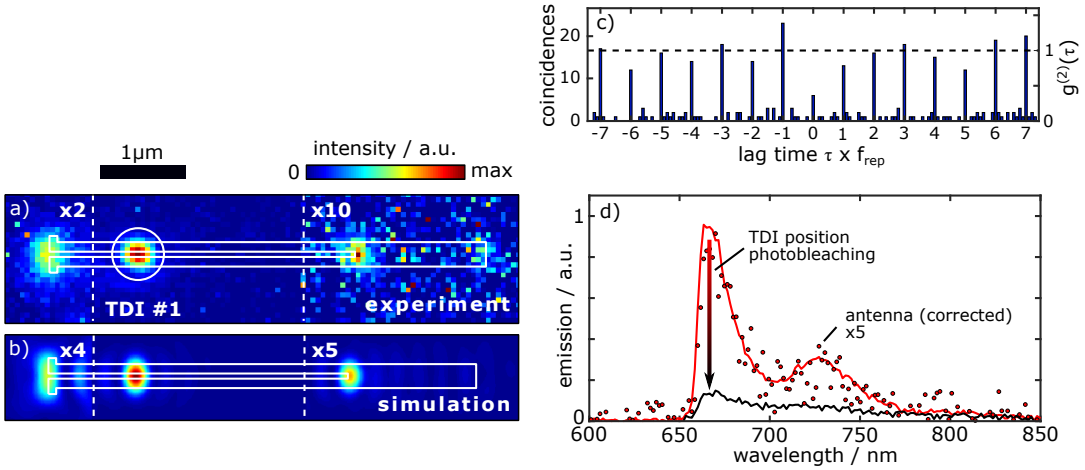

Figure 7.12: (a) Widefield fluorescence image of TDI #1 (marked with white circle) in the gap of a silver plasmonic circuit remotely excited via pump pulses focused to the antenna (perpendicular polarization). (b) Simulated far-field image of an electric dipole placed at a position matching the one of the TDI molecule in the experiment ($\lambda_0 = 680\,\text{nm}$, $NA = 1.4$). The Al_2O_3 and PMMA layer is neglected for numerical simplicity. (c) Fluorescence coincidences of the emission detected at the TDI position with both APD 1 and APD 2 (detection spot size 600 nm, c.f. white circle in (a)) as a function of lag time τ in units of the inverse laser repetition rate f_{rep}, demonstrating photon antibunching at zero lag time. (d) Emission spectrum recorded at the TDI position before and after the photobleaching event (red and black line, respectively). The emission at the antenna position, corrected by the emission after photobleaching, follows the spectral shape of TDI's emission spectrum (red dots, multiplied by 5).

Further characterization of TDI #1 In the following, TDI #1 is considered in more detail, as all desired measurements, including the stimulated emission depletion via propagating plasmons (see section 7.6), could be performed before the photobleaching event of this molecule (c.f. time trace in figure 7.9a, top inset). The widefield fluorescence image of TDI #1 (figure 7.12a) can be reproduced by the simulation of electric dipole emission using the numerical model described in subsection 4.1.5. Here, the whole plasmonic circuit (dimensions c.f. figure 7.8b and section 7.5) is included in the numerical domain, neglecting thin cover layers (Al_2O_3 and PMMA) for numerical simplicity. An electric dipole ($\lambda_0 = 680\,\text{nm}$) is placed in the center of the gap with in-plane orientation across the gap at a height of 20 nm above the glass-air interface. Subsequently, the radiation is imaged as described in section 4.2 ($\lambda_0 = 680\,\text{nm}$, $NA = 1.4$) and the intensity in the image plane is plotted (figure 7.12b). The exact intensity ratio of the three emission spots, e.g., TDI respectively dipole, antenna and mode detector position, depends on several factors. First, at the excitation position on the antenna, in the experiment not only waveguide emission of the TDI is detected but also an additional contribution of directly excited background (silver) fluorescence (c.f. figure 7.9a). Second, the waveguide geometry as well as the dipole position and orientation are simplified and idealized in the numerical modeling. Third, an experimentally lowered propagation length of the antisymmetric mode ~2 µm (c.f.

appendix C) compared to a theoretical value of ~3.4 µm at 680 nm (c.f. figure 6.4b) lowers the propagation efficiency along the distance 2.5 µm to the mode detector by $\exp(-2.5/2)/\exp(-2.5/3.4) \approx 0.6$. Thus, by taking these differences between the simulation and experiment into consideration, also the slightly different relative intensities at the waveguide ends are explained.

Photon antibunching in the fluorescence of TDI #1 Additional to the single-step photobleaching event (c.f. figure 7.9a, top inset), a further evidence for TDI #1 being a single molecule is found in the strong suppression of photon coincidence events at zero lag time (figure 7.12c). The expected raw coincidences can be calculated following Beveratos *et al.* [219] and Beirne *et al.* [220], which particularly yields for the coincidences c_{bg} involving the background luminescence

$$c_{bg} = \frac{t_{int}}{f_{rep}} \left[n^{(1)} \cdot n_{bg}^{(2)} + n^{(2)} \cdot n_{bg}^{(1)} - n_{bg}^{(1)} \cdot n_{bg}^{(2)} \right] \approx 6 \quad , \tag{7.13}$$

using $f_{rep} = 1.953\,\mathrm{MHz}$, a total integration time $t_{int} = 30\,\mathrm{s}$, the total count rates $n^{(i)}$ ($n^{(1)} \approx 1200\,\mathrm{s}^{-1}$, $n^{(2)} \approx 1470\,\mathrm{s}^{-1}$) and the count rate due to background luminescence from the sample $n_{bg}^{(i)}$ in APD channel i (about 12 % from the total count rate). Thus, the 6 coincidences observed in the single time bin at zero lag time (c.f. figure 7.12c) are expected due to the recorded background luminescence. The background count rate is evaluated by the count rate after the single-step photobleaching of the TDI #1 (c.f. figure 7.9a, top inset) subtracted by the dark count rate of the APD. Note that coincidences involving the APD dark counts are distributed rather equally over all time bins, with (on average) less than one coincidence per time bin (c.f. figure 7.12c). The normalization of the total coincidences is performed following Beirne *et al.* [220], under consideration that the coincidences involving dark counts are distributed across the whole time. This yields the normalized correlation function $g^{(2)}(\tau)$ (c.f. equation 7.2) on the right axis of figure 7.12c. At a lag time $\tau = 0$, a value $g_2(\tau = 0) = 0.36$ is calculated, where the non-zero value is limited by the background luminescence discussed above. This value is well below 0.5, i.e., it displays a clear photon antibunching, which is characteristic for single-photon emitters such as single molecules.

Emission spectrum of TDI #1 As a further characterization of TDI #1, the emission spectrum at its position in the gap is recorded (figure 7.12d, red line), featuring the typical TDI emission spectrum with a clear vibronic progression. By contrast, after photobleaching of TDI #1, a weaker, broad and unstructured emission spectrum is recorded (figure 7.12d, black line). This emission cannot be explained by other TDI molecules, as the emission does not bleach and does not fit to the vibronic structure of TDI's emission. Therefore, it is attributed to luminescene of the milled silver nanostructure, as mentioned before and observed by Kumar *et al.* [195]. The emission spectrum at the antenna position, subtracted by the silver emission detected after TDI's photobleaching, clearly resembles the typical TDI vibronic progression (figure 7.12d, red dots), further demonstrating the remote detection of TDI's fluorescence via the waveguide.

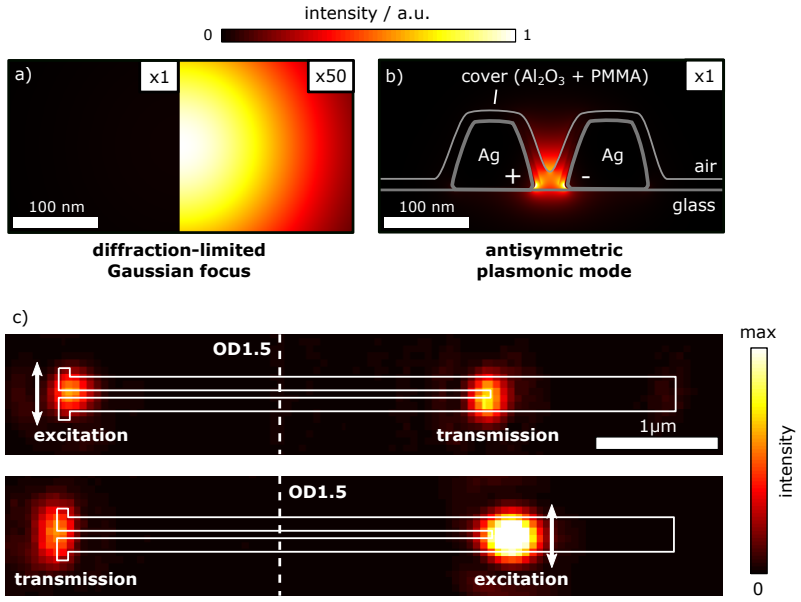

Figure 7.13: Comparison of the local intensity between (a) a diffraction-limited Gaussian far-field focus ($NA = 1.4$) and (b) the antisymmetric mode of a silver two-wire transmission line at $\lambda_0 = 760\,\text{nm}$. At the same transmitted power, the local intensity in the plasmonic gap is up to ~50 times larger (c.f. scaling factors in inset). (c) Widefield imaging of the silver plasmonic circuit (#2) upon focusing the depletion pulses on the antenna (top) and near end of the mode detector (bottom) with a perpendicular polarization (white arrow). In both cases, an equally strong transmission of the depletion pulses via the antisymmetric plasmonic waveguide mode is detected. The intensity in the area around the laser excitation is software-attenuated by a factor of ~31.6 (OD 1.5) for best visibility of the transmission.

7.6 SINGLE-MOLECULE STED WITH PROPAGATING PLASMONS

In this section, the coupled TDI #1 in the gap of the silver two-wire transmission line is forced to undergo stimulated emission depletion via propagating plasmons and the efficiency is compared to the case of a diffraction-limited Gaussian depletion focus. The maximum intensity I_0 of a Gaussian focus normalized to its total power P_0 is given by [104]

$$\frac{I_0}{P_0} = \frac{2\sqrt{2\ln(2)}}{\pi \cdot \text{FWHM}^2} \quad , \tag{7.14}$$

which is proportional to the inverse square of its full width at half maximum (FWHM). Compared to a diffraction-limited Gaussian depletion focus at 760 nm (experimental FWHM = 270 nm, c.f. figure 7.2a, right), the antisymmetric mode of a silver two-wire transmission line traveling inside the tiny nanogap is confined beyond the diffraction limit. Thus, it features, at the same transmitted power, a local intensity up to ~50 times enhanced compared to the Gaussian (figure 7.13a,b). To apply the depletion pulses via the antisymmetric mode to TDI #1, in a first step, the propagation of the depletion

pulses through the waveguide circuit is presented. The antisymmetric waveguide mode can be launched by focused depletion pulse excitation with perpendicular polarization either at the antenna (figure 7.13c, top) or at the near end of the mode detector (figure 7.13c, bottom). Without the PMMA cover layer, in both cases, a total transmission of 0.3 % through the circuit is achieved, clearly superior to the transmission recorded for the silver circuit investigated in chapter 6 (c.f. figure 6.8b). With PMMA cover, the transmission reaches 0.12 %, which is likely reduced due to the increased refractive index of the PMMA layer compared to air, modifying the incoupling and propagation efficiencies.

Stimulated emission depletion of TDI #1 in the gap After confirming the excitation of the antisymmetric mode at the antenna and inner end of the mode detector, the stimulated emission depletion of TDI #1 located within the gap of the two-wire transmission line is presented. The delay of the depletion pulses with respect to the pump pulses is still fixed to 50 ps (c.f. section 7.4). The experiment is conducted as follows (figure 7.14a): The TDI #1 is remotely excited via pump pulses focused to the fixed position on the antenna with a perpendicular polarization (c.f. section 7.5). Moreover, the linearly polarized depletion pulse focus (pulse energy 6.0 pJ) is raster-scanned over the whole waveguide, while the resulting fluorescence is detected at the fixed position of the molecule with the avalanche photodiode APD 1. In case of a parallel polarization of the depletion pulses, a constant fluorescence level of TDI #1 independent of the depletion pulse focus position is found (figure 7.14b). This behavior results from the fact that a parallel polarization can neither launch the antisymmetric mode propagating in the gap (c.f. chapter 6) nor the fields can directly penetrate into nanogap at the TDI position (c.f. figure 6.11b). Thus, the molecule does not interact with the depletion pulses and an unperturbed fluorescence emission is detected. By contrast, perpendicularly polarized depletion pulses are able to excite the antisymmetric mode (c.f. figure 7.13c) and also directly penetrate into the nanogap (c.f. figure 6.11a). As a result, a strong reduction of the fluorescence is observed at three distinct positions (figure 7.14c). When the depletion pulses are focused directly to the TDI position, a strong stimulated emission depletion occurs and the fluorescence emission is suppressed close to the background level of about 24 counts per 80 ms time bin (c.f. horizontal cross-section in figure 7.14d). Strikingly, also when the depletion pulse is focused to the antenna and the inner end of the mode detector, the fluorescence is suppressed down to 31 % and 33 %, respectively. At these positions, the depletion pulse launches the antisymmetric waveguide mode propagating along the gap toward the molecule (c.f. figure 7.13c). Arriving at TDI #1, the plasmonic depletion pulse induces stimulated emission into the propagating antisymmetric plasmonic mode. Thus, the single-molecule stimulated emission of propagating plasmons into the waveguide is observed by detecting the depleted free-space fluorescence. The strong suppression down to about 30 % demonstrates that already the saturation regime of the stimulated emission via propagating plasmons is entered.

Fit to a model calculation The recorded fluorescence intensity $I(x)$ as a function of the depletion pulse focus position x along the center of the waveguide (figure 7.14d, blue dots) can be described by normalized Gaussian spots G at the positions x_n of the

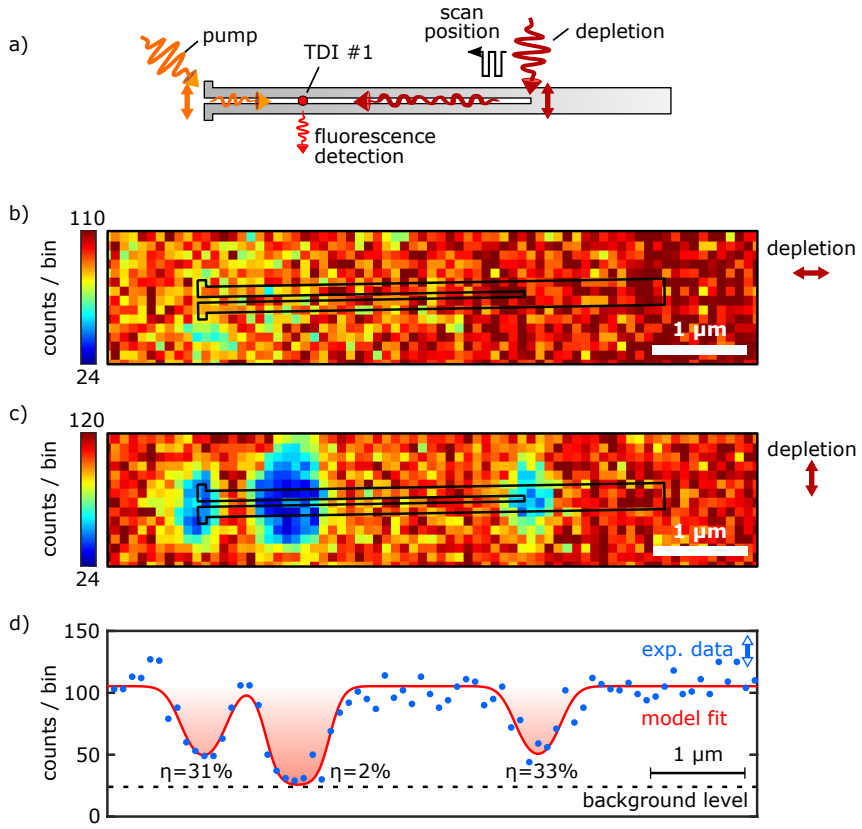

Figure 7.14: (a) Sketch of the experimental concept for single-molecule stimulated emission depletion (STED) via propagating plasmons. The TDI #1 is remotely excited via pump pulses on the antenna (perpendicular polarization, orange arrow). The linearly polarized depletion pulses are raster scanned across the silver waveguide circuit while recording the fluorescence at the fixed position of the TDI with APD 1. (b,c) Resulting fluorescence intensity maps for parallel and perpendicular depletion pulse polarization (dark red arrows), respectively. The data shown is binned (2×2 pixels) from the raw data. (d) Profile of the experimental data of panel (c) close to the center of the waveguide (blue dots) and fit of a model to the data (red line, c.f. text). STED of the TDI fluorescence is observed for the depletion pulse focused to the antenna, to the inner end of the mode detector and directly to the TDI position (red shaded areas).

antenna, TDI #1 molecule and inner end of the mode detector, taken as input to the exponential suppression of the fluorescence:

$$I(x) = I_{bg} + I_{TDI} \sum_n \exp\Big[- a_n G(x - x_n) \Big] \quad . \tag{7.15}$$

Here, $I_{bg} = 24$ represents the fixed average background counts, given by the dark counts of the detector (APD 1) and weak luminescence of the silver in the 80 ms time bin. a_n describes the saturation factor by which the depletion pulse fluence applied to the TDI molecule exceeds the saturating depletion pulse fluence. An optimization of the model parameters to the experimental data (figure 7.14d, red curve) yields the

average undisturbed TDI fluorescence counts $I_{TDI} = 81$ per 80 ms time bin and the suppression factors $\eta_n = \exp(-a_n)$ as listed in figure 7.14d. The intrinsic FWHM of the Gaussian G is optimized to about 450 nm, probably broadened compared to the depletion focus size (FWHM = 270 nm, c.f. figure 7.2a, right) due to the finite size of the silver nanostructure and finite pixel size. The width of the resulting fluorescence intensity dip is further broadened due to the nonlinear exponential dependency of the suppression on the local depletion intensity. This effect is most noticeable in the saturation regime, e.g., in the intensity cross-section at the TDI position in figure 7.14d, which is broadened to ~700 nm.

Deducing the saturating depletion pulse energy for the plasmonic mode Despite the shorter distance of the TDI molecule to the antenna, the fluorescence suppression after a depletion pulse via the antenna and via the mode detector is nearly equal (31 and 33 %, respectively, figure 7.14d). In numerical simulations, similar incoupling efficiencies of the depletion pulses into the waveguide are found at both positions. However, close to the antenna, the higher-order mode of the two-wire transmission line can appear, which is expected to be a short-ranged leaky mode at the depletion pulse wavelength (c.f. figure 6.4a,b). This short-ranged higher-order mode contribution interferes with the antisymmetric mode, resulting in a spatial beating pattern (c.f. figure 6.10a,b in section 6.6). Hence, in this case, the depletion pulse fluence at TDI #1 is most likely slightly reduced by a destructive interference of the antisymmetric mode with the higher-order mode at the position of the TDI in the gap. By contrast, after a depletion pulse via the mode detector, a similar fluorescence suppression is found in spite of larger propagation losses toward the molecule. Thus, no destructive interference is expected in this case, as the short-ranged leaky higher-order mode already has decayed along the way to TDI #1. In the following, the plasmonic depletion pulse energy arriving at the TDI #1 in the antisymmetric waveguide mode is estimated. The original pulse energy of the linearly polarized depletion pulse focused to the inner end of the mode detector is $E^0_{depl} = 6.0\,\mathrm{pJ}$. The full transmission T of the antisymmetric mode through the waveguide is known from widefield imaging (c.f. figure 7.14c) to be 0.3 % without PMMA cover and $T = 0.12\,\%$ with PMMA cover as in the case of TDI #1. The collection efficiency of the transmitted light at the antenna is simulated to be about $\eta^{as,ant}_{col} = 28\,\%$ and the propagation efficiency along the distance $l = 1\,\mu\mathrm{m}$ between TDI #1 and antenna is about $\exp(-l/l^{as}_p) = 61\,\%$ using the experimental propagation length of about $l^{as}_p = 2\,\mu\mathrm{m}$ (c.f. appendix C). In total, the depletion pulse energy arriving at TDI #1 in the antisymmetric plasmonic waveguide mode is estimated to

$$E^{as}_{depl} = E^0_{depl} \cdot \frac{T}{\eta^{as,ant}_{col} \mathrm{e}^{-l/l^{as}_p}} \approx 42\,\mathrm{fJ} \quad . \tag{7.16}$$

This plasmonic depletion pulse energy leads to a fluorescence suppression down to $\eta = 33\,\%$. Hence, the saturating depletion pulse energy can be estimated to (c.f. equation 7.5)

$$E^{as}_{sat} = -\frac{E^{as}_{depl}}{\ln(\eta)} \approx 38\,\mathrm{fJ} \quad . \tag{7.17}$$

Following the analogous approach for the depletion via the antenna, a saturation depletion pulse energy of 107 fJ is estimated using $\eta_{col}^{as,md} = 0.2$, $l = 2.5\,\mu m$ and $\eta = 0.31$. This value is most likely higher than the 38 fJ in equation 7.17 due to the above-mentioned destructive interference of the antisymmetric mode with the leaky short-ranged higher-order mode close to the excitation position at the antenna. The 38 fJ in equation 7.17 are about a factor of 30 lower than the optimum 1.2 pJ saturating depletion pulse energy from the stimulated emission depletion experiment with a diffraction-limited Gaussian far-field depletion focus (c.f. equation 7.7). Thus, the stimulated emission transition is triggered by a factor of about 30 more efficient with the antisymmetric plasmonic mode in the waveguide-gap. Stimulated emission is proportional to the local intensity of the stimulating radiation field (c.f. equation 2.13), which is up to ~50-fold enhanced for the antisymmetric waveguide mode compared to the diffraction-limited Gaussian (c.f. figure 7.13a,b). Thus, the experimentally detected efficiency enhancement is in accordance with theoretical expectations. Importantly, the enhancement demonstrated here is a broadband enhancement in a waveguide circuit, which is not limited to a specific resonance wavelength.

7.7 CONCLUSION AND OUTLOOK

In conclusion, this chapter demonstrates the efficient coupling of single organic dye molecules to a silver plasmonic waveguide circuit and the first observation of a single quantum emitter's interaction with a sequence of two plasmonic pulses propagating along a waveguide. The statement of single molecules is verified by the observation of clear single-step photobleaching events together with rare blinking events and photon antibunching demonstrated for selected single TDI molecules. By fluorescence widefield imaging upon remote excitation of single TDIs located in the nanogap of the silver two-wire transmission line, an efficient channeling of 68-84 % of the fluorescence emission into the antisymmetric plasmonic waveguide mode is estimated. An emission in the symmetric mode, by contrast, is not observed due to its weak near-field inside the gap. Moreover, the fluorescence lifetime of TDI in the gap is reduced up to nearly one order of magnitude compared to TDI in a thin PMMA film. Both experimental observations are in good accordance with numerical simulations of electric dipole emission, demonstrating the intended efficient coupling of single TDI molecules and the plasmonic waveguide.

A further main achievement of this chapter is the demonstration of a plasmonically-enhanced efficiency for stimulated emission depletion (STED) of a single TDI molecule located in the nanogap of a silver waveguide circuit. To address this issue, first, the STED effect of 21 individual single molecules in a thin PMMA film is quantified with diffraction-limited laser foci. Here, a saturation depletion pulse energy of 1.2 pJ for an optimally in-plane oriented TDI molecule with respect to a linearly polarized depletion focus is determined. Second, single-molecule STED experiments are performed with a TDI located in the nanogap of the silver plasmonic circuit. In particular, both the pump

pulse as well as the depletion pulse arrive at the molecule via a propagating plasmonic mode, realizing a fully remote STED via plasmonic near-fields. An efficient depletion of the fluorescence via the antisymmetric plasmonic mode is found, already entering the saturation regime of the stimulated emission. Together with a detailed estimation of the depletion pulse energy arriving in the antisymmetric plasmonic mode at the molecule, a saturating depletion pulse energy of about 38 fJ is estimated. This value is about 30 times lower than in the free-space reference experiment with a diffraction-limited depletion focus, which is in close agreement with the expected intensity enhancement of the antisymmetric plasmonic mode compared to the diffraction-limited Gaussian focus. Thus, a clear efficiency-enhancement of the single-molecule STED effect is demonstrated by confining the depletion pulses beyond the diffraction-limit. At the same time, the experiment demonstrates a (fluorescence-detected) nonlinear plasmon-plasmon interaction at a single quantum emitter, as the emitter transfers a propagating plasmon polariton from the pump pulse to a propagating plasmon polariton in the depletion pulse, an effect fully absent in linear optics.

It has to be noted that the scope of the measurements performed with single TDIs in the gap were severely limited by a fast photobleaching. While TDI is photostable up to several tens of minutes under linear excitation with pump pulses only (c.f. figure 7.3b), it photobleaches typically within a few seconds during STED experiments in the saturation regime. Thus, this chapter focused on selected proof-of-principle experiments. The fast photobleaching might be related to a non-zero probability of excited state absorption of TDI by the depletion pulse (c.f. discussion in section 7.4) and could be reduced in future experiments by the choice of a different or engineered dye molecule.

This chapter opens new avenues for single-molecule experiments as well as for quantum plasmonics. Cang *et al.* [233] demonstrated that the coupling of dye molecules with a plasmonic nanostructure reduces photobleaching due to the shortened excited state lifetime. The maximum observation time of single molecules in ultrafast nonlinear spectroscopy experiments, such as performed by Liebel *et al.* [226], could thus be enlarged by coupling with a plasmonic nanostructure, allowing for more detailed information to be captured. In particular, by using a plasmonic waveguide instead of a nanoparticle, the background luminescence of the nanostructure at the excitation spot is conveniently spatially separated from the molecule along the waveguide. Even experiments with ultrafast laser pulses of a few 10 fs duration are possible, as the linear chirp imposed on the pulses by 1 µm waveguide equals that of about 100 µm glass, which can be routinely precompensated.

Further engineering of the mode area and transmission of a plasmonic waveguide could push experiments of the coherent nonlinearity of single waveguide-coupled quantum emitters, as performed at cryogenic temperatures by the Sandoghdar and Lodahl groups [30, 209–211], to room temperature. These experiments detect not the fluorescence of the emitter but the coherent transient transmission (or reflection) of the waveguide mode at the quantum emitter. Future experimental concepts in this direction should consider that a pump pulse hitting a silver nanowire waveguide leads

to a strong photothermal modulation of a delayed probe pulse's transmission through the waveguide. This effect was observed in measurements using a chopper-modulation of the pump pulses and a lock-in demodulation of the probe pulse transmission through a single silver nanowire. A relative modulation of the probe transmission at 760 nm linearly increasing with the pump pulse energy was found, reaching a relative modulation of about $5 \cdot 10^{-3}$ at about 60 pJ pump pulse energy. Those very preliminary results are not presented here, as the observation of this effect was also published at the same time by Li *et al.* [234]. The tiny modulation of the probe transmission through the waveguide induced by stimulated emission at a single quantum emitter, by contrast, is expected to be a few 10^{-6} only at the chosen probe wavelength at room temperature. Thus, without applying further concepts to separate the contributions of both effects, the coherent single-molecule stimulated emission signal is hidden behind the much larger photothermal signal. One option could be to use, instead of a chopper-modulation of the pump pulses, a polarization-modulation of the pump pulses. This might allow to modulate the excitation and thus the stimulated emission of the molecule in the gap while achieving a constant, unmodulated photothermal effect of the pump pulses on the probe transmission.

In terms of quantum plasmonic circuitry, the flexible fabrication technique of silver circuits by focused ion beam milling from atomically-smooth, large-area, single-crystalline silver flakes easily allows to add further elements like beam splitters, routers, and interferometers, to finally form a high-quality functional plasmonic circuit. In the future, single molecules in a crystalline host could be deterministically positioned (c.f. Hail *et al.* [235]) at different locations in a plasmonic circuit at positions that offer extreme light-confinement and prospects of quantum optical networks could turn into reality.

8 TOWARD SENSITIVE OPTICAL PROBING WITH NANOSCALE CONFINEMENT

Parts of this chapter are published in *High-Q plasmonic nanowire-on-mirror resonators by atomically smooth single-crystalline silver flakes* by C. Schörner, and M. Lippitz, J. Chem. Phys. **155**, 23, 234202 (2021).

8.1 INTRODUCTION

The confinement of electromagnetic modes deeply beyond the diffraction limit is one of the most exciting and unique features of modern plasmonics. In particular, plasmonic constructs with a nanoscale gap have gained a huge attention, as optical fields can be concentrated into their insulating gap, realizing enormously intense optical near-fields [236]. As demonstrated by the geometry of a silver two-wire transmission line waveguide in chapters 6 and 7, this confinement beyond the diffraction limit strongly enhances the light-matter interaction with single quantum emitters. For the two parallel nanowires, the confinement of the antisymmetric mode propagating in the gap is determined by the separation of the two nanowires, which in turn is limited by the ion beam's focus size used for milling (~50-60 nm for the Ga-ion FIB setup in section 5.6).

However, much smaller gaps between metal nanostructures can be fabricated in lateral direction, for example with He-ion beam milling, realizing sub-5 nm gaps [15], or by self-assembly techniques, reaching values below 0.5 nm [236]. In contrast to the

lateral direction, plasmonic structures can be vertically separated from a plasmonic surface as well, such that the particle interacts with mirror charges in the underlying metal. Typical geometries investigated intensively by the Baumberg group [237] include spheres (*nanoparticle-on-mirror*) and cubes (*nanocube-on-mirror*), while elongated nanowires (*nanowire-on-mirror*) placed on a metal surface are mostly investigated by the Hongxing Xu group [121]. Particularly, the thickness of the insulating gap can be precisely defined down to the nanoscale, e.g., by a controlled deposition of a polymeric film in discrete steps [24, 203], by self-assembled monolayers [237] or by atomic layer deposition [121]. Thus, the plasmonic properties can be precisely tuned by the fabrication process, while the extreme light localization allows for unprecedented sensitivity in sensing applications and enables optical access to atomic-scale phenomena. Prominent examples range from resolving ultra-small environmental changes [121, 238] via single-molecule strong coupling with a nanocavity [22] to light-localization at single adatoms at surfaces ("picocavities") [18]. Strikingly, the Baumberg [239] and Galland group [240] observed, when light is confined to such small scales, that poorly understood dynamical phenomena related to the dynamic restructuring of metal nanoparticle surfaces, atomic-scale lattice defects and light-induced formation of domain boundaries appear. It is thus of great interest, for the realization of ultra-sensitive measurements of quantum emitters inside such confined near-fields, to determine to which degree the near-field enhancement and scattering spectra of the plasmonic modes are affected by those dynamical processes.

This chapter focuses on the geometry of a crystalline silver nanowire in a ~2 nm distance to a single-crystalline silver flake surface, forming a high-quality silver nanowire-on-mirror (NWoM) construct. First, the waveguide mode(s) along the long axis of the nanowire are investigated numerically as a function of the gap-size. A superior confinement of the propagating mode is found, which is highly promising for an extremely efficient coupling with single quantum emitters. Secondly, scattering simulations show that the structures do not only support a propagating mode along the wire but also resonant modes are accessible in transverse direction, being also strongly confined to the gap. Subsequently, nanowire-on-mirror constructs of different geometry are investigated experimentally and characterized by darkfield spectroscopy. High-quality plasmonic resonances are demonstrated with their linewidths reaching the theoretical limit given by numerical scattering simulations. Moreover, a balanced detection setup is presented that allows for optical probing with a sensitivity down to about $1 \cdot 10^{-6}$ at 1 Hz bandwidth. The setup is further constructed for a high mechanical stability and minimum beam-pointing fluctuations. The noise characteristics of the setup are demonstrated at the flat and smooth surface of a silver flake for different optical powers and measurement bandwidths. Finally, nanowire-on-mirror constructs are probed for parallel and perpendicular polarization with respect to the nanowire's long axis, finding enhanced signal fluctuations when a nanocavity is probed resonantly. These measurements demonstrate important steps and first measurements toward an ultra-sensitive optical probing of light-matter interactions within a nanocavity supporting extreme confinement of light. Thus, the insights of this chapter pave the way toward future plasmon-enhanced interferometric scattering experiments of single quantum emitters.

8.2 EXPERIMENTAL SETUPS

The optical measurements presented in this chapter are performed in two separate setups. First, an existing optical setup is used for darkfield spectroscopy to unmask the scattering properties of plasmonic nanowire-on-mirror constructs. Second, a balanced detection setup is constructed that allows for ultra-sensitive optical probing of a sample's reflected light originating from a (close to) diffraction-limited area. Both setups are briefly described in the following.

Darkfield spectroscopy In order to experimentally characterize the fabricated nanowire-on-mirror constructs in terms of their plasmonic cavity resonances, darkfield mircoscopy and spectroscopy are employed. Briefly, the sample is illuminated under high angles (~80°) by a Halogen lamp (U-LH100L-3, Olympus) via a darkfield objective (MPlanFL N BD P, 100×, $NA = 0.9$, Olympus) mounted in a commercial darkfield-compatible microscopy stage (Olympus). The scattered light is collected by the same objective within its numerical aperture (opening half-angle $\arcsin(NA) \approx 64°$) and guided either to an RGB imaging camera (SC30, Olympus) via a beamsplitter or to a spectrometer (Isoplane SCT 320, Princeton Instruments, blaze wavelength 500 nm) equipped with a back-illuminated CCD camera (Pixis 400, Princeton Instruments). The detected spectrum $I_{NWoM}(\lambda)$ is normalized to the spectrum measured at a certified reflectance standard (USRS-99-010, labsphere) $I_{labsphere}(\lambda)$. In both cases, a background spectrum is subtracted, which is measured aside from the considered nanowire-on-mirror $\left(I^{bg}_{NWoM}(\lambda)\right)$ and at a non-illuminated spot at the labsphere $\left(I^{bg}_{labsphere}(\lambda)\right)$, respectively. Thus, the normalized (dimensionless) scattering spectrum is given by

$$I_{scat}(\lambda) = \frac{I_{NWoM}(\lambda) - I^{bg}_{NWoM}(\lambda)}{I_{labsphere}(\lambda) - I^{bg}_{labsphere}(\lambda)} \quad . \tag{8.1}$$

As mentioned, the excitation angle in the darkfield setup is larger than the maximum collection angle of the objective determined by its numerical aperture ($NA = 0.9$). Thus, also plasmonic modes with out-of-plane character are excited.

A stable balanced detection setup As outlined in the introduction, it is an open question to what extent plasmonic resonances confined to a nanometer-scale gap diffuse in their spectral position with time. While rather large, long-term changes of the resonance wavelength can be tracked by darkfield scattering spectroscopy [238], fast and ultra-small changes of the resonance-wavelength demand ultra-sensitive measurement concepts. In the following, a stable balanced detection setup is presented (figure 8.1) that allows for ultra-sensitive (differential) detection of the reflected intensity originating from a (close to) diffraction-limited area on the sample.

As light-source, a single-mode fiber-coupled superluminescent diode (SLD-381 HP, Superlum) is used (center wavelength 797 nm, spectral FWHM 17 nm). After outcou-

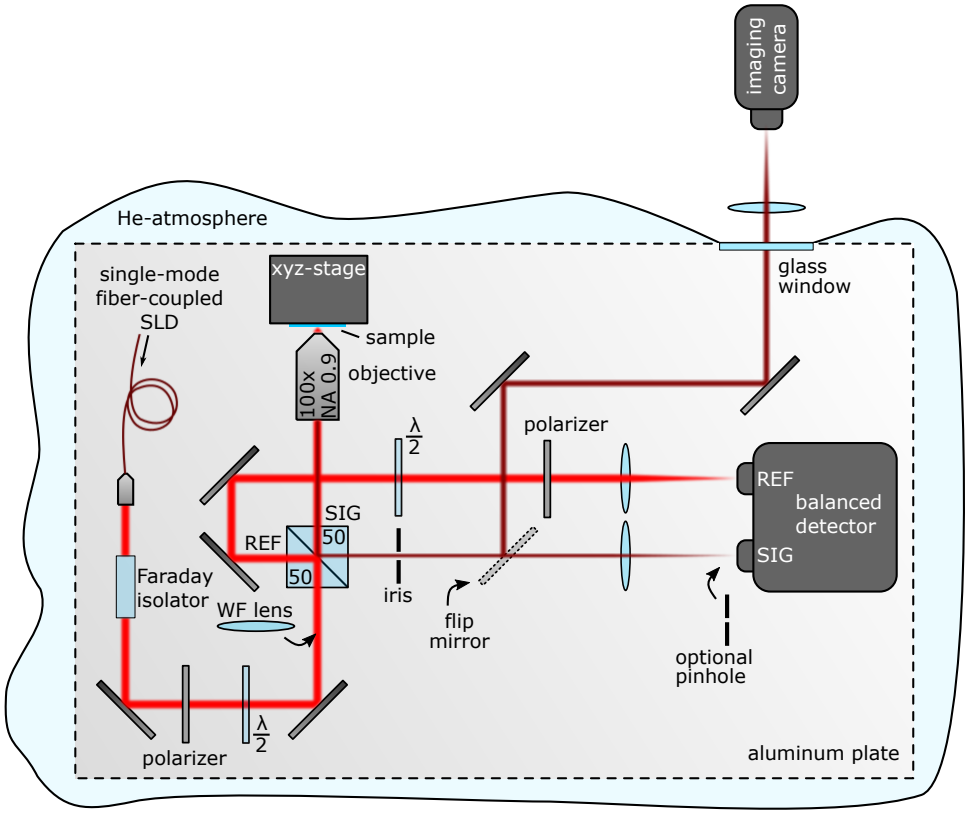

Figure 8.1: Sketch of the developed setup for ultra-sensitive balanced detection constructed on an aluminum plate and placed inside an inflatable polyethylene chamber. The excitation and reference path are displayed in red, while the signal path and the imaging path are skatched in dark red. Explanation see text. Photographs are given in appendix D. Adapted from J. Chem. Phys. **155**, 234202 (2021), with the permission of AIP publishing.

pling to free-space (F220APC-780, thorlabs), a Faraday isolator is passed to prevent any optical feedback of the experiment back into the superluminescent diode. Afterward, a linear polarizer and a half-wave plate define a variable linear polarization direction. Subsequently, the beam is split into a *reference* (REF) and *signal beam* (SIG) at a 50:50 beamsplitter (BS014, thorlabs). The power of the reference beam can be adjusted by a half-wave plate followed by a linear polarizer in front of the reference (REF) input of an auto-balanced photodetector (Nirvana 2007, New Focus). The signal beam, by contrast, is guided to an air-objective (MPlanFL N BD P, 100×, $NA = 0.9$, Olympus) and is focused to a (close to) diffraction-limited spot on the sample. The reflected light is collected by the same objective and reflected by the beamsplitter toward the signal (SIG) input of the Nirvana photodetector. For imaging purposes, the reflected light can alternatively be guided via a flip mirror to an sCMOS imaging camera (Zyla 4.2, Andor, tube lens 200 mm). A widefield lens (WF lens) can be flipped in the light path in front of the objective to obtain a large-area illumination of the sample. In some cases, broadband visible light is used for imaging to obtain better contrast between certain nanowire-on-mirror structures and the underlying silver flake. The sample including the nanostructures of interest can be positioned manually with a stable mechanical

xyz-stage (MDE122, Elliot Martock) with high-precision adjusters providing 20 nm of adjustment resolution and 2 mm of travel in each direction. This way, the nanostructures of interest can be brought in the area of the light-focus for optical investigations. Note that no additional piezo actuator is used for maximum mechanical stability of the sample relative to the objective. The main balanced detection setup is further fixed on a separate aluminum plate (thickness 10 mm, size 55 cm × 40 cm) with a light beam height of only 25 mm above the plate's surface to ensure high mechanical stability of the optical elements (c.f. photograph in appendix D, figure D.1). Furthermore, the whole aluminum plate can be placed in an inflatable polyethylene chamber with built-in gloves for manual adjustments within the chamber (AtmosBag Z530204, Sigma-Aldrich). An additional home-built glass-window in the chamber allows to place the imaging camera outside this chamber to avoid any turbulent gas flow inside the chamber caused by the camera fan. Moreover, the chamber can be inflated with helium gas at atmospheric pressure. Helium gas offers a refractive index much closer to unity ($n_{He} = 1.000036$) than that of air ($n_{air} = 1.000293$), with a concomitant lower change of its refractive index to changes in its pressure. Thus, density fluctuations of the helium gas inside the chamber are expected to cause smaller deflections of the light beam [241].

Interferometric scattering detection Placing a nanoscale object into a beam of light will lead to a certain amount of scattering of light by that object. According to the optical theorem, the resulting extinction of the incident beam is determined by the interference of the incident field and the scattered field. Notably, this concept holds true also for a reflection measurement. Besides the replacement of the incident field by a reflected field, in both a transmission and a reflection configuration, the interference with the scattered field determines the extinction signal [242]. In total, an intensity I_{SIG} is detected, resulting from the interference between the reflected field E_{refl} and the scattered field E_{scat} according to [242, 243]

$$I_{SIG} \propto \int\int |E_{refl} + E_{scat}|^2 dxdy = |\bar{E}_{refl}|^2 + |\bar{E}_{scat}|^2 + 2\bar{E}_{refl}\bar{E}_{scat}|\alpha|\cos(\phi) \quad . \tag{8.2}$$

Here, the bars indicate the positive amplitudes of the fields, ϕ is the phase angle between reflected and scattered field, and α is a complex (spatial) mode overlap factor between the two fields on the detector ($|\alpha| \leq 1$). The latter can be optimized by putting a confocal pinhole in front of the detector [242]. Note that equation 8.2 assumes full temporal coherence of the two fields. The importance of equation 8.2 is the fact that the weak scattering field from the nano-object can be amplified by the strong reflected field from the sample interface. Thus, this concept has developed into an important imaging technique, termed *interferometric scattering* (iScat) *microscopy*, capable of detecting extremely weak scattering signals [244], e.g., of single metal nanoparticles observed by Lindfors *et al.* [245], single quantum dots investigated by Kukura *et al.* [242] or single molecules detected by the Sandoghdar group [41, 42].

Nirvana operation principle As reviewed by the Orrit group [243], small changes of the detected intensity in equation 8.2 can be easily hidden in noise originating

from photon shot noise, power fluctuations of the light source and electronic detection noise. In order to eliminate the output power fluctuations of the light source ("intensity noise"), a balanced detection scheme is applied. The Nirvana detector reduces common mode noise, i.e., the noise common to both the signal and reference channel, typically by over 50 db from DC to 125 kHz. More specifically, the Nirvana's common-mode rejection ratio CMRR is defined according to the manufacturer by [246]

$$\mathrm{CMRR} = 20 \cdot \log_{10}\left(\frac{V_{common-mode}}{V_{auto-balanced}}\right) \quad , \tag{8.3}$$

where $V_{common-mode}$ is the detector output voltage proportional to the (common-mode) light power on the reference and signal photodiodes at a specific frequency, and $V_{auto-balanced}$ is the corresponding output voltage in auto-balanced mode.

The Nirvana uses auto-balance circuitry with a low-frequency feedback loop that adjusts the gain of the reference photodiode to exactly balance both the signal and reference photocurrents. For optimum performance, the reference photodiode should receive about twice the optical power of the signal photodiode. The speed of the auto-balancing effect is determined by the gain-compensation cutoff frequency f_{cut}, which can be thought of as the inverse of time required for the circuitry to adjust to power changes in the reference or signal channel. This cutoff frequency f_{cut} must be below any modulation frequency for best noise cancellation. It depends on the optical power in both signal P_{SIG} and reference channel P_{REF}, and on the setting of a loop bandwidth knob on the Nirvana detector (c.f. Nirvana manual [246]). The latter is fixed to the maximum value of 100 in the following, yielding $f_{cut} \approx 1.35\,\mathrm{kHz}$ at $P_{SIG} = 100\,\mu\mathrm{W}$ and a power ratio of $P_{REF}/P_{SIG} = 2$.

The LOG-output of the Nirvana is fed into a low-noise voltage preamplifier (SR560, Stanford Research Systems) with an amplification set to $1 \cdot 10^3$. A built-in low-pass filter (roll-off -20 dB/decade) is enabled with a filter corner (cutoff) frequency f_c set in the range 1 Hz to 1 kHz, being lower than f_{cut} of the Nirvana, defining the final measurement bandwidth. This way, tiny output voltage fluctuations of the Nirvana LOG-output are amplified and pushed above the electronic detection noise of the voltage amplifier and data acquisition electronics (ADwin-Gold, Jäger). This detection noise is determined in a separate measurement where the voltage amplifier input is terminated by a 50 Ω resistor, yielding a recorded root-mean-square (rms) noise of 2.3 mV. Divided by the amplification factor, this corresponds to a detection noise

$$\sigma_{det} = 2.3\,\mu\mathrm{V} \quad , \tag{8.4}$$

at the level of the Nirvana LOG-output, which was recorded independent of f_c, and represents a limit for the minimum output voltage fluctuation of the Nirvana that can be detected. In the following, all voltage levels will be given at the level of the Nirvana output, i.e., the measured voltage is divided by the amplification factor $1 \cdot 10^3$.

Sensitivity of the Nirvana LOG-output The voltage U at the Nirvana detector's LOG-output at room temperature (from DC to f_{cut}) is given by [246]

$$U = -\ln\left(\frac{P_{REF}}{P_{SIG}} - 1\right) \cdot 1\,\mathrm{V} \quad , \tag{8.5}$$

with P_{REF} and P_{SIG} being the optical power in the reference and signal channel of the detector. The expected voltage change dU as a result of (uncorrelated) power fluctuations dP_{REF} and dP_{SIG} in both channels is thus given by

$$dU = \left[\frac{P_{REF}}{P_{SIG}} - 1\right]^{-1} \sqrt{\left(\frac{dP_{REF}}{P_{SIG}}\right)^2 + \left(\frac{P_{REF}\,dP_{SIG}}{P_{SIG}^2}\right)^2} \cdot 1\,\mathrm{V} \quad . \tag{8.6}$$

Assuming an experiment where the dominant optical power fluctuations appear in the signal channel involving the optical path to the sample, the voltage change dU at the LOG-output due to the power fluctuation dP_{SIG} reads as

$$dU = 2\frac{dP_{SIG}}{P_{SIG}} \cdot 1\,\mathrm{V} \quad , \tag{8.7}$$

at an optical power ratio $P_{REF}/P_{SIG} = 2$. Thus, an optical power fluctuation in the signal input of the Nirvana results in a proportional voltage change at the detector's LOG-output.

8.3 NOISE CHARACTERISTICS AND SHOT NOISE LIMIT

After having discussed the fundamentals of the balanced photodetector, this section characterizes the experimentally achieved noise levels, including a comparison to the expected shot noise limit.

Shot noise limit The optical powers P_{SIG} and P_{REF} in the signal and reference channel of the Nirvana result in photocurrents I that are proportional to the respective optical power P according to [247]

$$I = \frac{P\lambda}{hc}\eta e \quad , \tag{8.8}$$

where hc/λ is the photon energy, η is the quantum yield of the detector and e is the elementary charge. For the Nirvana 2007, the photodiode responsivity is typically about $R_{PD} = 0.5\,\mathrm{A/W}$ at 800 nm wavelength [246], yielding a photocurrent $I = P \cdot R_{PD}$. This photocurrent features a squared rms shot noise I_{SN}^2 which is given by the Schottky-relation [61, 247]

$$I_{SN}^2 = 2eI\Delta f \quad , \tag{8.9}$$

with the frequency bandwidth Δf. The uncorrelated shot-noise-induced photocurrent fluctuations in the signal and reference channel of the Nirvana result in shot-noise-induced voltage fluctuations at the Nirvana LOG-output, which can be calculated with equation 8.6 considering the proportionality of the photocurrents with their respective optical power. As an example, at a wavelength $\lambda = 800\,\text{nm}$ with optical powers $P_{SIG} = 100\,\mu\text{W}$ and $P_{REF} = 200\,\mu\text{W}$, the shot-noise-induced voltage fluctuations at the Nirvana LOG-output are given by

$$\sigma_{SN} \approx 2.0 \cdot 10^{-7} \frac{\text{V}}{\sqrt{\text{Hz}}} \quad , \tag{8.10}$$

which amounts to about $\sigma_{SN} = 6.2\,\mu\text{V}$ at a bandwidth of $\Delta f = 1\,\text{kHz}$. Actually, when a low-pass filter defines the measurement bandwidth as in the used setup, for noise calculations not the filter cutoff frequency f_c but the equivalent noise bandwidth (ENBW) Δf_{ENBW} needs to be considered as bandwidth Δf. The ENBW is defined as the bandwidth of a brickwall filter transmitting the same integrated white noise power as that of the considered real filter. In case of a low-pass filter of first order (roll-off -20 db/decade) with cutoff frequency f_c, the equivalent noise bandwidth is calculated via [247]

$$\Delta f_{ENBW} = \frac{\pi}{2} f_c \quad . \tag{8.11}$$

Thus, at $f_c = 1\,\text{kHz}$, for the example discussed above, the expected shot-noise-induced voltage fluctuations amount to about $\sigma_{SN} = 8\,\mu\text{V}$ rms.

Noise characteristics of the setup In the following, the output voltage noise levels of the setup are characterized and the influence of important measurement parameters such as the optical power in the signal channel P_{SIG} and the measurement bandwidth Δf are studied. Output voltage time traces are recorded while the focus of the signal beam is fixed to a smooth and clean position on a silver flake.

First, the influence of the measurement bandwidth on the recorded noise level at the LOG-output of the Nirvana is studied. At a fixed optical power in the signal input of the Nirvana $P_{SIG} = 100\,\mu\text{W}$ ($P_{REF} = 200\,\mu\text{W}$), output time traces are recorded for varying low-pass cutoff frequency in the range $f_c = 1\,\text{Hz}\ldots1\,\text{kHz}$ (figure 8.2a). The output voltage features noise which, particularly for the time trace recorded at $f_c = 1\,\text{kHz}$, nearly resembles the appearance of pure white noise [247]. This property is also verified by a rather flat Fourier transformation of the time trace. Furthermore, a reduction of f_c results in a reduced noise level. Randomly appearing voltage-spikes with positive and negative sign are observed in the voltage time traces (e.g. figure 8.2a, bottom time trace at 33 s). The amount and the amplitude of the spikes reduced with the time leaving the setup untouched and, particularly, the spikes were nearly absent in He-atmosphere. Thus, they are attributed to small dust particles diffusing through either the signal or reference beam and settling slowly under the influence of gravity. When such a differential, time-varying loss appears only in one of the two optical paths, it will be detected by the Nirvana. Some voltage spikes feature

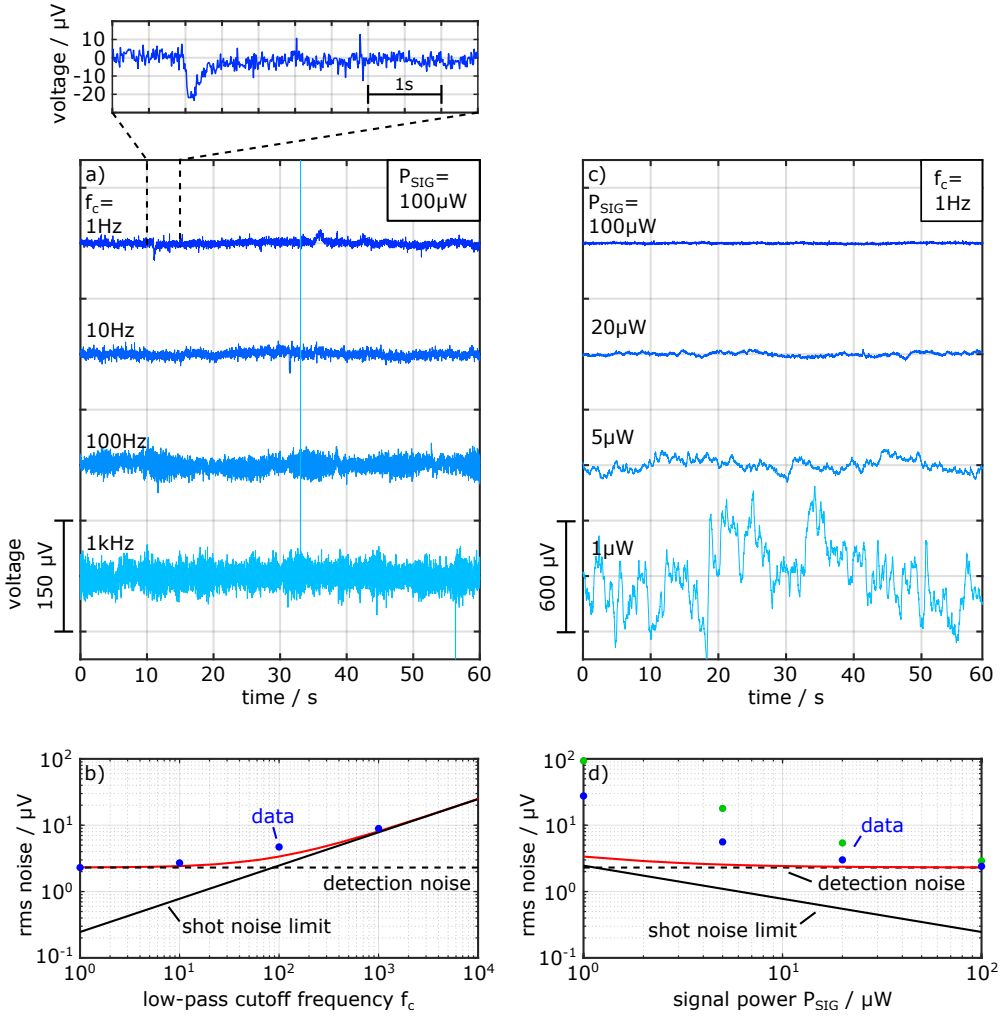

Figure 8.2: (a) Output voltage time trace recorded with the SLD-focus at a smooth silver flake surface with $P_{SIG} = 100\,\mu W$ signal power as a function of the bandwidth varied via the low-pass cutoff frequency f_c. Top: Zoom to an output voltage fluctuation with an amplitude of -20 µV. (b) Determined minimum rms noise levels from the time traces shown in (a) evaluated within a 2 s time span (blue dots, c.f. text) compared to the calculated shot noise level (solid black line), the detection noise (dashed black line) and the square root of the sum of the squares of both (red line). (c) Output voltage time traces at $f_c = 1\,Hz$ as a function of the signal power P_{SIG}. (d) Determined minimum rms noise levels from the time traces shown in (c) (blue dots 2 s and green dots 10 s time span, c.f. text) compared to the calculated shot noise level (solid black line), the detection noise (dashed black line) and the square root of the sum of the squares of both (red line). All time traces in (a) and (c) are recorded with the setup in He-atmosphere sampled each 10 ms and are corrected by a linear offset.

an output voltage amplitude of only -20 µV (c.f. figure 8.2a, top inset, detected with $f_c = 1\,\text{Hz}$). According to equation 8.7, such an output voltage change corresponds to a relative power fluctuation of only -10^{-5} in the signal path[1] and is detected here with a signal-to-noise ratio of close to 10. To quantify the recorded noise levels, the rms noise is evaluated in all possible 2 s time spans within a time trace and the minimum of the noise values is determined for each setting of f_c (figure 8.2b, blue dots). While for $f_c = 1\,\text{Hz}$ a noise level close to the detection noise of $\sigma_{det} = 2.3\,\mu\text{V}$ rms is detected (figure 8.2b, black dashed curve), at $f_c = 1\,\text{kHz}$, a noise level limited by the above-calculated shot noise of $\sigma_{SN} = 8\,\mu\text{V}$ rms is observed (figure 8.2b, black solid curve). The noise levels calculated within the full 60 s time trace are slightly larger due to environmental influences on the signal, such as dust particle spikes and coupling of acoustic signals into the setup.

A second important parameter for the best performance of the Nirvana detector is the optical power in the signal path P_{SIG}, which is varied at a fixed setting $f_c = 1\,\text{Hz}$ and time traces of the output voltage are recorded (figure 8.2c). While at $P_{SIG} = 100\,\mu\text{W}$ the noise is limited by the electronic detection noise as mentioned before, reducing P_{SIG} down to 1 µW leads to a strong increase of the detected noise (figure 8.2b, bottom time trace), which resembles the appearance of flicker noise [247]. Again, the minimum rms noise from all possible 2 s and 10 s time spans of each time trace is determined (figure 8.2d, blue and green dots, respectively). Importantly, the calculated noise increases for decreasing optical signal power P_{SIG} to levels significantly above the expected shot noise and detection noise. Therefore, an additional noise contribution not considered so far appears. Specifically, as the signal power is reduced, the Nirvana's common-mode rejection ratio strongly decreases [246]. As a consequence of the degraded noise-canceling performance of the Nirvana, the intensity noise of the superluminescent diode cannot be canceled completely and thus appears (in part) at the output of the Nirvana. In the considered low-frequency range, the output of a superluminescent diode is dominated by "1/f" noise (flicker noise) [248], which results in the observed increased flicker noise contribution at the Nirvana output (c.f. figure 8.2b, bottom time trace).

Thus, to obtain the lowest possible noise, the following two points need to be considered. First, the experiment should be performed at high optical power in the signal input P_{SIG} to ensure the best common-mode rejection ratio of the Nirvana, as far as the optical power is compatible with the nanostructure under investigation. Secondly, the measurement bandwidth needs to be chosen as a compromise between tolerable noise level and temporal resolution. At $P_{SIG} = 100\,\mu\text{W}$ and $f_c = 1\,\text{kHz}$, a shot-noise-limited voltage noise of about 8 µV rms is achieved. For smaller settings of f_c, noise levels of down to 2.3 µV rms are possible, limited by the detection noise. Notably, such a tiny output voltage noise allows to detect ultra-small relative fluctuations of the signal beam power by $1 \cdot 10^{-6}$ (c.f. equation 8.7), which is a sensitivity sufficient to detect the extinction of light by single quantum dots or even single molecules [41, 42, 242].

1 The voltage amplitude of -20 µV and the temporal shape of the fluctuation might be limited by the impulse response function of the detection system, which has a time constant $\frac{1}{2\pi f_c} \approx 0.16\,\text{s}$ at $f_c = 1\,\text{Hz}$.

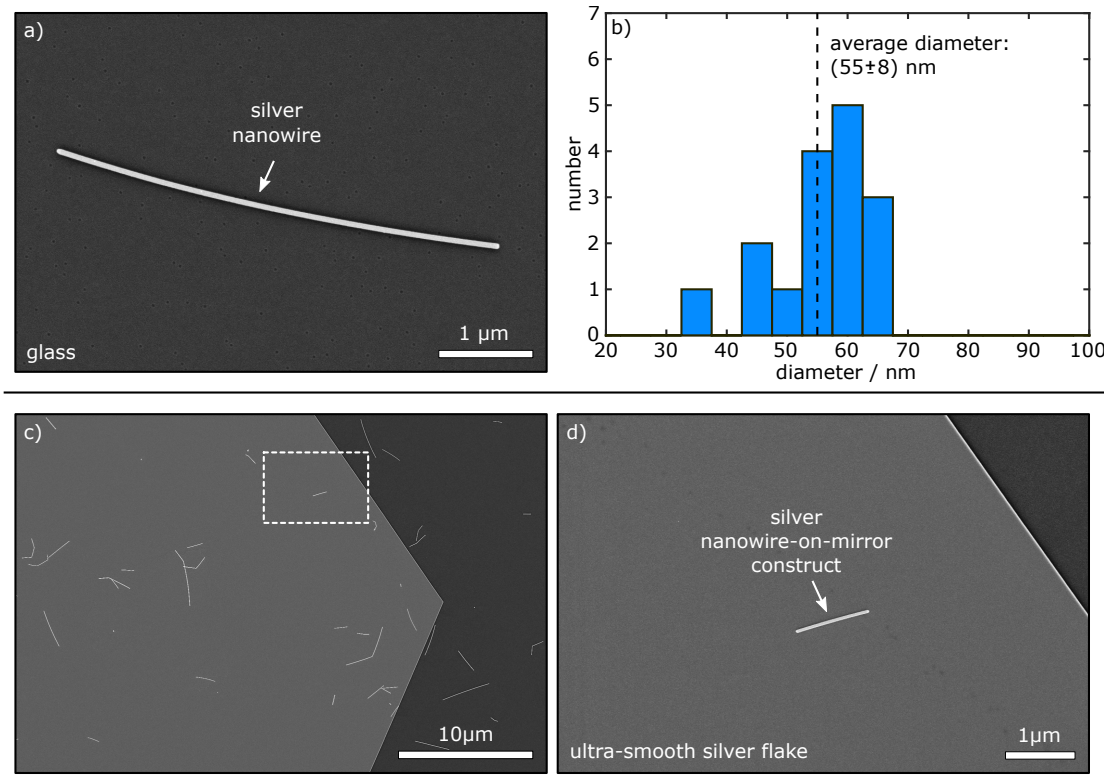

Figure 8.3: (a) Scanning electron micrograph of a typical silver nanowire on glass. (b) Histogram of the diameter of isolated nanowires determined by SEM imaging. The average diameter is (55 ± 8) nm and the length is typically a few µm. (c) Scanning electron micrograph of a smooth and clean silver flake with silver nanowires attached to the surface. (d) Isolated silver nanowire on the flake surface termed silver nanowire-on-mirror construct. Panel (d) is a zoom-in to the area marked by the white dashed line in (c). The samples were sputtered with 1.6 nm Pt after all optical measurements and before SEM imaging.

8.4 SILVER NANOWIRE–ON–MIRROR CONSTRUCT

Two silver structures in nanoscale proximity to each other offer the possibility of extreme light confinement in the insulating gap between the two, enabling the study of atomic-scale phenomena in the gap [239, 240] and the perspective to enhance light-matter interactions with quantum emitters. Silver nanowire-on-mirror constructs particularly feature multiple functionalities, as they offer both propagating waveguide modes along the long axis of the nanowire and also plasmonic resonances oscillating in a transverse plane that are strongly confined to the few-nanometer gap.

Fabrication of nanowire-on-mirror constructs Nanowire-on-mirror constructs are fabricated based on single-crystalline silver flakes (synthesis protocol #2, c.f. section 5.2), which provide an atomically-smooth surface, and commercially available silver nanowires (PL-AgW100-IP-25m, PlasmaChem). These wires have a five-fold twinned

crystal structure, which results in a pentagonal cross-section with {100} side facets, and typically are a few µm long with a diameter ranging from 30 nm to 70 nm (figure 8.3a,b). A diluted solution in isopropanol (1:10 stock solution) is drop cast on a silver flake sample and very gently rinsed with ethanol and dried with N_2-gas. If needed, a spacer layer on the silver flakes (e.g., PMMA) can be introduced before placement of the nanowires. The wires themselves are coated by a poly-(vinylpyrrolidinone) (PVP) surface layer, which is employed as a capping agent during synthesis to ensure a one-dimensional growth. The thickness of such a PVP coating can range from 1-2 nm [121, 237] up to 10-20 nm [249]. Wang *et al.* [249] showed that, after washing with ethanol as applied here, a typical PVP thickness of a nanowire is a few nanometers. The corners of such metal nanowires are typically rounded to some degree. In the following, a rounding radius of 20 % of the wire diameter is assumed in simulations, which is similar to experimental high-resolution transmission electron microscopy data of a gold nanowire's cross-section from Chen *et al.* [121]. Due to the high crystallinity of the silver nanowires used here, their surface is typically ultra-smooth. Together with the atomically-smooth surface of the supporting silver flake (c.f. section 5.5), the nanowire-on-mirror geometry features two parallel, ultra-smooth and flat surfaces. The separation of the surfaces, i.e., the gap-size, is given by the PVP coating layer (and optional additional spacer layers). This way, isolated and clean nanowire-on-mirror constructs of defined geometry are fabricated (figure 8.3c,d).

Waveguide modes In the case of two parallel silver nanowires considered in chapters 6 and 7, the waveguide modes hybridize into the propagating antisymmetric and symmetric mode. Analogously, a silver nanowire in nanoscale separation to a silver flake surface interacts with mirror charges in the underlying silver surface. As a result, similar to the case of the two parallel nanowires, two propagating hybrid modes are formed. One propagating mode is localized at the top corner of the nanowire, which, however, is not considered further due to a huge mode area. More interestingly, the second mode is propagating in the nanoscale insulating gap between the wire and the underlying surface, offering an extreme confinement of the near-field.

Compared to the two-wire transmission line with a gap of 60 nm limited by the fabrication procedure (c.f. chapters 6 and 7), nanowire-on-mirror structures can be fabricated with much smaller gaps and with a concomitant superior confinement of the waveguide mode to the gap. In case of a 60 nm diameter silver nanowire in a 10 nm distance to a silver surface, an emitter's decay rate into the propagating plasmonic mode γ_{pl} surpasses several hundred times the vacuum decay rate γ_0 (figure 8.4a). The optimum emitter orientation is vertical in this case, as this is the direction of strongest near-field in the gap. As a result of the extreme light confinement, emission rates of quantum emitters are strongly enhanced and photons are channeled extremely efficiently into the waveguide. The emitter-waveguide coupling efficiency, i.e., the β-factor, reaches values close to unity for well-positioned emitters. Kumar *et al.* [179] investigated this efficient coupling numerically and demonstrated experimentally the excitation of this waveguide mode for nanowires of ~100-200 nm diameter and a gap-size of around 16 nm where nitrogen-vacancy centers in diamonds were placed.

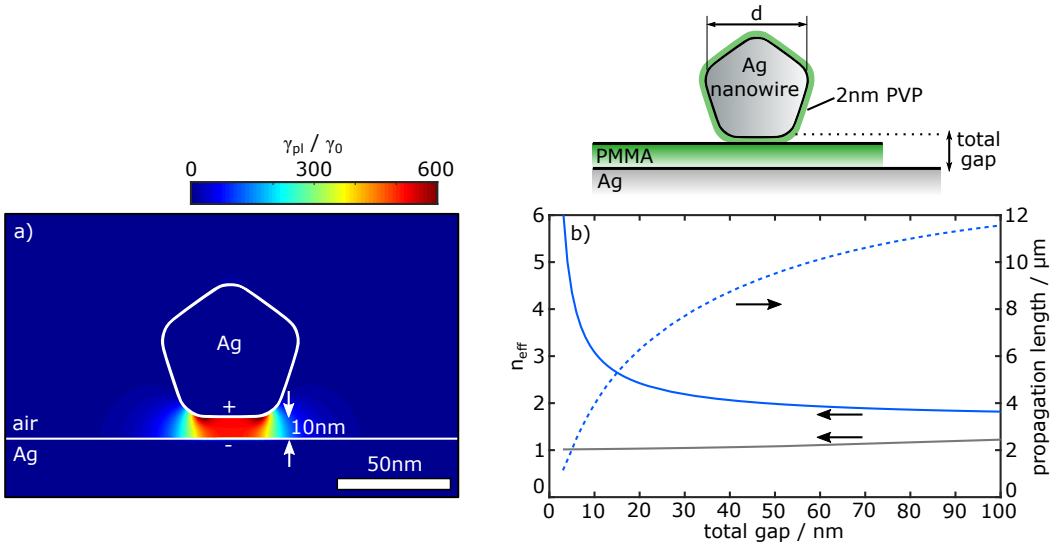

Figure 8.4: (a) Simulated decay rate of a vertically oriented emitter (electric dipole) into the plasmonic waveguide mode propagating in the gap along the long axis of a nanowire-on-mirror (γ_{pl}) normalized to the decay rate in vacuum (γ_0). A nanowire with $d = 60\,\text{nm}$ diameter and 10 nm air gap is considered exemplarily at $\lambda_0 = 800\,\text{nm}$. (b) Real part of the effective mode index n_{eff} (blue, solid) and propagation length (blue, dashed) of the propagating gap-mode as a function of the total gap-size between the silver wire and surface ($\lambda_0 = 800\,\text{nm}$). The total gap consists here of a PMMA layer and a 2 nm PVP layer coating the nanowire (c.f. top sketch). A second propagating mode localized mostly at the top corner of the nanowire is not considered further here (gray line).

According to the simulations presented here, as the gap decreases further, i.e., the confinement is enhanced, the real part of the effective mode index n_{eff} for the propagating waveguide mode increases (figure 8.4b, solid blue line). Particularly, for gap-sizes well below 10 nm, values far beyond $n_{eff} = 3$ are reached and thus the surface plasmon polariton wavelength λ_0/n_{eff} gets much smaller than the free space wavelength λ_0. As the plasmonic confinement is inevitably linked to loss, the propagation length of the waveguide mode decreases as the gap shrinks down (figure 8.4b, dashed blue line).

Cavity plasmon resonance For tiny gap-sizes far below 10 nm, it becomes clear from figure 8.4b that the construct becomes inappropriate as long-range plasmonic waveguide along the long nanowire axis because the propagation length eventually drops below 1 µm. Therefore, the waveguide mode along the long nanowire axis is not considered further. At the same time, when the gap approaches the few-nanometer scale, the surface plasmon polariton wavelength λ_0/n_{eff} of the propagating mode in the gap becomes comparable to the bottom facet width of the nanowire. When the waveguide mode propagates not along the long nanowire axis but along the short axis of the nanowire's bottom facet, it gets reflected multiple times at the opposing facet edges forming a nanoscale Fabry-Pérot cavity for propagating gap-plasmons. For a certain combination of bottom facet width, gap-size and free-space wavelength λ_0, a

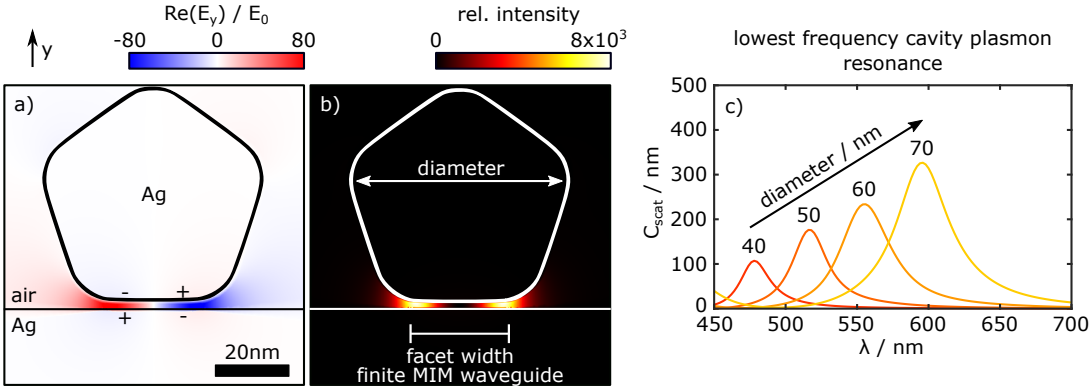

Figure 8.5: (a) Simulated real part of the out-of-plane y-component of the total electric field in a nanowire-on-mirror cavity. The structure is excited from top ($\alpha = 0°$) with a plane wave of amplitude E_0 polarized along the short nanowire axis. A 60 nm diameter silver nanowire without cover layer with a 2 nm air-gap to the silver surface is considered. (b) Corresponding total near-field intensity relative to the incident plane wave. The bottom facet width of the NWoM represents a finite metal-insulator-metal (MIM) waveguide cavity. (c) Scattering cross-section per length of the nanowire-on-mirror evaluated in a solid angle corresponding to $NA = 0.9$ for a wire diameter of 40-70 nm. Both panels (a) and (b) are displayed on the lowest frequency cavity plasmon resonance at 555 nm. Adapted from J. Chem. Phys. **155**, 234202 (2021), with the permission of AIP publishing.

standing wave pattern builds up in the gap along the short nanowire axis. Particularly, the lowest frequency standing-wave pattern, confined to the few-nanometer gap, can be observed as a sharp resonance peak in scattering experiments. As demonstrated by Jiang *et al.* [250], it is excited and detected exclusively with a polarization perpendicular to the long axis of the nanowire, i.e., along the short axis. The system along the short nanowire axis forms a defined metal-insulator-metal (MIM) waveguide nanocavity, where the MIM waveguide mode continuum in the gap is reshaped into discrete states. The resonance wavelength depends linearly on the nanowire diameter but also nonlinearly and very sensitively on changes of the gap-size, as shown by Chen *et al.* [121].

The behavior of the lowest frequency nanocavity mode of the nanowire-on-mirror construct can be studied with the two-dimensional numerical scattering model described in subsection 4.1.1. When exciting a 60 nm nanowire with 2 nm vacuum spacing to a silver surface with a plane wave incident from the top ($\alpha = 0°$), the lowest frequency cavity resonance can be observed by strong, resonantly enhanced near-fields featuring one node along the nanowire's bottom facet (figure 8.5a). Correspondingly, the near-field intensity at two positions in the gap close to each of the two facet edges is strongly enhanced relative to the incident plane wave (figure 8.5b). Evaluating the scattered power in a solid angle corresponding to $NA = 0.9$ from top as a function of the incident wavelength, the scattering cross-section per length of the wire is calculated, featuring a clear resonance that red-shifts for increasing diameter (figure 8.5c).

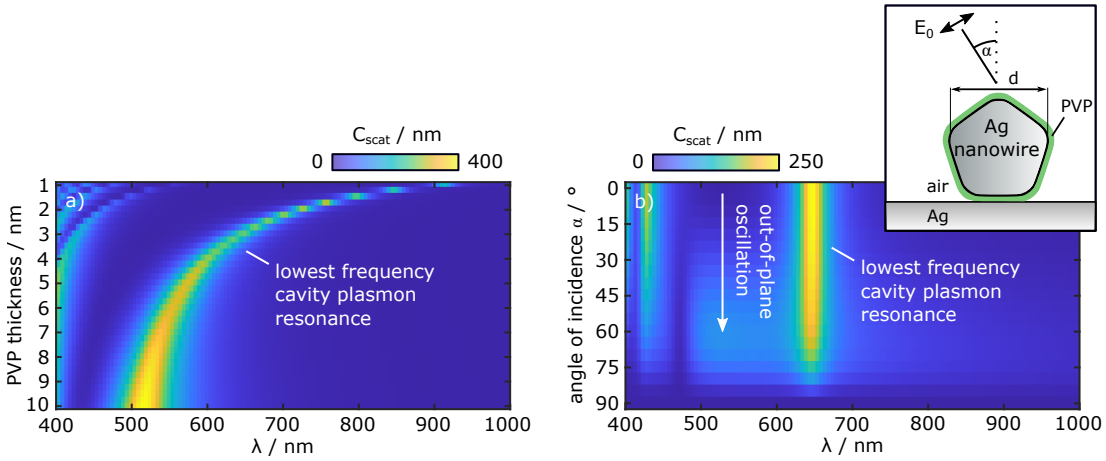

Figure 8.6: (a) Simulated scattering cross-section C_{scat} per length of the nanowire-on-mirror structure as a function of the PVP surface cover thickness, i.e., the gap-size (c.f. sketch in the inset of (b)). The structure ($d = 60\,\text{nm}$) is excited from top ($\alpha = 0°$) with a plane wave polarized along the short nanowire axis and the scattered power is evaluated in a solid angle corresponding to $NA = 0.9$ from top. (b) Simulated scattering spectrum with 3 nm PVP layer as a function of incident angle α from 0° to 90° with p-polarized excitation (c.f. inset). Details see text. Adapted from J. Chem. Phys. **155**, 234202 (2021), with the permission of AIP publishing.

The spectral position of this resonance is strongly sensitive to the size and material of the gap. Taking into account the PVP surface layer that separates the nanowire from the supporting silver surface leads to a red-shift of the cavity resonance compared to a vacuum gap. For decreasing thickness of the PVP layer, i.e., for decreasing gap-spacing, the cavity resonance strongly red-shifts across the visible spectrum into the near-infrared region (figure 8.6a). For a 60 nm wire with 3 nm PVP layer, the lowest frequency cavity resonance is located at about 630 nm, while for lower wavelengths at ~420 nm a higher-order standing wave resonance appears (figure 8.6b, $\alpha = 0°$). As a function of increasing angle of incidence α of the exciting plane wave, these modes continuously decrease in scattering intensity while keeping their spectral position. Moreover, in the spectral range between the mentioned modes (at ~530 nm), a scattering feature of non-Lorentzian shape appears with a maximum scattering at about $\alpha = 60\,°$ (figure 8.6b). A clear dip in the far-field scattering spectrum remains at about 470 nm. Such behavior is linked to hybridization of different modes, which, e.g., can lead to constructive interference in the near-field but destructive interference in the far-field. Such hybridization effects are demonstrated in the literature for a nanoparticle- and nanocube-on-mirror nanocavity, respectively, by Tserkezis et al. [251] and Chikkaraddy *et al.* [237]. To perform such an analysis, a deconvolution into the underlying basis states is needed, which, however, is beyond the coverage of the used numerical scattering model.

In total, the lowest frequency nanocavity resonance is most efficiently excited by a horizontal input field, while blue-shifted from its resonance, a mode appears that is best excited with higher angles of incidence ($\alpha \approx 60°$), signaling an out-of-plane plasmon oscillation (vertical dipole) [237]. Noteworthy, a resonantly driven nanowire-on-mirror

mode is not only source of far-field scattering but is also an efficient source of surface plasmons propagating at the metal-air interface away from the nanowire [252].

Characterization of fabricated nanowire-on-mirror cavities In the following, the experimental scattering behavior of fabricated nanowire-on-mirror constructs is presented exemplarily for NWoM #1 and #2, which feature a wire diameter of about 40 nm and 60 nm, respectively (figure 8.7a,b). In the darkfield microscope, the nanowire-on-mirror constructs appear colorful, clearly separated from the dark background of the silver surface (figure 8.7c,d, inset). Typically, the center of the wire is imaged with a constant color along the long wire axis. In most cases, this feature is surrounded by a halo of different color (figure 8.7c, inset). In other cases, either only the central feature is observed (typically green) or only the halo feature is visible on the camera (figure 8.7d, inset).

The corresponding darkfield spectra show a prominent peak in the visible to near-infrared region, i.e., at 617 nm for NWoM #1 and 764 nm for NWoM #2 (figure 8.7c,d). Blue-shifted with respect to that peak, a different scattering feature appears with a maximum at about 500 nm (570 nm) for NWoM #1 (#2). Comparing the spectra with the darkfield image, it becomes clear that the lowest frequency peak is responsible for the central color of the wire in its darkfield image. By contrast, the blue-shifted feature appears as a green (yellow) halo in the darkfield image of NWoM #1 (#2).

Two-dimensional scattering simulations of the nanowire-on-mirror constructs with the numerical model described in subsection 4.1.1 support the experimental data using the measured wire diameters and sub-2 nm PVP layers (figure 8.7c,d, black dashed line, 80° angle of incidence, p-polarized). Particularly, the lowest frequency scattering peak can be attributed to the cavity resonance displayed in figure 8.5a,b. The blue-shifted scattering feature is related to an out-of-plane plasmon oscillation that is efficiently excited by high angles of incidence (c.f. figure 8.6b). This out-of-plane character further manifests itself in the halo-like appearance in the darkfield images. Analogously to the doughnut-like point spread function of an out-of-plane dipole (c.f. section 4.3), the out-of-plane character results in the halo appearance with a minimum of the intensity in the center of the wire's darkfield image.

The shifted spectral positions of the lowest frequency cavity plasmon resonances of the two different nanowire-on-mirror constructs are, besides slight variations in the PVP layer thickness, mainly explained by the varying wire diameter, resulting in a varying cavity length that changes the resonance wavelength (c.f. figure 8.5c). Noteworthy, the experimentally observed linewidth of the cavity resonance approaches the limit given by the simulations (c.f. figure 8.7c,d), which is only possible for an extraordinarily high surface quality [121] of both the silver nanowire and the supporting single-crystalline silver flake. Furthermore, the resonance linewidth (FWHM = 82 meV at 1.62 eV for NWoM #2) is lower compared to all NWoM systems reported in the literature by the Hongxing Xu group, which (partly) incorporate gold instead of silver, e.g., of silver nanowires on a gold film (FWHM = 110 meV at 1.61 eV) [121] or a gold nanowire on a gold film (FWHM > 155 meV at 1.76 eV) [250].

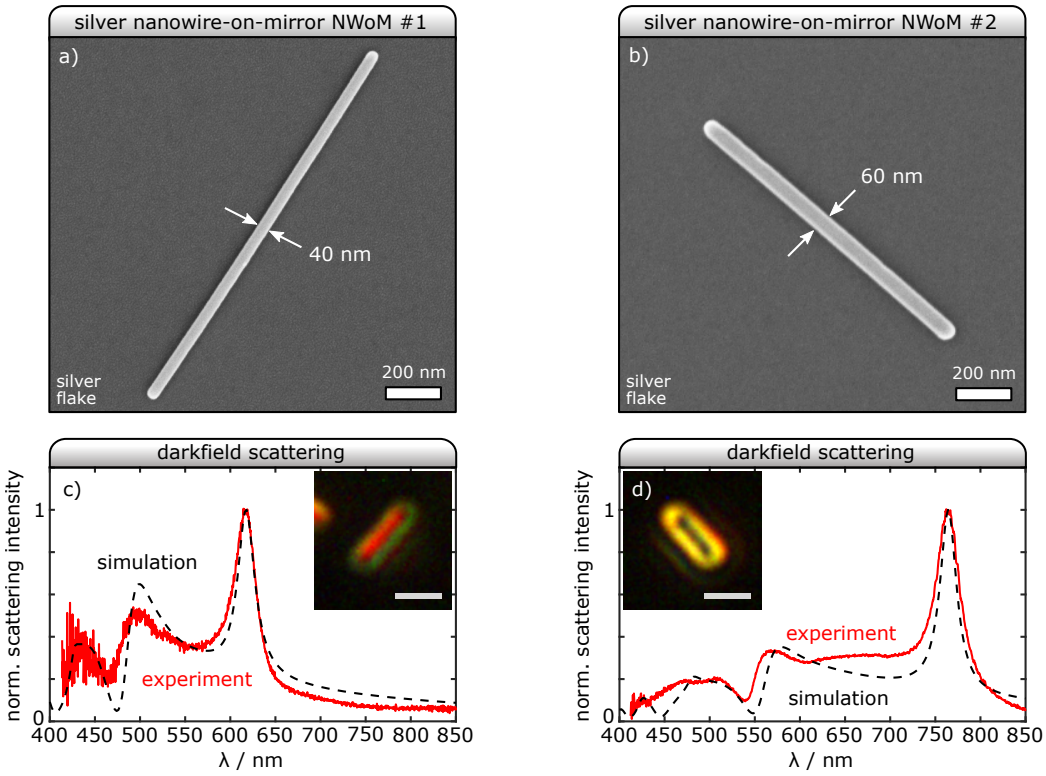

Figure 8.7: (a,b) Scanning electron micrograph of two selected nanowire-on-mirror constructs NWoM #1 and #2. Images are flipped and rotated to match the orientation of the respective optical darkfield image in (c,d). The sample was sputtered by 1.6 nm Pt after optical measurements and before SEM imaging. (c,d) Corresponding normalized experimental scattering spectra obtained via darkfield scattering spectroscopy (red). The inset shows the respective darkfield scattering image (scale bar 1 µm). The scattering simulations (black dashed lines) use a diameter $d = 40$ nm with 1.9 nm PVP thickness and diameter $d = 60$ nm with 1.7 nm PVP thickness for panel (c) and (d), respectively. In both simulation cases, an angle of incidence $\alpha = 80°$ with p-polarized excitation is used and the scattered power is evaluated in a solid angle corresponding to $NA = 0.9$. Adapted from J. Chem. Phys. **155**, 234202 (2021), with the permission of AIP publishing.

8.5 OPTICAL PROBING OF NANOWIRE-ON-MIRROR CAVITIES

In this section, further nanowire-on-mirror cavities are probed optically by darkfield spectroscopy and in the balanced detection setup described in section 8.2. For the latter measurements, the setup performance at a smooth silver flake surface position serves as an important reference case (c.f. section 8.3). Particularly, on a clean position, only the reflected field originating from the flake surface is relevant to the equation 8.2 of interferometric scattering detection. Thus, just the reflected signal beam at the silver surface is detected via the balanced photodetector. Nanowire-on-mirror constructs placed in the focus of the signal beam of the superluminescent diode (SLD), however, do act as additional scatterer on the silver flake surface. Particularly, at the

plasmonic resonances, which are distributed across the visible to near-infrared region, the scattering becomes significant, as revealed by darkfield spectroscopy.

While darkfield spectroscopy is performed under high angle illumination, the Gaussian-like focus in the balanced detection setup is incident from the vertical direction. From numerical simulations, it becomes clear that also low angle plane wave illumination efficiently excites the lowest frequency cavity plasmon resonance (c.f. figure 8.6b). A Gaussian beam can be considered as a superposition of a continuum of plane waves and thus efficiently excites the desired cavity resonance when focused close to the diffraction limit [252]. When the Gaussian beam is focused to the nanowire-on-mirror construct, not only the reflected field in equation 8.2 originating from the flake surface is detected but also the field scattered by the nanowire and, in general, its interference with the reflected field. Whether the interference term is dominant compared to the pure scattering contribution depends on the relative magnitude between the reflected and scattered fields as well as their phase relation [245]. This detection scheme, together with the balanced detection, allows for a sensitive optical probing of time-varying phenomena of the scattering behavior at the wavelength of the signal beam.

Experimental results of the balanced detection measurements Experimentally, two further nanowire-on-mirror cavities (NWoM #3 and #4) of diameter 45 nm and 60 nm are considered in the following (figure 8.8a,b). Notably, both constructs are perfectly isolated from other wires on the ultra-smooth surface of the silver flake and no residue or sample contamination can be observed. Similar to NWoM #1 and #2, mainly the slight difference in the wire diameter leads to the different spectral position of the lowest frequency cavity resonance of NWoM #3 and #4 at 627 nm and 774 nm, respectively (figure 8.8c,d). Importantly, the spectrum of the superluminescent diode does not overlap with the cavity resonance of NWoM #3 but is located in the steep red edge of the cavity resonance of NWoM #4. Thus, the SLD-light is not scattered significantly by NWoM #3, as it is probed far off resonance. By contrast, the SLD-light is scattered strongly by NWoM #4, as the cavity is probed resonantly. The spectral position in the red edge of the resonance ensures a maximum change of the scattered field and thus a maximum change of the detected intensity upon tiny spectral shifts of the resonance wavelength [111]. In addition to this spectral difference in probing the cavities on or off their resonance, a further distinction can be drawn by the polarization of the incident signal beam. Even the scattering of light by a single, resonant cavity can be switched off by rotating the signal beam polarization to an orientation parallel to the long wire axis. In this case, the polarization component along the long nanowire axis is not able to excite the considered cavity resonance along the short nanowire axis and the cavity thus does not scatter [250].

Time traces of the Nirvana LOG-output at $P_{SIG} = 100\,\mu W$ and $f_c = 1\,Hz$ are recorded at both NWoM #3 and #4 with a polarization parallel and perpendicular to the long wire axis. In case of NWoM #3, a relatively low level of signal fluctuations is detected (figure 8.8e). The minimum rms noise within all possible 2 s (10 s) time intervals is about 3 µV (5 µV), being very similar for both polarization directions and only slightly

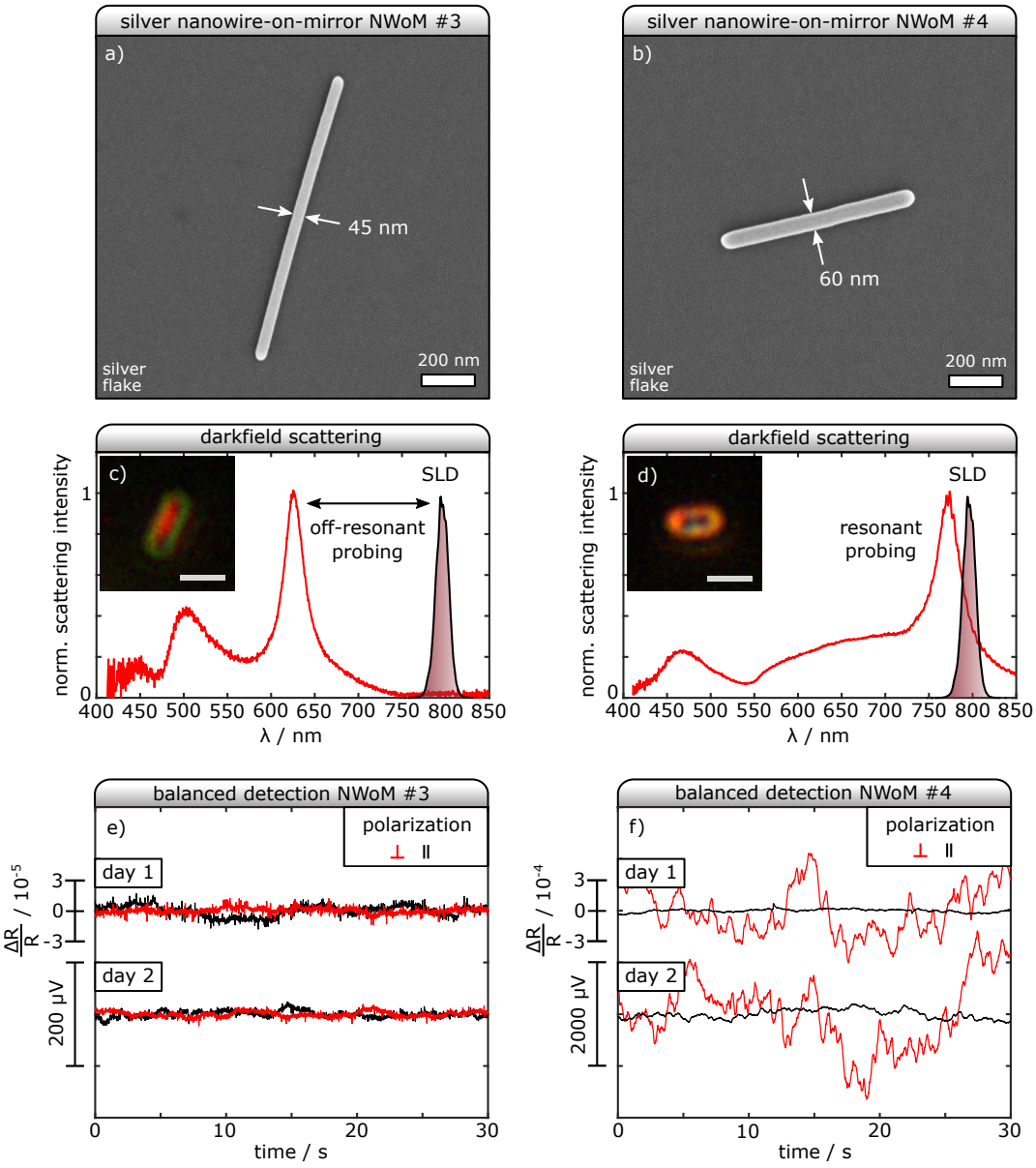

Figure 8.8: (a,b) Scanning electron micrograph of nanowire-on-mirror constructs #3 and #4 after optical measurements. Images are flipped and rotated to match the orientation of the respective optical darkfield image in (c,d). The sample was sputtered with 1.6 nm Pt before imaging. (c,d) Corresponding normalized experimental scattering spectra obtained via darkfield scattering spectroscopy (red) and spectrum of the superluminescent diode (SLD, black line). The inset shows the corresponding darkfield scattering images (scale bar 1 µm). (e,f) Output voltage time traces in the balanced detection setup with the NWoM cavity in the signal beam focus for both a polarization perpendicular (red) and parallel (black) to the long wire axis. The data is sampled in He-atmosphere at $P_{SIG} = 100\,\mu W$, $f_c = 1\,Hz$ and corrected by a linear offset. Note the different voltage scales in (e) and (f). The scale for the normalized differential reflection $\Delta R/R$ of the sample in the signal beam focus is calculated based on equation 8.7. Panel d) adapted from J. Chem. Phys. **155**, 234202 (2021), with the permission of AIP publishing.

above the noise level determined at the flat silver flake position (c.f. figure 8.2b). In distinct contrast to these results, strongly enhanced and anisotropic signal fluctuations are detected for the resonant NWoM #4 (figure 8.8f). The time traces were recorded on two different days, where the Gaussian focus was repeatedly placed manually to the wire. In all cases, the detected signal fluctuations for a perpendicular polarization clearly surpass the fluctuations for a parallel polarization. The amplitude of the signal fluctuations varied between further different measurements, also depending on the specific manual positioning of the NWoM relative to the signal beam focus.

Experimental results of darkfield spectroscopy In order to gain further insight and to check for changes of the cavities' scattering behavior after optical probing with focused SLD-light in the balanced detection setup, darkfield spectroscopy of the cavities is performed again after the focused probing with SLD-light.

Nanowire-on-mirror #1, which was not probed with focused SLD-light, still features nearly the same spectral position of the lowest frequency cavity plasmon resonance (figure 8.9a). By contrast, the tail of the resonance of NWoM construct #2 is excited by the SLD-spectrum and was exposed to it during widefield imaging and rather shortly in a focused condition compared to constructs #3 and #4. A small but clear red-shift of NWoM #2 cavity resonance by 8.6 nm is observed (figure 8.9b). Furthermore, darkfield spectroscopy is performed at NWoM cavity #3 and #4 that were probed for several minutes with intense focused light of the SLD (c.f. figure 8.8). While the cavity resonance of NWoM #3 shifted by about 9 nm into the red (figure 8.9c), the scattering spectrum of construct #4 changed markedly (figure 8.9d). Particularly, the lowest frequency cavity plasmon resonance can no longer be observed within the experimental range of 400-850 nm. Instead, a broad scattering peak ranging from 550 to 800 nm is detected. The darkfield image still displays a reddish halo, similar to the freshly prepared condition (figure 8.9d, inset).

Discussion of darkfield spectra The presented nanowire-on-mirror constructs were investigated optically by darkfield spectroscopy and in the balanced detection setup. During those measurements, the sample was exposed about 10-15 hours to air and several hours to He-atmosphere. In between the measurements, the sample was stored in a vacuum chamber to prevent any kind of degradation. In the scanning electron micrographs recorded after all optical measurements, no degradation or change of the nanowires' shape is obvious, even at the positions investigated with intense, focused SLD-light (c.f. figure 8.8a,b). A significant (not light-induced) chemical degradation during the measurements is less likely because the resonance of NWoM #1 did neither change in center wavelength nor in spectral width (c.f. figure 8.9a). Thus, the observed red-shifts of the darkfield scattering resonances are attributed to subtle changes of the morphology, particularly in the tiny nanogap where the resonant plasmonic near-field is located. Specifically, the morphology changes seem to be light-induced, as the not SLD-probed (not in a focused condition) NWoM #1 features a stable spectral position of the plasmonic resonance, while the SLD-probed NWoM #2 - #4 display significant

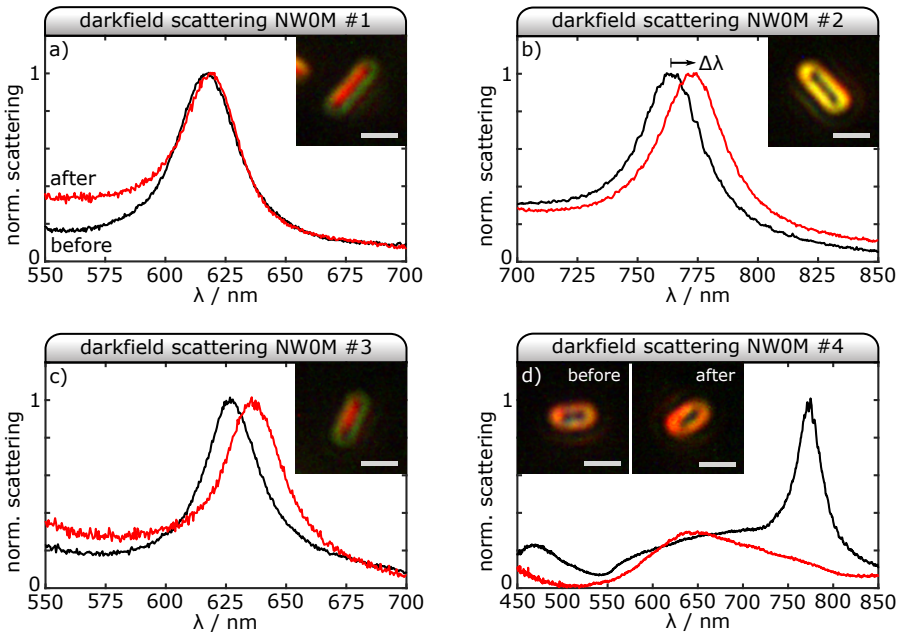

Figure 8.9: (a-d) Darkfield spectra of nanowire-on-mirror constructs #1 - #4, freshly prepared (black) and after optical investigations in the balanced detection setup (red). The inset shows the darkfield image of the freshly prepared constructs (scale bar 1 µm). The construct in (a) was not investigated with focused SLD-light, while the one in (b) was shortly illuminated. The cavities in (c) and (d) were investigated with focused SLD-light over several minutes. The construct in (d) shows a strong change of the scattering spectrum (red, scaled to 0.3 of maximum value), although its darkfield image appears to be similar after the measurements than before (insets). Details see text.

changes. The observations of the NWoM cavities suggest that these light-induced changes are more pronounced the longer the structure is illuminated by intense light. Moreover, when the light frequency matches the plasmonic cavity resonance, a several thousand times enhancement of the near-field intensity in the few-nanometer gap results (c.f. figure 8.5b). Based on the results of NWoM #4 compared to NWoM #3, this strong enhancement accordingly leads to a comparatively more drastic light-induced structural change. Two geometric options are most obvious to explain a spectral red-shift of the cavity resonance. First, a decreasing gap-size (c.f. figure 8.6a) and, second, an increased facet width of the cavity (c.f. figure 8.5c).

In current literature, it is well established that surface atoms of plasmonic nanoparticles can hop along and between different facet planes. This effect can be optically driven, leading to a dynamic reconstruction of the nanoparticle's surface. In a gold nanocube-on-mirror cavity, where the (100) bottom facet of a gold nanocube faces the (111) surface of the underlying gold surface, a light-induced red-shift of plasmonic resonances was observed by Xomalis *et al.* [238]. They reported a red-shift of up to 15 nm for non-resonant irradiation (~30 s, 1 mW/µm^2) and attributed it to a light-induced atomic-scale reconstruction that slightly increases the cavity's facet width.

Silver has a face-centered cubic crystal lattice, just like gold, with similar surface free energies of the different crystal planes [253]. The five side surfaces of a pentagonal silver nanowire are {100} facets [254] and, in a nanowire-on-mirror construct, one of them faces the (111) plane of the silver flake below. Moreover, the cavity resonance of the NWoM construct is particularly sensitive to its facet width, which defines the length of the resonator. Optical probing in the balanced detection setup was performed with intensities of about 1 mW/μm^2 in the focal region of the signal beam. In this regard, the red-shifts of the plasmon resonance observed experimentally in this section could, analogously to Xomalis *et al.* [238], be explained by light-induced atomic rearrangements that lead to an increased facet width of the NWoM cavity. In particular, the resonance red-shift of NWoM #2 from 764.4 to 773.0 nm, i.e., by 8.6 nm, is a relative shift by only about 1.1 %. Based on the total diameter of NWoM #2 of 60 nm, its bottom facet width is about 25 nm in length, depending on the assumed edge rounding. Simulations show that a facet growth by only 0.8 nm results in the detected red-shift. This corresponds to a growth of the facet width by about the length of one atom at each side of the facet, a change much too small to be observed via scanning electron microscopy. Alternatively, the red-shift could be explained by a shrinking of the PVP thickness by about 60 pm, e.g., as a result of a subtle reorganization within the PVP layer. For NWoM #3, similar numbers are calculated. Whether the resonance red-shift of NWoM #2 results from an increasing facet length by ~0.8 nm or a shrunk gap-size by ~60 pm, or a combination of both, cannot be clarified unambiguously here. Nevertheless, these tiny numbers impressively demonstrate the outstanding sensitivity of the cavity resonance to subtle structural changes within a few-nanometer gap.

In contrast to the tiny red-shifts of the plasmon resonance observed for NWoM #2 and #3, the lowest frequency cavity resonance of NWoM #4 was no longer observed experimentally, suggesting a red-shift by more than 80 nm beyond the experimental limit of 850 nm. The reason for this extreme change might be related to the resonantly enhanced plasmonic near-field in this cavity. While the spectrum of the superluminescent diode had no overlap with the cavity resonance of NWoM #3, NWoM #4 was initially probed close to resonance (c.f. figure 8.8d), leading probably to a more drastic light-induced change within the cavity. As a result, the plasmon resonance might have been progressively detuned far into the red until the overlap with the SLD-spectrum decreased again. In simulations, a shift of the cavity resonance from initially 774 nm to 940 nm can, for example, be achieved by just removing the rounding at the bottom facet edges, leading effectively to an enlarged facet width. In the final darkfield measurement of NWoM #4, a broad and featureless scattering spectrum is detected with a maximum in the red spectral range. This scattering retains the out-of-plane character as seen by the halo-like appearance in the darkfield image (c.f. figure 8.9d, inset). The spectral shape cannot be reproduced in simulations assuming a homogeneous facet width along the whole nanowire length. It could thus be related to a spatially inhomogeneous change within the cavity's gap, resulting in a broadened scattering spectrum.

Discussion of the balanced detection measurements After having discussed the spectral red-shift of the cavity resonance and identifying light-induced atomic-scale reconstructions as the most probable origin, the experimental results in the balanced detection setup remain to be discussed. Recent studies of the Baumberg [239] and Galland group [240] have clearly demonstrated that plasmonic nanocavities are highly dynamic systems, e.g., in their emission behavior. However, it is still unclear whether the gradual detuning of the plasmonic cavity resonance observed in this section is subject to spectral diffusion or spectral jumps at shorter timescales. The interferometric scattering measurements in the balanced detection setup presented in this chapter are one step toward the discovery of this phenomenon. These measurements have demonstrated clearly increased signal fluctuations as a function of time only for the resonantly probed NWoM #4 and particularly for a polarization of the signal beam along the short wire axis (c.f. figure 8.8f). Thus, the increased signal fluctuations seem to be linked to the resonant scattering of the investigated NWoM cavity. Based on the fundamental equation of the interferometric scattering detection (c.f. equation 8.2), several possible mechanisms need to be discussed that can lead to fluctuations at the output of the balanced detector. The most evident mechanisms are the spectral diffusion of the cavity resonance, subtle beam-pointing fluctuations or tiny mechanical movements in the setup, and noise properties of the light source.

First, the noise characteristics of the superluminescent diode need to be discussed. Any optical feedback from the experiment back into the active region of the diode is prohibited by a Faraday isolator, ensuring optimum performance of the SLD. The intensity noise of the SLD-output is well-canceled by the Nirvana at 100 µW signal beam power, as observed in the measurements at a smooth silver flake position (c.f. figure 8.2). Thus, the increasing signal fluctuations cannot be explained by intensity noise originating from the SLD. However, light sources like superluminescent diodes do also feature phase noise, which is represented by a time-dependent (fluctuating) phase function of the output radiation field [255]. Phase noise of the light source can lead to excess noise in interferometric detection schemes, as it can be interferometrically converted to intensity noise on the detector. An important requirement for the appearance of this excess noise is that the path length difference in the interferometer is not negligible compared to the coherence length of the light source [256]. This noise would only appear in the signal channel and thus would be detected by the Nirvana. However, based on the nanoscale separation of the nanowire from the silver surface, the path length difference is very small compared to the coherence length of the SLD (~20 µm). Thus, this mechanism is regarded as a less probable origin of the observations.

Another notorious issue in experimental setups are tiny time-dependent signal variations due to mechanical movements of the sample relative to the focused light spot [238]. The setup in figure 8.1 is constructed on a solid aluminum base plate where all optical elements are fixed directly to, resulting in a low beam height of only 25 mm above the plate. The sample is further mounted on a very mechanically stable stage with low mechanical travel in each dimension. Thus, mechanical movements of the optical elements relative to each other are minimized by a robust design. Furthermore, the superluminescent diode is single-mode fiber-coupled, ensuring minimum beam-

pointing fluctuations originating from the light source [41]. Light beams are further known to be deflected by density fluctuations in random air currents. To address this issue, the whole balanced detection setup is placed in a polyethylene chamber inflatable with helium. The refractive index of the latter is much closer to unity than that of air ($n_{He} = 1.000036$, $n_{air} = 1.000293$). Hence, density fluctuations inside the chamber induce smaller beam deflections, as demonstrated by Abbondanzieri *et al.* [241]. In particular, a time-dependent variation of the signal beam focus position relative to the NWoM cavity, caused by tiny beam-pointing fluctuations or mechanical movements of the sample relative to the objective, results in two effects. First, the scattering amplitude changes accordingly, which translates into a changed signal intensity on the detector. A second effect may appear if the interference term in equation 8.2 contributes. When the point-spread function of the cavity's scattered field and the focus of the reflected field vary in relative position on the detector as a function of time, also the spatial mode overlap factor between the two fields on the detector and thus the detected intensity varies as a function of time. All the different arrangements noted above were made to minimize mechanical movements and beam-pointing fluctuations in the setup. In the future, a proper reference experiment, e.g., with a stable non-resonant nanoscale scatterer, needs to be designed to first quantify and then exclude these mechanisms as origin of the detected signal fluctuations.

Finally, a possible spectral diffusion of the plasmonic cavity resonance could explain the observed signal fluctuations. The basic mechanism for detecting a spectral diffusion of the plasmon resonance is that a spectral shift of the resonance leads to a change of the relative scattered amplitude at the signal beam wavelength located at a spectral edge of the resonance. Thus, a resonance wavelength shift is mapped into a differential change of the detected intensity in the signal channel. According to equation 8.7, the fluctuations recorded for the resonantly probed NWoM in figure 8.8f correspond to relative signal power fluctuations in the order of a few 10^{-4}. This value can only be related to a corresponding resonance wavelength shift with a theoretical consideration of the interferometric scattering signal according to equation 8.2. This includes knowledge of the relative amplitudes of the reflected and scattered field, their relative phase angle ϕ and also knowledge of the complex mode overlap factor on the detector. For the phase angle ϕ, in particular, a Gouy-phase shift by $-\pi/2$ of the reflected Gaussian beam [104], a reflection phase from the reflection at the silver surface and the relative phase of the driven plasmonic resonance relative to the incident field needs to be taken into account. The determination of these parameters remains open work to be revealed numerically and experimentally with future extensions of the setup (see section 8.6).

In conclusion, the origin of the observed signal fluctuations lies most probably either in subtle beam-pointing fluctuations respectively tiny random movements of the sample relative to the SLD-light focus, which could not be avoided at the current stage despite the optimized setup design, or in a spectral diffusion of the plasmon resonance.

8.6 CONCLUSION AND OUTLOOK

In conclusion, this chapter demonstrates first important steps toward an ultra-sensitive optical probing of plasmonic nanocavities by an interferometric scattering detection technique. A setup is presented that sensitively probes the reflected optical intensity originating from a (close to) diffraction-limited spot positioned on a sample surface. To address the intensity noise of the superluminescent diode, a balanced photodetector is used. An ultra-low relative noise level is demonstrated at a smooth silver flake surface position, reaching a relative sensitivity of about $4 \cdot 10^{-6}$ at ~1 kHz measurement bandwidth and 100 µW signal beam power, a value limited by the photon shot noise. At a bandwidth of ~1 Hz, a relative sensitivity down to about $1 \cdot 10^{-6}$ is achieved, limited currently by the detection noise. This extraordinarily low relative noise opens up the optical study of extremely tiny time-dependent phenomena on the nanoscale.

A plasmonic nanocavity is a very promising system for such sensitive optical investigations in multiple respects. First, in a plasmonic cavity, the electromagnetic near-field is resonantly enhanced to unprecedented strengths within a nanoscale volume. As a consequence, light-matter interactions are boosted, offering interesting prospects for an efficient coupling with quantum emitters. Second, plasmonic cavities constructed from two metal structures separated by a nano- to atomic-scale gap have recently been shown to be highly dynamic systems on their own (c.f. Baumberg [239] and Galland group [240]). Poorly understood dynamical phenomena at this scale demand sensitive measurement techniques in order to reveal their origin. In this chapter, particularly nanowire-on-mirror constructs are investigated. These are constructed from chemically-grown crystalline silver nanowires attached to the ultra-smooth surface of a single-crystalline silver flake, with a gap-separation formed by the few-nanometer PVP surface layer of the individual nanowire. Besides a waveguide mode localized within the nanogap that propagates along the long nanowire axis, numerical simulations give insights into transverse resonant cavity modes confined to the gap. Along the short nanowire axis, the structure represents a metal-isolator-metal waveguide cavity formed by the bottom facet of the nanowire, the PVP spacer and the bottom silver flake surface. The resonant behavior of such cavities is studied experimentally by darkfield imaging and spectroscopy. An excellent agreement of experimental darkfield scattering spectra with numerical scattering simulations taking into account a sub-2 nm PVP gap-spacing is found. Compared to the 236 pm distance between the top (111) crystal planes of the silver flake, the achieved gap-sizes thus correspond to a spacing of below 8 silver atomic layers. This analogy illustrates the need for crystalline and ultra-smooth material for the construction of high-quality functional structures advancing toward atomic-scale dimensions. Particularly, the linewidth of the lowest frequency cavity plasmon resonance in the experiment is found to approach the theoretical limit given by the simulations. Silver as the material of both the nanowire and the underlying surface results in a narrow linewidth of the cavity resonance beyond the linewidth of any nanowire-on-mirror construct reported in the literature by the Hongxing Xu group [121, 250], which are all involving gold. The fabrication from pure silver also allows to observe out-of-plane and higher-order cavity modes in the visible spectral

range not clearly observed for the reported constructs involving gold. Furthermore, tiny red-shifts of the cavity resonance are detected by darkfield spectroscopy. These are attributed to light-induced, atomic-scale structural changes within the nanogap of the cavity, highlighting the outstanding sensitivity of the cavity resonance to subtle environmental changes.

Nanowire-on-mirror constructs were further optically probed in the mechanically stable balanced detection setup under helium atmosphere with the goal of detecting tiny time-dependent phenomena such as spectral diffusion or spectral jumps of the resonance wavelength. Strong signal fluctuations as a function of time were detected when a nanocavity is probed resonantly with the proper polarization of the incident light along the short nanowire axis. Based on the discussion in section 8.5, tiny beam-pointing fluctuations and/or mechanical movements of the sample relative to the light focus cannot be excluded as origin of the observations at the current stage. In such ultra-sensitive setups, the shielding against environmental influences, such as vibrations and acoustic coupling into the setup, should be given top priority. In future work, these influences need to be quantified precisely, e.g., with a stable non-resonant subwavelength scatter.

To address such issues, the experimental setup needs to be redesigned and extended by an additional piezo actuator to obtain a confocal interferometric scattering (iScat) imaging capability. This would allow systematic iScat studies of reference scatterers and nanowire-on-mirror cavities. Particularly, the iScat imaging contrast of a cavity on the silver surface could be determined, including the sign of the contrast, i.e., whether the cavity appears brighter or darker with respect to the background. This approach would give experimental insight into important iScat parameters such as the relative scattering amplitude and phase angle ϕ with a precise lateral positioning of the light focus with respect to the scatterer, which are indispensable for a detailed quantification of the observations. Furthermore, the setup could be extended to perform *in situ* darkfield spectroscopy while balanced detection of the iScat signal. The simultaneous performance of these two techniques should allow to identify important correlations, e.g., between the cavity resonance wavelength and signal fluctuations at the signal beam wavelength recorded by the balanced photodetector. Without this *in situ* performance of both measurement techniques, it remains unclear at the current stage how fast the light-induced red-shift of the resonantly probed cavity resonance of NWoM #4 actually was and where the resonance wavelength was located in the specific moment where the Nirvana voltage time traces were recorded.

In a further step, quantum emitters could be positioned into the nanogap at the intense hot-spots of a resonant nanocavity. While the extinction of a diffraction-limited laser beam by a single quantum emitter is a tiny effect at room temperature [41, 42, 242], a high-quality resoant plasmonic nanocavity should allow to significantly boost this effect. Thus, plasmonically-enhanced interferometric scattering studies of quantum emitters in a nanocavity at room temperature can be envisioned for future pioneering work in the field of quantum plasmonics.

9 CONCLUSION AND OUTLOOK

This thesis is dedicated to the scientific fields of plasmon-enhanced light-matter interaction and plasmonic nanocircuitry, which have the visionary, future goal to realize an integrated functional quantum plasmonic nanocircuit [31] implementing quantum information processing routines with increased speed compared to conventional electronics [32]. In order to push the borders of current state-of-the-art fundamental research toward this far-reaching goal, this thesis addresses several key-topics such as numerical modeling, high-quality chemical synthesis and top-down nanofabrication of complex-shaped plasmonic circuits, the reduction of plasmonic loss by a smart choice of materials, the comprehensive experimental study of the interaction of isolated quantum emitters with multiple sub-diffraction-limited plasmonic modes and first steps toward maximizing the degree of confinement as well as coupling efficiency with quantum emitters.

In chapter 5, single-crystalline silver flakes are introduced as the high-quality basis for all plasmonic constructs investigated in this thesis. These flakes are built-up from pure silver and feature a high aspect ratio with a huge lateral size of up to ~50 µm and a height of only a few tens of nanometers. The single-crystallinity of the silver across the whole flake, which is verified by an electron backscatter diffraction analysis, results in the typical hexagonal outer shape with sharp and straight edges aligned with internal crystal planes. Furthermore, an extraordinarily high surface quality is demonstrated by atomic force microscopy, visualizing ultra-smooth surfaces with a surface roughness limited by rare discrete atomic-scale steps. These outstanding properties of the presented silver flakes make them the perfect plasmonic platform. On the one hand, the silver flakes are ideally suited for the top-down fabrication of crystalline plasmonic nanostructures by focused ion beam milling. On the other hand, they also provide top-quality silver surfaces for vertically constructed plasmonic nanocavities assembled onto the flake with atomic-scale separation. Furthermore, a long-term chemical stability of the silver flakes and nanostructures is achieved by a few-nanometer layer of Al_2O_3 deposited by atomic layer deposition.

Following this newly established nanofabrication with single-crystalline silver, chapter 6 demonstrates the first realization and application of a complex-shaped single-crystalline silver plasmonic circuit. In contrast to past implementations with gold, silver reduces plasmonic propagation loss and opens up the visible spectral region for studying the light-matter interaction with visible wavelength quantum emitters. The realized circuit consists of several distinct elements, i.e., an optical antenna, a two-wire transmission line waveguide and a mode detector. The antenna and mode detector allow to excite and detect *in situ* the contributions of different modes propagating

along the two-wire transmission line. Furthermore, a tiny, ~20 nm-sized polystyrene bead doped with a few tens of dark-red fluorophores is attached to the silver structure. As a result, about 63 % of its fluorescence is channeled efficiently into the available plasmonic waveguide modes. The excitation of this coupled bead can be modulated by the polarization of the incident field due to polarization-sensitive plasmonic near-fields close to the nanostructure. The bead is further remotely excited via propagating waveguide modes, while a second, uncoupled bead in a sub-diffraction-limited distance is not excited. Notably, the best excitation of the coupled bead is achieved for a specific superposition of the excited waveguide modes. In addition to this multi-mode, super-resolving remote excitation, a remote detection of the coupled bead's fluorescence at the waveguide ends is achieved, realizing a fully remote excitation and detection of its fluorescence via the circuit. Notably, the operation of the circuit and its coupling with locally positioned quantum emitters are in good agreement with simulations based on numerical models and calculations discussed in chapter 4.

Chapter 7 is closely connected to chapter 6 and investigates single isolated terrylene diimide molecules placed inside the 60 nm gap of a plasmonic two-wire transmission line. With an estimated efficiency of about 68-84 %, the vast majority of the molecules' fluorescence is funneled into the antisymmetric plasmonic mode propagating along the nanogap. At the same time, a reduction of the excited state lifetime of up to about one order of magnitude and a photon antibunching in the single-molecule fluorescence is demonstrated. Moreover, single-molecule stimulated emission depletion is investigated both with diffraction-limited laser foci and with propagating plasmons confined to the nanogap. The comparison of these experiments shows that the efficiency of triggering the stimulated emission transition is about 30 times enhanced in the plasmonic gap where the near-field intensity is enhanced. The single-molecule stimulated emission depletion experiments demonstrate an interaction of a single molecule with a sequence of two plasmonic pulses propagating along the waveguide gap. Thus, for the first time, a single-molecule nonlinearity in a plasmonic waveguide is realized experimentally.

Finally, in chapter 8, silver nanowires in a few-nanometer separation to the ultra-smooth surface of a silver flake are investigated. This construct, termed nanowire-on-mirror, has distinct similarities to the plasmonic two-wire transmission line discussed in chapters 6 and 7. Simplified, the nanowire-on-mirror geometry can be imagined as a kind of two-wire transmission line with vertically separated wires where the bottom wire is replaced by a silver surface. As a result, both constructs support a propagating waveguide mode localized within the nanogap between the two silver parts. While the gap-size of the two-wire transmission line is limited by about 60 nm due to the fabrication process, nanowire-on-mirror constructs with sub-2 nm gaps are realized. This distance corresponds to only about 8 atomic layers along the [111] normal direction of a silver flake. Considering the nanowire-on-mirror construct along the short wire axis reveals a nanoscale metal-insulator-metal waveguide cavity, with a ~2 nm height and a 20-30 nm width, that supports different resonant plasmonic modes. Particularly, the lowest frequency cavity plasmon resonance is investigated comprehensively in numerical simulations and characterized experimentally for different constructs with darkfield spectroscopy, finding an excellent agreement taking a sub-2 nm gap into

account. In scattering spectra, the cavity resonance appears as a sharp peak located within the visible to near-infrared region, which is extremely sensitive to environmental changes. Red-shifts of the resonances by a few nanometers are detected and attributed to subtle, light-induced, atomic-scale reconstructions within the tiny nanogap. The linewidth of the cavity resonance is narrow and beyond the one of any nanowire-on-mirror construct reported in the literature, which all incorporate (partly) gold instead of silver. Furthermore, a stable setup operating under He-atmosphere is constructed that detects the reflected intensity from a (close to) diffraction-limited area on the sample using a balanced photodetector, reaching a sensitivity of down to $1 \cdot 10^{-6}$ at ~1 Hz measurement bandwidth. First measurements at resonant and off-resonant nanowire-on-mirror cavities are performed for a parallel and perpendicular polarization of the incident light with respect to the wire, finding enhanced signal fluctuations at the detector when a construct is probed resonantly. Future improvements of the setup toward interferometric scattering microscopy of nanowire-on-mirror cavities, as well as the correlation of the balanced detection with *in situ* darkfield spectroscopy, are proposed to reveal further details and the origin of the observed effect.

In conclusion, this thesis has realized different plasmonic constructs of extraordinary quality and functionality fabricated for the first time from purely crystalline silver, opening up new quantum plasmonic experiments in the visible spectral range. The interaction of quantum emitters with plasmonic modes was investigated with multiple plasmonic fields distributed both in space and time. The number of emitters coupled to the nanostructures has been gradually decreased in the course of the thesis, reaching the limit of single molecules as quantum emitters in chapter 7. Starting from the diffraction limit with a typical length scale of a few 100 nm in the visible regime, the plasmonic constructs have confined the electromagnetic near-field to successively smaller subwavelength scales. While the gap in the two-wire transmission line reached a scale of about 60 nm, sub-2 nm gaps were finally realized in the nanowire-on-mirror geometry, a separation approaching the atomic scale.

The confinement of electromagnetic fields to such deep sub-diffraction-limited scales, on the one hand, leads to fascinating phenomena such as an unprecedented enhancement of the light-matter interaction with quantum emitters. On the other hand, however, maximizing the degree of confinement of visible to near-infrared radiation by plasmonics comes at a cost, namely that an increased loss in the metal is unavoidable. This fact has extensive consequences for plasmonic waveguide circuits, as always a compromise between confinement and achievable propagation distance needs to be agreed upon, limiting the total size, complexity and therefore functionality of the structure. Different waveguide geometries try to find the best compromise achievable by maximizing a suitable figure of merit [82, 175], however, they are always facing serious limitations. In this sense, as pointed out by Khurgin [257, 258], a paradigm-changing direction of future research includes the search for novel materials with lower loss while preserving the plasmonic confinement. Choosing single-crystalline silver as plasmonic material, despite silver still being a traditional noble metal, is certainly a major step in this direction. This thesis has demonstrated the feasibility of fabricating rather complex-shaped waveguide circuits from crystalline silver instead of gold with

the clear advantage of silver being the currently most-preferred low-loss plasmonic material in the visible to near-infrared region [77, 125].

Important applications of the emitter-waveguide system for future quantum information technologies [67, 174] include (ultra-fast) single-plasmon sources [24, 80], a single-photon transistor on a plasmonic platform [31] and the entanglement between distant quantum emitters [26, 27]. It can be envisioned that future quantum plasmonic circuits synergize the efficient on-chip generation of single plasmons [191], linear and nonlinear interaction with single quantum emitters [30, 211], beam splitting and interference [259], as well as on-chip single-plasmon detection [259–261]. The inefficient intermediate interconversion with far-field photons could thus be completely omitted. The realization of such fully integrated quantum plasmonic circuits, together with engineered low-loss materials and a deterministic integration of quantum emitters [235, 262], could finally result in successful quantum information processing on a true nanoscale footprint [32, 174].

APPENDIX

A TWO-WIRE TRANSMISSION LINE WAVEGUIDE MODE SUPERPOSITIONS

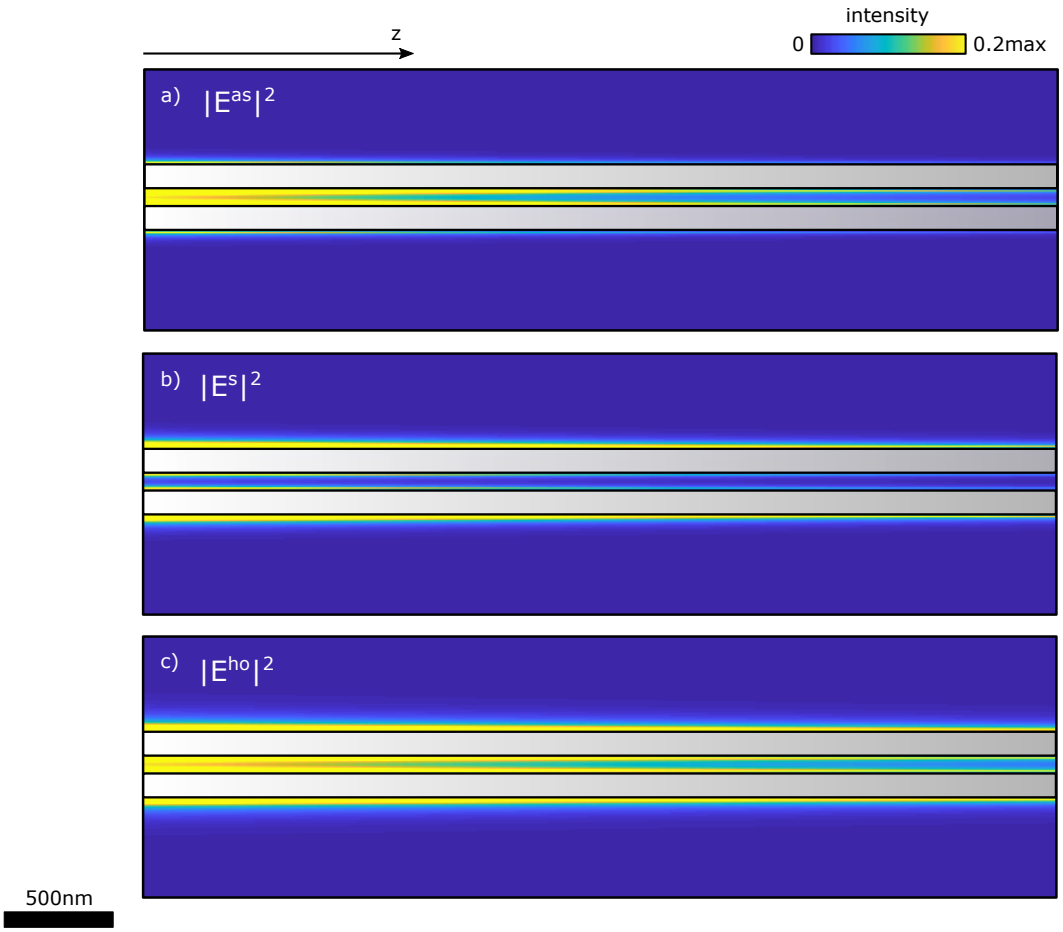

Figure A.1: (a-c) Simulated near-field intensity at 620 nm vacuum wavelength in a plane 5 nm above the substrate for a pure antisymmetric (E^{as}), symmetric (E^{s}) and higher-order mode (E^{ho}) of the two-wire transmission line, respectively. The fields are propagated along the waveguide direction z according to equation 6.1 and their square magnitude is shown. The modal fields are taken as displayed in figure 6.3 with their real parts of the effective mode index and propagation lengths as displayed in figure 6.4 of chapter 6. The two-wire transmission line is overlaid as a sketch (white-gray) for clarity. The colorscale is limited to 20 % of the maximum value of each panel for better visibility.

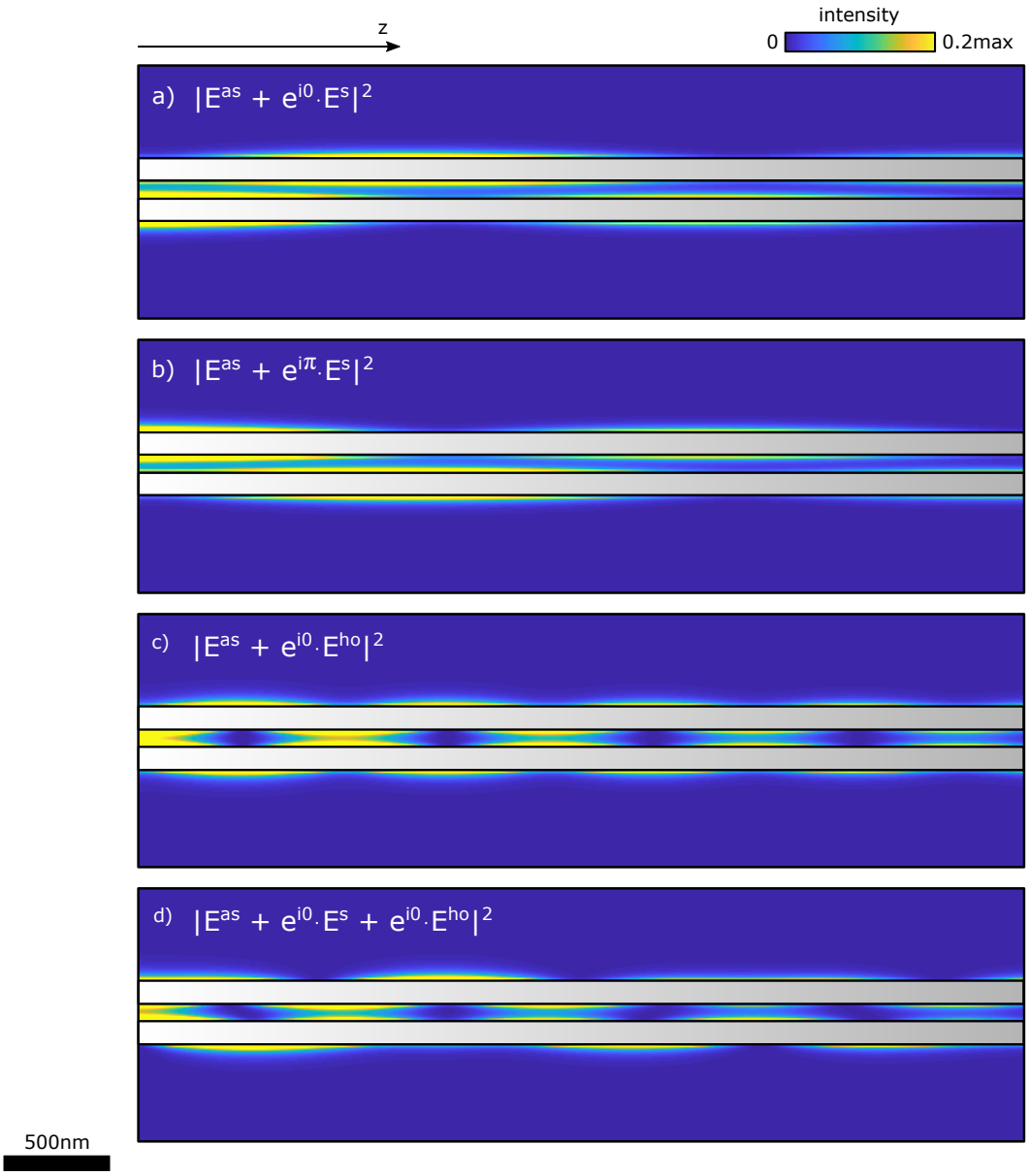

Figure A.2: (a-d) Simulated near-field intensity at 620 nm vacuum wavelength in a plane 5 nm above the substrate for different superpositions of the antisymmetric (E^{as}), symmetric (E^{s}) and higher-order mode (E^{ho}) of the two-wire transmission line. The fields are propagated along the waveguide direction z according to equation 6.1, superimposed coherently and their square magnitude is shown. The superposition of the modes is specified as inscription in each panel. The modal fields are taken as displayed in figure 6.3 with their their real parts of the effective mode index and propagation lengths as displayed in figure 6.4 of chapter 6. Introducing a relative phase shift between the modes (e.g., panel (a) vs. (b)) leads to a change of the beating pattern along the waveguide. The two-wire transmission line is overlaid as a sketch (white-gray) for clarity. The colorscale is limited to 20 % of the maximum value of each panel for better visibility.

B PULSE CHARACTERIZATION OF THE WHITE LIGHT LASER

In chapter 7, single molecules interact sequentially with a pump pulse and a depletion pulse of a supercontinuum white light laser. The detected fluorescence signals of the molecules are averaged over many interaction cycles with the two laser pulses. Fiber supercontinuum generation taking place in the laser source typically results in noisy output spectra of the laser [263]. In particular, when nonlinear processes of the sample are investigated with such a laser source, it is of great importance for quantitative interpretation of the experimental data to characterize the two optical laser pulses in terms of their individual pulse-to-pulse intensity variation and the correlation between the two.

A real-time detection technique is needed that monitors the output spectra of the laser source on a pulse-to-pulse basis without averaging over successive pulses. Such a technique is given by the time stretch dispersive Fourier transform [264]. By guiding the laser pulses through a highly dispersive optical fiber, a wavelength-to-time conversion is achieved, generating an intensity time trace that can be captured with a fast oscilloscope. For the measurements presented here, the fiber output of the laser source (610-770 nm) is connected via fibers (1.5 m SM600, 0.5 m SM980) to a $l = 600\,\mathrm{m}$ long single-mode fiber (630 HP), which is connected to a fiber (P5-980A) spliced to the fiber of a 25 GHz VIS-IR detector (model 1431, New Focus). The detector output is recorded with an 8 GHz oscilloscope[1] (WaveMaster 808Zi-A, LeCroy) and is cut into equally long time frames around the individual laser pulses. The wavelength λ can be numerically calculated from the time t within the time frame by successive integration of the following relation:

$$\frac{d\lambda}{dt} = \frac{1}{D(\lambda) \cdot l} \quad . \tag{B.1}$$

The constant of integration is determined from the known borders of the used wavelength range (610-770 nm). The total dispersion $D(\lambda)$ is given by the known dispersion (unit ps/nm/km) of the $l = 600\,\mathrm{m}$ single-mode fiber (630 HP), neglecting the contribution of the short other fibers. Furthermore, the recorded intensity is transformed from time domain I_t to wavelength domain I_λ by using the relation $I_\lambda = I_t \cdot D(\lambda) \cdot l$.

It is observed that the spectra of individual laser pulses feature a strong pulse-to-pulse variation in spectral shape and intensity (figure B.1a). To quantify these variations

1 The measurements were performed together with Prof. Dr. Georg Herink. The oscilloscope was kindly provided by the Department of Engineering Thermodynamics and Transport Processes, University of Bayreuth.

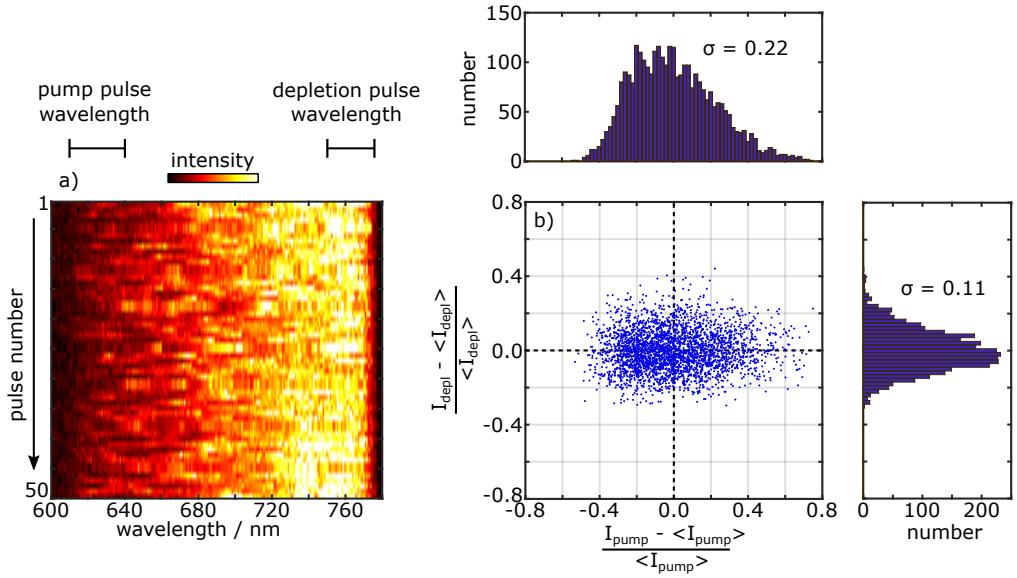

Figure B.1: (a) Intensity-spectra of a sequence of 50 individual optical pulses (610-770 nm) of the supercontinuum white light laser source recorded with the time stretch dispersive Fourier transform technique. (b) Correlation plot of the pump pulse intensity I_{pump} (610-640 nm) and depletion pulse intensity I_{depl} (750-770 nm) which are normalized as labeled to the corresponding mean of all 3126 values $< I_{pump} >$ and $< I_{depl} >$, respectively. The standard deviation σ of the normalized pump and depletion pulse intensity is given in the respective histogram.

for the relevant pump (~610-640 nm) and depletion (~750-770 nm) wavelength ranges, the intensity is integrated up in the respective ranges to yield intensity values of the individual pump I_{pump} and depletion pulses I_{depl}. Subsequently, a mean intensity averaged from 3126 pulses, i.e., $\langle I_{pump} \rangle$ and $\langle I_{depl} \rangle$, respectively, is subtracted and the result is normalized to the corresponding mean value. These normalized values are plotted for the 3126 consecutive pulses in a correlation plot between pump and depletion pulse intensity (figure B.1b). The variation of the pump and depletion intensity is captured in two histograms demonstrating that the normalized intensity variation is larger for the pump pulses (standard deviation 0.22) compared to the depletion pulses (standard deviation 0.11). Furthermore, especially the histogram of the pump pulse intensity is asymmetric and non-Gaussian in shape as a result of extreme-values from optical rogue wave events [265]. It should be noted that for pump and depletion wavelength ranges which are narrower and in close proximity to each other, the histograms get more and more asymmetric and positive correlations appear in the correlation plot. However, for the chosen wavelength ranges, the intensity of the pump and depletion pulses are nearly uncorrelated (correlation coefficient 0.05) and both feature an acceptable pulse-to-pulse intensity variation.

C PROPAGATION LENGTH ESTIMATION FOR THE ANTISYMMETRIC MODE

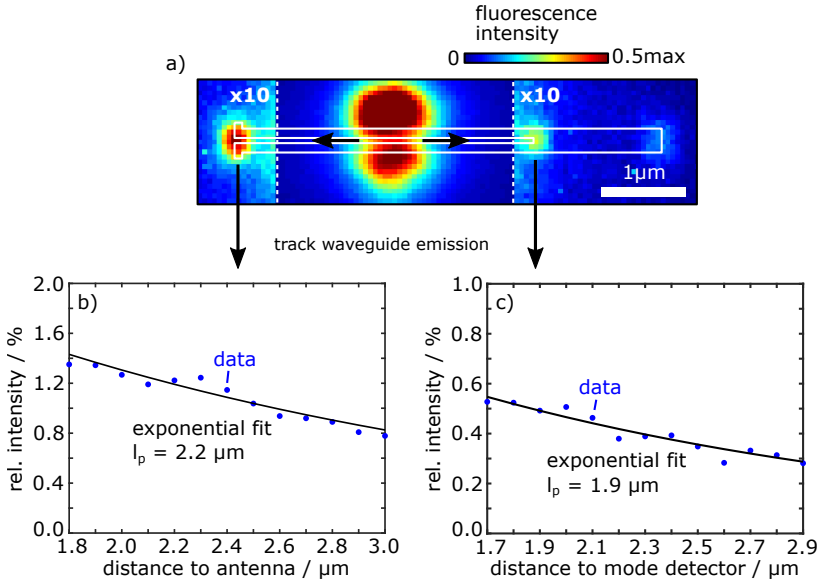

Figure C.1: (a) Fluorescence widefield image of an ensemble of TDI molecules in a thin PMMA layer on the silver circuit with a pump focus at the center and polarized perpendicular to the waveguide axis. The waveguide emission intensity at the antenna (b) and the inner end of the mode detector (c) normalized to the emission intensity at the excitation position as a function of the distance of the excitation position to the antenna and inner end of the mode detector, respectively (blue dots, c.f. text). The propagation length l_p is estimated by a single exponential fit in each case (black lines).

In order to estimate the propagation length of the plasmonic waveguide mode(s) in the silver plasmonic circuit investigated in chapter 7 (circuit #2 in figure 7.8a), a thin PMMA film with an ensemble concentration of TDI is spin coated onto the structure as described in chapter 7. Thus, along the two-wire transmission line, a constant density of TDI molecules is present. When exciting the ensemble with pump pulses focused to the two-wire waveguide part polarized perpendicular to the waveguide axis, waveguided fluorescence emission is detected mostly at the antenna and the inner end of the mode detector (figure C.1a). This waveguided emission needs to be separated from the large background emission directly excited via the pump pulses, which is done by fitting the waveguided emission with a sum of a Gaussian and an exponential background. The integrated intensity of the Gaussian is normalized to the respective integrated intensity at the excitation position, yielding a relative intensity. This relative

intensity is evaluated as a function of the distance of the pump focus to the antenna (figure C.1b, blue dots) and inner end of the mode detector (figure C.1c, blue dots). In both cases, the data decays with increasing distance between excitation position and detection position at the respective waveguide end. The decreased intensity is explained by propagation loss, which can be quantified by fitting an exponential decay to the data (figure C.1b,c, black line). In both cases, an exponential decay length of about 2 µm is found. A much weaker emission is detected at the far end of the mode detector than at its near end and thus the emission is guided mainly by the antisymmetric mode. Therefore, both determined values of l_p (figure C.1b,c) rather reflect the propagation length l_p of the antisymmetric plasmonic waveguide mode than the one of the symmetric mode. The slightly higher value of l_p determined via tracking of the waveguided emission at the antenna position might result from a smaller fraction of emission being guided in the symmetric mode with lower loss which is also outcoupled at the antenna.

D PHOTOGRAPH OF THE BALANCED DETECTION SETUP

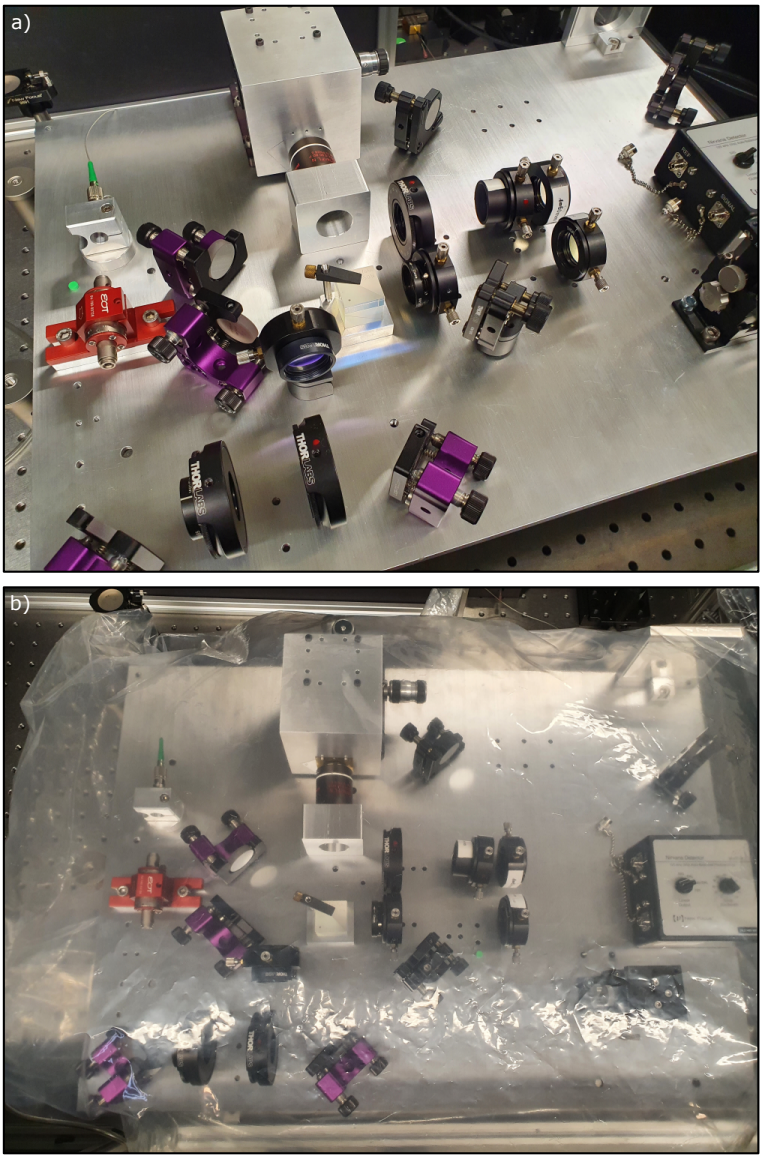

Figure D.1: (a) Photographic picture of the balanced detection setup in air. (b) Setup assembled in the polyethylene chamber inflated with helium gas.

BIBLIOGRAPHY

1. Abbe, E. Beiträge zur Theorie des Mikroskops und der mikroskopischen Wahrnehmung. *Archiv für Mikroskopische Anatomie* **9,** 413–468 (1 1873).
2. Rayleigh, L. Investigations in optics, with special reference to the spectroscope. *Phil. Mag* **8,** 261–274, 403–411, 477–486 (1879).
3. Minsky, M. Memoir on inventing the confocal scanning microscope. *Scanning* **10,** 128–138 (1988).
4. Denk, W, Strickler, J. & Webb, W. Two-photon laser scanning fluorescence microscopy. *Science* **248,** 73–76 (1990).
5. Zumbusch, A., Holtom, G. R. & Xie, X. S. Three-Dimensional Vibrational Imaging by Coherent Anti-Stokes Raman Scattering. *Phys. Rev. Lett.* **82,** 4142–4145 (20 1999).
6. Rust, M. J., Bates, M. & Zhuang, X. Sub-diffraction-limit imaging by stochastic optical reconstruction microscopy (STORM). *Nature Methods* **3,** 793–796 (10 2006).
7. Betzig, E., Patterson, G. H., Sougrat, R., Lindwasser, O. W., Olenych, S., Bonifacino, J. S., Davidson, M. W., Lippincott-Schwartz, J. & Hess, H. F. Imaging Intracellular Fluorescent Proteins at Nanometer Resolution. *Science* **313,** 1642–1645 (2006).
8. Hell, S. W. & Wichmann, J. Breaking the diffraction resolution limit by stimulated emission: stimulated-emission-depletion fluorescence microscopy. *Opt. Lett.* **19,** 780–782 (1994).
9. Kasper, R., Harke, B., Forthmann, C., Tinnefeld, P., Hell, S. W. & Sauer, M. Single-Molecule STED Microscopy with Photostable Organic Fluorophores. *Small* **6,** 1379–1384 (2010).
10. Blom, H. & Widengren, J. Stimulated Emission Depletion Microscopy. *Chemical Reviews* **117,** 7377–7427 (2017).
11. Synge, E. A suggested method for extending microscopic resolution into the ultra-microscopic region. *The London, Edinburgh, and Dublin Philosophical Magazine and Journal of Science* **6,** 356–362 (1928).
12. Novotny, L. The history of near-field optics. *Progress in Optics* **50** (ed Wolf, E.) 137 –184 (2007).
13. Hu, J., Liu, C.-H., Ren, X., Lauhon, L. J. & Odom, T. W. Plasmonic Lattice Lenses for Multiwavelength Achromatic Focusing. *ACS Nano* **10,** 10275–10282 (2016).
14. Lal, S., Link, S. & Halas, N. J. Nano-optics from sensing to waveguiding. *Nat. Photonics* **1,** 641–648 (2007).

15. Scholder, O., Jefimovs, K., Shorubalko, I., Hafner, C., Sennhauser, U. & Bona, G.-L. Helium focused ion beam fabricated plasmonic antennas with sub-5 nm gaps. *Nanotechnology* **24,** 395301 (2013).

16. Huang, J.-S., Feichtner, T., Biagioni, P. & Hecht, B. Impedance Matching and Emission Properties of Nanoantennas in an Optical Nanocircuit. *Nano Letters* **9,** 1897–1902 (2009).

17. Jeong, H.-H., Choi, E., Ellis, E. & Lee, T.-C. Recent advances in gold nanoparticles for biomedical applications: from hybrid structures to multi-functionality. *J. Mater. Chem. B* **7,** 3480–3496 (22 2019).

18. Benz, F., Schmidt, M. K., Dreismann, A., Chikkaraddy, R., Zhang, Y., Demetriadou, A., Carnegie, C., Ohadi, H., de Nijs, B., Esteban, R., Aizpurua, J. & Baumberg, J. J. Single-molecule optomechanics in "picocavities". *Science* **354,** 726–729 (2016).

19. Carnegie, C., Griffiths, J., de Nijs, B., Readman, C., Chikkaraddy, R., Deacon, W. M., Zhang, Y., Szabó, I., Rosta, E., Aizpurua, J. & Baumberg, J. J. Room-Temperature Optical Picocavities below 1 nm^3 Accessing Single-Atom Geometries. *The Journal of Physical Chemistry Letters* **9,** 7146–7151 (2018).

20. Urbieta, M., Barbry, M., Zhang, Y., Koval, P., Sánchez-Portal, D., Zabala, N. & Aizpurua, J. Atomic-Scale Lightning Rod Effect in Plasmonic Picocavities: A Classical View to a Quantum Effect. *ACS Nano* **12,** 585–595 (2018).

21. Tame, M. S., McEnery, K. R., Özdemir, c. K., Lee, J., Maier, S. A. & Kim, M. S. Quantum plasmonics. *Nat. Physics* **9,** 329–340 (2013).

22. Ojambati, O. S., Chikkaraddy, R., Deacon, W. D., Horton, M., Kos, D., Turek, V. A., Keyser, U. F. & Baumberg, J. J. Quantum electrodynamics at room temperature coupling a single vibrating molecule with a plasmonic nanocavity. *Nature Communications* **10,** 1049 (1 2019).

23. Feist, J., Galego, J. & Garcia-Vidal, F. J. Polaritonic Chemistry with Organic Molecules. *ACS Photonics* **5,** 205–216 (2018).

24. Hoang, T. B., Akselrod, G. M. & Mikkelsen, M. H. Ultrafast Room-Temperature Single Photon Emission from Quantum Dots Coupled to Plasmonic Nanocavities. *Nano Letters* **16,** 270–275 (2016).

25. Zhu, W., Esteban, R., Borisov, A. G., Baumberg, J. J., Nordlander, P., Lezec, H. J., Aizpurua, J. & Crozier, K. B. Quantum mechanical effects in plasmonic structures with subnanometre gaps. *Nature Communications* **7,** 11495 (1 2016).

26. Gonzalez-Tudela, A., Martin-Cano, D., Moreno, E., Martin-Moreno, L., Tejedor, C. & Garcia-Vidal, F. J. Entanglement of Two Qubits Mediated by One-Dimensional Plasmonic Waveguides. *Phys. Rev. Lett.* **106,** 020501 (2 2011).

27. Hensen, M., Heilpern, T., Gray, S. K. & Pfeiffer, W. Strong Coupling and Entanglement of Quantum Emitters Embedded in a Nanoantenna-Enhanced Plasmonic Cavity. *ACS Photonics* **5,** 240–248 (2018).

28. Guebrou, S. A., Symonds, C., Homeyer, E., Plenet, J. C., Gartstein, Y. N., Agranovich, V. M. & Bellessa, J. Coherent emission from a disordered organic semiconductor induced by strong coupling with surface plasmons. *Phys. Rev. Lett.* **108,** 66401 (2012).

29. Kim, J.-H., Aghaeimeibodi, S., Richardson, C. J. K., Leavitt, R. P. & Waks, E. Super-Radiant Emission from Quantum Dots in a Nanophotonic Waveguide. *Nano Letters* **18,** 4734–4740 (2018).

30. Javadi, A, Söllner, I, Arcari, M, Hansen, S. L., Midolo, L, Mahmoodian, S, Pregnolato, T, Lee, E. H., Song, J. D., Stobbe, S & Lodahl, P. Single-photon non-linear optics with a quantum dot in a waveguide. *Nature Communications* **6,** 8655 (1 2015).

31. Chang, D. E., Sørensen, A. S., Demler, E. A. & Lukin, M. D. A single-photon transistor using nanoscale surface plasmons. *Nature Physics* **3,** 807–812 (2007).

32. Bouwmeester, D., Ekert, A. & Zeilinger, A. *The Physics of Quantum Information* 1st ed. (Springer-Verlag Berlin Heidelberg GmbH, Berlin, 2000).

33. Moerner, W. E. & Orrit, M. Illuminating Single Molecules in Condensed Matter. *Science* **283,** 1670–1676 (1999).

34. Basché, T., Moerner, W., Orrit, M. & Wild, U. *Single-Molecule Optical Detection, Imaging and Spectroscopy* (VCH Verlagsgesellschaft mbH, Weinheim, 1997).

35. Faez, S., van der Molen, S. J. & Orrit, M. Optical tracing of multiple charges in single-electron devices. *Phys. Rev. B* **90,** 205405 (20 2014).

36. Tian, Y., Navarro, P. & Orrit, M. Single Molecule as a Local Acoustic Detector for Mechanical Oscillators. *Phys. Rev. Lett.* **113,** 135505 (13 2014).

37. Moerner, W. E. & Kador, L. Optical detection and spectroscopy of single molecules in a solid. *Phys. Rev. Lett.* **62,** 2535–2538 (21 1989).

38. Orrit, M. & Bernard, J. Single pentacene molecules detected by fluorescence excitation in a p-terphenyl crystal. *Phys. Rev. Lett.* **65,** 2716–2719 (21 1990).

39. Chong, S., Min, W. & Xie, X. S. Ground-State Depletion Microscopy: Detection Sensitivity of Single-Molecule Optical Absorption at Room Temperature. *The Journal of Physical Chemistry Letters* **1,** 3316–3322 (2010).

40. Gaiduk, A., Yorulmaz, M., Ruijgrok, P. V. & Orrit, M. Room-Temperature Detection of a Single Molecule's Absorption by Photothermal Contrast. *Science* **330,** 353–356 (2010).

41. Kukura, P., Celebrano, M., Renn, A. & Sandoghdar, V. Single-Molecule Sensitivity in Optical Absorption at Room Temperature. *The Journal of Physical Chemistry Letters* **1,** 3323–3327 (2010).

42. Celebrano, M., Kukura, P., Renn, A. & Sandoghdar, V. Single-molecule imaging by optical absorption. *Nature Photonics* **5,** 95–98 (2011).

43. Reinhold, J. *Quantentheorie der Moleküle* 5th ed. (Springer Fachmedien, Wiesbaden, 2015).

44. Demtröder, W. *Molekülphysik* ISBN: 978-3-486-71489-0 (De Gruyter, Berlin, Boston, 2013).
45. Köhler, A. & Bässler, H. *Electronic Processes in Organic Semiconductors* ISBN: 9783527685172 (John Wiley & Sons, Ltd, 2015).
46. Kelley, A. M. *Condensed-Phase Molecular Spectroscopy and Photophysics* ISBN: 9781118493052 (John Wiley & Sons, Ltd, 2012).
47. Parson, W. W. *Modern Optical Spectroscopy* ISBN: 978-3-662-46776-3 (Springer Berlin Heidelberg, Berlin, Heidelberg, 2015).
48. Groß, H., Hamm, J. M., Tufarelli, T., Hess, O. & Hecht, B. Near-field strong coupling of single quantum dots. *Science Advances* **4** (2018).
49. Bransden, B. H. & Joachain, C. J. (Longman Group Limited, New York, 1996).
50. McHale, J. L. *Molecular Spectroscopy* 2nd ed. (CRC Press, Boca Raton, 2017).
51. Andersen, M. L., Stobbe, S., Sørensen, A. S. & Lodahl, P. Strongly modified plasmon–matter interaction with mesoscopic quantum emitters. *Nature Physics* **7,** 215–218 (2011).
52. Tighineanu, P., Sørensen, A. S., Stobbe, S. & Lodahl, P. Unraveling the Mesoscopic Character of Quantum Dots in Nanophotonics. *Phys. Rev. Lett.* **114,** 247401 (24 2015).
53. Loudon, R. *The quantum theory of light* 3rd ed. ISBN: 9780198501770 (Oxford Univ. Press, Oxford [u.a.], 2003).
54. Haken, H. & Wolf, H. C. *Molekülphysik und Quantenchemie: Einführung in die experimentellen und theoretischen Grundlagen* 5th ed. ISBN: 3540303154 (Springer, Berlin [u.a.], 2006).
55. Novotny, L. & Hecht, B. *Principles of Nano-Optics* (Cambridge University Press, 2012).
56. Lakowicz, J. R. *Principles of Fluorescence Spectroscopy* 3rd ed. (Springer Science + Business Media, New York, 2006).
57. Valeur, B. & Berberan-Santos, M. N. *Molecular Fluorescence: Principles and Applications* ISBN: 9783527650002 (John Wiley & Sons, Ltd, 2012).
58. Clear, C., Schofield, R. C., Major, K. D., Iles-Smith, J., Clark, A. S. & McCutcheon, D. P. S. Phonon-Induced Optical Dephasing in Single Organic Molecules. *Phys. Rev. Lett.* **124,** 153602 (15 2020).
59. Kastrup, L. & Hell, S. W. Absolute Optical Cross Section of Individual Fluorescent Molecules. *Angewandte Chemie International Edition* **43,** 6646–6649 (2004).
60. Demtröder, W. *Molekülphysik: Theoretische Grundlagen und experimentelle Methoden* 2nd ed. (Oldenbourg, München, 2013).
61. Demtröder, W. *Laser Spectroscopy 1* 5th ed. (Springer-Verlag Berlin Heidelberg, Heidelberg, 2014).
62. Kador, L. Stochastic theory of inhomogeneous spectroscopic line shapes reinvestigated. *The Journal of Chemical Physics* **95,** 5574 (1991).

63. Rebane, K. K. & Rebane, I. Peak value of the cross-section of zero-phonon line's absorption. *Journal of Luminescence* **56,** 39 –45. ISSN: 0022-2313 (1993).

64. Striebel, M., Wrachtrup, J. & Gerhardt, I. Absorption and Extinction Cross Sections and Photon Streamlines in the Optical Near-field. *Scientific Reports* **7,** 15420 (2017).

65. Wrigge, G., Gerhardt, I., Hwang, J., Zumofen, G. & Sandoghdar, V. Efficient coupling of photons to a single molecule and the observation of its resonance fluorescence. *Nature Physics* **4,** 60–66 (2008).

66. Rebane, K. K. Zero-phonon line as the foundation stone of high-resolution matrix spectroscopy, persistent spectral hole burning, single impurity molecule spectroscopy. *Chemical Physics* **189,** 139 –148. ISSN: 0301-0104 (1994).

67. Toninelli, C. *et al.* Single organic molecules for photonic quantum technologies. *arXiv,* 2011.05059 (2020).

68. Wang, D., Kelkar, H., Martin-Cano Diego and-Rattenbacher, D., Shkarin, A., Utikal, T., Götzinger, S. & Sandoghdar, V. Turning a molecule into a coherent two-level quantum system. *Nature Physics* **15,** 483–489 (2019).

69. Pitarke, J. M., Silkin, V. M., Chulkov, E. V. & Echenique, P. M. Theory of surface plasmons and surface-plasmon polaritons. *Reports on Progress in Physics* **70,** 1–87 (2006).

70. Maier, S. A. *Plasmonics: Fundamentals and Applications* (Springer Science+Business Media LLC, 2007).

71. Jackson, J. D., Witte, C., Diestelhorst, M. & Müller, K. *Klassische Elektrodynamik* ISBN: 978-3-11-033447-0 (De Gruyter, Berlin, Boston, 2014).

72. Raza, S., Bozhevolnyi, S. I., Wubs, M. & Mortensen, N. A. Nonlocal optical response in metallic nanostructures. *Journal of Physics: Condensed Matter* **27,** 183204 (2015).

73. Hohenester, U. *Nano and Quantum Optics* (Springer Nature Switzerland AG, 2020).

74. Ashcroft, N. & Mermin, N. *Festkörperphysik* ISBN: 9783486582734 (Oldenbourg, 2007).

75. Johnson, P. B. & Christy, R. W. Optical Constants of the Noble Metals. *Phys. Rev. B* **6,** 4370–4379 (12 1972).

76. Zeman, E. J. & Schatz, G. C. An accurate electromagnetic theory study of surface enhancement factors for silver, gold, copper, lithium, sodium, aluminum, gallium, indium, zinc, and cadmium. *The Journal of Physical Chemistry* **91,** 634–643 (1987).

77. Baburin, A. S., Merzlikin, A. M., Baryshev, A. V., Ryzhikov, I. A., Panfilov, Y. V. & Rodionov, I. A. Silver-based plasmonics: golden material platform and application challenges [Invited]. *Opt. Mater. Express* **9,** 611–642 (2019).

78. Han, Z. & Bozhevolnyi, S. I. Radiation guiding with surface plasmon polaritons. *Reports on Progress in Physics* **76,** 016402 (2012).

79. Maier, S. A., Brongersma, M. L., Kik, P. G., Meltzer, S., Requicha, A. A. G. & Atwater, H. A. Plasmonics - A Route to Nanoscale Optical Devices. *Advanced Materials* **13,** 1501–1505 (2001).

80. Siampour, H., Kumar, S., Davydov, V. A., Kulikova, L. F., Agafonov, V. N. & Bozhevolnyi, S. I. On-chip excitation of single germanium vacancies in nanodiamonds embedded in plasmonic waveguides. *Light: Sci. Appl.* **7,** 61 (2018).

81. Wei, H., Pan, D., Zhang, S., Li, Z., Li, Q., Liu, N., Wang, W. & Xu, H. Plasmon Waveguiding in Nanowires. *Chem. Rev.* **118,** 2882–2926 (2018).

82. Bermúdez-Ureña, E., Gonzalez-Ballestero, C., Geiselmann, M., Marty, R., Radko, I. P., Holmgaard, T., Alaverdyan, Y., Moreno, E., García-Vidal, F. J., Bozhevolnyi, S. I. & Quidant, R. Coupling of individual quantum emitters to channel plasmons. *Nat. Commun.* **6,** 7883 (2015).

83. Novotny, L. & Hafner, C. Light propagation in a cylindrical waveguide with a complex, metallic, dielectric function. *Phys. Rev. E* **50,** 4094–4106 (5 1994).

84. Novotny, L. Effective Wavelength Scaling for Optical Antennas. *Phys. Rev. Lett.* **98,** 266802 (26 2007).

85. Zhang, S., Wei, H., Bao, K., Håkanson, U., Halas, N. J., Nordlander, P. & Xu, H. Chiral Surface Plasmon Polaritons on Metallic Nanowires. *Phys. Rev. Lett.* **107,** 096801 (9 2011).

86. Conway, J., Sahni, S. & Szkopek, T. Plasmonic interconnects versus conventional interconnects: a comparison of latency, crosstalk and energy costs. *Opt. Express* **15,** 4474–4484 (2007).

87. Oulton, R. F., Bartal, G., Pile, D. F. P. & Zhang, X. Confinement and propagation characteristics of subwavelength plasmonic modes. *New Journal of Physics* **10,** 105018 (2008).

88. Li, Z., Bao, K., Fang, Y., Huang, Y., Nordlander, P. & Xu, H. Correlation between Incident and Emission Polarization in Nanowire Surface Plasmon Waveguides. *Nano Letters* **10,** 1831–1835 (2010).

89. Song, M., Bouhelier, A., Bramant, P., Sharma, J., Dujardin, E., Zhang, D. & Colas-des Francs, G. Imaging Symmetry-Selected Corner Plasmon Modes in Penta-Twinned Crystalline Ag Nanowires. *ACS Nano* **5,** 5874–5880 (2011).

90. Zia, R., Selker, M. D. & Brongersma, M. L. Leaky and bound modes of surface plasmon waveguides. *Phys. Rev. B* **71,** 165431 (16 2005).

91. Castro-Lopez, M., Manjavacas, A., de Abajo, J. G. & van Hulst, N. F. Propagation and localization of quantum dot emission along a gap-plasmonic transmission line. *Opt. Express* **23,** 29296–29320 (2015).

92. Chen, Y., Nielsen, T. R., Gregersen, N., Lodahl, P. & Mørk, J. Finite-element modeling of spontaneous emission of a quantum emitter at nanoscale proximity to plasmonic waveguides. *Phys. Rev. B* **81,** 125431 (12 2010).

93. Su, L., Lu, G., Kenens, B., Rocha, S., Fron, E., Yuan, H., Chen, C., Van Dorpe, P., Roeffaers, M. B. J., Mizuno, H., Hofkens, J., Hutchison, J. A. & Uji-i, H. Visualization of molecular fluorescence point spread functions via remote excitation switching fluorescence microscopy. *Nature Communications* **6,** 6287 (1 2015).

94. Raab, M., Vietz, C., Stefani, F. D., Acuna, G. P. & Tinnefeld, P. Shifting molecular localization by plasmonic coupling in a single-molecule mirage. *Nature Communications* **8,** 13966 (1 2017).

95. Baiyasi, R., Jebeli, S. A. H., Zhang, Q., Su, L., Hofkens, J., Uji-i, H., Link, S. & Landes, C. F. PSF Distortion in Dye–Plasmonic Nanomaterial Interactions: Friend or Foe? *ACS Photonics* **6,** 699–708 (2019).

96. Blanquer, G., van Dam, B., Gulinatti, A., Acconcia, G., De Wilde, Y., Izeddin, I. & Krachmalnicoff, V. Relocating Single Molecules in Super-Resolved Fluorescence Lifetime Images near a Plasmonic Nanostructure. *ACS Photonics* **7,** 393–400 (2020).

97. Barnes, W. L., Horsley, S. A. R. & Vos, W. L. Classical antennae, quantum emitters, and densities of optical states. *Journal of Optics* (2020).

98. Li, Q., Wei, H. & Xu, H. Quantum Yield of Single Surface Plasmons Generated by a Quantum Dot Coupled with a Silver Nanowire. *Nano Lett.* **15,** 8181–8187 (2015).

99. Teperik, T. V., Nordlander, P., Aizpurua, J. & Borisov, A. G. Robust Subnanometric Plasmon Ruler by Rescaling of the Nonlocal Optical Response. *Phys. Rev. Lett.* **110,** 263901 (26 2013).

100. Altewischer, E., van Exter, M. P. & Woerdman, J. P. Plasmon-assisted transmission of entangled photons. *Nature* **418,** 304–306 (2002).

101. Akimov, A. V., Mukherjee, A, Yu, C. L., Chang, D. E., Zibrov, A. S., Hemmer, P. R., Park, H & Lukin, M. D. Generation of single optical plasmons in metallic nanowires coupled to quantum dots. *Nature* **450,** 402–406 (7168 2007).

102. Jin, J. *The finite element method in electromagnetics* (John Wiley & Sons, Inc., 1993).

103. Liu, G. & Quek, S. *The Finite Element Method: A Practical Course* (Elsevier Science Ltd, 2003).

104. Saleh, B. E. & Teich, M. C. *Grundlagen der Photonik* (Wiley-VCH, 2008).

105. Malitson, I. H. Refraction and Dispersion of Synthetic Sapphire. *J. Opt. Soc. Am.* **52,** 1377–1379 (1962).

106. Crut, A., Maioli, P., Del Fatti, N. & Vallée, F. Optical absorption and scattering spectroscopies of single nano-objects. *Chem. Soc. Rev.* **43,** 3921–3956 (11 2014).

107. Dorfmüller, J., Vogelgesang, R., Weitz, R. T., Rockstuhl, C., Etrich, C., Pertsch, T., Lederer, F. & Kern, K. Fabry-Pérot Resonances in One-Dimensional Plasmonic Nanostructures. *Nano Letters* **9,** 2372–2377 (2009).

108. *Comsol Multiphysics - RF module user's guide version 5.4* (COMSOL, 2018).

109. Bohren, C. F. & Huffman, D. R. *Absorption and Scattering of Light by Small Particles* ISBN: 9783527618156 (John Wiley and Sons, Ltd, 2007).

110. Scaffardi, L. B., Lester, M., Skigin, D. & Tocho, J. O. Optical extinction spectroscopy used to characterize metallic nanowires. *Nanotechnology* **18,** 315402 (2007).

111. Zijlstra, P., Paulo, P. M. R. & Orrit, M. Optical detection of single non-absorbing molecules using the surface plasmon resonance of a gold nanorod. *Nature Nanotechnology* **7,** 379–382 (6 2012).

112. Prämassing, M., Liebtrau, M., Schill, H. J., Irsen, S. & Linden, S. Interferometric near-field characterization of plasmonic slot waveguides in single- and polycrystalline gold films. *Opt. Express* **28,** 12998–13007 (2020).

113. Bozhevolnyi, S. I. *Plasmonic Nanoguides and Circuits* (Pan Stanford Publishing Pte. Ltd., 2009).

114. Geisler, P., Razinskas, G., Krauss, E., Wu, X.-F., Rewitz, C., Tuchscherer, P., Goetz, S., Huang, C.-B., Brixner, T. & Hecht, B. Multimode Plasmon Excitation and In Situ Analysis in Top-Down Fabricated Nanocircuits. *Phys. Rev. Lett.* **111,** 183901 (18 2013).

115. Geisler, P., Krauss, E., Razinskas, G. & Hecht, B. Transmission of Plasmons through a Nanowire. *ACS Photonics* **4,** 1615–1620 (2017).

116. Yang, J., Hugonin, J.-P. & Lalanne, P. Near-to-Far Field Transformations for Radiative and Guided Waves. *ACS Photonics* **3,** 395–402 (2016).

117. Wolf, E. & Gabor, D. Electromagnetic diffraction in optical systems - I. An integral representation of the image field. *Proceedings of the Royal Society of London. Series A. Mathematical and Physical Sciences* **253,** 349–357 (1959).

118. Richards, B., Wolf, E. & Gabor, D. Electromagnetic diffraction in optical systems, II. Structure of the image field in an aplanatic system. *Proceedings of the Royal Society of London. Series A. Mathematical and Physical Sciences* **253,** 358–379 (1959).

119. Schörner, C., Motamen, S., Simon, L., Reiter, G. & Hildner, R. Self-Interference of Exciton Emission in Organic Single Crystals Visualized by Energy-Momentum Spectroscopy. *ACS Omega* **3,** 6728–6736 (2018).

120. Qian, H. & Elson, E. L. Analysis of confocal laser-microscope optics for 3-D fluorescence correlation spectroscopy. *Appl. Opt.* **30,** 1185–1195 (1991).

121. Chen, W., Zhang, S., Deng, Q. & Xu, H. Probing of sub-picometer vertical differential resolutions using cavity plasmons. *Nature Communications* **9,** 801 (2018).

122. Le Ru, E. & Etchegoin, P. Rigorous justification of the $|E|^4$ enhancement factor in Surface Enhanced Raman Spectroscopy. *Chemical Physics Letters* **423,** 63 –66 (2006).

123. Lewis, L. N. Chemical catalysis by colloids and clusters. *Chemical Reviews* **93,** 2693–2730 (1993).

124. Atwater, H. A. & Polman, A. Plasmonics for improved photovoltaic devices. *Nature Materials* **9,** 205–213 (2010).

125. Rodionov, I. A., Baburin, A. S., Gabidullin, A. R., Maklakov, S. S., Peters, S., Ryzhikov, I. A. & Andriyash, A. V. Quantum Engineering of Atomically Smooth Single-Crystalline Silver Films. *Scientific Reports* **9,** 12232 (2019).

126. Wild, B., Cao, L., Sun, Y., Khanal, B. P., Zubarev, E. R., Gray, S. K., Scherer, N. F. & Pelton, M. Propagation Lengths and Group Velocities of Plasmons in Chemically Synthesized Gold and Silver Nanowires. *ACS Nano* **6,** 472–482 (2012).

127. Huang, J.-S., Callegari, V., Geisler, P., Brüning, C., Kern, J., Prangsma, J. C., Wu, X., Feichtner, T., Ziegler, J., Weinmann, P., Kamp, M., Forchel, A., Biagioni, P., Sennhauser, U. & Hecht, B. Atomically flat single-crystalline gold nanostructures for plasmonic nanocircuitry. *Nat. Commun.* **1,** 150 (2010).

128. Park, J. H., Ambwani, P., Manno, M., Lindquist, N. C., Nagpal, P., Oh, S.-H., Leighton, C. & Norris, D. J. Single-Crystalline Silver Films for Plasmonics. *Advanced Materials* **24,** 3988–3992 (2012).

129. Hong, H. Y., Ha, J. S., Lee, S.-S. & Park, J. H. Effective Propagation of Surface Plasmon Polaritons on Graphene-Protected Single-Crystalline Silver Films. *ACS Applied Materials & Interfaces* **9,** 5014–5022 (2017).

130. Lee, H., Jeong, K.-Y., Kang, T., Seo, M.-K. & Kim, B. A twin-free single-crystal Ag nanoplate plasmonic platform: hybridization of the optical nano-antenna and surface plasmon active surface. *Nanoscale* **6,** 514–520 (1 2014).

131. Deckert-Gaudig, T., Erver, F. & Deckert, V. Transparent Silver Microcrystals: Synthesis and Application for Nanoscale Analysis. *Langmuir* **25,** 6032–6034 (2009).

132. Lim, G.-H., Han, I., Yu, T. & Lim, B. Aqueous-phase synthesis of silver nanoplates: Enhancing lateral growth via a heat-up process. *Chem. Phys. Lett.* **568-569,** 135 –139 (2013).

133. Lyutov, D. L., Genkov, K. V., Zyapkov, A. D., Tsutsumanova, G. G., Tzonev, A. N., Lyutov, L. G. & Russev, S. C. Synthesis and structure of large single crystalline silver hexagonal microplates suitable for micromachining. *Mater. Chem. and Phys.* **143,** 642 –646 (2014).

134. Chang, C.-W., Lin, F.-C., Chiu, C.-Y., Su, C.-Y., Huang, J.-S., Perng, T.-P. & Yen, T.-J. HNO_3-Assisted Polyol Synthesis of Ultralarge Single-Crystalline Ag Microplates and Their Far Propagation Length of Surface Plasmon Polariton. *ACS Appl. Mater. Interfaces* **6,** 11791–11798 (2014).

135. Wang, C.-Y., Chen, H.-Y., Sun, L., Chen, W.-L., Chang, Y.-M., Ahn, H., Li, X. & Gwo, S. Giant colloidal silver crystals for low-loss linear and nonlinear plasmonics. *Nat. Commun.* **6,** 7734 (2015).

136. Zhang, X.-Y., Zhou, H.-L., Shan, F., Xue, X.-M., Su, D., Liu, Y.-R., Chen, Y.-Z., Wu, J.-Y. & Zhang, T. Synthesis of silver nanoplate based two-dimension plasmonic platform from 25 nm to 40 μm: growth mechanism and optical characteristic investigation in situ. *RSC Adv.* **7,** 55680–55690 (2017).

137. Elechiguerra, J. L., Reyes-Gasga, J. & Yacaman, M. J. The role of twinning in shape evolution of anisotropic noble metal nanostructures. *J. Mater. Chem.* **16,** 3906–3919 (40 2006).

138. Xia, Y., Xiong, Y., Lim, B. & Skrabalak, S. Shape-Controlled Synthesis of Metal Nanocrystals: Simple Chemistry Meets Complex Physics? *Angewandte Chemie International Edition* **48,** 60–103 (2009).

139. Rycenga, M., Cobley, C. M., Zeng, J., Li, W., Moran, C. H., Zhang, Q., Qin, D. & Xia, Y. Controlling the Synthesis and Assembly of Silver Nanostructures for Plasmonic Applications. *Chem. Rev.* **111,** 3669–3712 (2011).

140. Krauss, E., Kullock, R., Wu, X., Geisler, P., Lundt, N., Kamp, M. & Hecht, B. Controlled Growth of High-Aspect-Ratio Single-Crystalline Gold Platelets. *Crystal Growth & Design* **18,** 1297–1302 (2018).

141. Demtröder, W. *Experimentalphysik 3: Atome, Moleküle und Festkörper* (Springer Spektrum, 2016).

142. Frøseth, A. G., Derlet, P. M. & Van Swygenhoven, H. Twinning in Nanocrystalline fcc Metals. *Advanced Engineering Materials* **7,** 16–20 (2005).

143. Dahmen, U., Hetherington, C. J. D., Radmilovic, V., Johnson, E., Xiao, S. Q. & Luo, C. P. Electron Microscopy Observations on the Role of Twinning in the Evolution of Microstructures. *Microscopy and Microanalysis* **8,** 247–256 (2002).

144. Lofton, C. & Sigmund, W. Mechanisms Controlling Crystal Habits of Gold and Silver Colloids. *Advanced Functional Materials* **15,** 1197–1208 (2005).

145. Großmann, S., Friedrich, D., Karolak, M., Kullock, R., Krauss, E., Emmerling, M., Sangiovanni, G. & Hecht, B. Nonclassical Optical Properties of Mesoscopic Gold. *Phys. Rev. Lett.* **122,** 246802 (24 2019).

146. Bai, X., Zheng, L., Li, N., Dong, B. & Liu, H. Synthesis and Characterization of Microscale Gold Nanoplates Using Langmuir Monolayers of Long-Chain Ionic Liquid. *Crystal Growth & Design* **8,** 3840–3846 (2008).

147. Bögels, G., Pot, T. M., Meekes, H., Bennema, P. & Bollen, D. Side-Face Structure and Growth Mechanism of Tabular Silver Bromide Crystals. *Acta Crystallographica Section A* **53,** 84–94 (1997).

148. Bögels, G., Meekes, H., Bennema, P. & Bollen, D. The role of 100 side faces for lateral growth of tabular silver bromide crystals. *Journal of Crystal Growth* **191,** 446 –454 (1998).

149. Frank, B., Kahl, P., Podbiel, D., Spektor, G., Orenstein, M., Fu, L., Weiss, T., Horn-von Hoegen, M., Davis, T. J., Meyer zu Heringdorf, F.-J. & Giessen, H. Short-range surface plasmonics: Localized electron emission dynamics from a 60-nm spot on an atomically flat single-crystalline gold surface. *Sci. Adv.* **3,** e1700721 (2017).

150. Goldstein, J., Newbury, D., Joy, D., Lyman, C., Echlin, P., Lifshin, E., Sawyer, L. & Michael, J. *Scanning Electron Microscopy and X-Ray Microanalysis* (Springer Science+Business Media, 2003).

151. Fultz, B. & Howe, J. M. *Transmission Electron Microscopy and Diffractometry of Materials* 3. ed. (Springer Science+Business Media, 2008).

152. Nolze, G. Euler angles and crystal symmetry. *Crystal Research and Technology* **50,** 188–201 (2015).

153. Carneiro, Í. & Simões, S. Recent Advances in EBSD Characterization of Metals. *Metals* **10,** 1097 (2020).

154. Kuttge, M., Vesseur, E. J. R., Verhoeven, J., Lezec, H. J., Atwater, H. A. & Polman, A. Loss mechanisms of surface plasmon polaritons on gold probed by cathodoluminescence imaging spectroscopy. *Applied Physics Letters* **93,** 113110 (2008).

155. Binnig, G., Quate, C. F. & Gerber, C. Atomic Force Microscope. *Phys. Rev. Lett.* **56,** 930–933 (9 1986).

156. Reifenberger, R. *Fundamentals of Atomic Force Microscopy* (World Scientific, 2015).

157. Giessibl, F. J. Atomic Resolution of the Silicon (111)-(7x7) Surface by Atomic Force Microscopy. *Science* **267,** 68–71 (1995).

158. Gross, R. & Marx, A. *Festkörperphysik* ISBN: 978-3-11-035870-4 (De Gruyter Oldenbourg, Berlin, Boston, 2014).

159. Roobol, S. B., Cañas Ventura, M. E., Bergman, M., van Spronsen, M. A., Onderwaater, W. G., van der Tuijn, P. C., Koehler, R., Ofitserov, A., van Baarle, G. J. C. & Frenken, J. W. M. The ReactorAFM: Non-contact atomic force microscope operating under high-pressure and high-temperature catalytic conditions. *Review of Scientific Instruments* **86,** 033706 (2015).

160. Luh, D.-A., Liu, C.-W., Cheng, C.-M., Tsuei, K.-D., Wang, C.-H. & Yang, Y.-W. Single-crystalline silver films on mica. *Thin Solid Films* **645,** 215 –221. ISSN: 0040-6090 (2018).

161. Wang, X., Santschi, C. & Martin, O. J. F. Strong Improvement of Long-Term Chemical and Thermal Stability of Plasmonic Silver Nanoantennas and Films. *Small* **13,** 1700044 (2017).

162. Taylor, C. E., Garvey, S. D. & Pemberton, J. E. Carbon Contamination at Silver Surfaces: Surface Preparation Procedures Evaluated by Raman Spectroscopy and X-ray Photoelectron Spectroscopy. *Analytical Chemistry* **68,** 2401–2408 (1996).

163. Baburin, A. S., Ivanov, A. I., Ryzhikov, I. A., Trofimov, I. V., Gabidullin, A. R., Moskalev, D. O., Panfilov, Y. V. & Rodionov, I. A. *Crystalline structure dependence on optical properties of silver thin film over time* in *2017 Progress In Electromagnetics Research Symposium - Spring (PIERS)* (2017), 1497–1502.

164. Rao, K. D. M., Hunger, C., Gupta, R., Kulkarni, G. U. & Thelakkat, M. A cracked polymer templated metal network as a transparent conducting electrode for ITO-free organic solar cells. *Phys. Chem. Chem. Phys.* **16,** 15107–15110 (29 2014).

165. Kusar, P., Gruber, C., Hohenau, A. & Krenn, J. R. Measurement and Reduction of Damping in Plasmonic Nanowires. *Nano Letters* **12,** 661–665 (2012).

166. Ditlbacher, H., Hohenau, A., Wagner, D., Kreibig, U., Rogers, M., Hofer, F., Aussenegg, F. R. & Krenn, J. R. Silver Nanowires as Surface Plasmon Resonators. *Phys. Rev. Lett.* **95,** 257403 (25 2005).

167. Broas, M., Kanninen, O., Vuorinen, V., Tilli, M. & Paulasto-Kröckel, M. Chemically Stable Atomic-Layer-Deposited Al_2O_3 Films for Processability. *ACS Omega* **2,** 3390–3398 (2017).

168. Detavernier, C., Dendooven, J., Pulinthanathu Sree, S., Ludwig, K. F. & Martens, J. A. Tailoring nanoporous materials by atomic layer deposition. *Chem. Soc. Rev.* **40,** 5242–5253 (11 2011).

169. Puurunen, R. L., Saarilahti, J. & Kattelus, H. *Implementing ALD Layers in MEMS Processing* in *ECS Transactions* (ECS, 2007).

170. Hiller, D. *et al.* Low temperature silicon dioxide by thermal atomic layer deposition: Investigation of material properties. *Journal of Applied Physics* **107,** 064314 (2010).

171. Liu, H., Guo, S., Yang, R. B., Lee, C. J. J. & Zhang, L. Giant Blistering of Nanometer-Thick Al_2O_3/ZnO Films Grown by Atomic Layer Deposition: Mechanism and Potential Applications. *ACS Applied Materials & Interfaces* **9,** 26201–26209 (2017).

172. Gramotnev, D. K. & Bozhevolnyi, S. I. Plasmonics beyond the diffraction limit. *Nat. Photonics* **4,** 83–91 (2010).

173. Fang, Y. & Sun, M. Nanoplasmonic waveguides: towards applications in integrated nanophotonic circuits. *Light: Sci. Appl.* **4,** e294 (2015).

174. Davanco, M., Liu, J., Sapienza, L., Zhang, C.-Z., De Miranda Cardoso, J. V., Verma, V., Mirin, R., Nam, S. W., Liu, L. & Srinivasan, K. Heterogeneous integration for on-chip quantum photonic circuits with single quantum dot devices. *Nature Communications* **8,** 889 (1 2017).

175. Siampour, H., Kumar, S. & Bozhevolnyi, S. I. Nanofabrication of Plasmonic Circuits Containing Single Photon Sources. *ACS Photonics* **4,** 1879–1884 (2017).

176. Rothe, M., Zhao, Y., Kewes, G., Kochovski, Z., Sigle, W., van Aken, P. A., Koch, C., Ballauff, M., Lu, Y. & Benson, O. Silver nanowires with optimized silica coating as versatile plasmonic resonators. *Scientific Reports* **9,** 3859 (1 2019).

177. Kress, S. J. P., Antolinez, F. V., Richner, P., Jayanti, S. V., Kim, D. K., Prins, F., Riedinger, A., Fischer, M. P. C., Meyer, S., McPeak, K. M., Poulikakos, D. & Norris, D. J. Wedge Waveguides and Resonators for Quantum Plasmonics. *Nano Lett.* **15,** 6267–6275 (2015).

178. Kumar, S., Huck, A. & Andersen, U. L. Efficient Coupling of a Single Diamond Color Center to Propagating Plasmonic Gap Modes. *Nano Lett.* **13,** 1221–1225 (2013).

179. Kumar, S., Andersen, S. K. H. & Bozhevolnyi, S. I. Extremely Confined Gap-Plasmon Waveguide Modes Excited by Nitrogen-Vacancy Centers in Diamonds. *ACS Photonics* **6,** 23–29 (2018).

180. Gan, F., Sun, C., Wang, Y., Li, H., Gong, Q. & Chen, J. Multimode Metallic Double-Strip Waveguides for Polarization Manipulation. *Advanced Materials Technologies* **2,** 1600248 (2017).

181. Dai, W.-H., Lin, F.-C., Huang, C.-B. & Huang, J.-S. Mode Conversion in High-Definition Plasmonic Optical Nanocircuits. *Nano Lett.* **14,** 3881–3886 (2014).

182. Rewitz, C., Razinskas, G., Geisler, P., Krauss, E., Goetz, S., Pawłowska, M., Hecht, B. & Brixner, T. Coherent Control of Plasmon Propagation in a Nanocircuit. *Phys. Rev. Appl.* **1,** 014007 (1 2014).

183. Krauss, E., Razinskas, G., Köck, D., Grossmann, S. & Hecht, B. Reversible Mapping and Sorting the Spin of Photons on the Nanoscale: A Spin-Optical Nanodevice. *Nano Letters* **19,** 3364–3369 (2019).

184. Thomaschewski, M., Yang, Y., Wolff, C., Roberts, A. S. & Bozhevolnyi, S. I. On-Chip Detection of Optical Spin–Orbit Interactions in Plasmonic Nanocircuits. *Nano Letters* **19,** 1166–1171 (2019).

185. Chen, T.-Y., Obermeier, J., Schumacher, T., Lin, F.-C., Huang, J.-S., Lippitz, M. & Huang, C.-B. Modal Symmetry Controlled Second-Harmonic Generation by Propagating Plasmons. *Nano Letters* **19,** 6424–6428 (2019).

186. Kolesov, R., Grotz, B., Balasubramanian, G., Stöhr, R. J., Nicolet, A. A., Hemmer, P. R., Jelezko, F. & Wrachtrup, J. Wave–particle duality of single surface plasmon polaritons. *Nat. Phys.* **5,** 470–474 (2009).

187. De Torres, J., Ferrand, P., Colas des Francs, G. & Wenger, J. Coupling Emitters and Silver Nanowires to Achieve Long-Range Plasmon-Mediated Fluorescence Energy Transfer. *ACS Nano* **10,** 3968–3976 (2016).

188. See, K.-M., Lin, F.-C. & Huang, J.-S. Design and characterization of a plasmonic Doppler grating for azimuthal angle-resolved surface plasmon resonances. *Nanoscale* **9,** 10811–10819 (30 2017).

189. Kumar, U., Viarbitskaya, S., Cuche, A., Girard, C., Bolisetty, S., Mezzenga, R., Colas des Francs, G., Bouhelier, A. & Dujardin, E. Designing Plasmonic Eigenstates for Optical Signal Transmission in Planar Channel Devices. *ACS Photonics* **5,** 2328–2335 (2018).

190. Kewes, G., Schoengen, M., Neitzke, O., Lombardi, P., Schönfeld, R.-S., Mazzamuto, G., Schell, A. W., Probst, J., Wolters, J., Löchel, B., Toninelli, C. & Benson, O. A realistic fabrication and design concept for quantum gates based on single emitters integrated in plasmonic-dielectric waveguide structures. *Sci. Rep.* **6,** 28877 (2016).

191. Wu, X., Jiang, P., Razinskas, G., Huo, Y., Zhang, H., Kamp, M., Rastelli, A., Schmidt, O. G., Hecht, B., Lindfors, K. & Lippitz, M. On-Chip Single-Plasmon Nanocircuit Driven by a Self-Assembled Quantum Dot. *Nano Lett.* **17,** 4291–4296 (2017).

192. Blauth, M., Jürgensen, M., Vest, G., Hartwig, O., Prechtl, M., Cerne, J., Finley, J. J. & Kaniber, M. Coupling Single Photons from Discrete Quantum Emitters in WSe_2 to Lithographically Defined Plasmonic Slot Waveguides. *Nano Lett.* **18,** 6812–6819 (2018).

193. Siebrand, W. Radiationless Transitions in Polyatomic Molecules. I. Calculation of Franck-Condon Factors. *The Journal of Chemical Physics* **46,** 440–447 (1967).

194. Rurack, K. & Spieles, M. Fluorescence Quantum Yields of a Series of Red and Near-Infrared Dyes Emitting at 600-1000 nm. *Analytical Chemistry* **83,** 1232–1242 (2011).

195. Kumar, S., Lu, Y.-W., Huck, A. & Andersen, U. L. Propagation of plasmons in designed single crystalline silver nanostructures. *Opt. Express* **20,** 24614–24622 (2012).

196. Zhang, O., Lu, J., Ding, T. & Lew, M. D. Imaging the three-dimensional orientation and rotational mobility of fluorescent emitters using the Tri-spot point spread function. *Applied Physics Letters* **113,** 031103 (2018).

197. Castro-Lopez, M., Manjavacas, A., de Abajo, J. G. & van Hulst, N. F. Propagation and localization of quantum dot emission along a gap-plasmonic transmission line. *Opt. Express* **23,** 29296–29320 (2015).

198. Wang, Y., Kong, M., Xu, Y. & Zhou, Z. Analysis of scattering loss due to sidewall roughness in slot waveguides by variation of mode effective index. *J. Opt.* **20,** 025801 (2018).

199. Peng, R. & Li, D. Fabrication of nanochannels on polystyrene surface. *Biomicrofluidics* **9,** 024117 (2015).

200. Sakat, E., Wojszvzyk, L., Greffet, J.-J., Hugonin, J.-P. & Sauvan, C. Enhancing Light Absorption in a Nanovolume with a Nanoantenna: Theory and Figure of Merit. *ACS Photonics* **7,** 1523–1528 (2020).

201. Lu, L., Zeng, W., Hu, S., Chen, D., Lei, J. & Ren, N. Polarization-dependent fluorescence of CdSe/ZnS quantum dots coupling to a single gold-silver alloy nanotube. *J. Alloys Compd.* **731,** 753 –759 (2018).

202. Shegai, T., Huang, Y., Xu, H. & Käll, M. Coloring fluorescence emission with silver nanowires. *Applied Physics Letters* **96,** 103114 (2010).

203. Kumar, S. & Bozhevolnyi, S. I. Excitation of Hybrid Plasmonic Waveguide Modes by Colloidal Quantum Dots. *ACS Photonics* **6,** 1587–1593 (2019).

204. Kumar, S., Leißner, T., Boroviks, S., Andersen, S. K. H., Fiutowski, J., Rubahn, H.-G., Mortensen, N. A. & Bozhevolnyi, S. I. Efficient Coupling of Single Organic Molecules to Channel Plasmon Polaritons Supported by V-Grooves in Monocrystalline Gold. *ACS Photonics* **7,** 2211–2218 (2020).

205. Huck, A. & Andersen, U. L. Coupling single emitters to quantum plasmonic circuits. *Nanophotonics* **5,** 483–495 (2016).

206. Huck, A., Kumar, S., Shakoor, A. & Andersen, U. L. Controlled Coupling of a Single Nitrogen-Vacancy Center to a Silver Nanowire. *Physical Review Letters* **106,** 096801 (2011).

207. Li, Q., Pan, D., Wei, H. & Xu, H. Plasmon-Assisted Selective and Super-Resolving Excitation of Individual Quantum Emitters on a Metal Nanowire. *Nano Letters* **18,** 2009–2015 (2018).

208. Grandi, S., Nielsen, M. P., Cambiasso, J., Boissier, S., Major, K. D., Reardon, C., Krauss, T. F., Oulton, R. F., Hinds, E. A. & Clark, A. S. Hybrid plasmonic waveguide coupling of photons from a single molecule. *APL Photonics* **4,** 086101 (2019).

209. Faez, S., Türschmann, P., Haakh, H. R., Götzinger, S. & Sandoghdar, V. Coherent Interaction of Light and Single Molecules in a Dielectric Nanoguide. *Physical Review Letters* **113,** 213601 (2014).

210. Türschmann, P., Rotenberg, N., Renger, J., Harder, I., Lohse, O., Utikal, T., Götzinger, S. & Sandoghdar, V. Chip-Based All-Optical Control of Single Molecules Coherently Coupled to a Nanoguide. *Nano Letters* **17,** 4941–4945 (2017).

211. Türschmann, P., Le Jeannic, H., Simonsen, S. F., Haakh, H. R., Götzinger, S., Sandoghdar, V., Lodahl, P. & Rotenberg, N. Coherent nonlinear optics of quantum emitters in nanophotonic waveguides. *Nanophotonics* **8,** 1641–1657 (2019).

212. Piatkowski, L., Accanto, N., Calbris, G., Christodoulou, S., Moreels, I. & van Hulst, N. F. Ultrafast stimulated emission microscopy of single nanocrystals. *Science* **366,** 1240–1243. ISSN: 0036-8075 (2019).

213. Zhang, W., Caldarola, M., Lu, X. & Orrit, M. Plasmonic Enhancement of Two-Photon-Excited Luminescence of Single Quantum Dots by Individual Gold Nanorods. *ACS Photonics* **5,** 2960–2968 (2018).

214. Silani, Y., Hubert, F. & Acosta, V. M. Stimulated Emission Depletion Microscopy with Diamond Silicon Vacancy Centers. *ACS Photonics* **6,** 2577–2582 (2019).

215. Piwoński, H., Sokolowski, A. & Waluk, J. In Search for the Best Environment for Single Molecule Studies: Photostability of Single Terrylenediimide Molecules in Various Polymer Matrices. *The Journal of Physical Chemistry Letters* **6,** 2477–2482 (2015).

216. Mais, S., Tittel, J., Basché, T., Bräuchle, C., Göhde, W., Fuchs, H., Müller, G. & Müllen, K. Terrylenediimide: A Novel Fluorophore for Single-Molecule Spectroscopy and Microscopy from 1.4 K to Room Temperature. *The Journal of Physical Chemistry A* **101,** 8435–8440 (1997).

217. Allresist. *Product information for E-Beam Resist AR-P 671 series* https://www.allresist.com/. Accessed: 02.03.2021.

218. Plakhotnik, T., Moerner, W., Palm, V. & Wild, U. P. Single molecule spectroscopy: maximum emission rate and saturation intensity. *Optics Communications* **114,** 83–88. ISSN: 0030-4018 (1995).

219. Beveratos, A., Kühn, S., Brouri, R., Gacoin, T., Poizat, J.-P. & Grangier, P. Room temperature stable single-photon source. *The European Physical Journal D* **18,** 191–196 (2002).

220. Beirne, G., Michler, P., Jetter, M. & Schweizer, H. Single-photon emission from a type-B InP/GaInP quantum dot. *Journal of Applied Physics* **98,** 093522 (2005).

221. Rittweger, E., Rankin, B., Westphal, V. & Hell, S. Fluorescence depletion mechanisms in super-resolving STED microscopy. *Chemical Physics Letters* **442,** 483–487. ISSN: 0009-2614 (2007).

222. Bullock, J. E., Vagnini, M. T., Ramanan, C., Co, D. T., Wilson, T. M., Dicke, J. W., Marks, T. J. & Wasielewski, M. R. Photophysics and Redox Properties of Rylene Imide and Diimide Dyes Alkylated Ortho to the Imide Groups. *The Journal of Physical Chemistry B* **114,** 1794–1802 (2010).

223. Boyd, R. W. *Nonlinear Optics* (Elsevir, 2008).

224. Min, W., Lu, S., Chong, S., Roy, R., Holtom, G. R. & Xie, X. S. Imaging chromophores with undetectable fluorescence by stimulated emission microscopy. *Nature* **461,** 1105–1109 (2009).

225. Tian, P., Keusters, D., Suzaki, Y. & Warren, W. S. Femtosecond Phase-Coherent Two-Dimensional Spectroscopy. *Science,* 1553 (2003).

226. Liebel, M., Toninelli, C. & van Hulst, N. F. Room-temperature ultrafast nonlinear spectroscopy of a single molecule. *Nature Photonics* **12,** 45–49 (2018).

227. Mueller, S., Draeger, S., Ma, X., Hensen, M., Kenneweg, T., Pfeiffer, W. & Brixner, T. Fluorescence-Detected Two-Quantum and One-Quantum–Two-Quantum 2D Electronic Spectroscopy. *The Journal of Physical Chemistry Letters* **9,** 1964–1969 (2018).

228. Tiwari, V., Matutes, Y. A., Gardiner, A. T., Jansen, T. L. C., Cogdell, R. J. & Ogilvie, J. P. Spatially-resolved fluorescence-detected two-dimensional electronic spectroscopy probes varying excitonic structure in photosynthetic bacteria. *Nature Communications* **9,** 4219 (2018).

229. Peyser, L. A., Vinson, A. E., Bartko, A. P. & Dickson, R. M. Photoactivated Fluorescence from Individual Silver Nanoclusters. *Science* **291,** 103–106. ISSN: 0036-8075 (2001).

230. Siampour, H., Wang, O., Zenin, V. A., Boroviks, S., Siyushev, P., Yang, Y., Davydov, V. A., Kulikova, L. F., Agafonov, V. N., Kubanek, A., Mortensen, N. A., Jelezko, F. & Bozhevolnyi, S. I. Ultrabright single-photon emission from germanium-vacancy zero-phonon lines: deterministic emitter-waveguide interfacing at plasmonic hot spots. *Nanophotonics* **9,** 953–962 (2020).

231. Vallée, R., Tomczak, N., Gersen, H., van Dijk, E., García-Parajó, M., Vancso, G. & van Hulst, N. On the role of electromagnetic boundary conditions in single molecule fluorescence lifetime studies of dyes embedded in thin films. *Chemical Physics Letters* **348,** 161 –167. ISSN: 0009-2614 (2001).

232. Kreiter, M., Prummer, M., Hecht, B. & Wild, U. P. Orientation dependence of fluorescence lifetimes near an interface. *The Journal of Chemical Physics* **117,** 9430–9433 (2002).

233. Cang, H., Liu, Y., Wang, Y., Yin, X. & Zhang, X. Giant Suppression of Photobleaching for Single Molecule Detection via the Purcell Effect. *Nano Letters* **13,** 5949–5953 (2013).

234. Li, Q., Chen, L., Xu, H., Liu, Z. & Wei, H. Photothermal Modulation of Propagating Surface Plasmons on Silver Nanowires. *ACS Photonics* **6,** 2133–2140 (2019).

235. Hail, C. U., Höller, C., Matsuzaki, K., Rohner, P., Renger, J., Sandoghdar, V., Poulikakos, D. & Eghlidi, H. Nanoprinting organic molecules at the quantum level. *Nature Communications* **10,** 1880 (2019).

236. Kern, J., Großmann, S., Tarakina, N. V., Häckel, T., Emmerling, M., Kamp, M., Huang, J.-S., Biagioni, P., Prangsma, J. C. & Hecht, B. Atomic-Scale Confinement of Resonant Optical Fields. *Nano Letters* **12,** 5504–5509 (2012).

237. Chikkaraddy, R., Zheng, X., Benz, F., Brooks, L. J., de Nijs, B., Carnegie, C., Kleemann, M.-E., Mertens, J., Bowman, R. W., Vandenbosch, G. A. E., Moshchalkov, V. V. & Baumberg, J. J. How Ultranarrow Gap Symmetries Control Plasmonic Nanocavity Modes: From Cubes to Spheres in the Nanoparticle-on-Mirror. *ACS Photonics* **4,** 469–475 (2017).

238. Xomalis, A., Chikkaraddy, R., Oksenberg, E., Shlesinger, I., Huang, J., Garnett, E. C., Koenderink, A. F. & Baumberg, J. J. Controlling Optically Driven Atomic Migration Using Crystal-Facet Control in Plasmonic Nanocavities. *ACS Nano* **14,** 10562–10568 (2020).

239. Carnegie, C., Urbieta, M., Chikkaraddy, R., de Nijs, B., Griffiths, J., Deacon, W. M., Kamp, M., Zabala, N., Aizpurua, J. & Baumberg, J. J. Flickering nanometre-scale disorder in a crystal lattice tracked by plasmonic flare light emission. *Nature Communications* **11,** 682 (2020).

240. Chen, W., Roelli, P., Ahmed, A., Verlekar, S., Hu, H., Kippenberg, T. J., Tagliabue, G. & Galland, C. Intrinsic Luminescence Blinking from Plasmonic Nanojunctions. *arXiv,* 2007.14817 (2020).

241. Abbondanzieri, E. A., Greenleaf, W. J., Shaevitz, J. W., Landick, R. & Block, S. M. Direct observation of base-pair stepping by RNA polymerase. *Nature* **438,** 460–465 (2005).

242. Kukura, P., Celebrano, M., Renn, A. & Sandoghdar, V. Imaging a Single Quantum Dot When It Is Dark. *Nano Letters* **9,** 926–929 (2009).

243. Jollans, T., Baaske, M. D. & Orrit, M. Nonfluorescent Optical Probing of Single Molecules and Nanoparticles. *The Journal of Physical Chemistry C* **123,** 14107–14117 (2019).

244. Taylor, R. W. & Sandoghdar, V. Interferometric Scattering Microscopy: Seeing Single Nanoparticles and Molecules via Rayleigh Scattering. *Nano Letters* **19,** 4827–4835 (2019).

245. Lindfors, K., Kalkbrenner, T., Stoller, P. & Sandoghdar, V. Detection and Spectroscopy of Gold Nanoparticles Using Supercontinuum White Light Confocal Microscopy. *Phys. Rev. Lett.* **93,** 037401 (3 2004).

246. *Nirvana Auto-Balanced Photoreceivers - Model 2007 & 2017 User's Manual* (Newport).

247. Heilmann, R. *Rauschen in der Sensorik* ISBN: 978-3-658-29214-0 (Springer Vieweg, Wiesbaden, 2020).

248. Yurek, A., Taylor, H., Goldberg, L., Weller, J. & Dandridge, A. Quantum noise in superluminescent diodes. *IEEE Journal of Quantum Electronics* **22,** 522–527 (1986).

249. Wang, J., Jiu, J., Araki, T., Nogi, M., Sugahara, T., Nagao, S., Koga, H., He, P. & Suganuma, K. Silver Nanowire Electrodes: Conductivity Improvement Without Post-treatment and Application in Capacitive Pressure Sensors. *Nano-Micro Letters* **7,** 51–58 (2015).

250. Jiang, W., Hu, H., Deng, Q., Zhang, S. & Xu, H. Temperature-dependent dark-field scattering of single plasmonic nanocavity. *Nanophotonics* **9,** 3347–3356 (2020).

251. Tserkezis, C., Esteban, R., Sigle, D. O., Mertens, J., Herrmann, L. O., Baumberg, J. J. & Aizpurua, J. Hybridization of plasmonic antenna and cavity modes: Extreme optics of nanoparticle-on-mirror nanogaps. *Phys. Rev. A* **92,** 053811 (5 2015).

252. Li, Y., Hu, H., Jiang, W., Shi, J., Halas, N. J., Nordlander, P., Zhang, S. & Xu, H. Duplicating Plasmonic Hotspots by Matched Nanoantenna Pairs for Remote Nanogap Enhanced Spectroscopy. *Nano Letters* **20,** 3499–3505 (2020).

253. Galanakis, I., Papanikolaou, N. & Dederichs, P. Applicability of the broken-bond rule to the surface energy of the fcc metals. *Surface Science* **511,** 1 –12 (2002).

254. Sun, Y., Mayers, B., Herricks, T. & Xia, Y. Polyol Synthesis of Uniform Silver Nanowires: A Plausible Growth Mechanism and the Supporting Evidence. *Nano Letters* **3,** 955–960 (2003).

255. Zhou, P., Peng, H., Chen, Y., Xu, H., Jia, B. & Xiao, Q. Independence between intensity and phase noise of superluminescent diodes in the low-frequency domain. *Appl. Opt.* **56,** 8275–8282 (2017).

256. Yurek, A., Goldberg, L., Weller, J. & Taylor, H. Fringe visibility and phase noise in superluminescent diodes. *IEEE Journal of Quantum Electronics* **23,** 1256–1260 (1987).

257. Khurgin, J. B. & Boltasseva, A. Reflecting upon the losses in plasmonics and metamaterials. *MRS Bulletin* **37,** 768–779 (2012).

258. Khurgin, J. B. How to deal with the loss in plasmonics and metamaterials. *Nature Nanotechnology* **10,** 2–6 (1 2015).

259. Heeres, R. W., Kouwenhoven, L. P. & Zwiller, V. Quantum interference in plasmonic circuits. *Nature Nanotechnology* **8,** 719–722 (2013).

260. Falk, A. L., Koppens, F. H. L., Yu, C. L., Kang, K., de Leon Snapp, N., Akimov, A. V., Jo, M.-H., Lukin, M. D. & Park, H. Near-field electrical detection of optical plasmons and single-plasmon sources. *Nature Physics* **5,** 475–479 (2009).

261. Heeres, R. W., Dorenbos, S. N., Koene, B., Solomon, G. S., Kouwenhoven, L. P. & Zwiller, V. On-Chip Single Plasmon Detection. *Nano Letters* **10,** 661–664 (2010).

262. Zadeh, I. E., Elshaari, A. W., Jöns, K. D., Fognini, A., Dalacu, D., Poole, P. J., Reimer, M. E. & Zwiller, V. Deterministic Integration of Single Photon Sources in Silicon Based Photonic Circuits. *Nano Letters* **16,** 2289–2294 (2016).

263. Møller, U., Sørensen, S. T., Jakobsen, C., Johansen, J., Moselund, P. M., Thomsen, C. L. & Bang, O. Power dependence of supercontinuum noise in uniform and tapered PCFs. *Opt. Express* **20,** 2851–2857 (2012).

264. Goda, K. & Jalali, B. Dispersive Fourier transformation for fast continuous single-shot measurements. *Nature Photonics* **7,** 1749–4893 (2013).

265. Lafargue, C., Bolger, J., Genty, G., Dias, F., Dudley, J. M. & Eggleton, B. J. Direct detection of optical rogue wave energy statistics in supercontinuum generation. *Electronics Letters* **45,** 217–219 (2009).

EIDESSTATTLICHE VERSICHERUNG

Hiermit versichere ich an Eides statt, dass ich die vorliegende Arbeit selbstständig verfasst und keine anderen als die von mir angegebenen Quellen und Hilfsmittel verwendet habe.

Weiterhin erkläre ich, dass ich die Hilfe von gewerblichen Promotionsberatern bzw. –vermittlern oder ähnlichen Dienstleistern weder bisher in Anspruch genommen habe, noch künftig in Anspruch nehmen werde.

Zusätzlich erkläre ich hiermit, dass ich keinerlei frühere Promotionsversuche unternommen habe.

Bayreuth, den

Christian Andreas Schörner

COLOPHON

This document was typeset using the typographical look-and-feel `classicthesis` developed by André Miede and Ivo Pletikosić. The style was inspired by Robert Bringhurst's seminal book on typography "*The Elements of Typographic Style*".